Studying the Time Response of a Vacuum Phototriode and Measurement of Gamma Radiation Damage to High Voltage Capacitors and Resistors

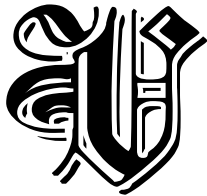A thesis submitted for the degree of Doctor of Philosophy

By

Ignacio Yaselli

School of Engineering and Design

Brunel University

October 2008

Abstract

acuum phototriodes (VPT) are the photodetectors used in the endcaps of the Electromagnetic Calorimeter of the Compact Muon Solenoid experiment at the Large Hadron Collider at CERN. Software, interfacing with the commercial program "SIMION 3D" was written to allow the simulation of the temporal response of the VPT. Applying Ramo's Theorem enabled the time development of the VPT signal to be calculated. In order to validate the simulations, experiments were performed using a 60 ps laser pulses (λ = 435 nm) incident on a number of VPT samples. The simulation reproduced the basic features of the operation of the VPT such as gain vs. voltage, and gain vs. magnetic field strength. The simulation also confirmed the need for a fine mesh anode to achieve a useful gain when operating at high magnetic fields.

The experimental work represents the first measurements of the time response of a VPT when excited with a very fast light pulse. Both the simulated and experimental response from the VPT were observed to be fast (few ns) and quite complex. Discrepancies between the simulated and experimental signals were partially explained by a SPICE model which includes the VPT inter-electrode capacitances and lead inductances. We conclude that the VPT are fast photodetectors with an intrinsic response time of order 1ns for this geometry.

The VPT high-voltage filter cards, which operate at 1 kV and in an intense radiation environment, are critical components. A number of commercial off-the-shelf high voltage resistors and capacitors were evaluated at gamma doses up to 345 kGy. No significant change in value or leakage current was observed. As a result of these studies we were able to demonstrate that these inexpensive components were suitable for use in the 3100 filter cards subsequently installed in the CMS apparatus.

Acknowledgments

This thesis would not have been possible without the guidance of my supervisor Prof. Peter Hobson, and without the inspiration and support of my wife Maria Alejandra who has bearded with me throughout my research. I would also like to thank my mother for making me believe I was doing something important, and my mother in law for believing and investing in me.

I have a heartfelt "thank you" for my GP Dr M Marshall from Brunel's medical centre, my surgeon Mr Spalding and his team from Hammersmith Hospital for giving me back my health.

I would also like to thank David Cockerill for his inputs in the final chapters of this thesis, Christopher Selby who assembled the jigs for the experiments, and Dr D Leslie who very kindly agreed to proof read this thesis.

Finally, this project was founded by the Science & Technology Facilities Council.

Table of Content

Chapter 1 Introduction

I n 2008 the world's largest particle accelerator, the "Large Hadron Collider" (LHC), will begin its operation. It is a 27 km diameter ring buried 100 m under the outskirts of Geneva. Four main experiments with acronyms ATLAS, CMS, ALICE and LHCb, will try to answer some of the question proposed by the Standard Model of Particle Physics, specially the one which relates to the Highs Boson and the origin of mass, by analysing the aftermath of a head on collision of two protons each at a centre-of-mass energy of 7 TeV [1].

The "Compact Muon Solenoid" (CMS) [1] is one of these experiments. It was designed to have a very good muon detection system and was engineered around a 4 T solenoid magnet. The large internal radius of the magnet (3 m) allowed the calorimeters (HCAL & ECAL) to be installed inside the solenoid, as it can be seen from Figure 1-1.
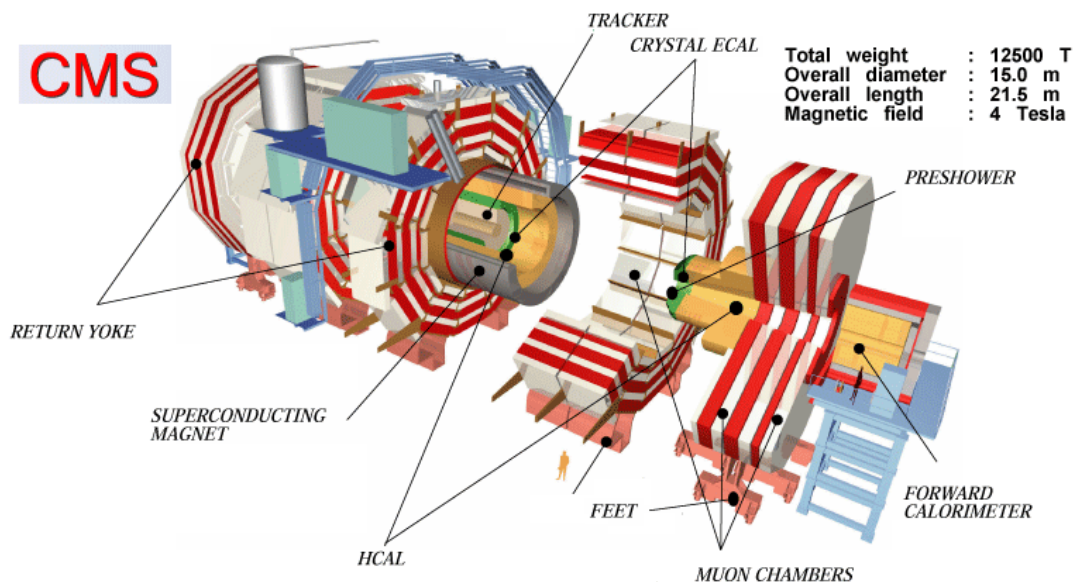
Figure 1-1 the Compact Muon Solenoid (CMS) [2]

The Hadron Calorimeter (HCAL) consist of layers of dense materials (brass or steel) interleaved with plastic scintillator (or quartz strips) with the purpose of measuring the energy of hadrons such as pions, kaons, protons, and neutrons.

The Electromagnetic Calorimeter (ECAL) consists of an array of lead tungstate crystal attached to photodetectors (either APD or VPT). This provides a high resolution measurement of the energy of electrons and photons which is important in order to satisfy the requirements for detecting the Higgs Boson decay into two photons.

Finally, the Tracker is made from silicon strip sensors to measure the momentum of charged particles and the mass to charge ratio from the curvature of the trajectory of these particles as they move in the 4 T magnetic field.
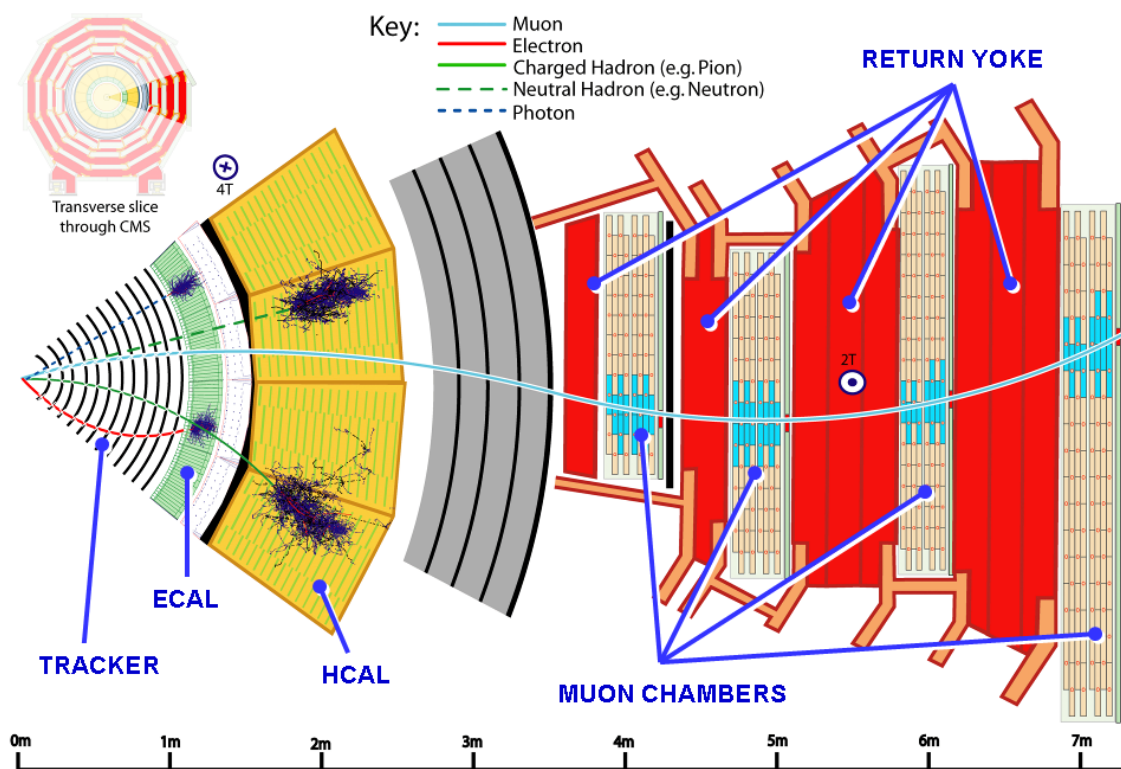
Figure 1-2 CMS transverse slice showing the different CMS systems, and typical interactions of elementary particles [2].

Each event is analysed by identifying the resulting particles from the proton collision by the characteristic signature of their trail. For example:

Electrons interact with the Tracker by ionizing the individual silicon strips layers before being completely absorbed at the ECAL. Photons on the other hand do not interact with the tracker (unless they pair-convert), but are absorbed completely by the ECAL. Positrons have a signature similar to the electrons, but due to their opposing charge, their trajectory bends to the other

way. In the case of a charged hadron such as a pion, it will deposit the majority of its energy at the HCAL instead of the ECAL. Neutrons (which are hadrons) will be absorbed by the HCAL, but since they have no charge their trajectory will not be bent by the magnetic field, so their signature is the energy deposit they leave at the HCAL. Finally, a muon will not be absorbed, but as they are charged, they leave a ionization trail which bent twice in opposite directions due to the fact that that the magnetic field is reversed in the return yoke.

The energy of electrons and photons is measured by the ECAL using the scintillation process in the lead tungstate crystals that occurs when the crystals are ionised by these particles. The intensity of the light emitted depends linearly on the on the energy of the ionising particle and is detected by a photodetector which is glued to the rear end of the crystal. In the endcaps, these photo detectors are the vacuum phototriode (VPT).
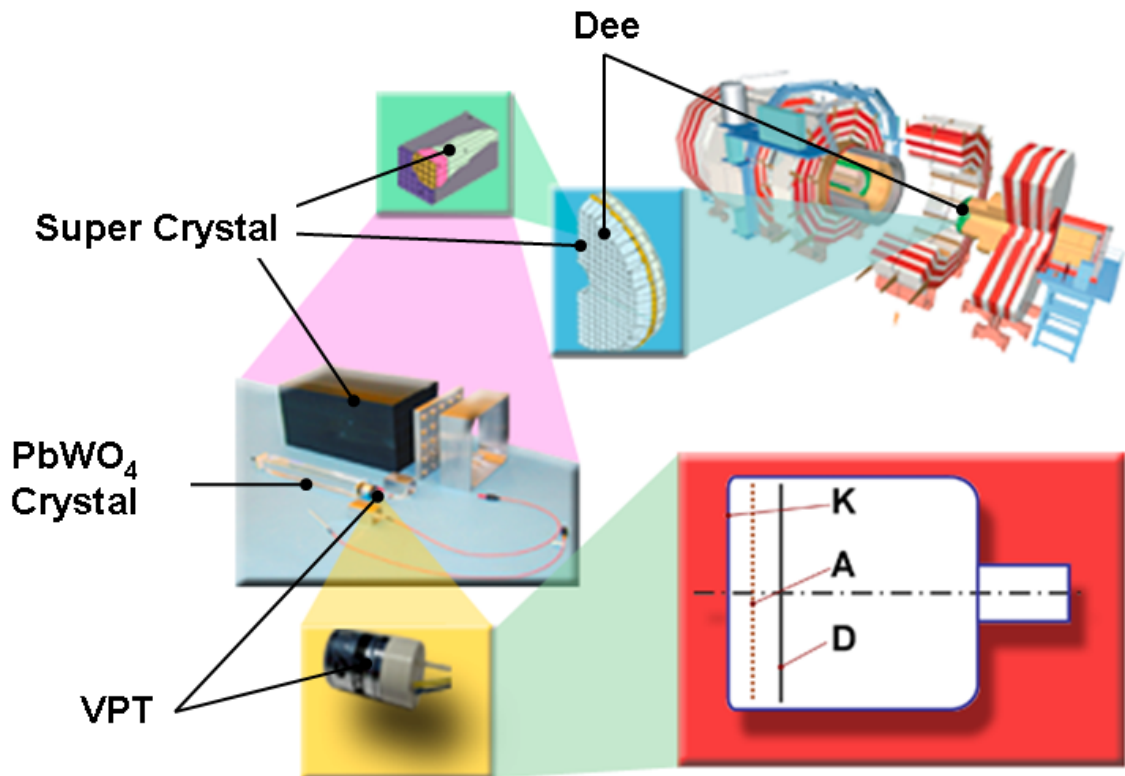
Figure 1-3 VPT in CMS: The VPT are glued to the PbWO$_4$ crystals which are grouped in set of 25 to form supercrystals. These supercrystals cover the detector side of the Dees. There are two Dees on each of the two Endcaps [1].

As can be seen in Figure 1-3, a subdetector known as supercrystal is formed from 25 $PbWO_4$ crystals arranged in a 5×5 matrix, each of which with a VPT glued at the rear end. The ECAL endcaps are formed by two Dees which in turn are constructed from 138 complete supercrystals and 18 partial supercrystals. This means that in total each Dee contains 3662 crystals and VPT [1].

From the beam's perspective, the ECAL Endcaps were design to cover the pseudorapidity range from 1.49 to 3.0. The pseudorapidity (η) is a Lorents invariant coordinate defined as $η=-\ln(\tanθ/2)$, where θ is the angle of the particle motion with respect to the primary beam axis. This is equivalent to a range of 5° to 26° relative to the beam axis.

It is predicted that the LHC will produce 8×10^8 [1] inelastic collisions per second, and as it can be seen from Figure 1-4 and Figure 1-6, the radiation dose of the ECAL endcaps could go up to $5 \ kGy/year$, and as seen from Figure 1-5 the neutron and charged hadron fluence may reach $2.2 \times 10^{14} \ cm^{-2}$ [3]. Because of the latter, the ECAL endcaps would be a very harsh environment for silicon detectors such as avalanche photo diodes (APD), which had to be confined at the barrel region where the radiation dose is much lower.
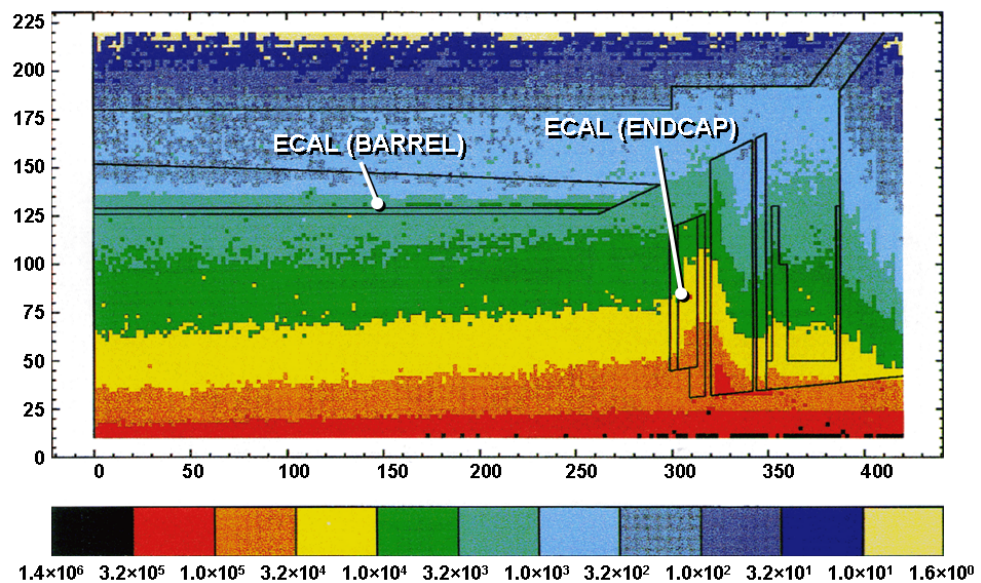
Figure 1-4 The absorbed dose (Gy) in the tracker and in the ECAL region of CMS [3].
Values correspond to an integrated luminosity of $5 \times 10^5 \ pb^{-1}$ [3]. (Axes in cm)
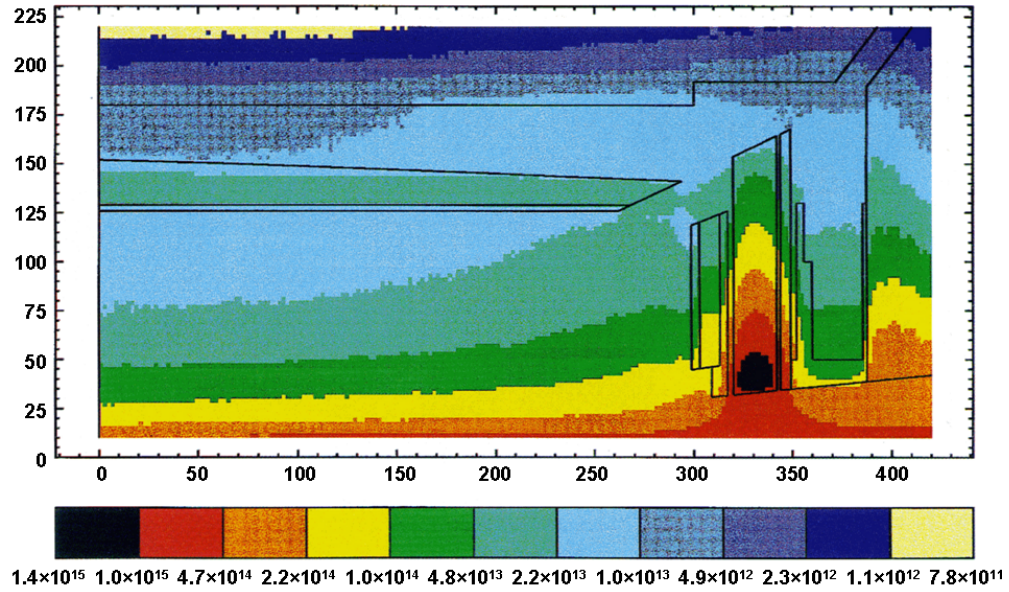
Figure 1-5 The neutron and charged hadron fluence (cm⁻²) for E > 100 keV in the tracker and in the ECAL region of CMS. Values correspond to an integrated luminosity of 5×10^5 pb⁻¹ [3]. (Axes in cm)
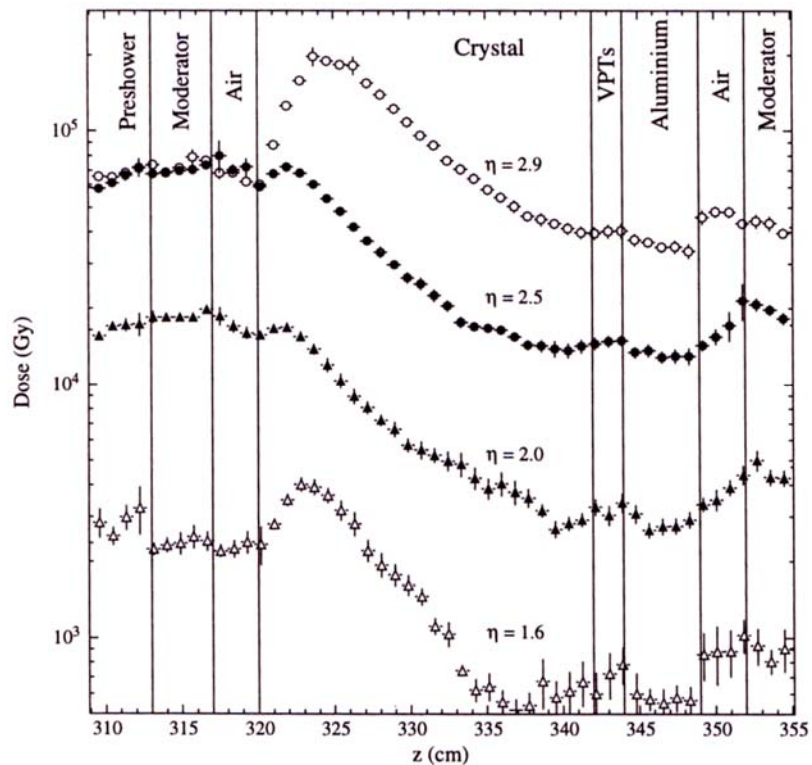
Figure 1-6 Total dose in the endcap crystals for four η-values A $\eta = 1.6$ is close to the endcap/barrel junction region this (equivalent to $\theta = 22.82°$); and $\eta = 2.9$ is nearly at the centremost edge of the endcap (equivalent to $\theta = 6.29°$). All values correspond to an integrated luminosity of 5×10^5 pb⁻¹ [3].

The photomultiplier tubes are the vacuum equivalent to avalanche photodiodes; however, contrary to APD, a photomultiplier can be manufactured to operate in environments with a very high neutron fluence. The high gain from these devices comes from the multiple dynodes, each of which provides a further stage of electron multiplication and therefore an avalanche effect as shown in Figure 1-7. The potential given to the dynodes resembles a voltage divider, supplying increasing voltages from the cathode to the anode.
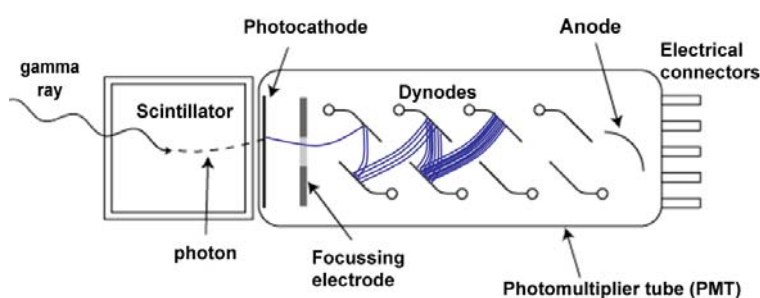
Figure 1-7 A photomultiplier in zero magnetic field.
A multi stage dynode configuration allows a high gain (10^6) photodetector by creating an avalanche of electrons. The number of electrons is increased at every dynode in a proportional ratio to the incident electrons energy. The dynodes voltages are based on a voltage divider providing incremental voltages along the tube, and towards the anode.

As it can be seen from Figure 1-8, the magnetic forces acting on the electrons force them on paths parallel to the field lines, interrupting the avalanche of electrons by impeding electron reaching the next dynode. When using photomultipliers on magnetic environments, they are usually wrapped on a mu metal film. These acts as the equivalent of a Faraday cage on a magnetic environment, but they saturate and thus become ineffective shielding for $B > 0.7\ \mathrm{T}$. Because of this, conventional photomultipliers cannot to be used on the ECAL of CMS.
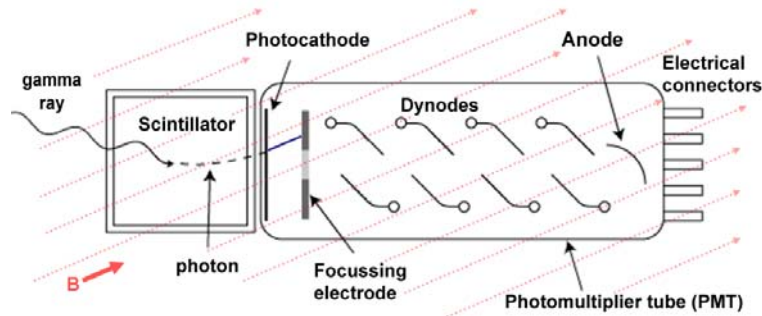
Figure 1-8 a photomultiplier in a strong uniform magnetic field.
Magnetic field forces electrons to a trajectory parallel to the field lines. Because of this, the avalanche of electrons in the photomultiplier tube can not reach consecutive dynodes, and therefore can not make progress

   Fine mesh vacuum photodetector have been used in calorimeters of previous experiments at the LEP such as phototriodes in OPAL and phototetrodes in the STIC detector of DELPHI. Vacuum phototriodes (VPT) have three electrodes parallel to each other, with the fine mesh anode between the photocathode and the dynode. The cathode converts the light flux into an electron flux, the dynode multiplies the number of electrons by the process of secondary electron emission, and the anode collects the signal and serves as the output for the VPT. Phototetrodes are similar to VPT only that they have an extra dynode which is transmissive and is located within the cathode and the anode.

Experiment:	CMS [4]	OPAL [5]	DELPHI [6]
Device:	VPT	VPT	phototetrode
Manufacturer:	RIE	Philips	Hamamatsu
Model:	FEU 190	RTC 1501/FL	2149-03
Cathode diameter:	18 mm	76.2 mm	22 mm
Cathode type:	bialkali	bialkali	bialkali
QE:	18% @ 430 nm	26% @ 420 nm	10% @ 500 nm
Anode dark current:	< 1 nA	low	~ 0.1 nA
# of dynodes:	1	1	2
Typical Gain at 0T:	10	21	30
Typical gain at 4T:	8 @ 15°	--	~ 8 @ 15°

Table 1-1 comparison between fine mesh vacuum photodetectors.
The parameter for each of the devices were taken from their respective experiment collaborations.

In comparison, at zero magnetic field, phototetrodes have a larger gain than VPT mainly due to the extra stage of electron multiplication, however, at 4 T the phototetrodes and the VPT have similar gains which means that the gain falls drastically on phototetrodes when compared to VPT. Furthermore, in the range of 3 T – 4 T while the gain of the VPT is less affected by the variation on the strength of the magnetic field, it is not so with phototetrodes. Because of this VPT were selected over the phototetrodes for the ECAL endcaps of CMS.

One of the reasons for using VPT in the CMS ECAL endcaps is that they are proven technology. However, there is neither data nor simulation on the time response of these potentially very fast devices. Adding to the understanding of these important photodetectors would provide a huge advantage in their design improvement and consideration for their use in future experiments.

The development of a computer model is also important due to the fact that there are limitations to the experimental measurements of the VPT performance. The UK CMS group has two magnets at their disposal for testing VPT: the superconducting magnet at Brunel University operates at 4 T for a fixed VPT angle to the field of 15°; while at the Rutherford Appleton Laboratory (RAL) there is a magnet which allows testing at various axial field angles, but at maximum strength of 1.8 T. Because of this, and due to the fact that VPT will be used at angles up to 26° at a uniform field of 4 T[*], it raises the importance of being able to predict the response of a VPT outside of the measuring capabilities of the UK CMS group. A good simulation (i.e. one which matches real data well), would give us confidence that we can predict the VPT behaviour at 4 T and at any angle; furthermore, it would allow for the development of improved configurations of VPT structure (non-planar dynodes for example).

The importance of the time response of the VPT comes from their application. At the LHC primary collisions occur every 25 ns. The response of a photodetector should be fast enough to prevent a signal overlap from multiple events. The VPT are glued to the rear end of a $PbWO_4$ crystal, which emits

---

[*] Since the supercrystals are supposed to cover the pseudorapidity range down to 1.48, and since the magnetic field is uniform and parallel to the beam axis, it is equivalent to say that the VPT will be operating at an angle up to 26° relative to the magnetic field.

light when it is ionised by electrons, positrons and photons. The violet-blue scintillation light illuminates the VPT's photocathode releasing photoelectrons which are accelerated towards the anode due to the potential difference between the cathode and the anode ($V_K \ll V_A$), where some of these photoelectrons will be absorbed by hitting any of the wires of the anode mesh. The photoelectrons that pass though the gap between the mesh wires are slightly decelerated (due to the anode-dynode potential difference $V_A > V_D$) before they hit the dynode. The collision of a photoelectron with the dynode's surface can result in the release of many secondary electrons which are accelerated back towards the anode. The moving electrons induce a current to flow in the anode, the magnitude of which depends not only on the number of photons hitting the cathode, but also on the bias of the VPT.

The first part of the thesis is about VPT, the simulation model created for understanding them, and the experimental measurement of their time response characteristics. In contrast to the second part, this one was not time critical, in fact, the VPT were already prototyped, tested, and ordered before the beginning of this project. Furthermore, the VPT that were used in these experiments are from a batch which has been mass produced, and are being used in the supercrystals that will be installed on the endcap calorimeter of CMS.

From the outset, it was decided that the computer model will be centred around the use of a software package known as SIMION7 for two reasons:

- The first reason is due to economical aspects, other alternatives like CPO are available, but these are much more expensive ($15,000 US for CPO vs. $1,000 US for SIMION [7]), and in addition, their licences require renovation each year. SIMION on the other hand, does not require renewal of licenses, and the price of the package is much more affordable.
- The second reason is that there was already some familiarity in the Brunel HEP Group with this package.

SIMION 3D version 7.0 (SIMION7) was designed for the modelling of complex problems requiring electrostatic simulations of charged particles [8]. The

simulations are done in an environment known as the workbench where the potential arrays of the electrode structures can be loaded. The charged particles used for the simulation of VPT are electrons, which are defined (in the SIMION7 environment) as a special case of an ion with a specific mass and charge.

In order to create the computer model, a production VPT was cut open so that the measurements of the internal structure could be taken with the purpose of implementing the potential arrays. These measurements were taken and repeated several times throughout the research using a digital caliper, with an accuracy of $\pm 0.02\,\text{mm}$. In addition, as explained in Chapter 6, the measurements of the internal structure were also used to calculate the capacitances between the electrodes and the inductances on each of the leads of the VPT, so as to create an electronic equivalent of the VPT for Spice simulations.

One of the trades off in the SIMION7 software, with respect to the more expensive alternatives such as CPO, is the inability to simulate secondary emissions. Because of this, a separate program was written to simulate the dynode properties of electron multiplication. In addition this new program was needed to collect the data generated by the tracking of electrons by SIMION, in order to compute the current induced at the anode. This program was called SADYS due to its main purposes: Signal Analysis and DYnode Simulation.

In order to test the results from the simulation, apparatus was set up which fired a $60\,\text{ps}$ pulse from a 435 nm laser onto a real VPT. The signal was measured with a digital oscilloscope sampling at a rate of $10\,\text{G}$ samples/second with an analogue bandwidth of 3 GHz. Different experiments were carried out in order to match each of the simulations. However, the experimental apparatus for measuring the time response of the VPT were too bulky for the superconducting magnet at Brunel, and therefore experiments under magnetic field were not undertaken.

In CMS the VPT are connected to the biasing voltages and to the readout system by a HV filter card. This acts as a low pass filter from the biasing voltage to the VPT (eliminating noise at the HV lines) and a high pass filter between the

VPT and the preamplifier eliminating the high DC voltages from the bias and protecting the preamplifier from discharges from the VPT.

Due to its proximity to the VPT, these filters have to survive the same harsh radiation environments. This raised the importance of selecting components which could survive such environments.

As opposed to space launched equipment, where they benefit from a huge budget for a very limited amount of components, where they could spend tens or hundreds of pounds per component, the CMS experiment could not afford custom made radiation hard component supplied by specialist manufacturers. However, it was known that certain types of commercial off-the-shelf components may be radiation tolerant, but as they are not manufactured on strict guidelines, the radiation tolerance could be different from batch to batch.

This brings the importance of the second part of the project. It was necessary to determine which type of resistors and capacitors that would change the least during their working life under the high radiation levels they will be operating in CMS. Furthermore, this part of the project was also time critical, because a total of 3100 HV filter cards had to be made, and the data supplied by these experiments would only be relevant to a particular batch of components.

Capacitors and resistors were thoroughly tested before and after irradiation. However, due to some changes in the filter design, a new set of components needed the same study. In order to avoid confusion between the different set of components, the results for each set are given in different chapters.

All the work in this project: measurements of the internal structure of the VPT; experimental work on the VPT, capacitors and resistors; modelling, simulation and data analysis of the VPT; was done by myself. This excludes the calculation of the lead inductance of the VPT, the Spice simulation of the experimental setup, and the calculation of the radiation dose of the resistors and capacitors which was done by my supervisor Prof. Peter Hobson.

References

1 S Chatrchyan et al., *"The CMS experiment at the CERN LHC"* <u>Journal of Instrumentation</u> **3** (2008) S08004

2 The CMS collaboration [online]. Available: <u>http://cms.cern.ch/</u> [accessed on 14 May 2008]

3 CMS The Electromagnetic Calorimeter Project, Technical Design Report CERN/LHCC 97-33, CMS TDR 4, 15 December 1997 [online]. Available <u>http://cmsdoc.cern.ch/cms/TDR/ECAL/ecal.html</u> [accessed on 09 May 2008]

4 N.A. Bajanov, et al., "*Fine-mesh photodetectors for CMS Endcap electromagnetic calorimeter.*" <u>Nuclear Instruments and Methods in Physics Research A</u> **442** (2000): 146-149.

5 M. Akrawy et al., "*Development studies for the OPAL end cap electromagnetic calorimeter using vacuum photo triode instrumented leadglass*", <u>Nuclear Instruments and Methods in Physics Research Section A</u>, **290.1**, (1990): 76-94

6 M. Bonesini, et al., "*Study of Hamamatsu R2149 phototetrodes in magnetic field*". DELPHI 96-175 CAL 133 (December 1996)

7 Scientific Instrument Service website "<u>http://www.sisweb.com/</u>" (20/02/2008)

8 David A. Dahl, "*SIMION 3D version 7.0 User's Manual*", <u>Idaho National Engineering and Environmental Laboratory</u> (Feb 2000)

Chapter 2 Theory of the VPT

acuum Phototriodes (VPT) are devices that convert a light pulse into an electrical signal whose magnitude is proportional to the light's intensity. This is done by a three step process: first light flux is converted into an electron flux at the photocathode; then, this electron flux is amplified at the dynode by a process of secondary emission. While the electrons move within the VPT, they induce a current at the anode which is taken out as the signal.

In the VPT discussed in this thesis the three electrodes are parallel to each other, with the anode between the photocathode and the dynode such as shown in Figure 2-1. The electrons released from the cathode are accelerated towards the anode due to the electric field that exists between the photocathode and anode. The anode is a mesh which absorbs a proportion of the electrons that hit its wires. The electrons which are not absorbed by the anode (i.e. the proportion that pass though the gaps between the wires) make their way to the dynode. When electrons hit the dynode, they release secondary electrons in a proportion relative to the incident electrons energy. Due to the positive potential difference between anode and dynode, the secondary electrons are also accelerated towards the anode. Due to absorption at the anode, the secondary electrons may have three different trajectories: they may be directly absorbed by the anode; some will pass the anode, but are absorbed as they are accelerated back; and the remaining electrons that pass the anode a second time and are absorbed at the dynode. These secondary dynode hits may release tertiary electrons if they have sufficient energy.

In CMS, the VPT would be biased close to their operation limit at $V_K = 0\,V$, $V_A = 1000\,V$ and $V_D = 800\,V$. These voltages allow a strong acceleration for the photoelectrons at the cathode-anode region, as well as a strong deceleration for the secondary electron that pass through the anode. The anode-dynode potential difference accelerates the secondary electrons towards

the anode; therefore, it is required that $V_A > V_D$. However, if the anode voltage is much greater than the dynode voltage ($V_A \gg V_D$), the photoelectrons would decelerate too much and would have no energy left for releasing secondary electrons. These biasing voltages satisfy the highest gain by setting the anode at operating limit and setting the dynode close to its optimum voltage for a maximum number of secondary electrons and a reasonable acceleration. The effect of different biasing voltages will be seen in Chapter 5 for the simulated signal and Chapter 6 for the experimental measurements.
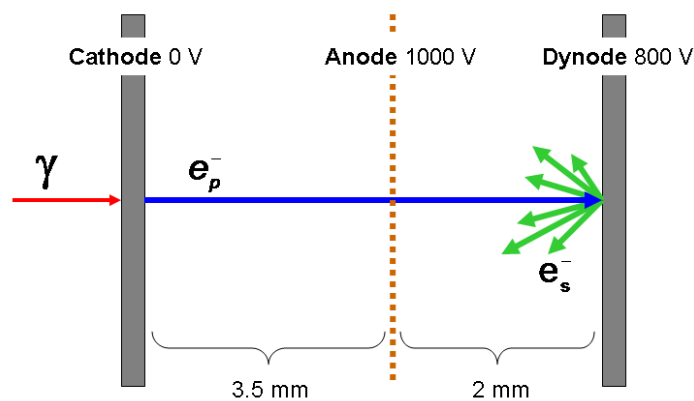
Figure 2-1 Typical VPT configuration: photons (in red) release photoelectrons (in blue) from the cathode which travel through the VPT passing the anode and hitting the dynode releasing secondary electrons (in green).

In order to allow DC coupling to the oscilloscope in the experimental set-up, V_A is held to ground via a $50\,\Omega$ resistance, so in order to keep the same potential difference with respect to the anode, the cathode and dynode were set to $V_K = \text{-1000 V}$ and $V_D = \text{-200 V}$.

In order to create a model of the VPT, it is required to know the internal structure characteristics. The production technical specification for the VPT states that:

- The overall length ≤ 46.0 mm
- The seal off stub shall be protected and covered completely by the base (socle).
- External diameter $= 26.5\,^{+0.0}_{-0.7}$ mm .
- Measured over the conductive coating and the insulating film applied to the glass envelope.

- External diameter of the VPT base (socle) = $26.5\,^{+0}_{-1.2}$ mm .

- The envelope shall be coated with a conducting paint connected to the cathode pin and protected by a thin, insulating sleeve.

- The angle between the normal to the VPT faceplate and the axis of the cylindrical envelope shall be $\leq 1°$.

- The face plate planarity shall be $\pm 50\,m$, concave or convex.

- The active diameter of the anode mesh shall be $\geq 19.0\,mm$ and the photocathode diameter shall be ≥ 22.0 mm .

- The construction schematics produced by the manufacturer Research Institute Electron (RIE) are given in the drawing PAГC.433242.012 Г4 (Figure 2-2)
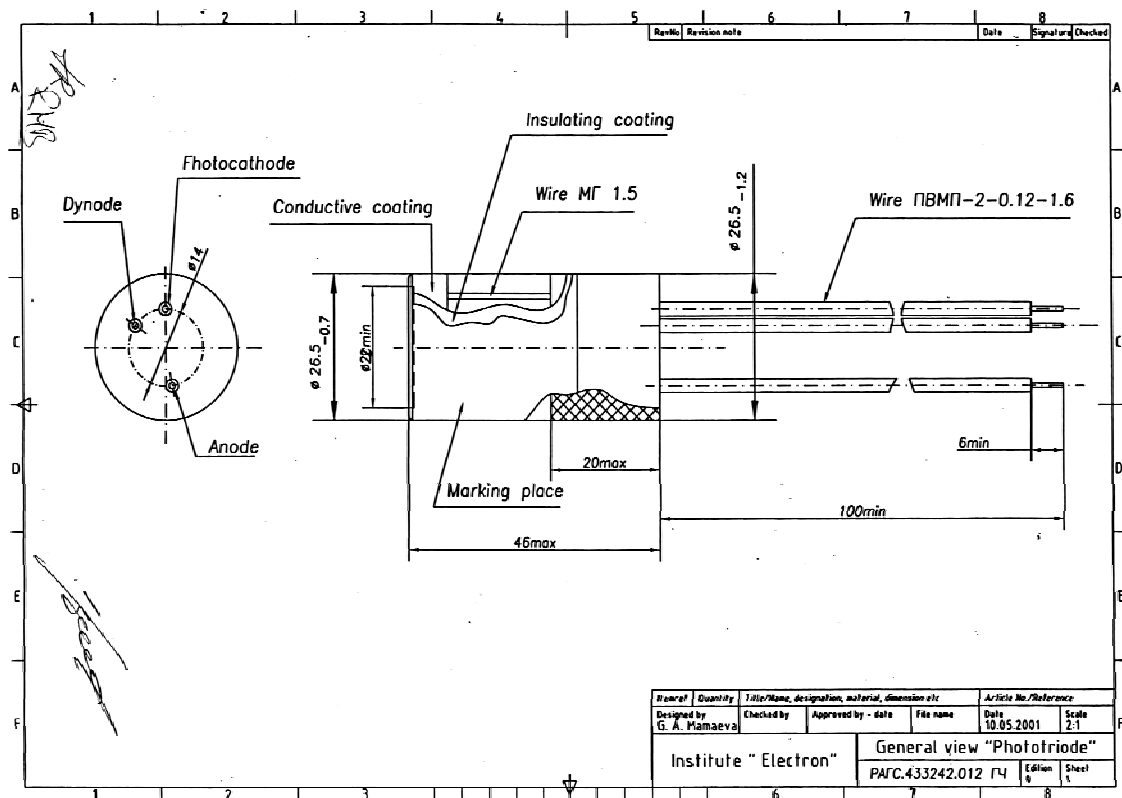
Figure 2-2 VPT production technical specification drawing [1]

As it can be seen from the technical specification, the information available about the internal dimensions of the VPT was very vague as shown in Figure 2-2. The technical drawing does not show the separation between the electrodes. Furthermore, for the manufactured VPT, the anode mesh is supported by a ring which is not known if it has been considered. Moreover, the manufacturing process might have included a slight error on the dimensions and separations of the electrodes, albeit within tolerance, and hence introduce a

slight different from the specifications. However, it can be safely assumed that the manufacturing process would produce standardized VPTs which dimensions should not differ considerably between devices.

Because of all of this, it was decided that for accurately modelling a RIE VPT[†], it would be necessary to measure the internal structure of a production line VPT. In order to do this, a random VPT[‡] was cut open and delivered to Brunel University from the Rutherford Appleton Laboratory (RAL).

Figure 2-3 shows a RIE VPT at various stages of opening, so that measurements could take place.

(a)   (b)   (c)
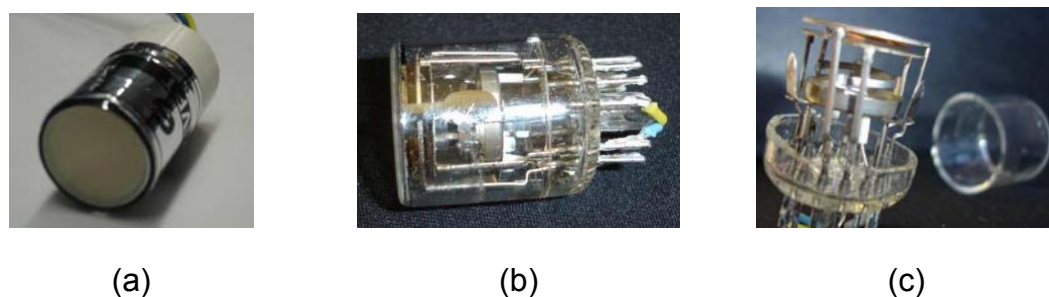
Figure 2-3: Real Production RIE VPT. (a) Standard VPT before opening. (b) Cut VPT, anode and dynode are now visible through the glass. (c) Cut and opened VPT in display.

Figure 2-4 shows the measured components as well as their relative positions. These measurements were repeated several times with a digital caliper[§] to ensure that the dimensions of the internal structure accurately describe the device. These measurements were verified later for reasons explained in Chapter 6.

[†] These are the actual VPT being installed in CMS

[‡] This particular VPT was taken from a approved production batch and could have been installed in CMS, therefore, the measurements and hence the model can be assumed to be representative of the devices use in the endcaps.

[§] The Digital caliper used was a WORKSHOP Electronic Digital Caliper with a resolution of 0.01 mm and accuracy of ±0.02 mm (< 100 mm)

Figure 2-4 shows: top-left: the cathode surrounded by the outer glass of the VPT; bottom-left: the anode mesh (in light brown) surrounded by the anode mesh support ring (in blue); top-right: the dynode; bottom-right: the separation and thickness of the electrodes, note the cathode-anode separation from the inside of the glass, and the thickness of the anode mesh is only a fraction of the supporting ring.
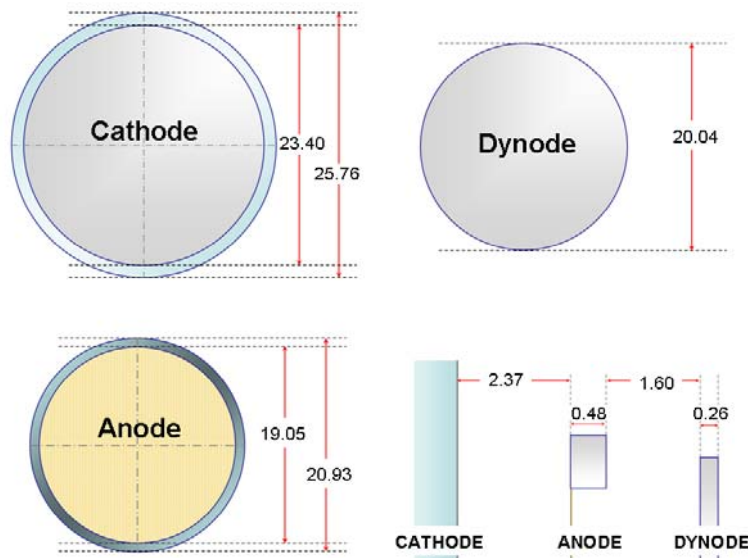
Figure 2-4: Measurements (in millimetres) of cathode, anode, dynode and spacing between the electrodes of a cut open production RIE VPT.

On the following pages each part of the VPT is explained as well as how they react to their environment. More importantly, how and why electrons behave the way they do whilst flying[**] inside the VPT.

[**] SIMION7 refers to the moving ions in empty space as to be flying; moreover, the simulation start button is an instruction to make the defined ions to fly. Thus such terminology is consistently used in this thesis in order to differentiate to the movement within a solid such as in the case of the dynode or the cathode which is more commonly associated with drifting.

The cathode and how the photons are converted into photoelectrons.

The cathode is made of two parts: the window, where the light enters the device, is typically made of borosilicate glass[††], and the deposit of photoemissive semiconductor material on the inside, which in the case of the VPT used in CMS is a bialkali compound of potassium caesium antimony KCsSb

When light hits the cathode, only a small portion is absorbed, while most of it does not contribute to the photoemissive process either because it is reflected or because it passed through. The absorbed photons excite electrons which would then drift through the material. Those of which did not loose all of their energy migrating towards the surface, escape to the vacuum. Because these electrons are freed by photons they are called photoelectrons.

However, there are limitations to the photoemission process, which include, at high wavelength the photosensitive threshold of the material (around $600\,\mathrm{nm}$ for $KCsSb$), and at short wavelength the cut-off wavelength of the window ($270\,\mathrm{nm}$ for borosilicate glass). Furthermore, the energy of each electron does not depend on the light intensity because the energy transferred to the photoelectron comes from a single photon[‡‡]. Because of this, depending on the materials thickness, the photons are required to have a minimum energy[§§] such

---

[††] Another material that could be used for the window is quartz due to that it does not change its transparency by irradiation. However, due to differences in the thermal expansion with the rest of the glass body of the device the production cost is too high, making them economically unfeasible in this application.

[‡‡] This relation holds up until very high energies (such as x-ray) where there are more electrons released per photon. However, these considerations are not required due to that the spectrum of light used experimentally and theoretically for the model, does not go that far.

[§§] An exception to this is at very high intensity and focused laser beams, semi-states are created on the surface, where multiple photons can aid to the release of a single electron.

that, not all the transferred energy is lost by the electron trying to escape the cathode.

The ratio between the number of photons and photoelectrons is known as the Quantum Efficiency (QE). For the proposed VPT to be used in CMS, QE ranges from 18% to 20% [2] at light of wavelength $\lambda = 430 \, \text{nm}$. Since QE is characteristic of the device (it can not be modified), in order to increase the number of photoelectrons, the light intensity must be increased.

The Anode

The anode is the electrode where the signal is taken out from. As the electrons move across the VPT, they induce a charge that changes with time, thus creating a current on the anode which is referred as the signal. If the anode was 100% transparent, and therefore all the electrons were able to pass through, the current induced by electrons as they approach the anode would be equal but opposite to the current induced as they move away from the anode. If this signal is then integrated over the period of its duration, as when the signal is amplified, the resulting integrated signal will average zero. To overcome this problem, it was required that the anode had some level of absorption, which is achieved by making it as a mesh with a probability of absorption related to its transparency. Because of this, the anode also affects the signal, affecting it by two parameters: its transparency and its resolution
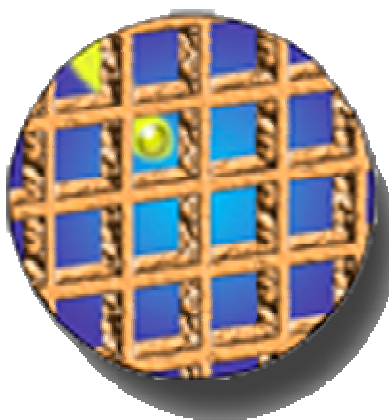
Figure 2-5 Representation of the anode mesh; electrons are absorbed when hitting the solid wires, and let through otherwise

As suggested by Figure 2-5, the mesh can be visualised as inter-crossing vertical and horizontal wires. The transparency of the mesh is given by the proportion of the area of the mesh that is covered by the holes between the wires and the total area of the mesh. Bateman [3] stated that an opaque anode mesh (35% transparent) would absorb most of the electrons abruptly cutting the signal. On the other hand a more transparent mesh (of about 70% transparency) would result in about 10% of the signal being produced by tertiary electrons. Bateman finally suggested that a transparency of 50% should be the optimum, and later found to be correct to a first approximation.

The resolution of the mesh is defined by the number of horizontal (or vertical) wires (lines) for each millimetre (lines/mm). Bajanov [2], investigated the relative gain G/G_0[***] for the VPT with external diameters of 21 and 25 mm, and with anode mesh resolution ranging from 30 to 100 lines per millimetre (lines/mm); all of which were 50% transparent. In this paper, it was claimed that it was important for the purpose of simplification of calibration procedures that G/G_0 remained constant in the range of 3 T to 4 T as the angle of the endcap with the magnetic field varied. This requirement was satisfied by the 60 and 100 lines/mm meshes for an average angle of 15°. The RIE produced FEU -190 with 100 lines/mm VPT was selected for the CMS Endcap as it had a better performance in the range of 6° to 26°.

[***] G/G_0 is the ratio of the gain at high magnetic field (G) with respect to zero field (G_0)

Signal Formation

The acceleration of a charge q with mass m in an electric field E is given by:

$$a = \frac{q \cdot E}{m} \tag{2-1}$$

Due to the planar geometries of the electrodes of the VPT, the electric field will be given by

$$E = \frac{\Delta V}{d} \tag{2-2}$$

were ΔV is the potential difference of the electrodes.
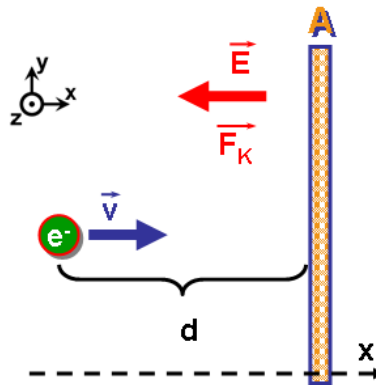
Figure 2-6 an electron in an electric field will move accelerating towards the highest potential. This motion induces a current to flow at an electrode at a distance d from the electron.

When a charge q moves, it induces a current i to flow in an electrode at a distance d from the charge. This current can be calculated using the Shockley–Ramo [4] theorem, which states that:

$$i = -q \cdot \vec{v} \cdot \vec{F}_k \tag{2-3}$$

where $\vec{v}$ is the instantaneous velocity of the charge q; the weighting field $\vec{F}_K$, is the field that q would feel at a distance d of the measuring electrode when it is set to unit potential and the other electrodes set to zero.

The weighting field is **not** an electric field. While the electric field determines the charge trajectory and velocity, the weighting field depends only on geometry; acting as a coupler between the motion of the charge (in this case an electron), and the measuring electrode (in the case of a VPT that would be the

anode). However, from the vectorial point of view, they both point towards the same direction. Moreover, in the special case when the charge is between two planar electrodes, the electric field and the weighting field have the same form.

Equation 2-3 states that the current is a scalar product of two vectors. From this equation one can infer that: a) no current would be induced when the q moves perpendicularly to $\vec{F_K}$, b) the current would be grater when q moves parallel to $\vec{F_K}$. Therefore, if $\vec{v} = [v_X\ v_Y\ v_Z]$ (such that $v_X \perp v_Y \perp v_Z$), and "x" is the axis parallel (but opposite) to $\vec{F_K}$, then $i = q \cdot v_X \cdot F_k$.

In the very special case of a plane-parallel electrode VPT, where electrons would always be between two parallel electrode plates (cathode - anode or anode - dynode), the weighting fields and the electric field would be of the same form. i.e. the electric field at a distance d of the anode would be given by:

$$E = \frac{V}{d} \tag{2-4}$$

The weighting field would then be obtained by setting the anode at unit potential $V_A = 1$ (the dimensions are dropped) and the potential of all the other electrodes are set to zero.

So the weighting field for an electron in a VPT is given by:

$$F_K = \frac{1}{d} \tag{2-5}$$

Finally, the scalar product of the velocity and the weighting field (Eq. 2-1) reveals that the induced current depends on the velocity component parallel to the electric field and not on the perpendicular component. Therefore, if "x" is the axis normal to the anode and hence parallel to the electric field, the induced current in the anode would be:

$$i_A = q_e \cdot v_x \cdot \frac{1}{d} \tag{2-6}$$

where v_x is the velocity component of the electron parallel to the weighting field, and q_e is the charge of the electron.

As will be seen later on in Chapter 3 and Chapter 4, the parameters such as the position, velocity, direction and energy of each electron, are known at every instance of time; therefore from v_x and d, the instantaneous induced current can be computed. Finally, using the principle of superposition, the total current at the anode is calculated by the sum of all the currents due to each electron at the time "t"

$$i_A(t) = \sum_n i_n(t) \qquad\qquad (2\text{-}7)$$

The Dynode

The dynode surface is coated with a material with high secondary electron emission coefficient. Typically, the structures of dynodes are made with AgMg, CuBe and NiAl; this is because the oxide that forms at the exposed surface has a sufficient secondary emission coefficient. Some other materials such as $SbCs_3$, which is a photo emitter, also has a good secondary emission coefficient, and can be deposited on the surface in the same way as is done on photo cathodes [5].

When photoelectrons hit the dynode they release secondary emissions by a three step process. As the primary electron is absorbed, its energy is transferred to electrons in the material. These excited electrons migrate towards the surface loosing energy through inelastic interactions with other electrons. Those with sufficient energy to escape the potential barrier are released contributing to the secondary emission.

There are two main parameters related to the secondary emission, the first one is the number of secondary electrons released from the dynode. This number depends on the secondary emission coefficient (δ) which is characteristic of the dynode's material. As shown in Figure 2-7, the number of secondary electrons increases proportionally to the primary electrons incident energy E_P, until it reaches a maximum at E'_P. Incident electrons with higher energies will release secondary electrons deeper in the material, which after migrating towards the surface their probability to escape the potential barriers start to decrease at a rate $E_P^{1-\alpha}$ [5].
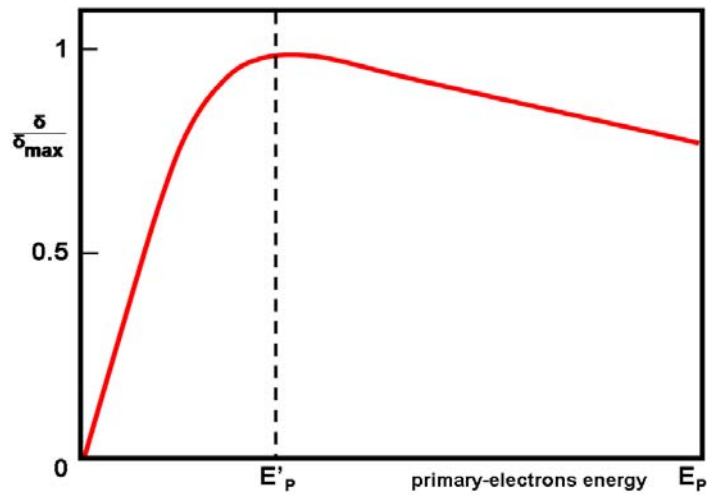
Figure 2-7 Relative variation of secondary emission coefficient δ as a function of primary-electrons energy E_P. For energies above E'_P , δ falls off proportionally to $E_P^{1-\alpha}$ [5]

There are two main parameters related to the secondary emission. The second parameter is the energy spectrum of the released electrons. A typical energy distribution for the secondary electrons is shown in Figure 2-8, note that the part parked by **S** (the distribution of the real secondary electrons) is centred at a few eV (approximately 5 eV for KCsSb dynode) and falls rapidly in either direction. The peak marked with **P** corresponds to primary electrons which are elastically back scattered with almost all of their initial energy.
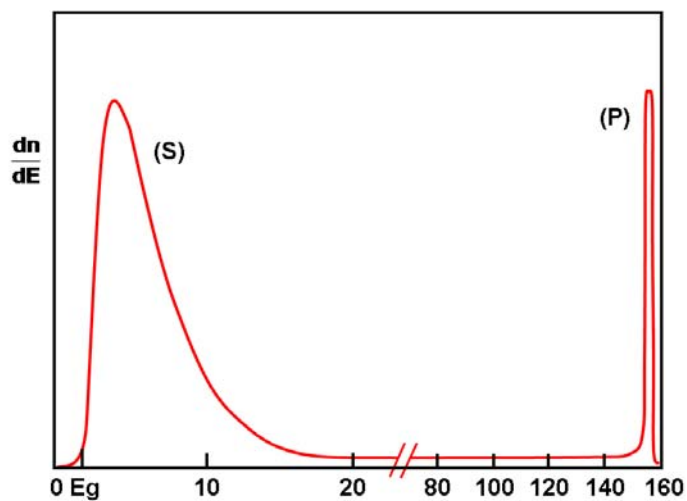
Figure 2-8 Distribution of secondary electrons energies E above the Fermi level E_F [5]

A previous model of a VPT was developed by Bateman [3] in order run a monte carlo simulation of the effect of an axial magnetic field on the gain of the VPT. This model however, was not intended to simulate the timing characteristics of these devices, nor does it model the electrical impulse generated by the VPT.

The distribution of the low energy secondary electrons spectrum of Bateman's model was given by a difference of exponentials with the values of 1eV and 5eV as the scale constants:

$$\frac{dN}{dE_S} = const(e^{-E_S/5} - e^{-E_S/1}),$$
(2-8)

Where E_s is the second emission energy in eV.
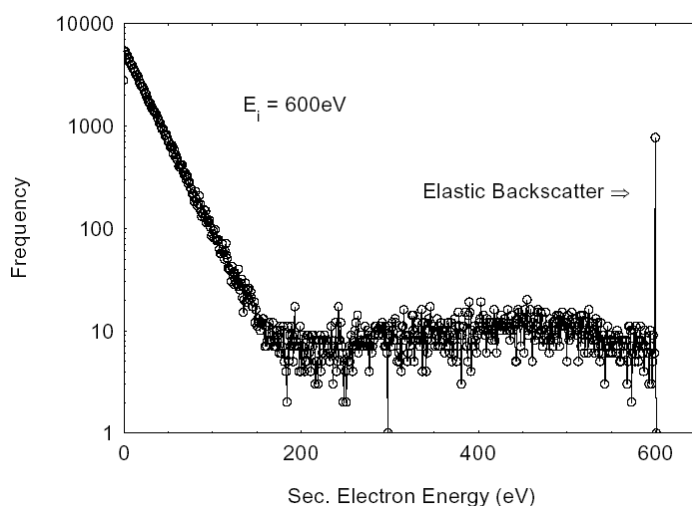
Figure 2-9 "A typical secondary electron spectrum generated by Bateman's model in the case of a CsSb dynode and for an incident electrons energy of E_i = 600 eV . A logarithmic scale is used to show the large dynamic range."

Figure 2-9 shows Bateman's model for the secondary electron energy distribution generated by an incident electron with $600\,eV$.

The second part of Batemans model for the dynode simulation was to compute the number of secondary electrons in proportion to the incident electrons energy E_P. This was done by an exponential approach, so that:

$$n(E_P) \approx N_{max}(1 - e^{-Vd/E_{scale}}) ,$$ (2-9)

where N_{max} is the maximum number of secondary emission obtainable and E_{scale} is the characteristic energy of the surface in eV. These constant where fitted experimentally to values of $N_{MAX} = 35.9$ and $E_{SCALE} = 304$ eV for dynodes coated with $CsSb$.
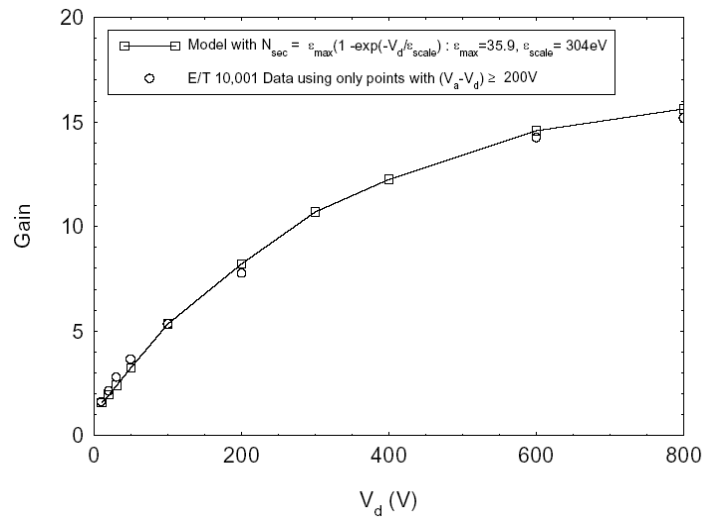
Figure 2-10 Bateman's dynode gain. The Monte Carlo simulation was compared to measurements taken at Brunel and found to be in good agreement.

Bateman's model assumes a planar geometry, ignoring the edge effect of the electrodes, thus is only relevant on the centre of the VPT. In addition, it does not include a timing analysis and time response model for the device. Mostly because it was known that the VPT was fast enough for their applications, therefore, their model focused on how to get the highest gains at high magnetic field. This left a gap in the understanding of the VPTs, which if further developments and applications are to take place, it may be essential to fully understand the VPT's time response.

The model of the VPT presented in this thesis takes a much simpler approach in the dynode simulation. As it was previously said, the distribution of the real secondary electrons in Figure 2-8 is centred at approximately 5 eV for KCsSb dynode, and falls rapidly in either side of this peak. Note also that the inelastic backscattering represents a very small proportion of the total events reaching at

most 0.1%. Because of this, it was suggested that, as a first approximation, an initial energy of about 5 eV for each secondary electron would be a sufficient implementation for simulating the time response of the VPT.

Secondly, as the primary electron is absorbed at the dynode, it looses energy at a rate of $E_P^{1-\alpha}$ (where α is characteristic of the material used for the dynode) as it penetrates the material up to a depth proportional E_P. At these greater depths, the released secondary electrons would need to migrate greater distances to reach the surface loosing most of their energy, and thus decreasing their probability to escape the potential barrier. This effect produces a "saturation" region in the yield of the dynode, which depends strictly on the material used for its surface as it was shown in Figure 2-7.

The model here presented ignores the characteristic properties of the material. However, in practice, at approximately the energy where this effect was thought to cause a decrease in the VPT gain, the simulation shed some light on a very interesting phenomenon. Although this will be explained later in more detail in Chapter 5 (Figure 5-15), the simulation showed that the depth at which the secondary electrons are created, did not affect the signal as it was expected to, confirming therefore, that the decision to ignore the material properties as a first approximation was valid.

The first part of Figure 2-7 (the rise to the maximum at E'_P), can be approximated to a straight line which slope depends on the ratio of the secondary emission coefficient $\dfrac{\delta}{\delta max}$.

The approximation used for the gain of the dynode set the generation of N secondary electrons following a linear proportion to the kinetic energy (in eV) given by:

$$N_{SECONDARY} = \frac{KE_{PRIMARY}}{m} \tag{2-10}$$

where $m = \dfrac{\delta max}{\delta}$ is the minimum energy required for creating a secondary electron. A clue of value was obtained from Bateman's generated dynode gain, which matched data from measurements from Brunel. It was projected that for

an incident electron of $1000\ eV$, the dynode gain would approximate 20 secondary electrons. In order to satisfy this, m was set to 40.

Effect of Magnetic Field

In addition to the hostile radiation environment in which the VPT operates in CMS, the $4\ T$ magnetic field plays a big part on the performance of the device.

By definition, the force acting on a particle of charge q is that given by $\vec{F}_B = q \cdot \vec{v} \times \vec{B}$. This means that the force $\vec{F}_B$ will always be perpendicular to the velocity ($\vec{v}$) and the magnetic field ($\vec{B}$).
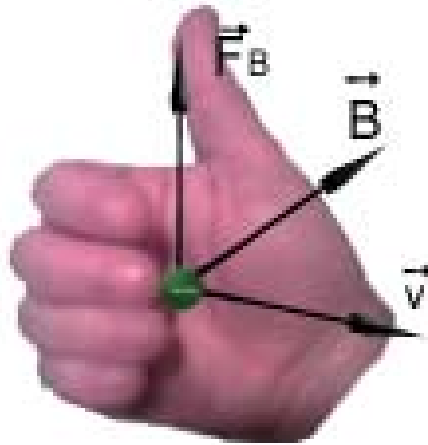
Figure 2-11: Right hand rule for the direction of the magnetic force. First, set the fingers pointing in direction of the moving particle, and then close them towards the direction of the magnetic field. The thumb will then point in the direction of the magnetic force
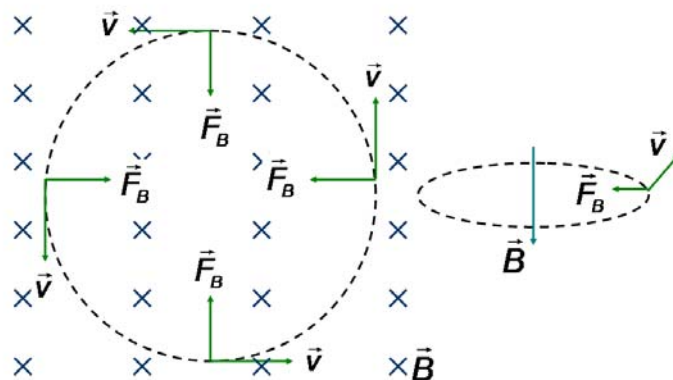
Figure 2-12: Circular motion of a charge particle moving in a magnetic field perpendicular to its motion. On the right the magnetic field points towards the paper. The force always points to the centre of the circle it describes when moving.

In the case when $\vec{B}$ is a uniform magnetic field perpendicular to $\vec{v}$, the charge q will feel the magnetic force $\vec{F}_B$ pointing always to the same point, thus experiencing a centripetal acceleration forcing a circular motion.

When $\vec{B}$ and $\vec{v}$ are not perpendicular to each other, the movement of the charge depends on two components; one due to the part of $\vec{v}$ parallel to $\vec{B}$ ($\vec{v}_{\parallel}$) and the other due to the part of $\vec{v}$ perpendicular to $\vec{B}$ ($\vec{v}_{\perp}$).

As previously discussed, since $\vec{v}_{\perp}$ and $\vec{B}$ are perpendicular to each other, the charge q will experience a circular motion. This motion has a radius given by:

$$r = \frac{m \cdot \vec{v}_{\perp}}{q \cdot \vec{B}} = \frac{m \cdot v}{q \cdot B} \sin(\varphi) \quad [6] \tag{2-11}$$

Where m is the mass of the charged particle, and φ is the angle between $\vec{v}$ & $\vec{B}$.
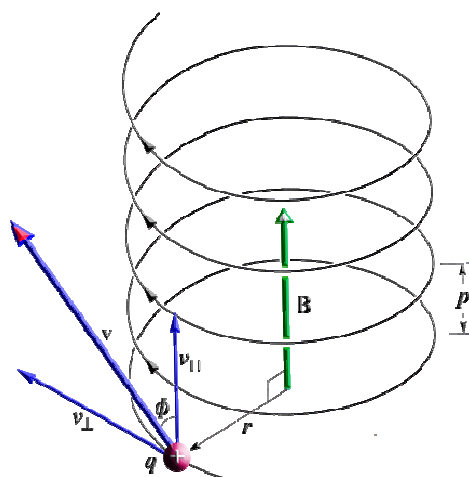
Figure 2-13 Helical Motion of a charged particle in a axial magnetic field6. The velocity component perpendicular to the magnetic field forces the circular motion. The magnetic field has no effect on the parallel component of the velocity.

The parallel component $\vec{v}_{\parallel}$ therefore describes the movement of the charge. As the charge moves forwards (along the magnetic field) and circularly (perpendicularly to the magnetic field) the superimposed movement describes a helix, the pitch (distance between adjacent turns) of which is given by:

$$P = \frac{2 \cdot \pi \cdot m \cdot v}{q \cdot B} \cdot \cos(\varphi) \ [6]$$ (2-12)

Because of this, it can be said that the path of the charge follows the magnetic field lines. This is an essential feature of a realistic simulation.

The VPT are tested at Brunel University using a 4 T magnet at a fixed axial angle of 15°. One can calculate the helical parameters of the electrons on the VPT under these conditions by using the formulas above:

The mass of a electron is $m_e = 9.11 \times 10^{-31}$ kg and the charge $q_e = 1.60 \times 10^{-19}$ C

$$r = \frac{m \cdot \vec{v}_\perp}{q \cdot \vec{B}} = \frac{m \cdot v}{q \cdot B} \sin(\varphi) = \frac{9.11 \times 10^{-31} \cdot v}{1.60 \times 10^{-19} \cdot 4} \cdot \sin(15)$$

$$r = 3.68 \times 10^{-7} \times v \ \mu m$$

$$P = \frac{2 \cdot \pi \cdot m \cdot v}{q \cdot B} \cdot \cos(\varphi) = \frac{2 \times \pi \times 9.11 \times 10^{-31} \cdot v}{1.60 \times 10^{-19} \cdot 4} \cdot \cos(15)$$

$$P = 8.64 \times 10^{-6} \times v \ \mu m$$

From simulations, the average speed at which the photoelectrons hit the anode is $18,66 \times 10^6$ m/s ; on the other hand, the maximum speed secondary electrons hit the anode is much less at $8,44 \times 10^6$ m/s (SIMION7 calculates speeds using relativistic computations when needed).

Therefore as the radius and pitch are directly proportional to the speed of the electron, the radius of the cyclotron from the cathode to the anode would be:

$$r_{KA} = 3.68 \times 10^{-13} \times 18.66 \times 10^6 = 6.87 \ \mu m$$

Wile the radius from the secondary emissions would have a maximum of

$$r_{DA} = 3.68 \times 10^{-13} \times 8.44 \times 10^6 = 3.11 \ \mu m$$

On the other hand, the pitch from the cathode to the anode is given by:

$$P_{KA} = 8.64 \times 10^{-12} \times 18.66 \times 10^{6} = 161.22 \text{ µm}$$

And from the dynode to the anode:

$$P_{DA} = 8.64 \times 10^{-12} \times 8.44 \times 10^{6} = 72.92 \text{ µm}$$

In addition, it should also be interesting to know what would be the theoretical maximum angle of operation assuming a 100% transparent mesh
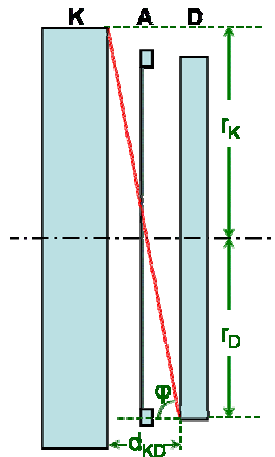
Figure 2-14 Calculating the theoretical angle of operation given a 100% transparent mesh. The red line indicates the path of an electron from a point at the border to the cathode to the diametric opposite at the dynode.

Calculating the maximum angle of the magnetic field (φ) at which the VPT would deliver some sort of signal, would reflect the most extreme case where a photoelectron is emitted at the border of the photocathode, and strikes on the diametric opposite at the dynode, and of course that the displacement would be parallel to the magnetic field Figure 2-14. However unlikely the circumstances (actual probabilities tending to zero), it would still require the photoelectron to travel from the cathode to the dynode which is a fixed distance. All in all, the maximum φ can be calculated with a single geometric problem.

$$\tan(\varphi) = \frac{r_K + r_D}{d_{KD}} = \frac{11.7 + 10.02}{4.45} = 4.88$$

$$\varphi = \tan^{-1}(4.88) = 78.42°$$

The above example shows that a VPT could in theory work up to almost 80°, however in practice this is not possible for a number of reasons. First, it is required that the whole VPT is illuminated and that a photoelectron is released at exactly the first point "seen" by the magnetic field. Since illumination is not guaranteed at the boundaries of the VPT, such a photoelectron would not be released.

The second reason, is that the mesh is not ideal, but it has a thickness and maximum angle for transparency, beyond which no photoelectron could pass, and thus reach the dynode

Capacitances within the VPT

Although not strictly part of the structure of the VPT, the capacitances within it affect the signal read from the anode. In order to calculate these capacitances, it was used the measured data given in Figure 2-3, which as stated before, was the result of averaging repeated measurement of a cut open VPT with a digital calliper, which accuracy is $\pm 0.02\,\text{mm}$.

In order to calculate the capacitance between two parallel plates, such as the electrodes, one can use Eq 2-13.

$$C = \varepsilon_0 \cdot \varepsilon_r \cdot \frac{A}{d} \tag{2-13}$$

where ε_0 is the permittivity of vacuum, ε_r is the relative permittivity of the dielectric, A is the active area, and d is the separation distance between the parallel plates.

As the VPT are vacuum devices, the relative permittivity of the space between electrodes is equal to 1.

Therefore:

$$C = \varepsilon_0 \cdot \frac{A}{d} \tag{2-14}$$

Anode – Dynode Capacitance
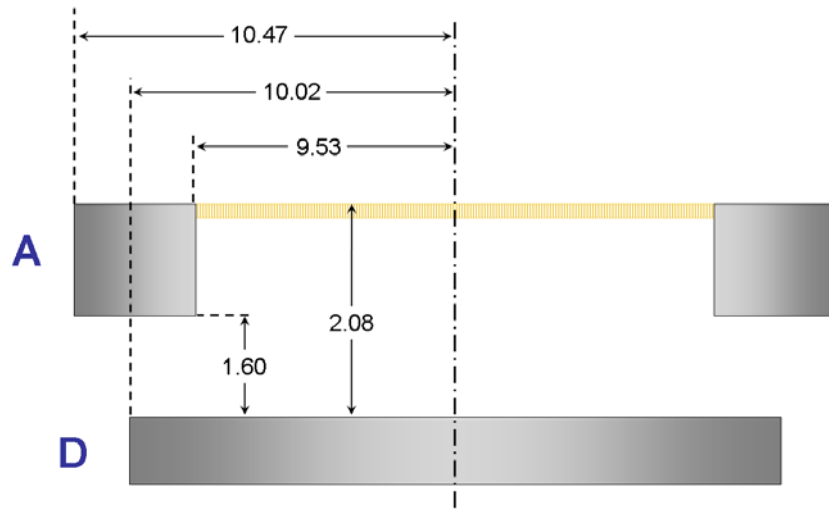
Figure 2-15 Anode and dynode measurements in mm

As the distance across the anode and the dynode is not constant throughout, it would be better to separate the geometries into simple ones, and calculate the capacitances for each one of them, and then sum to get the combined value. This results in three different parallel capacitances.

C_1 is a pair of parallel disks of $R_1 = 9.53 \text{ mm}$ separated in vacuum by a distance $D_1 = 2.08 \text{ mm}$.

C_2 is a pair of parallel rings with external radius $R_E = 10.02 \text{ mm}$ and internal radius $R_I = 9.53 \text{ mm}$ separated in vacuum by a distance $D_2 = 1.60 \text{ mm}$.

C_3 is a pair of parallel rings with external radius $R_E = 10.47 \text{ mm}$ and internal radius $R_I = 10.02 \text{ mm}$. As the separating distance tends to infinity, C_3 tends to 0, thus, being negligible.

$$C_1 = 2 \cdot \pi \cdot \varepsilon_0 \frac{R_1^2}{D_1} = 2 \cdot \pi \cdot \varepsilon_0 \frac{\left(9.53 \times 10^{-3}\right)^2}{2.08 \times 10^{-3}} \tag{2-15}$$

$$C_1 = 2.43 \text{ pF} \tag{2-16}$$

$$C_2 = 2 \cdot \pi \cdot \varepsilon_0 \frac{\left(R_E^2 - R_I^2\right)}{D_2} = 2 \cdot \pi \cdot \varepsilon_0 \frac{\left(\left(10.02 \times 10^{-3}\right)^2 - \left(9.53 \times 10^{-3}\right)^2\right)}{1.60 \times 10^{-3}} \tag{2-17}$$

$$C_2 = 0.33 \text{ pF} \tag{2-18}$$

$$\boxed{C_{AD} = C_1 + C_2 = 2.76 \text{ pF}} \tag{2-19}$$

Cathode – Anode Capacitance
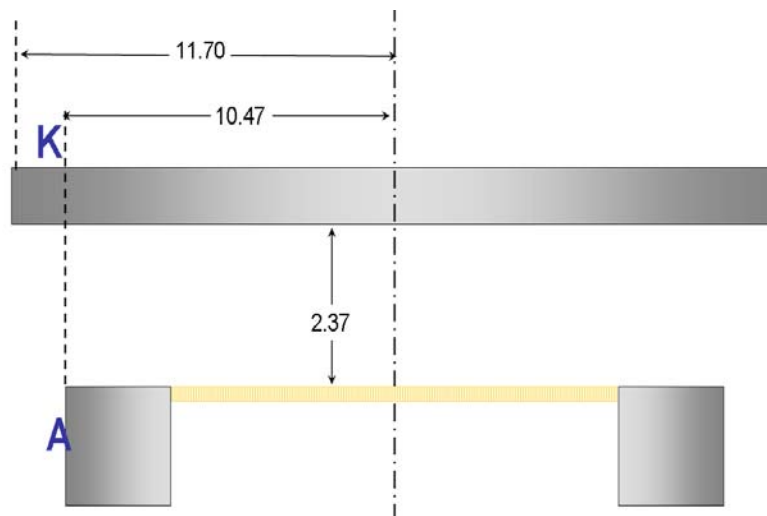
Figure 2-16 cathode and anode measurements in mm

With a similar reasoning as above, the capacitance between the anode and the cathode can be calculated by splitting the electrodes arrange into simple geometries. This would split the total capacitance in two parallel ones.

The first geometry, a ring with interior radius equal to $R_I = 10.47 \text{ mm}$, would have a separation distance tending to infinity, hence a contribution tending to nil.

The second one would therefore contribute to the totality of the anode-cathode capacitance. However, despite the anode being the same electrode with the uneven surface as in the calculation of the anode – dynode capacitance, Figure 2-16 shows that on the "cathode side", the distance between the anode and the cathode is constant throughout the anode area.

$$C = \varepsilon_0 \cdot \frac{A}{d} \tag{2-20}$$

$$C_{AK} = 2 \cdot \pi \cdot \varepsilon_0 \frac{R_A^{\ 2}}{D_{AK}} = 2 \cdot \pi \cdot \varepsilon_0 \frac{\left(10.47 \times 10^{-3}\right)^2}{2.37 \times 10^{-3}} \tag{2-21}$$

$$\boxed{C_{AK} = 2.57\,\text{pF}} \tag{2-22}$$

Cathode – Dynode Capacitance

The capacitance between the cathode and the dynode can be calculated by adding the anode-cathode capacitance in series with the anode-dynode capacitance as shown in Figure 2-17
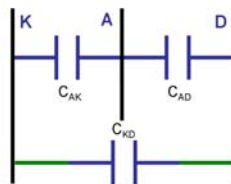
Figure 2-17 Electrode Capacitance

$$C_{KD} = \left(\frac{1}{C_{AK}} + \frac{1}{C_{AD}}\right)^{-1} = \left(\frac{1}{2.76 \times 10^{-12}} + \frac{1}{2.57 \times 10^{-12}}\right)^{-1} \tag{2-23}$$

$$\boxed{C_{KD} = 1.33\,\text{pF}} \tag{2-24}$$

Bibliography

- Paul A Tipler. "*Física*** Tercera Edición." Spain: <u>Editorial Reverté, S.A.</u>, 1994.

- Halliday, Resnick, Walker. "*Fundamentals of Physics Extended.*" <u>Ed. John Wiley & Sons, Inc</u>. (1997).

References

1 The CMS ECAL Crystal Endcap Information website (2001) "*VPT Production Technical Specification drawing*" [online]. Available: http://hepwww.rl.ac.uk/CMSecal/VPTs.htm [accessed on the 07th of March 2008]

2 N.A. Bajanov, et all. "*Fine-mesh photodetectors for CMS Endcap electromagnetic calorimeter.*" <u>Nuclear Instruments and Methods in Physics Research A</u> **442** (2000): 146-149.

3 J.E. Bateman. "*The operation of vacuum phototriodes in an axial magnetic field - a Monte Carlo study.*" <u>CMS Note</u> **59** (1998)

4 S. Ramo. "*Currents Induced by Electron Motion*" <u>Proceedings of the Institute of Radio Engineers</u> **27** (1939), p. 584.

5 "*Photomultiplier Tubes, principles & applications.*" France: Philips Photonics, (1994).

6 Halliday, Resnick, Walker. "*Fundamentals of Physics Extended.*" <u>Ed. John Wiley & Sons, Inc</u>. 1997

Chapter 3 SIMION7 Model Operation

he SIMION7 model is only one part of the simulation system, as it only simulates a specific set of ions which, in the case of the VPT simulation, are electrons (photoelectrons or secondary electrons, tertiary, etc…) The simulation focuses on what happens to the electrons whilst moving through the electro-magnetic field, the force of which depends on the internal geometries of the VPT. The signal analysis and the dynode simulation is described further on, in the next chapter.

Figure 3-1 Main components of the SIMION7 simulation model

SIMION7 Simulation Environment

The simulations are done on a three dimensional environment known as the **work bench** (WB), but in order to run them, several components of the simulation must come together, such as the electrodes and their potentials, the
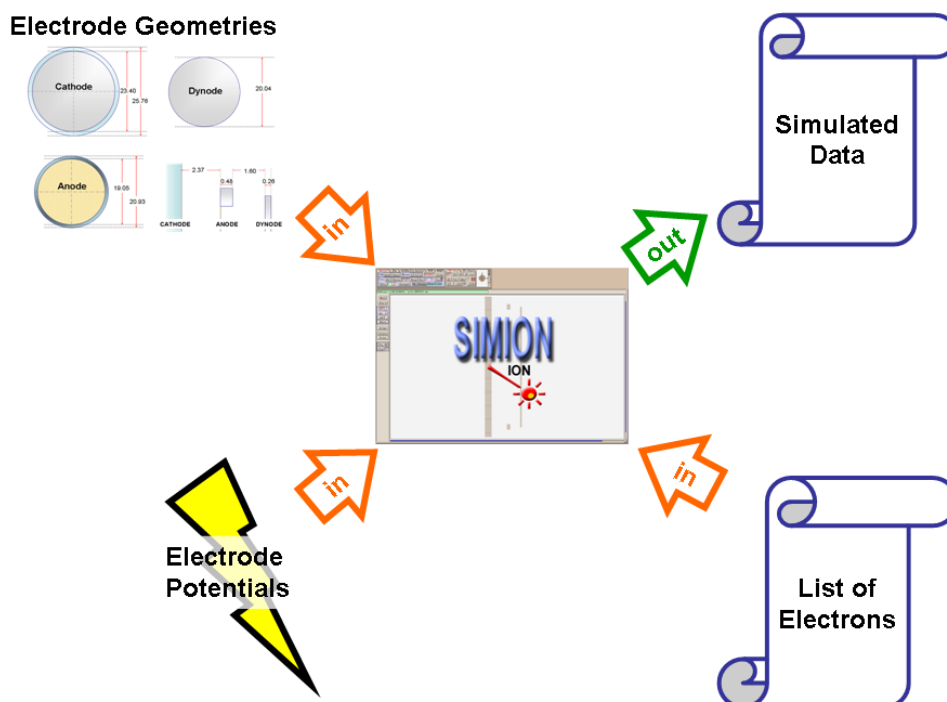
list of ions to be simulated along with their initial conditions, and small programs for tracking and recording the movement of the ions in the work bench.

The model consist of the geometry of the internal structure of the VPT, namely, the dimensions and separations of the electrodes. SIMION7 allows a model to be build by parts, so as to simplify the implementation of complex structures. Each of these parts are implemented in files called **potential arrays (PA)**, which can be either 2D or 3D grids, where each grid unit can represent empty space, an electrode, a magnetic pole or a field potential. An **instance** from each of these PA can then be loaded, scaled, rotated, and place to its desired dimensions, angle and location.

The best way of explaining the relation between potential arrays and instances in SIMION7 is through an example used by many authors explaining classes in C++:

Suppose that Bell is a 4 years old cat, it is brown, likes milk, and as all cats has four legs, a tail and it meows. It is not possible to have the species as a pet, because the species is a definition. However, it is possible to have a member of that species as pet and call it Bell.

In SIMION7, a potential array is a file containing the geometry, dimension, and other structural characteristics (much like the definition of a species). An instance is a functional copy of the PA (this would be Bell in the example). Furthermore, a simulation system could require several instances of the same PA (such as Bell and its siblings Lolly and Lupe).

There are properties of PA which are true for all instances of that PA such as what happens when an electron moves between A and B (in the example all cats meow, have four legs and a tail). Other properties are individual to each instance, such as orientation, location, and scale (this in the example would be colour, size, and age).

After assembling the device structure, magnitudes are then applied to the electrodes and poles by a process known as **fast adjusting**.

In order to run the simulation, ions must be defined, there are several ways of doing this, but in either case, this means loading a list of parameters which set the initial conditions for a ion such as: time, coordinates, kinetic energy and

direction. Other parameters include a way of characterising what type of particle the ion is, such as mass and charge; thus electrons are defined by setting these. Throughout this thesis the term ion is used when describing a SIMION7 feature and electron when it is specific to a VPT simulation. As no other charged particles were simulated, the terms ions and electron are used interchangeably.

SIMION7 uses the verb to fly for the process of running the simulation. This is because the simulation runs while the ions move in the empty space as if they were flying. Therefore, this thesis uses this term "**flying**" to indicate that an electron is moving, its velocity vector has a magnitude an elevation and azimuth, and it will still exist on the next iteration.

Other states include: "**hit electrode**" to indicate that the ion has hit an electrode, and as it will not move any more it will cease to exist on the next iteration; "**dead in water**" to indicate that the ion is in a trap, it does not move, and since the net force acting upon is zero and all gradients return it to point of equilibrium, it will not move on the next iteration; "**out of scope**" to indicate that the ion has left the WB the ion will move with a velocity vector but out of control and influence of the model but it will no longer be tracked; and "**killed**" which represent a termination by the user. These five states (flying, dead, dead in water, out of scope, and killed) are monitored by the status flag called **Splat**.

In order to track the electrons, small programs associated to some of the PA were written, and called when an ion was within the space defined by the PA's instance. At every time step, these user programs monitored the splat status for each ion, and prepared the data to be recorded, such as: which electrode was hit, kinetic energy, travelling direction and time lapsed between others.
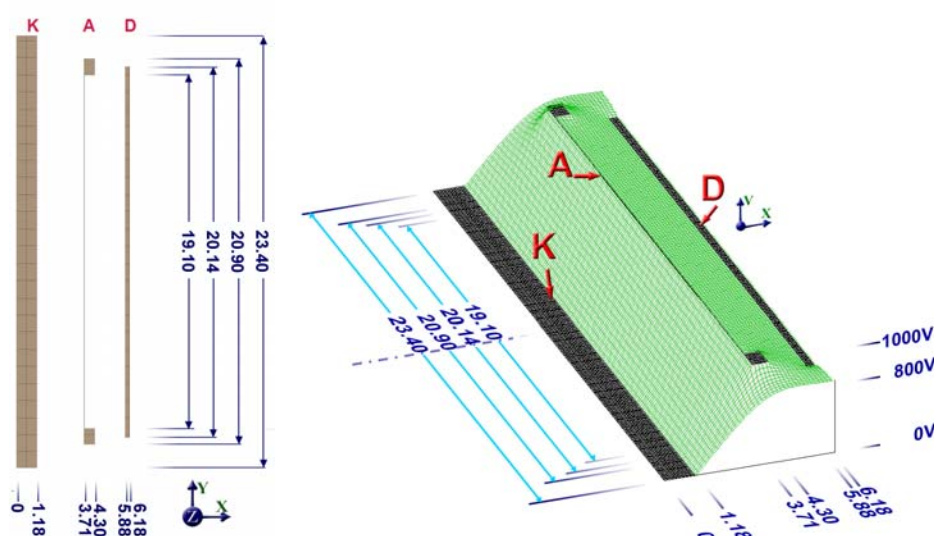
Figure 3-2 On the left: PA view of the three main electrode of the VPT (K = Cathode ; A = Anode ; D = Dynode); on the right: Potential energy view of VPT showing a representation of the electric fields of the VPT when voltages are applied to each electrode (V_K = 0 V , V_A = 1000 V , V_D = 800 V). Dimensions in mm and the vertical axis is in volts.

Coordinate system

SIMION7 supports several references for fixing the coordinate system, including any of the instances in the work bench. However, as each reference has its own unit of length, the reference selection could potentially complicate the instances placement and tracking of ions between instances. This is because lengths are given in grid units when using an instance as reference; therefore, since each instance is scaled by different magnitudes, grid units in one instance will have different dimensions (in mm) compared to another instance. Furthermore, as each instance is limited by its dimension, it is not allowed to the track ions beyond its borders. Moreover, instances can be tilted, the references systems need not to be aligned (i.e. having the corresponding axis in parallel to each other); e.g. for a moving ion, the velocity component in the x axis of one instance can be different to another instance ($v_{X1} \neq v_{X2}$), they could even be perpendicular to each other.

The solution to the above problem is to use the work bench as a reference for the coordinate system. This reference uses absolute millimetres as units of length instead of grid units; therefore, it provides a standard length unit for tracking the movement of ions as they jump between instances.

In order to differentiate which reference is being used, the initial of the reference is subscripted to the coordinates; for example: the **w**ork **b**ench coordinates are given by X_{WB}, Y_{WB} and Z_{WB}.

The implemented VPT was placed such that its central axis coincided with X_{WB}, and so that each electrode laid in planes defined by Y_{WB} and Z_{WB}.
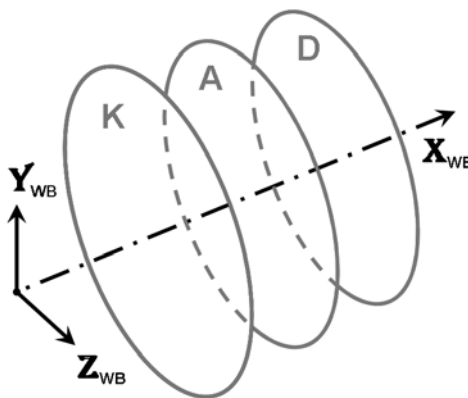
Figure 3-3 VPT orientation in the work bench, the axis of symmetry coincides with X_{WB}

SIMION7 frequently jumps between Cartesian and Polar coordinates systems, and sometimes it uses both; when defining a new ion, the starting location are given in Cartesian coordinates while the starting direction are given in Polar with the kinetic energy as magnitude and orientation given by elevation and azimuth angles. SIMION7 relates these systems as shown in Figure 3-4.
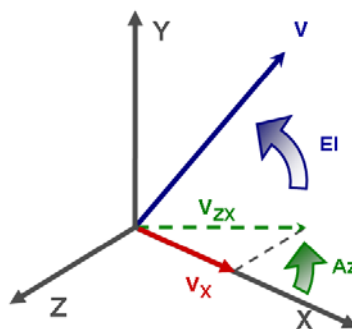
Figure 3-4 SIMION7 Cartesian and Polar coordinate systems

The angle of elevation (El) is the angle between $\vec{v}$ and the XZ plane which projection v_{zx} is given by

$$v_{zx} = v \cdot \cos(El) \tag{3-1}$$

$$v_Y = v \cdot \sin(El) \tag{3-2}$$

The azimuth angle (Az) is the angle between the X axis and v_{zx} (towards negative Z), therefore:

$$v_x = v_{zx} \cdot \cos(Az) = v \cdot \cos(El) \cdot \cos(Az) \tag{3-3}$$

$$v_z = v_{zx} \cdot \sin(Az) = v \cdot \cos(El) \cdot \sin(Az) \tag{3-4}$$

Potential Arrays and Instances

Potential Array (PA) is a file type in SIMION7 where the geometric characteristic of the physical structure of a VPT can be implemented. There are two types of PA: electrostatic, where the electrodes are implemented such as the photocathode, anode and dynode; and the magnetic, where poles are implemented so as to create a magnetic field.

The implementation of these files is done by a process whereby grid units are set to become part of a specific electrode or pole (similar to painting a monochromatic bitmap picture).

These grid units (gu) are the fundamental spatial unit used in SIMION7. Its dimension depends on the scaling factor of the instance (so a single grid unit could be $1nm$, $1km$, or anything in between).

There are mainly two SIMION7 rules regarding grid units, which the user need to consider for implementing any PA, and these are:

- The maximum permissible size for a PA is 50×10^6 gu.
- An electrode is only considered solid if it is at least $2\,gu$ thick; otherwise it will be treated as a 100% transparent surface (ideal grid).

In order to simulate a PA, a copy is called and placed at the work bench. This copy is referred as an instance, which is scaled to represent desired dimensions and given potential to its electrode. However, the work bench is not limited to

contain a single instance; instead, multiple instances can be called simultaneously and even be placed overlapping one another, allowing multiple objects to occupy the same space at the same time.

The use of instances has a great advantage as this allows a device to be designed in parts, implementing complex geometries at high resolutions and simple geometries at lesser ones.

With this in mind, the structure of the VPT was analysed: apart from the three electrodes (cathode, anode and dynode), each VPT is wrapped in aluminium foil (held at cathode potential). Furthermore, the anode was not as solid as the cathode and the dynode; instead, it had a mesh with a resolution of 100 lines/mm and that overall it was 50% transparent. Moreover, magnetic testing was required.

For the purpose of simplicity, it was decided to implement similar typed geometries together separated from the more complex ones, and the electrostatics PA separated from the magnetic ones (the cathode and the dynode were disks; the aluminium foil wrapping the VPT was a cylinder; the magnetic field had poles instead of electrodes; and the anode mesh was considerably more complex than the others). The resulting potential arrays were called: Real Mesh, Pseudo VPT, Casing, and Magnetic Field.
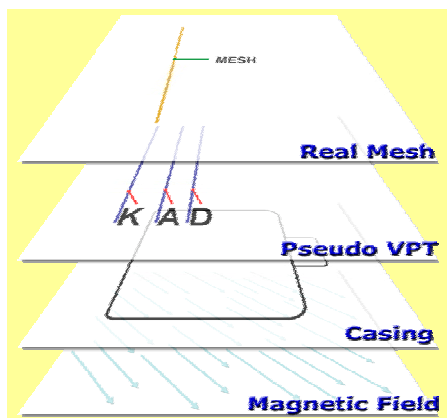

Figure 3-5 Potential Array layers

On the work bench an instance of each PA was placed overlapping one another as suggested in Figure 3-5. They were placed in order of precedence to avoid conflict; such as what instance is doing the tracking at a given point in space. This is because ions move on the instance with the highest precedence;

jumping up when crossing the boundary into a higher precedence instance. Therefore, smaller instances (within larger ones) will only be jumped into if they have precedence. When the ion crosses the boundary out of an instance, it jumps down to the next highest precedent available

In the case of the VPT simulation, while the electron moves from the cathode to the dynode, it has to pass through the Anode. Real Mesh has precedence over Pseudo VPT, so the electron jumps instances while it is in the volume define by the mesh instance, and then it jumps back to the Pseudo VPT instance when it leaves.

Real Mesh

As it was explained in the previous chapter, the anode of the VPT is 50% transparent, which means that statistically, 50% of the electrons travelling through it will pass and the other 50% will be absorbed. This is achieved by horizontal and vertical wire lines forming a mesh structure. The transparency of the mesh is achieved by ensuring the area of the wires and the area of the holes between the wires are approximately equal. The size of the holes is given by the resolution of the mesh, which is given by the number of wires lines in each millimetre[*].

The anode mesh in a VPT is supported by a solid metal ring, which if implemented at the resolution required for the mesh, it would use most of the grid points of the maximum available for each PA. Furthermore, as the surface of the ring is uniformly solid, there is no need for its implementation at such precision. Therefore, the anode ring was implemented in the same PA as the cathode and the dynode.

In chapter 2, it was shown that, for the cut open VPT, the anode mesh has diameter of $19.05\,\text{mm}$. Its resolution of $100\,\text{lines/mm}$ meant that in total the anode would have an approximate of 1905 lines of wires horizontally and 1905 lines vertically. Even with the help of symmetry tools, the implementation of a

---

[*] The inverse of the resolution gives the separation in mm between the wires. Thus, for a mesh resolution of $100\,\text{l/mm}$, each wire would be separated by $10\,\mu\text{m}$.

full anode mesh would not be possible as it would use more than the total maximum of available grid units for each PA of 50 million points [1]. However, it is foreseen that that SIMION 3D version 8 (SIMION8) would allow PAs with almost 200 million points [2].

In order to overcome this problem, the mesh was implemented by a combination of two different structure types. The first type involved the implementation of a realistic mesh at the maximum size possible. The second type was the implementation of a mesh 100% transparent to define the electric field correctly. As SIMION7 allows two objects to be at the same place, and at the same time, both structures were then overlapped. The argument for this was that an electron would not feel a difference between the two at long distances; therefore, the transparent mesh would provide the potential on the gaps not covered by the realistic mesh. As the electron approaches the realistic mesh it would be affected by the same electric field it would as if the realistic mesh were complete. Since the trajectory of electrons is affected by the presence of a magnetic field, the realistic mesh would then be moved to intercept the electrons. In order for this to work, the area of illumination should be always smaller than the area covered by the real mesh.

Due to SIMION7 rules, extra considerations had to be considered, which meant that the mesh could not have been implemented using the maximum number of grid points available:

- The SIMION7 design rules state that for a surface to be considered solid a depth of at least 2 grid units as well as a thickness of 2 grids units is required. Failing to do this, may result in an unexpected transparent surface.

- Room must be allowed on the X axis for two reasons: 1.) to enable tracking of the moving electrons, and 2.) the geometry of the mesh would start being relevant at distances of 5 times the hole's size; thus decreasing the amount of grid units available for creating a realistic mesh. Because of this, the maximum PA size could not be used for the implementation of the mesh.

For the implementation of the mesh, an array of 11×10^6 points was used with a total memory used of 110Mb of RAM. This can be described as one of the biggest limitations SIMION7 had to offer for simulating the VPTs: array size is very limited to an absolute maximum number of 50×10^6 points, a maximum of 250 instances are allowed and only if the computer is able to cope with the memory overheads every point in a PA and each ion uses. The latter one is the main reason why simulations limit the amount of photoelectrons to 100. The number of secondary electrons would average 1000[†] and rarely peaking at 1200. Setting up memory for a conservative 1500 electrons at a time already causes the computer to start running slowly especially during magnetic field tests, thus it was necessary to compromise the illumination characteristics for a model that could run on a typical laptop[‡].

The 11×10^6 points reserved for implementing Real Mesh were distributed in 11 points on the x axis, 1000 on the y axis, and 1000 points on the z axis. The geometry was mirrored on the y and z axis, thus duplicating the dimensions and quadrupling the mesh area. From the 11 points on the x axis only 2 points were used for the mesh, the remaining points were left blank to allow the tracking of the electron as it approaches the anode mesh.

Figure 3-6 shows a magnified in view of the mesh; as it can be seen, each line is two points thick and is separated by two points from the next one.

[†] Approximately 20 secondary electrons per photoelectron times 50% of the initial photoelectron which passes through the mesh

[‡] Dell Inspiron 5100 with a Intel Pentium 4 CPU 2.80 GHz with 1GB RAM running Microsoft Windows XP (Home Edition) Version 2002, Service Pack 2
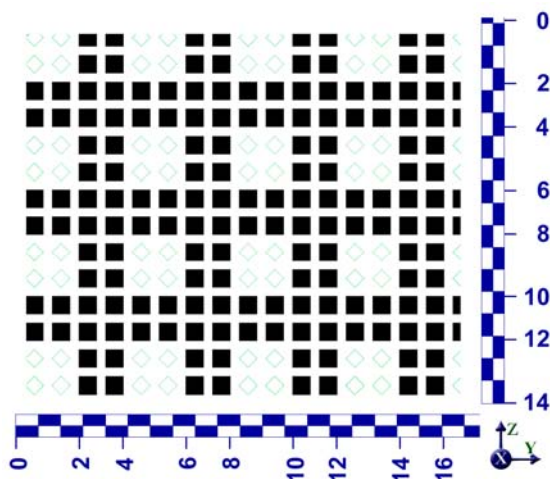
Figure 3-6 Zoomed in view of the implementation of the Anode mesh. Black squares are solid material, units on axis is "grid units" (gu)

The instance of the mesh was scaled at 0.005 mm/gu to achieve the resolution of 100 lines/mm and placed at $X_{WB} = +2.503$ mm to coincide with the ideal mesh of the pseudo VPT.

Pseudo VPT

Pseudo VPT is a configuration of the three electrodes: cathode, anode, and dynode. However due to the complexity of the anode mesh, Pseudo VPT has an ideal mesh (100% transparent). The outer support ring of the mesh however is solid (0% transparent) as are the cathode and dynode. SIMION7 treats an ideal mesh as an equipotential surface which, as having the same value as the real mesh, has no effect over long distances on the potential variance seen by the moving electron. The cathode and dynode were implemented as simple solid discs.

As this geometry was simple, it was designed as a cross section of a differential surface as it is shown in Figure 3-7. This cross-section was then rotated on the x axis forming three discs (cathode, anode, and dynode).
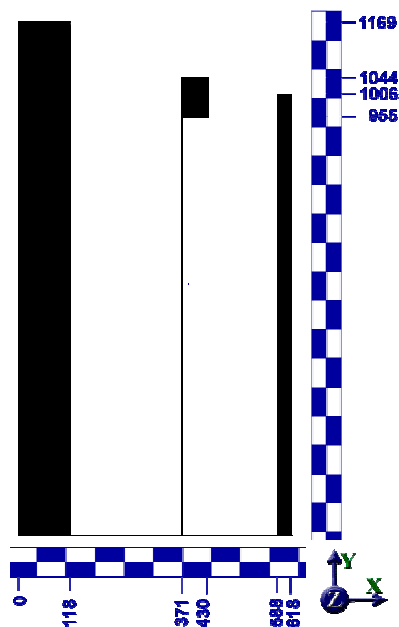
Figure 3-7 Pseudo VPT half cross section. The units are in SIMION7 grid units

The instance was scaled to 0.01 mm/gu and placed at $X_{WB} = 1.180$ mm. This scaling allows the instances to have dimensions very close to the real measured dimensions with an error of ±0.01 mm.

Casing

The VPT is covered in aluminium foil and is simulated as a solid grounded electrode. There are two main reasons for simulating this casing: 1st) it provides the correct electrostatics, as it surrounds the VPT with the same potential as the cathode[§]; 2nd) for computational reasons, the casing absorbs stray electrons (especially when simulating magnetic fields), because of this, the simulation stops the tracking of electrons which are not flying within the VPT, and therefore, are not contributing to the anode signal.

[§] On an actual VPT this casing is physically wired to the cathode.
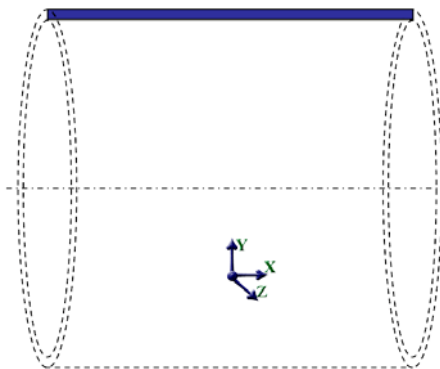
Figure 3-8 Aluminium casing

A strip of metal was implemented parallel to the "X" axis, then it was rotated on this axis to produce a cylinder with internal diameter of $2578\,\text{gu}$ and external diameter of $2582\,\text{gu}$.

The implemented instance was scaled at $0.01\,\text{mm/gu}$ and placed at $X_{WB} = -1.180\,\text{mm}$. This scaling transformed this instance to a cylinder of internal diameter equal to $25.78\,\text{mm}$ and external diameter of $25.82\,\text{mm}$.

Magnetic Field

Magnetic Field is the lowest of the layers and is uniform in nature. The size of the poles[**] are not important as long as the VPT is fully submerged in the field lines. The uniform field is given in gauss so for example to simulate a 4 T field then as one would have to set the poles so that the field has a uniform magnitude of $40\,\text{kgauss}$.

The geometry of the magnetic field PA was quite simple, two disks opposite to each other. It was decided to use a 100% transparent surface as poles so as to avoid any possibility of electron absorption (which would not be right at close distance to the VPT).

The array was design on the same principle as Pseudo VPT by defining a cross section differential surface which was then rotated about the x axis.

[**] SIMION7 uses poles to calculate the effect of magnetic fields as it would use electrodes for the manipulation of electric fields.

The disks of 100 grid units in diameter and separated by 100 grid units encapsulate a volumetric cube which is ideal for SIMION7 magnetic field calculations.

The instance was scaled such that

a) The field would be constant with a maximum change of 1×10^{-4} T and

b) The units of magnitude of the magnetic field equal the magnitude in gauss.

For this, the magnetic field instance was scaled to 0.4mm/gu and was located at X_{WB} = -16.00 mm and Z_{WB} = -5.00 mm. The angular effect was set with an azimuth angle $Az = -15°$ and an elevation $El = 0°$. These angle values were used in order to match the average angle of the range at which the VPT will be in operation in CMS as well as the axial angle of the 4 T magnet at Brunel University.

User Programs

User programs are optional files containing a reverse polish notation (RPN) styled codes that allow PA to be further customised. They allow access to simulation parameters which set initial conditions, adjust the magnitude of the electrode and poles, and more importantly (for the VPT simulation system), access the ion's parameters for monitoring and tracking as well as for triggering data recording.

Each user program is associated with a specific PA, and it will only run when the corresponding instance is active. As it was mention above, each instance is given a level of precedence to pre-select which instance should be active at a point in space covered by multiple instances. This is of particular importance as SIMION7 can only run a single user program at a time. Therefore, by ordering the instances according to their relative precedence, it is ensured that the correct user program runs when it is supposed to. Any running user program would go into standby when an ion jumps to an instance at a higher level of precedence so as to allow the user program associated to the current instance

to run. User programs on standby resume when the ion returns to the corresponding instance.

For example in the case of the VPT simulation, the interest was in tracking only the electrons flying inside the VPT. For each experiment the magnetic field does not change during the operation of the device, and neither does the aluminium foil that covers the VPT. As each user program can only track electrons while they are in the corresponding instance, and since the electron jumps from the Pseudo VPT to Real Mesh and back, it is required that these last two PA have user programs defined for tracking such electrons.

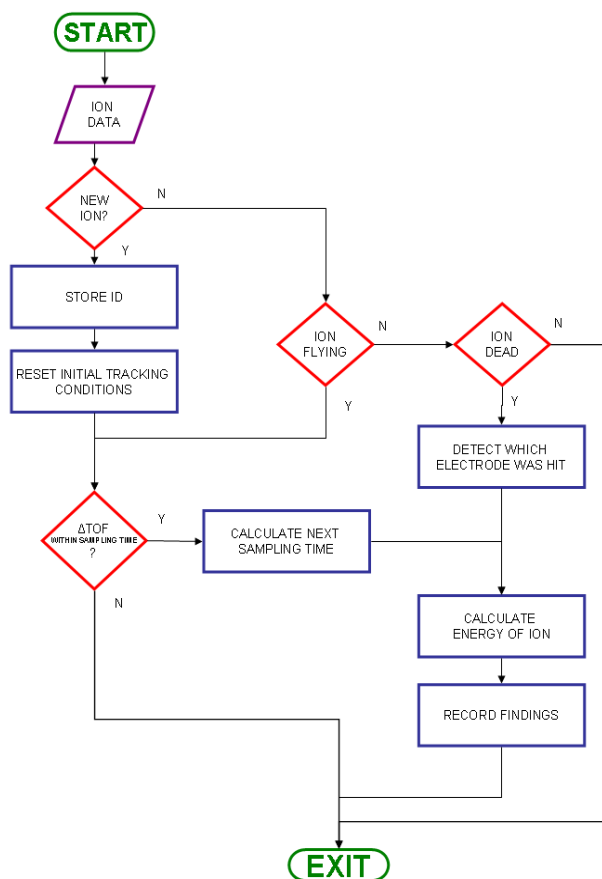**Figure 3-9 User program flow chart**

Figure 3-9 shows the user program flowchart for Pseudo VPT and for Real Mesh. These user programs are almost identical to each other, the only difference being is the number of electrodes the program has to take into account. SIMION7 does not distinguish between electrodes when it records a hit. This is not a problem while at Real Mesh, since it is a single electrode PA

(an electrode hit would always be on the anode mesh), but it is a problem while on the Pseudo VPT; the anode is solid not only on 50% of the mesh but also in the supporting ring, which is located on this PA. Thus, in order to differentiate between anode hits and dynode hits, it was necessary to introduce an additional section to the code. This was important due to the fact that only the electrons the hit the dynode contribute towards the generation of secondary electrons, while the anode hits are mainly used timing analysis and transmission gain of the device.

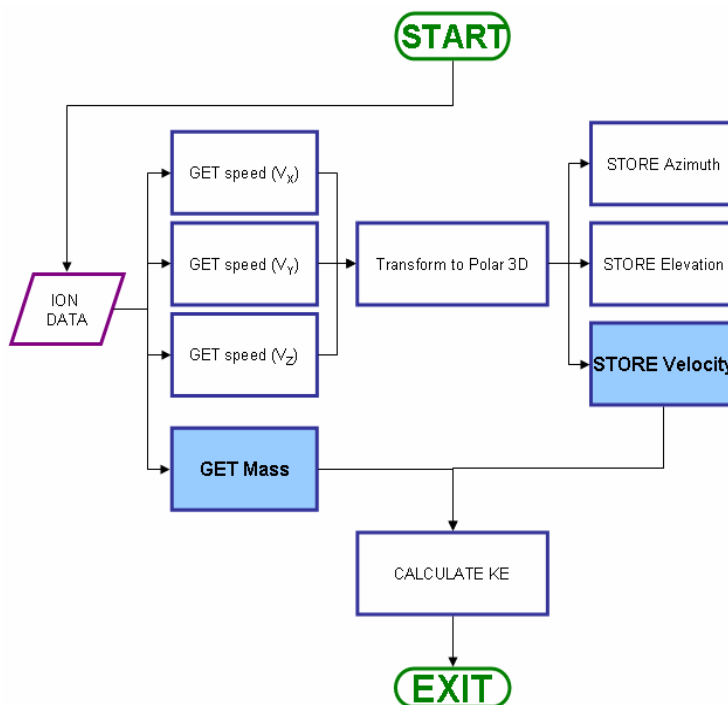**Figure 3-10 Flowchart for the calculation of kinetic energy**

User programs are composed in several well defined subprograms called Program Segments, each one being optional; in other words, not all program segments are needed. More information on user programs can be found in the SIMION7 User Manual [1] and a copy of the code for Real Mesh and Pseudo VPT can be found in Appendix A and Appendix B, respectively.

ION files

SIMION7 is designed to track ions moving across an electro-magnetic field. Electrons are treated as ions but with a specific mass and charge particular to electrons. SIMION7 accepts three different ways to define ions: individually, by group, and individually in a file.

Individually: Each individual ion is completely defined by modifying the initial condition parameters shown in Figure 3-11.
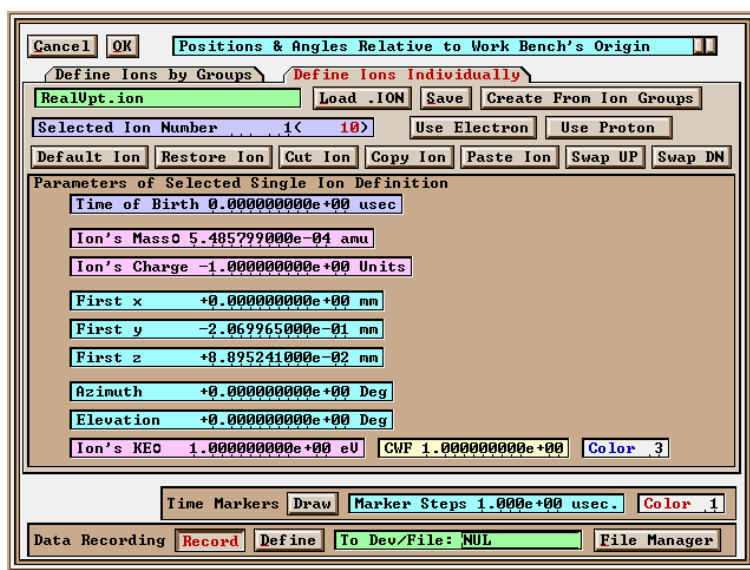
Figure 3-11 Ion Individual definition options

Note that the current coordinate system reference can be selected at the top left of the window.

By Group: Figure 3-12 shows the SIMION7 ion group definition window. This window includes the same parameters as in the individual ion definition, but it also includes a delta value associated with each of these parameters, which increments the initial condition parameter of the next ion.
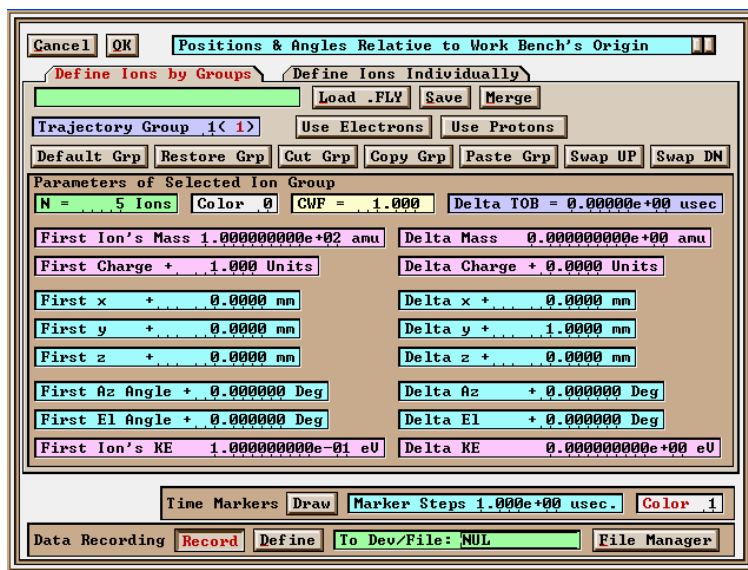
Figure 3-12 Ion group definition options

For example, note that in this particular case, 5 ions were created with $\Delta y = 1\ \text{mm}$, therefore, as the first ion has $y_1 = 0\ \text{mm}$, the following 4 ions would be created with the same parameters as the first, except that $y_2 = 1\ \text{mm}$, $y_3 = 2\ \text{mm}$, $y_4 = 3\ \text{mm}$, and $y_5 = 4\ \text{mm}$.

In the case of multiple delta values are defined, then they would be implemented simultaneously.

***Individually in a file*:** An ion description file (.ION) can be loaded. This file can be generated by a third party program, which is of the most value since initial photoelectrons and secondary electrons could be generated by a stochastic process, which provides a better representation of the real system. At the same time, using a program to generate an .ION file would eliminate the need to individually set the parameters of a large number of electrons.

Finally, the output of the SIMION7 simulation is fed to another program to generate secondary or further emissions as well as to collect the data and perform further analysis.

On the following pages, each of the components of the SIMION7 model will be described in more detail.

Individual Ion Definition Files are ASCII files where each line represents a single ion by comma separated parameters. These parameters are, in order:

TOB, MASS, CHARGE, X, Y, Z, Az, EI, KE, CWF, COLOR

These parameters can be skipped or omitted, and are defined below

Time Of Birth (TOB)

The "Time of Birth" is the time (in µs) at which the ION starts to exist in the simulation. This parameter is very useful in secondary emission simulation, as ions can have the start of their existence delayed.

In the VPT simulation, the photoelectrons and the secondary electron had to be simulated separately. Therefore, in order to have the timing of the secondary electrons consistent to the incident photoelectrons, the secondary electrons were created with a time delay equal to the time at which the incident photoelectron hit the dynode. By doing this, the signal generated by the secondary electrons could then be appended to the signal generated by the photoelectron.

MASS

The mass of the ions are represented in the Unified Atomic Mass Units (amu) system ($\text{electron mass} = 5.45 \times 10^{-4} \text{ u} = 9.11 \times 10^{-31} \text{ kg}$).

CHARGE

Elementary charge units (e.g. electron charge = -1) are defined to be the negative charge carried by a single electron and is equal to 1.602×10^{-19} C

Ion Starting Location (X, Y, Z)

These are the coordinates at which the ion would be created. The reference system used is the workbench and the coordinates X_{WB}, Y_{WB} and Z_{WB} are in mm.

In the VPT simulation, electrons are created in two distinct groups: the first is at the start with the creation of photoelectrons, and the second is at the dynode with secondary emissions.

Due to the size the realistic mesh $5\,mm\times5\,mm$, the photoelectrons were created with a uniform distribution within a circle of radius 3 mm, thus avoiding photoelectrons missing the mesh.

The secondary electrons were created at the same coordinates where the incident photoelectron hit the dynode.

Ion Starting Direction

The ion starting direction is defined by a pair of angles relative to the reference used to define the ions starting location (Figure 3-4). These angles are the Elevation (*El*) and Azimuth (*Az*), measured in degrees, and are applied in that order.

Ion Starting Kinetic Energy

The ion starting kinetic energy (KE) is defined in eV. It is immediately transformed into an initial velocity (in mm/µs) using the ion's mass and relativistic conversion (if required). This starting velocity is in the starting direction of the ion (described above).

Charge Weighting Factor (CWF)

The Charge Weighting Factor is of special interest in those simulations where charge repulsion is an issue. For these cases, and to speed up calculation, each ion is in fact a cloud of ions uniformly distributed within a cylinder. The CWF parameter allows specification of how many extra ions each ion represents. My simulation assigns a default unit to CWF which means that each ion counts for 100% of itself.

COLOR

SIMION7 allows individual ions to have different colours. These colours could range from a choice of 16 possibilities using integer numbers from 0 to 15. There might be occasions when all these variations are useful; however, for the purpose of the VPT model, a single colour is sufficient.

Fast Adjusting

Fast adjusting is associated with a specific call of a PA i.e. an instance. It has the values of the magnitude for each of the PA's electrodes or poles. Although user programs can access and change these values, it is of no use as in operating conditions the VPT would have a fixed biasing voltage, so that once set, no change is required during operation (or simulation for that matter).

Having said that, it is often necessary to understand how different biasing voltages affect the performance of the VPT. For this, it is possible to change the bias directly on the instance properties prior to simulation.

A note of caution: if changing of the biasing of the anode is needed, then it must be done on both instances: the Pseudo VPT and Real Mesh. Failure to do this may result in meaningless and unexpected behaviour.

SIMION7 Output

The output file of SIMION7 looks very similar to the input file (the ION file), the main difference being that it includes some extra data such as which electrode was hit and a identification number for the ion.

The parameters in order are:

TOB, MASS, CHA, X, Y, Z, AZ, EL, KE, CWF, COLOR, TOF, ELECTRODE, IonID.

All of the above, except ELECTRODE and IonID have been explained previously. Using the same parameters for the as inputs makes the inheritance process on the generation of secondary emissions much simpler.

ELECTRODE

This is a parameter generated by a user program and may have three different values:

0	the electron is flying and has not hit any electrode
1	the electron has hit the Anode
2	the electron has hit the dynode

These parameters help in the separation of the hits in the dynode (for secondary emissions) and the hits in the anode (for further analysis)

IonID

As SIMION7 would output one entry per line, and since all ions would generate more than a single entry (one at every sample) then it seems logical that there should be a way of telling which entry belongs to which ion.

IonID is a parameter that SIMION7 allocates to defined ions, and it is important for tracking, tracing and signal generation. Note that this number starts always at one, there is not way of presetting it to a specific value, so the Dynode simulation and Signal Generation program should identify whether the ion is a photoelectron or secondary electron by other means such as time and place of birth.

References

1 David A. Dahl, "*SIMION 3D version 7.0 User's Manual*", Idaho National Engineering and Environmental Laboratory (Feb 2000)

2 *SIMION™ 8.0: summary of changes.* 09/10/2007. [online]. [Accessed 14 March 2008]. Available from: http://www.simion.com/info/SIMION8

Chapter 4 SADYS Model

n order to compensate for certain limitations, SIMION7 allows communication with third party programs by allowing access to data exported from SIMION7, as well as importing ion definitions, which would be loaded to define the charged particles which are subsequently tracked in the simulations. This chapter discusses the program that was written by the author; Signal Analysis and DYnode Simulation (SADYS).
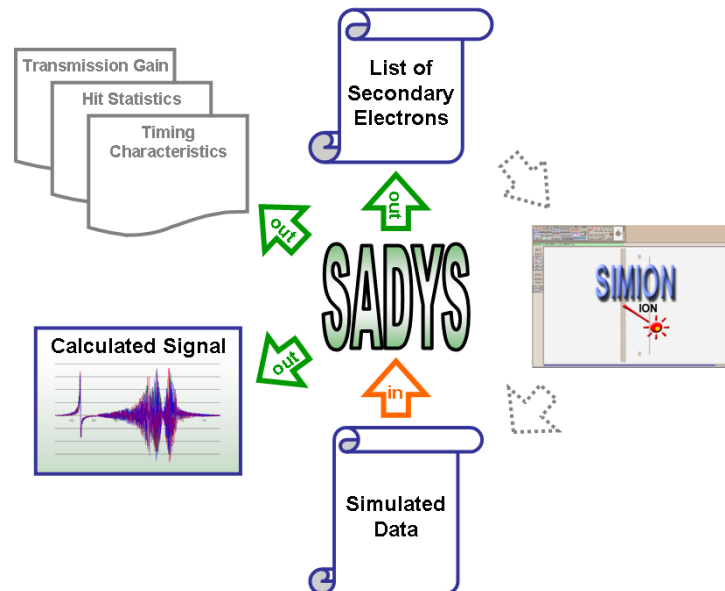
Figure 4-1 SADYS objectives.

The simulated data (SADYS input) is generated by the SIMION simulation from the list of secondary electrons (SADYS output). From this simulated data, the signal is calculated as well as other files of interest such as timing analysis and the electrode hit statistics.

It is the aim of this program to:

- Collect the data from SIMION7 so as to calculate the signal generated by the VPT.

- Generate a SIMION7 format input file containing the secondary electrons from the dynode simulation

- Generate any other files such as anode transmission gain, timing characteristics, and electrode hit statistics.

The Development of SADYS

The requirement to write SADYS arose from the need for simulating the secondary emissions from the dynode due to that SIMION7 does not handle a random creation of ions. However, it was soon realised that SADYS would also be required to do the analysis from the simulation. This allowed the SIMION7 user programs to be simplified so that their main task was to track the electrons through the VPT.

It should also be noted that the development of SADYS had to be concurrent to the SIMION7 User Program code. This was mainly due to the number and type of parameters passed from SIMION7 to SADYS constantly changed (either for allowing extra functions or for debugging). The implementation history can be seen from Figure 4-2
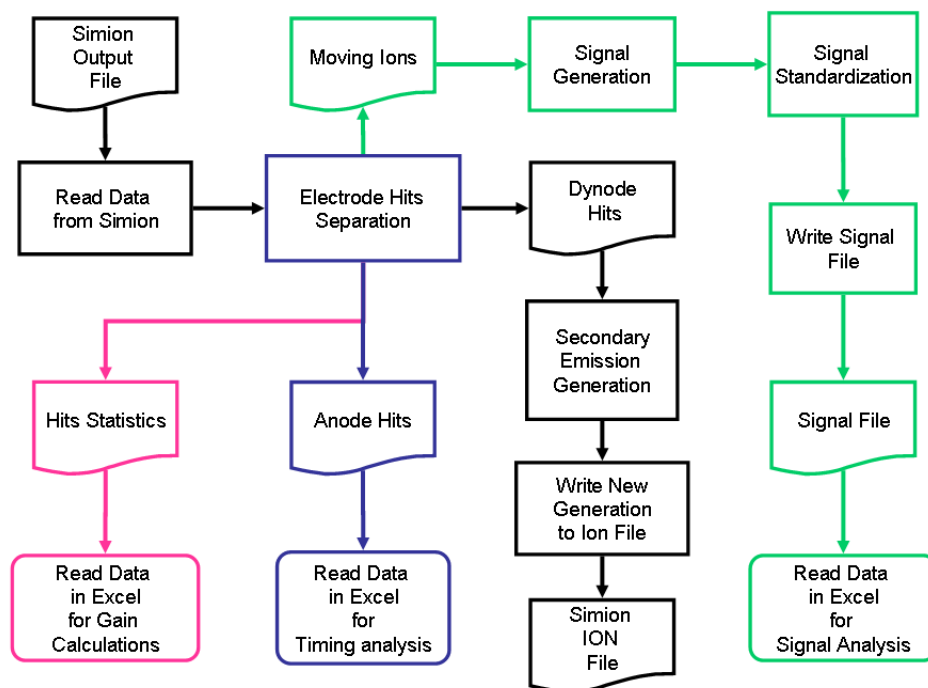
Figure 4-2 SADYS Order of Implementation

Black   First implementation: establishing communication between SIMION7 and SADYS; understanding what parameters were needed from SIMION7 to generate the next generation of Ions and understanding the format of ion definition files; basic generation of secondary emissions - at this stage, SIMION7 was set to record only hits at the dynode.

Blue   Second implementation: SIMION7 was set to record hits at anode and dynode, and to identify where hit was made. This modification was useful as it helps to understand the timing and duration of the signal.

Pink   Third implementation: the electrode hits statistics were generated to monitor the dynode gain or ratio of secondary emissions against fluctuations on the electrode voltages, magnetic field strength and magnetic field angle.

Green   Fourth implementation: SIMION7 was set to record all data (hits at both electrodes, and ions currently flying). The program was expanded to allocate the increase in data size (from under a thousand, to tens of thousands of data points). Ramo's theorem was implemented for the calculation of the signal contributions, due to each electron at different point in space. These were then standardized to fit into a single time frame for later calculation of the total induced current at the anode.

The communication between SADYS and SIMION7 was established around the ion definition files because these contain the minimum parameters SIMION7 needed to run its simulations. The user programs were set to record these parameters each time an electron hit the dynode from which SADYS generated the secondary emissions and stored then in an ION file.

Electrode Hit Separation

As the signal was generated at the anode, the second stage of the development of the code was to introduce a way of obtaining the hits at the anode, keeping separate from the hits at the dynode.

A problem with SIMION7 is that the output is to a single file, so inevitably the hits on the anode and the dynode would be on the same file. To solve this problem, a piece of code, in the SIMION7 User Program (SUP) was implemented to identify the electrode hit. By doing so, an extra parameter (named Electrode) was added to the SIMION7 output file (SADYS input file). It contained ether a 1 or a 2 for a hit on the anode or the dynode, respectively. Because of this, it was needed a module to separate the hits at the anode (for timing analysis) from the hits at the dynode (for the generation of secondary electrons). The flowchart for such code is shown in Figure 4-3.
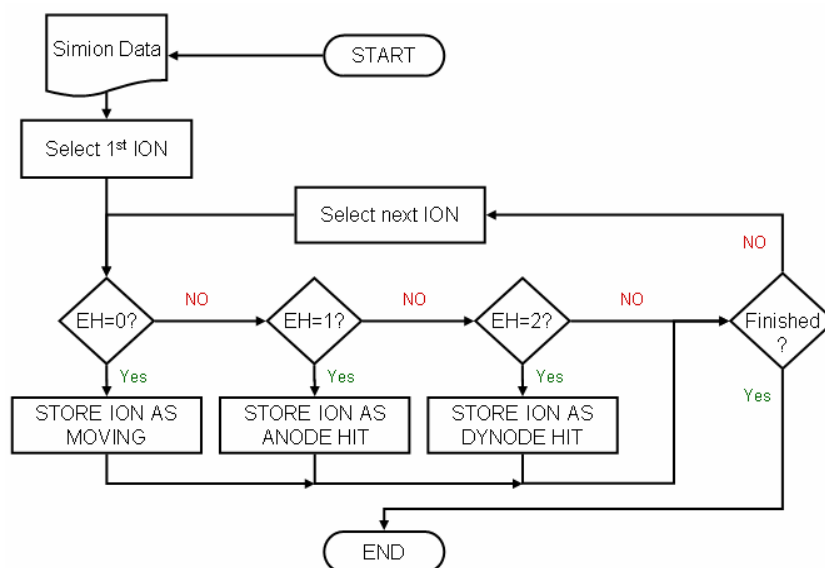

Figure 4-3 Flowchart of the electron hit separation

Due to the type of data received from SIMION7 it is assumed that an ion, or more appropriately an electron, can be in either of four main states (see chapter 3):

1. Flying

   The electron is moving, its velocity vector has a magnitude an elevation and azimuth. It exists, and it will still exist on the next iteration.

2. Dead

> The electron has hit an electrode, and will not move any more. It will cease to exist on the next iteration.

3. Dead in water

> The ion is in a trap, it does not move, and since the forces acting upon it are constant and in equilibrium, then it will not move on the next iteration.

> However, due to the geometry of the VPT this is impossible. The first reason is because the electric fields do not annihilate at any point within the device. Secondly, even if there was such a point, the magnetic field has an effect far greater than the electric fields, forcing movement towards an electrode or outside of the VPT.

4. Out of Scope.

> The electron has left the space and it is outside any instance. The ion will move with a velocity vector but out of control and influence of the model. Furthermore, it is assumed that the distance is far enough that it does not contribute to the signal.

> However, this case is of not importance as it is unlikely to happen, even in the strongest of fields. The reason for this is that the outer wrapping of the VPT is an aluminium casing. This will absorb the stray electrons which are not collected by either electrode, thus preventing it to "fly" into another device causing misreading.

The first two states have a major role and are very useful for the simulation. Firstly, and as will be explained in due time, an electron induces a current on the electrode while it is moving.

Secondly, it is also important to know when the electron hits the dynode. Secondary emission will depend on this, and the dynode gain will depend on the energy of the incident electron.

The Dynode Model

When an electron hits the dynode, it may release secondary electrons, which are then flown across the VPT. This part of the program, takes the hits from the dynode from which it generates the secondary emission using the simple model described in Chapter 2:

The number of secondary electrons is proportional to the incident electrons energy such that:

$$N_{SECONDARY} = \frac{KE_{PRIMARY}}{m}$$

(Eq. 4-1)

where m was set to 40 so that a primary electron with 1keV released 20 secondary electrons.

As it was shown in Figure 2-8, the energy distribution of the secondary electrons was centred at 5 eV for a KCsSb dynode. Due to the fact that the probability of secondary electrons with lower or higher energies falls dramatically, it was decided that as a first approximation, the secondary electron should be given an initial kinetic energy of 5 eV.
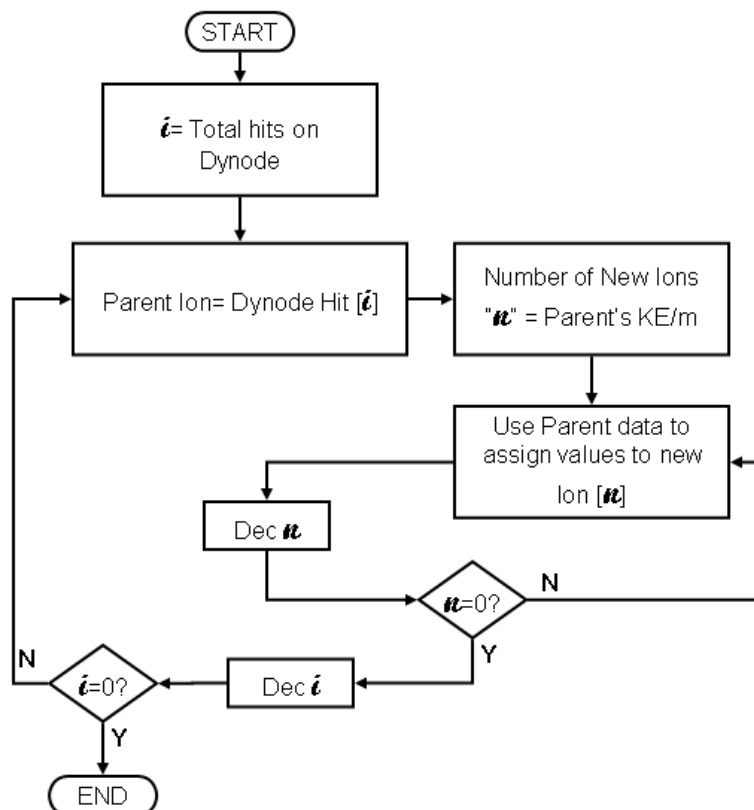

Figure 4-4 Secondary emission flow chart

But some assumptions are still in place regarding heredity[*].

- The time of birth of the secondary electrons should coincide with the elapsed time of the incident photoelectron.

- The secondary electrons should be created at the same coordinates where the incident photoelectron hit the dynode plane. Therefore, X, Y, and Z were inherited fully.

- The charge weighting factor (CWF) is relevant in simulations where the charge repulsion is an issue, such as when a high density cloud of electron may affect the electric potential just by their presence. This effect is not studied in this project, and therefore it is recommended for future developments on the simulation system. Therefore, for each defined electron, the CWF was set to its default.

- The orientation vectors of the new electrons should average to a vector normal to the dynode surface with a random distribution of $\pm 10°$ as shown in Figure 4-5.
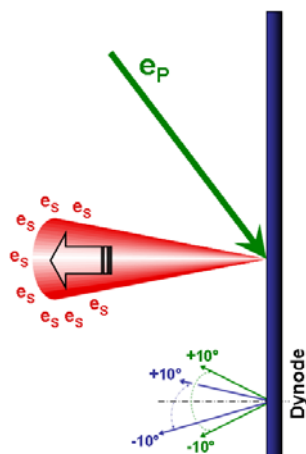
Figure 4-5 The direction of secondary emissions should in average be normal to the dynode, regardless of the incident electron's direction

---

[*] This project refers to heredity as the process of passing certain characteristics to the secondary electrons from the incident electron (parent electron); e.g. one should expect secondary electrons to be produce at the point where the incident electron hits the dynode, so they inherit their parent last coordinates

Random Number Generator

The C++ library has a *Random Number Generator (RNG)* which produces pseudo random numbers. It is known as pseudo because they are not at all random, as the numbers generated belong to a series of numbers which do not repeat in a very long time.

This is not a problem in many cases, except that when repeated, it will yield the same numbers as when the sequence is restarted. To prevent this, the library accepts a seed for the generation of the sequence. This seed can itself be a random number or be generated by other means.

After some research, it was concluded that the most practical way of generating this seed (without further needing to worry about its value) was to make it dependent on the time lapsed from midnight in seconds. In other words, in order for the experiment to show the same results, it would have to be done at **exactly** the same time each day[†]. As this is humanly impossible, it guarantees a random seed for the RNG.

The sequence generated randomness in the initial azimuth an elevation angles of the secondary electron.

Signal Generation

The signal is the total current induced in the anode from the electrons moving through the VPT. In order to generate this signal, the contribution each electron has is calculated, and then by applying the principle of superposition, the total current at a particular time is equal to the sum of the contributions of every electron at that time.

[†] For example: assuming the simulation on Day X was started at 14h:30m:37s, the seed for the RNG would bee 52237 (numbers of seconds from midnight). Thus in order to repeat the sequence of the pseudo number generator on Day Y (it would not be possible on the same day) the simulation would have to be run at exactly 14h:30m:37s so that the seed for both simulation be the same.

$$\frac{\begin{array}{ccccccc} i_{j\ t_0} & i_{j\ t_1} & i_{j\ t_2} & i_{j\ t_3} & \cdots & i_{j\ t_{max}} \\[4pt] i_{k\ t_0} & i_{k\ t_1} & i_{k\ t_2} & i_{k\ t_3} & \cdots & i_{k\ t_{max}} \\[4pt] i_{l\ t_0} & i_{l\ t_1} & i_{l\ t_2} & i_{l\ t_3} & \cdots & i_{l\ t_{max}} \\[4pt] i_{m\ t_0} & i_{m\ t_1} & i_{m\ t_2} & i_{m\ t_3} & \cdots & i_{m\ t_{max}} \\[4pt] \vdots & \vdots & \vdots & \vdots & & \vdots \\[4pt] i_{N\ t_0} & i_{N\ t_1} & i_{N\ t_2} & i_{N\ t_3} & \cdots & i_{N\ t_{max}} \end{array}}{\begin{array}{cccccc} i_{\Sigma\ t_0} & i_{\Sigma\ t_1} & i_{\Sigma\ t_2} & i_{\Sigma\ t_3} & \cdots & i_{\Sigma\ t_{max}} \end{array}} + \qquad \text{(Eq. 4-2)}$$

As discussed in Chapter 2, Ramo's theorem was used to calculate the induced current at the anode by:

$$i_t(x) = \frac{v_A \cdot q_e}{d_x}, \qquad\qquad \text{(Eq. 4-3)}$$

where: v_A is the speed at which the electron approaches the anode, $d_x{}^{\ddagger}$ is the minimum distance between the electron and the anode, and q_e is the charge of the electron. The distance d_x is always positive, however v_A changes sign depending on whether the electron is approaching the anode or moving away from it.

Note that v_x (the speed of the electron along the axis of the VPT) differs from v_A due to the fact that the latter suffers a sign reversal when the electron passes the anode. Apart from this, the magnitude remains the same. Thus, v_A does not only depend on v_x but also on where the electron is.

Figure 4-6 shows the relation between the v_A and v_x. On one hand, it is clear that as the electron moves from left to right (increasing in x) v_x is positive, and negative otherwise; on the other hand, the blue arrows show that v_A is positive when the movement is towards the anode. This divides the VPT in two regions, one in which v_x and v_A share the same sign (cathode-anode region)

---

‡ The subscript X is given due to the fact that the axis of the VPT lies on the X axis of the coordinate system used in the SIMION7 workbench

and one in which v_x and v_A have opposite signs. The sign relation between v_x and v_A is given the name of Orientation Correction (OC), and is given the values of ± 1 depending on the location of the electron. Therefore:

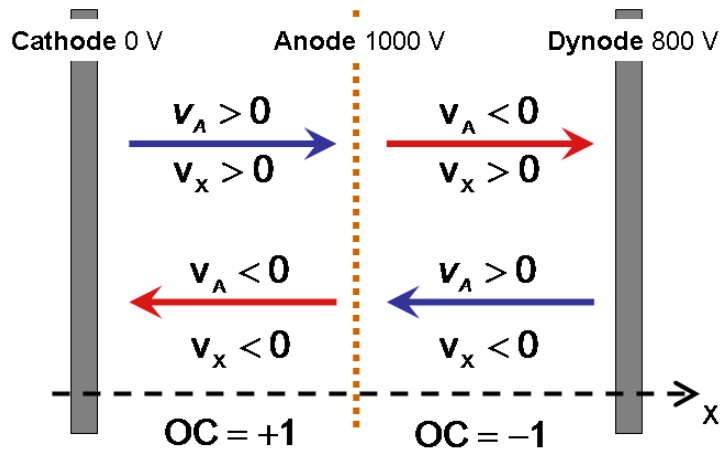$$v_A = OC \times v_x \qquad\qquad\qquad\qquad\qquad (Eq.\ 4\text{-}4)$$

Figure 4-6 Relation between V_A and V_X

Standardization of the Signal Output.

One of the main problems found is that SIMION7 does not sample at fixed time intervals, instead it checks for electromagnetic conditions at the sample point and uses this to calculate the forces acting on the electron at that particular point in space. It then uses numerical methods to calculate the next time step given the current kinetic energy and direction. If SIMION7 detects that the electron is approaching a boundary condition (such as a jumping between instances) it starts to increase the sampling rate, otherwise, it may even decrease this rate.

There are some advantages of sampling on the space domain, as the physical properties of the environment depend on the coordinates of the particle where the forces are acted upon. These forces are rarely time dependant.

The main disadvantage though, is that:

- Equally spaced samples have not necessarily equally spaced delays (speed is not constant as there are accelerations due to the forces).

- The motion in the "x" axis does not continually increase, and there is more than a single output for the same coordinates. Because of this, the concept of a function[§] can not be applied to the relation of position and induced current.

It is therefore impractical to use such a sampling method for the study of induced current, which after all, in signal analysis, is either a time or frequency domain phenomenon.

The first attempt to make the data useable was to produce a time sampled signal from this data.

- The first part consisted in over sampling on the space domain, so as to have some good quality data for the second part.

- A φ value was set to denote as the minimum time delay acceptable between samples, by considering two factors.

  o Approximate number of samples per electron: by this, I mean
  $$\varphi \approx \frac{\text{total length of the signal (in μs)}}{\text{number of samples}}$$
  (The total length of the signal was calculated by taking the average of previous runs of the simulation[**])

  o The maximum delay between the data samples. The idea of using this maximum, was for consistency and to reduce the unnecessary or excess data[††]

This method was very efficient for analysing individual electrons; however the signal is not due to a single electron but rather due to the accumulation of each electrons contribution.

This gives rise to a serious problem which can be described as follows:

[§] On of the requirement for a relation between an input and an output to be a function, is that for a specific input, there could be only one output.
[**] Timing simulations have been previously shown as part of the evolution of SADYS. These were exhaustive runs of over 500 initial hits at different parameter values such as magnetic field strength, magnetic field angle and dynode voltage. This data was considered for the estimation of τ
[††] SIMION7 generates a huge amount of data due to repetitions in sampling

Suppose we have four electrons, the signal contributions of which are plotted below Figure 4-7.
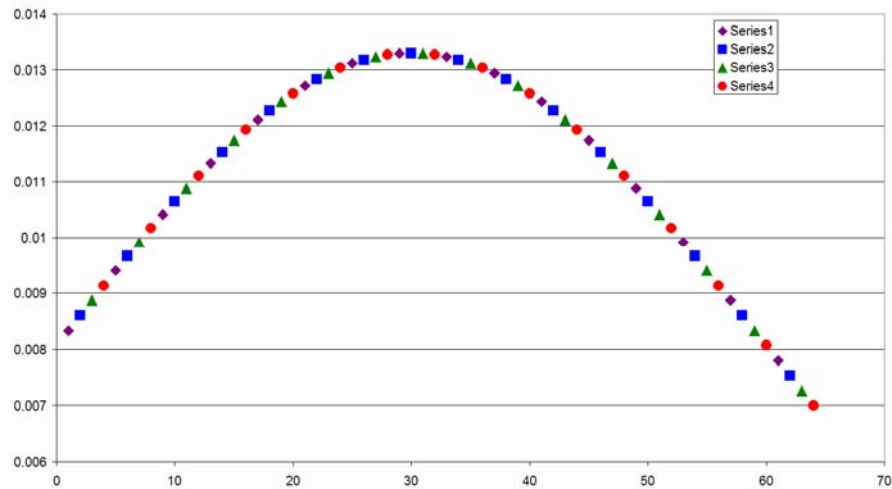

Figure 4-7 Example of unsynchronised data. All chart fit the same curve, although the data points do not coincide on the same time frame

As can be seen in Figure 4-7, series 1 to 4 can fit on the same curve, but they are not synchronised, as the data points correspond to different time values.

In order to calculate the total current on the anode at T_0 using superposition, it would mean adding all the individual contributions at T_0. The problem here is that for T_0 it is impossible to add the contributions of the four electrons because the data corresponds to different times. This would mean that in order to have same T valued contributions, one would have to predict the appropriate T_0 from the generated data.

This problem is also true for the case where the individual contributions are not equal; therefore, one can not "multiply" a contribution at T_0, by the number of electrons. This is because even if the advance in "x" of the electron vs. time is the same for all the electrons and depends on the EM field, the velocity component in "x" (V_x) might not, as it depends on accelerations and the route of the electron. The acceleration depends on the electromagnetic forces acting on the electron, which depend (in part) on the geometry of the field. The electric fields close to the borders, force the electrons to a route different to that at the axial centre of the field.

The case of the signal generated is a combination of these two problems which was solved by the projection of the signal contribution for each of the electron into a single standard time line. By doing this, each time contribution would then have their samples at the same time values; therefore, the principle of superposition could then be applied to calculate the total induced current at the anode.

This process is known as interpolation, which is a specific case of curve fitting. These are all methods of obtaining new data points which is not covered by the sampled data. The simplest form of interpolation (and therefore used in this project) is known as linear interpolation, as it tries to calculate a new data point from a straight line joining the sampled data points at each side.

The implementation of the linear interpolation assumed that:

a.   The contribution of each electron is a function in time $i(t)=f(t)$ and that it is continuous.

b.   From the limits theory on continuous functions, the value of any one point can be estimated by knowing the values of adjacent points.

c.   Therefore, if it is known two data points $(t_1 ; f(t_1))$ and $(t_2 ; f(t_2))$ then at a time t_y such that $t_1 \le t_y \le t_2$ it must satisfied that $f(t_y)$ is between $f(t_1)$ and $f(t_2)$
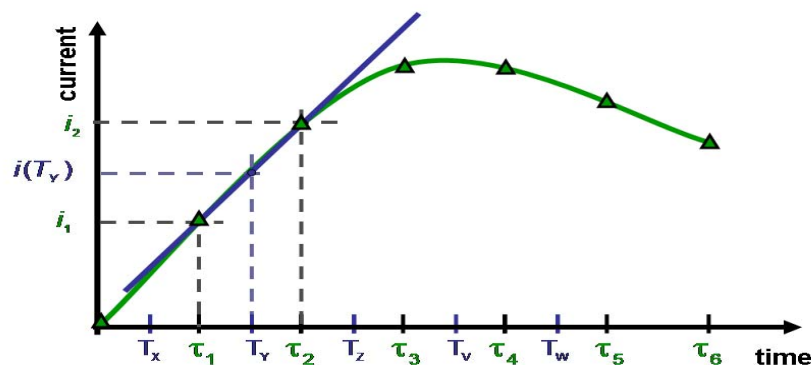

Figure 4-8 provided sufficient sampling frequency, the value of a function at a point between two samples, would yield a value between the evaluation of the function at the sample points. Choosing a straight line to represent the function between the sample points in order for calculating the contribution at a middle point is a good approximation.

The standardization of the signal output by linear interpolation has allowed multiple electrons to be sampled at a different times, to be projected on to a

single time frame, i.e., as it is described in Figure 4-9, linear interpolation allows for the projection of an **non equally** time spaced signal to a **equally** time spaced signal.
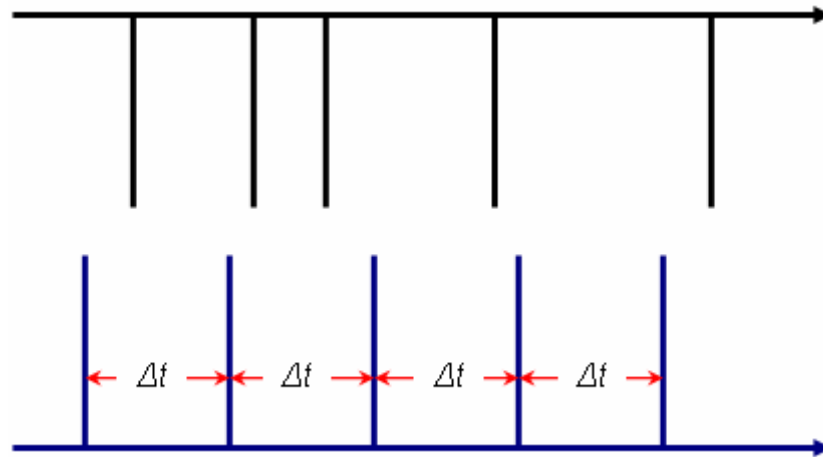
Figure 4-9 Different time-base samples

Chapter 5 Simulation Results

s described in the SIMION7 User Guide, the trajectories of the ions[*] are computed by the integration of three interdependent processes. Firstly, the electromagnetic forces are calculated from the ion's current location and speed. These forces are then used to calculate the acceleration and by numerical methods predict the ion's location and speed at the next time step. These time steps are continually modified to maximise the trajectory accuracy while trying to minimise the time steps per trajectory. This approach makes sense except when a constant time step is required as it is in the case of signal analysis.

Because each electron takes a slightly different trajectory within the VPT, the time steps associated with the flight of each electron do not match with the other electrons. Furthermore, since the signal of the VPT is the sum of the contributions of each individual electron, it would be more appropriate to have the time variables matching each other.

In order to compensate for these limitations, the data from SIMION7 had to be projected from a variable time step signal into a constant time step signal. By doing this, it was then possible to add the different contributions at each particular point in time. This inevitably caused a loss in the resolution of the signal.

In addition to this, as it will be shown later, the number of photoelectrons required for a realistic simulation is too high, and together with the resources required for holding the potentials array in memory, it would be just prohibitive to run a simulation at that level.

---

[*] In this thesis the term ion is used when describing SIMION7 features; electrons are defined in SIMION7 as a special case of an ion with a specific charge and mass. As no other charge particles are simulated in this project, the term ion and electron are used interchangeably.

Therefore, the simulation approach was changed from having a large sample size at very low resolution to a small sample size at very high resolution. In other words, it was decided to run simulations from a single photoelectron, and the resulting signal would be modified to compensate for the attenuation and multiplication factor that characterises different components of the VPT. The data from the simulation did not have to be resampled or projected to a different time frame, as it would not be combined with any concurrent signals; therefore retaining the full resolution of the signal. The subsequent signal from the secondary electron was then appended to the photoelectron signal without conflicting with the desired high resolution. Each photoelectron released multiple secondary electrons, and they all were simulated. From these secondary electrons, one with specific characteristics was selected to represent the signal due to secondary electrons. The remaining ones were used for extra information, which allowed the compensation required to transform the single electron signal into an estimated total signal.

This chapter aims to present the results from the simulation system that was designed to estimate the signal of a VPT under various configurations and settings.

Summary of the Theory and Simulation Procedure

The Vacuum Phototriode (VPT) is a device which converts a light pulse into an electrical signal whose amplitude is proportional to the light intensity. The gain of the VPT is set by the bias voltage of its three terminals: the photocathode, anode and dynode. A diagram of the VPT and its dimensions as implemented in SIMION7 is shown in Figure 5-1.
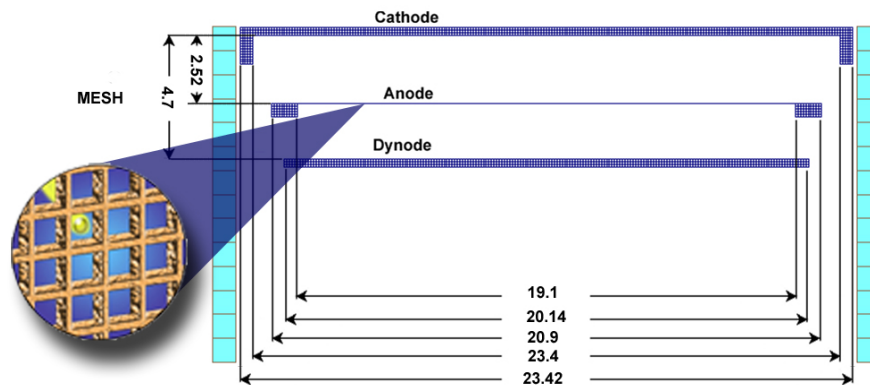

Figure 5-1 VPT as implemented in SIMION7 with measurements, and on the right a representation of the anode mesh

The simulation process starts with the creation of photoelectrons within the photocathode plate. The electrodes (anode and dynode) were fast adjusted[†] to the selected voltages. The photoelectrons were then loaded into SIMION7 and flown.
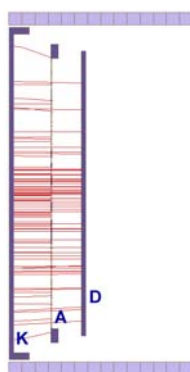

Figure 5-2 Flying Photoelectrons

i   **Cathode**

Electrons are produced where photons hit the cathode. These are known as photoelectrons.

ii   **Anode**

This is a fine mesh 50% transparent, and it statistically collects 50% of the electrons, when the magnetic field is absent.

The results from the SIMION7 simulation was read by SADYS, which generated the signal induced by the photoelectron and saved it

---

[†] Fast Adjustment is the process defined by SIMION7 whereby the magnitude of the electrodes and poles are adjusted.

into the signal file. SADYS also generated secondary electrons according to a simple model and stored them into a ION file. These secondary electrons were later loaded into SIMION7 and flown. SADYS was run again and appended the generated signal for each of the secondary electrons to the signal file which contained the photoelectron signal.
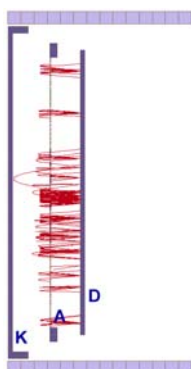

Figure 5-3 Flying Secondary Electrons

iii **Dynode**

Depending on the amount of energy with which the electrons hit the dynode, some electrons may be released from this electrode. The number of secondary emissions is proportional to the incident energy such that there are 20 secondary electrons for a 1000 eV photoelectron.

iv **Dynode**

Those released secondary electrons are flown towards the anode with an initial $KE = 5$ eV

Generally no further generations were created, but in case they were, they would be loaded and flown, and the process repeated until no further electrons were created.
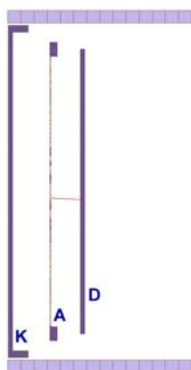

Figure 5-4 Flying Tertiary Electron

v **Anode**

Most of the secondary electrons (75%[‡]) are absorbed at this stage; 50% due to direct absorption and 50% of the remaining (i.e. 25% of the original number) pass the anode but are absorbed on their return.

vi **Dynode**

Some other electrons (25%) find their way back to the dynode, but as they do not have enough energy they do not produce more electrons. However, on some occasions (as in the case of an elastic back scatter which is not absorbed), the dynode is hit by secondary electrons which does have sufficient energy to produce third generations. And they will be flown.

[‡] The percentages given reflect the fact that as the anode is 50% transparent, then half the electron that arrive are absorbed by it (as long as $V_A > V_D$).

Once the simulation had finished, the signal file was read in to Microsoft® Office Excel 2003 where most of the analysis was performed.

Single Electron Simulation

The electrons moving through the VPT can be grouped in two categories: the primary electrons (photoelectrons) and the secondary electrons, which are released by the photoelectrons at the dynode. The single electron simulation is the study of the signal contribution of a single electron moving through the VPT; therefore, this simulation would study the signal from a single photoelectron and a single secondary electron released by the photoelectron (i.e. ignoring the dynode secondary emission coefficient).

As it will be seen in the following pages, the signal generated by a single electron depends on which trajectory it takes. Each of this single electron signals has characteristics unique to the corresponding trajectory, and therefore they are referred as the trajectory signature.

Photoelectrons

This simulation ignores the photoelectrons which hit the anode, as they do not release secondary electrons. The signal had to be compensated to account for the 50% of photoelectrons that hit the anode wires and therefore, being unable to continue towards the dynode, they do not contribute towards the amplitude of the signal. The compensation referred as the absorption factor will be described later in the Signal Estimation section (page 5-15).

Figure 5-5 shows the induced current at the anode by a single electron as it moves from the cathode to the anode. As this current depends on the relative velocity of the electron with respect to the anode, it changes sign when the electron stops moving towards the anode and starts moving away from the anode. This change of direction occurs in two distinct situations: the first as in this case, the electron has crossed the anode through one of the gaps between the wires, as the electron keeps moving, the change of sign happens suddenly. The second case is described later in page 5-8.
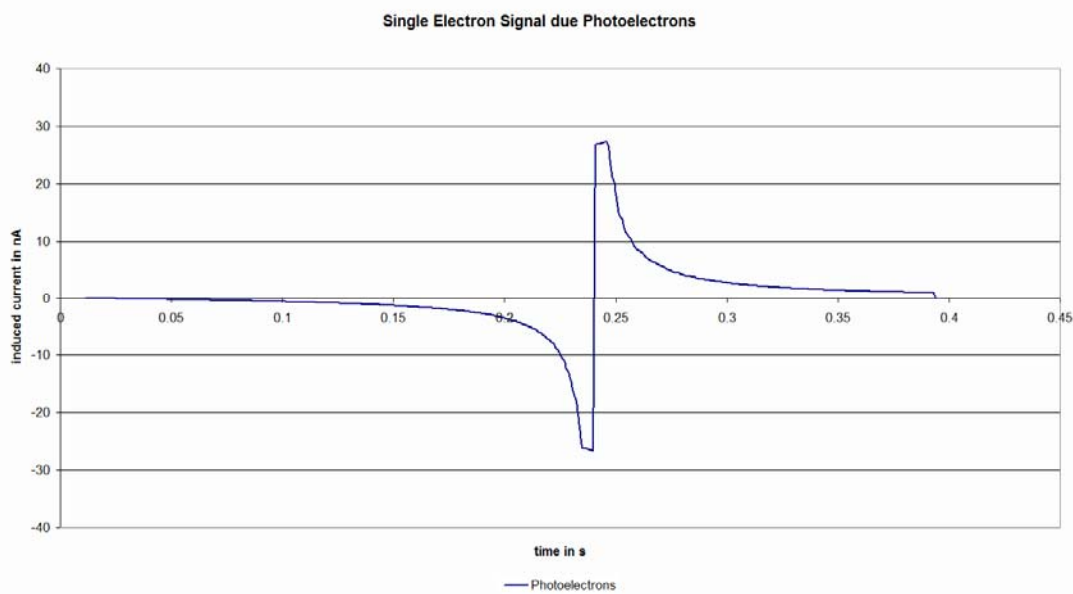
Figure 5-5 Signal simulation from a single photoelectron.

Secondary Electrons

Secondary electrons can either be absorbed **directly at the anode**, **indirectly absorbed at the anode** (pass the anode once, then be absorbed upon their return) or be **absorbed at the dynode**. The proportion of each trajectory varies randomly on single electron simulations. However, statistically speaking, the direct absorption should count for 50%[§] of the secondary electrons, the indirect absorption should count for 25% and the last 25% for the dynode absorption (assuming that the photoelectrons were created from a uniformly distributed area of the cathode). This means that the anode should absorb in total 75% of the secondary electrons, and the dynode just 25%. Due to the fact that strong magnetic fields force the electrons to move parallel to field lines, it affects the previously describe proportions in two ways: electrons are axially deviated out of the VPT and collected by the wrapping aluminium foil; the mesh becomes less transparent as electrons are collected on the internal walls of the holes between the wire lines.

[§] This is due to the transparency of the mesh; a 50% transparent mesh should absorb 50% of the electrons passing though it.

The trajectories presented here are the result of a typical simulation, where a single photoelectron hits the dynode. The trajectory signatures of the subsequent secondary electrons are then examined to analyse their differences and similarities.

Direct Absorption

These are the secondary electrons that are accelerated towards the anode, and hit a mesh wire. This particular simulation due to the original coordinates of the photoelectron yielded two single direct absorptions of secondary electrons, which for simulation purposes have ID numbers 503 and 509. Statistically speaking, if sufficient test are done, it should show that direct hits should account for 50% of the secondary electrons.

As it can be seen on Figure 5-6, the signal due to the secondary electrons abruptly stops at the same time. As it was expected, electrons will take the same time to reach the anode; this is due to the fact that under the same electric field, the forces acting on them have the same magnitude. Note also that as opposed to the photoelectrons, these do not pass the anode, and therefore their induced current does not change sign.
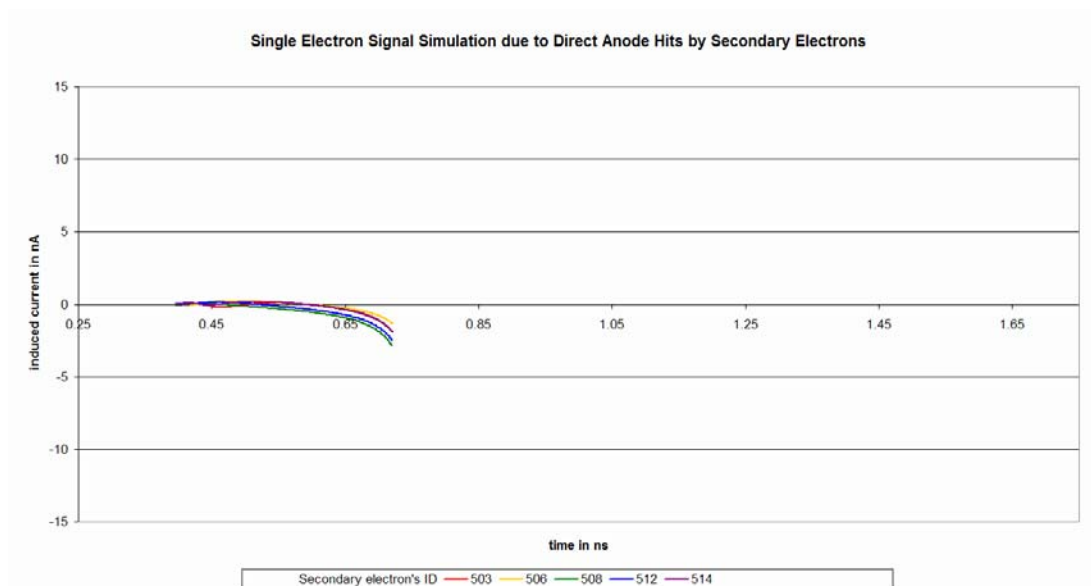

Figure 5-6 Signals due to secondary electrons which where directly absorbed by the anode. The secondary electrons ID is the identification number of a particular secondary electron which is given by the simulation system in order to track it.

Indirect Absorption

As it was said earlier, there are two distinct situations to expect a reversal in the anode current sign. As secondary electrons travel from the dynode to the anode, they pick up speed due to the accelerations from the electromagnetic forces. The electron that pass the anode through one of the gaps between the mesh wires feel a reversal of the acceleration, so they slow down to a stop before they are accelerated back towards the anode. In this second situation of current sign reversal, the change is gradual, where for an instant the electron is suspended in space with zero velocity. This is demonstrated in Figure 5-15 where it can be seen that as the energy of the secondary electron is increased (due to greater potential difference between the anode and dynode), the secondary electrons travel further from the anode before reaching a stop. Therefore as it can be seen on Figure 5-7, the induced current increases with the speed of the secondary electron, changes sign after passing the anode and then gradually decrease to zero, before increasing negatively again.

There are some fluctuations between each secondary electron induced current. But again, all the signals end at the same time at just over 1.05 ns. Note also that the general shape of the signal could have included the secondary electrons which are directly absorbed at almost 0.7 ns.
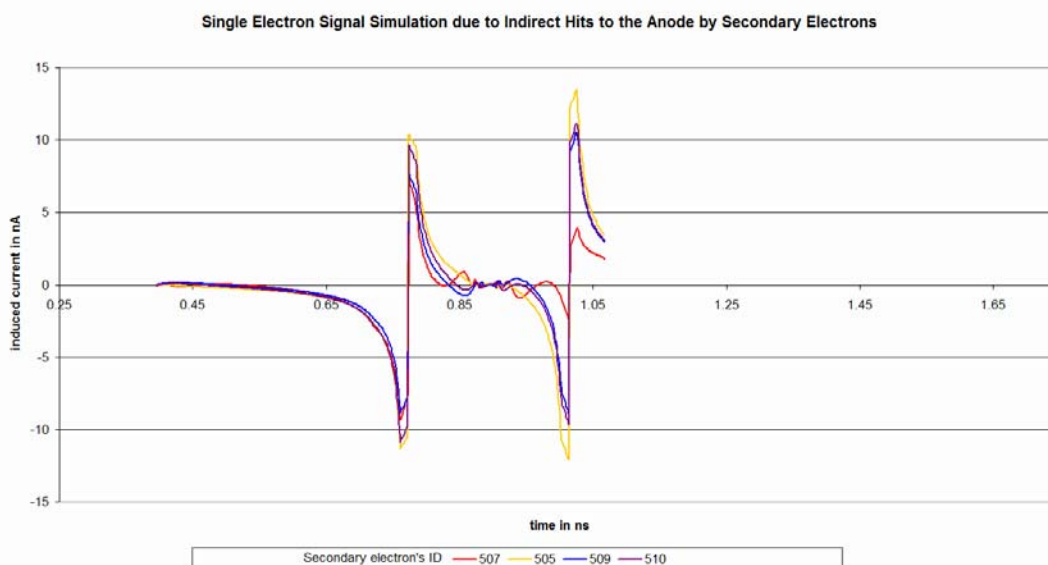

Figure 5-7 Signals due to secondary electrons which where indirectly absorbed by the anode. The secondary electrons ID is the identification number of a particular secondary electron which is given by the simulation system in order to track it.

Dynode Absorption

These are the secondary electrons which are accelerated towards the anode, pass through the gap between the mesh wires, decelerate to a stop, then accelerated back towards the anode where it passes for a second time, and finally decelerates before hitting the dynode.

There are some variations between different electrons but as it can be seen from Figure 5-8, the induce current from this trajectory can include the previous cases if it is truncated at 0.7 ns for direct anode hits or 1.05 ns for indirect anode hits.
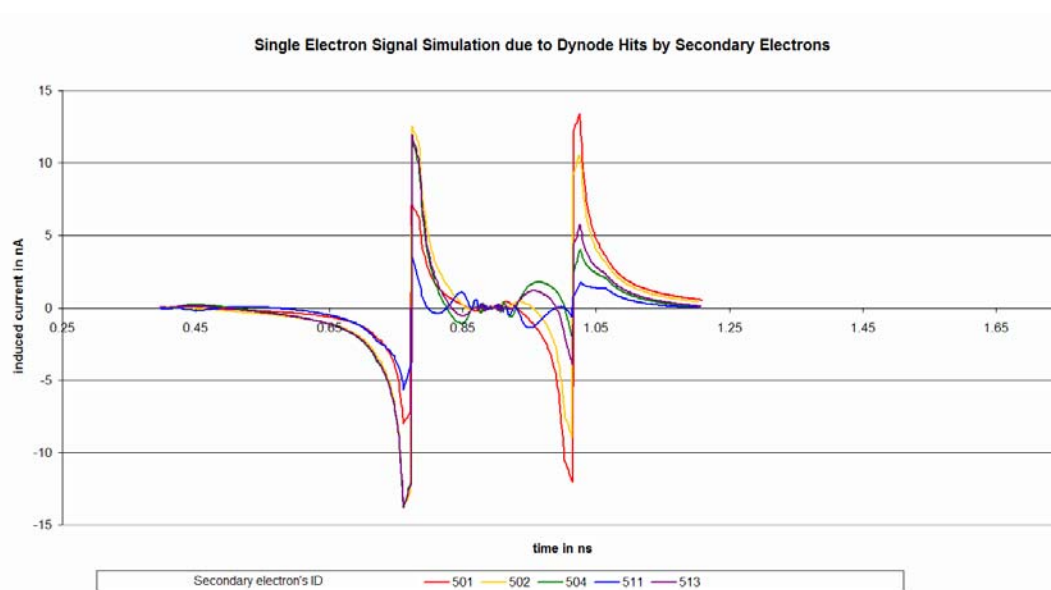

Figure 5-8 Signals due to secondary electrons which where absorbed by the dynode. The secondary electrons ID is the identification number of a particular secondary electron which is given by the simulation system in order to track it.

Trajectory Conclusions

Combining all the secondary emissions described earlier and colour coding for trajectory identification shows that, depending on the trajectory, the signals would have a specific signature. Figure 5-9 clearly shows that the main difference between the trajectories of the secondary electron is when the corresponding induced current terminates. The signals due to the different trajectories overlap each other, but the termination of each signal corresponds to when the electron is absorbed by the anode.
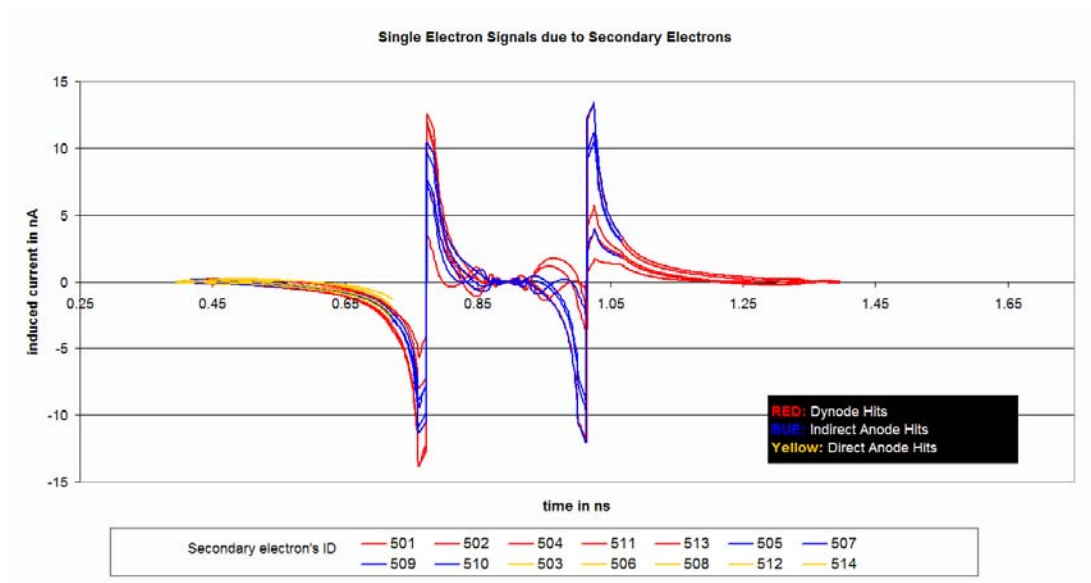
Figure 5-9 Combination of signals due to different trajectories. The colour coding represents the trajectory type of the secondary electrons. The secondary electrons ID is the identification number of a particular secondary electron which is given by the simulation system in order to track it.
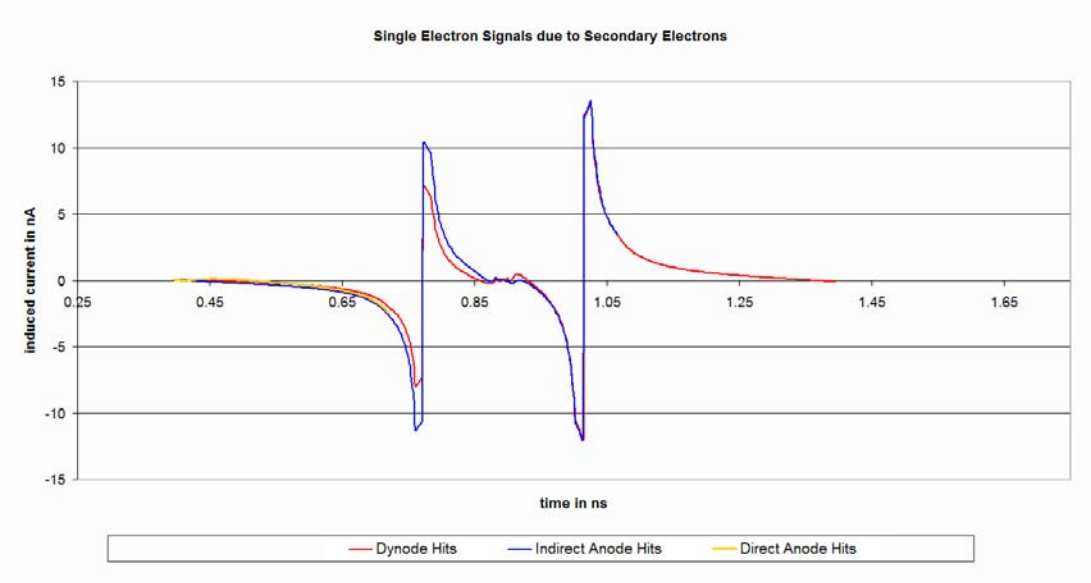
Figure 5-10 Overlapping triplet of signals for different secondary trajectories

Figure 5-10 shows the signal due to three arbitrary electrons whose signatures correspond for each of the different trajectories.

In Figure 5-11 it can be seen the signals shown in Figure 5-10 appended to the signal induced by the photoelectrons, furthermore, it also shows that by appending the signal from the dynode absorption of secondary electrons to the

induced current by the photoelectrons, the resulting signal would have included the other two secondary electron trajectories .
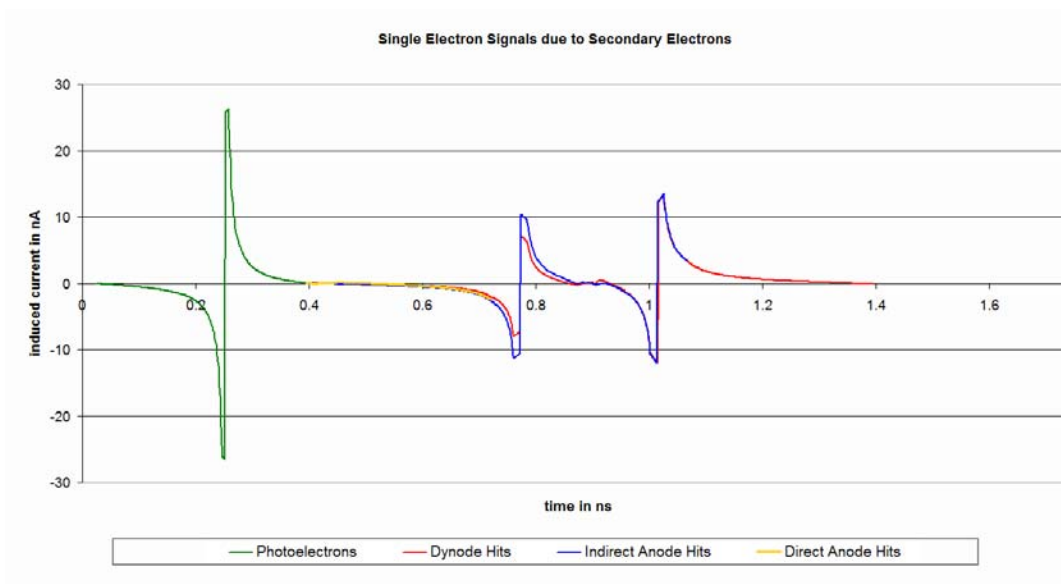

Figure 5-11 Single electron signals due to secondary electron trajectory (V_A = 1000 V and V_D = 600 V)

The trajectory that the electron takes induces a characteristic type of signal that stops when the electron is absorbed (this signal is referred as the trajectory signature). Generally, similar trajectories signatures stop at the same time, so they help to identify when the electrons are crossing the anode. This information is then used to identify the points in time at which the signal would be reduced (by 50%) in order simulate the anode absorption (which has 50% absorption at 0 T). This is required to estimate the total anode signal using the signal induced by a single electron.

Figure 5-11 shows the signal generated by a single photoelectron (in green) and that generated by a single secondary electron on three possible outcomes:

- Direct absorption by the anode (in yellow)

- The secondary electron passes the anode, and is absorbed when attracted back (in blue)

- The secondary electron passes the anode and then again when attracted back, and is finally re-absorbed by the dynode (in red)

As it can be seen from this figure, the final outcome includes the signal generated by the previous ones. Because of this, the results presented in this thesis are based on those secondary electrons that return to the dynode as their signal is more complete, and therefore, they would provide a better overall description of the anode signal.

The single electron simulation is the term used in this project to refer to the current induced by a single photoelectron which releases a single secondary electron. These tests are particularly useful to understand how the biasing of the VPT affects the motion of a single electron, and how this motion affects the signal induced at the anode. The results from these tests are given in Figure 5-12 and Figure 5-13.

The signals shown in Figure 5-12 are for the single electron simulation for a varying dynode voltage. In these test the potential differences between the cathode and anode is kept constant. By increasing the dynode voltage, the potential difference between the anode and dynode decreases. Because of this, the acceleration of the secondary electron also decreases. Note the overlap in the signal from the photoelectron is almost perfect, thus, it is suggested that the dynode voltage plays a very little role on the signal at this stage. However, the dynode does affect the rate of deceleration before the electrons hit it, thus, affecting the impact energy, which is related to the amount of secondary electrons (although the dynode gain is ignored for this study).
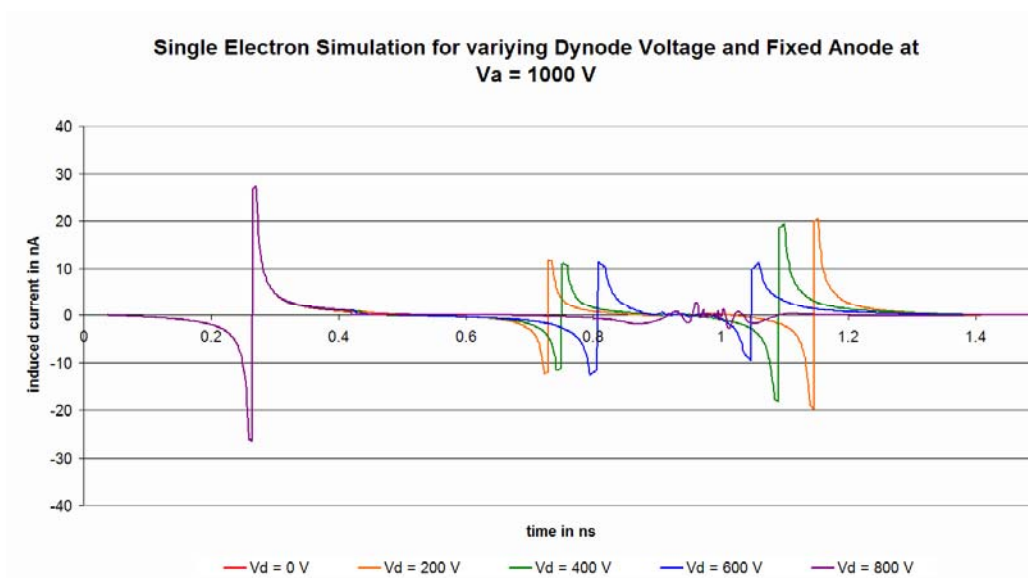

Figure 5-12 Single electron signals due to a varying dynode voltage

The signal due to each secondary electron is formed by two parts relative to the dynode (the anode is somewhere within the path of the electron): when moving away and when moving back. The secondary electron is accelerated away from the dynode at a rate proportional to V_{AD}. It passes the anode and starts to decelerate due to the cathode anode potential difference (V_{AK}), until it stops at a distance "x" from the anode (which also proportional to V_{AD}). At this point, the secondary electron is accelerated towards the anode and then decelerates before its final approach to the dynode.

As it can be seen from Figure 5-12, at low dynode voltages, V_{AD} is greater and therefore so is the acceleration to the anode. The secondary electron passes the anode faster and induces a greater current, however, due to its momentum, it travels further (towards the cathode) before reaching a stop. At this point the electron accelerate towards the anode due to V_{AK}, so it is accelerated at a greater rate, and thus, inducing a larger current. It finally passes the anode and decelerates due to V_{AD} before hitting the dynode.

At greater dynode voltages, the first acceleration of the secondary electron is reduced, therefore, the electron would take longer to reach the anode and at lower speeds, hence the lower induced current. Because of its smaller momentum, the secondary electron does not travel far before accelerating back to the anode and then continuing to the dynode.

So there are two distinctive secondary signatures: one with a single block, and the other consisting of two parts. These two signatures depend on how far the electron travels in the anode-cathode region, which means that if the electron leaves the area of influence, the induced current on the anode becomes negligible. If they do not leave the area of influence, the induced current would not experience a break.
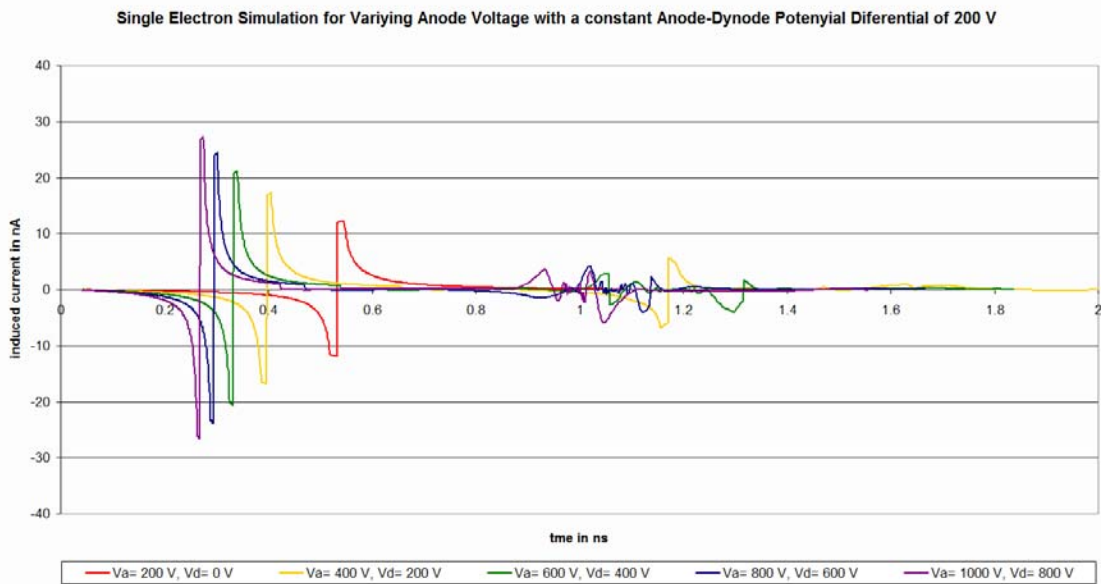
Single Electron Simulation for Variying Anode Voltage with a constant Anode-Dynode Potenyial Diferential of 200 V

Figure 5-13 Single electron simulation for a varying anode voltage but with a constant anode-dynode potential difference of 200 V

The first thing to notice about Figure 5-13 is that the signal due to the primary photoelectrons is quite different to the case where the anode potential was constant. Of course, as the anode voltage increases, so does the acceleration of the photoelectron. This has two consequences:

a) The induced current is directly related to the speed of the inducing electron, thus, the greater the speed, the greater the induced current.

b) as the speed is the distance travelled per unit time, given a fixed distance (the VPT dimensions do not change), the greater the speed of the electron the less time it has to induce current.

The second thing to notice is that all the secondary electrons are inducing currents of similar amplitude, independently of the anode voltage. This is due to two reasons:

a) As we know, the anode voltage affects the energy at which the photoelectron hits the dynode, thus, affecting the number of secondary electrons. However, this study ignores the gain of the dynode, therefore, there were no added contributions of multiple secondary electrons. Moreover, the model used in this work assumes that, regardless of the incident electron energy, any released secondary electron would have an

initial energy of $5\,eV$, so there is no relation between the incident electron energy and the released secondary electron initial energy.

b) As the potential difference between the anode and dynode was kept constant, and, since the initial energy of secondary electrons is the same for every case, then the acceleration (and therefore, speed) of the secondary electrons was the same, and because of this, the induced current should be of similar amplitude and last a similar amount of time.

Signal Estimation

The response of the VPT was estimated from the data obtained from the single electron simulation. This estimated signal was calculated by multiplying the single electron signal, the absorption signal, the dynode gain signal and the number of photoelectrons.

Figure 5-14 shows a sample of the estimation process. The data from the anode absorption marked the point in time when 50% of the electrons are absorbed (the last two green squares). The absorption function is a stepped function that starts at unity and reduces by half at these points (orange).

The dynode gain multiplier is a unit step function which starts just after the end of the photoelectron's signal and which value is proportional to the incident electrons energy.

As it is describe in equation 5-1, the dynode gain multiplier has the value of 1 until the time T_S after which the signal is given a value equal to the number of secondary electrons proportional to the incident photoelectrons energy.

$$\text{Dynode Gain Multiplier} = \begin{cases} 1 & \forall\, t < T_s \\ \dfrac{E_P}{m} & \forall\, t > T_s \end{cases} \tag{5-1}$$

where $m = 40$ so that there would be 20 secondary electrons for a incident electron hitting the dynode with 1000 eV.

This function only scales the signal generated by the secondary electrons, while leaving the one due to the photoelectrons untouched.
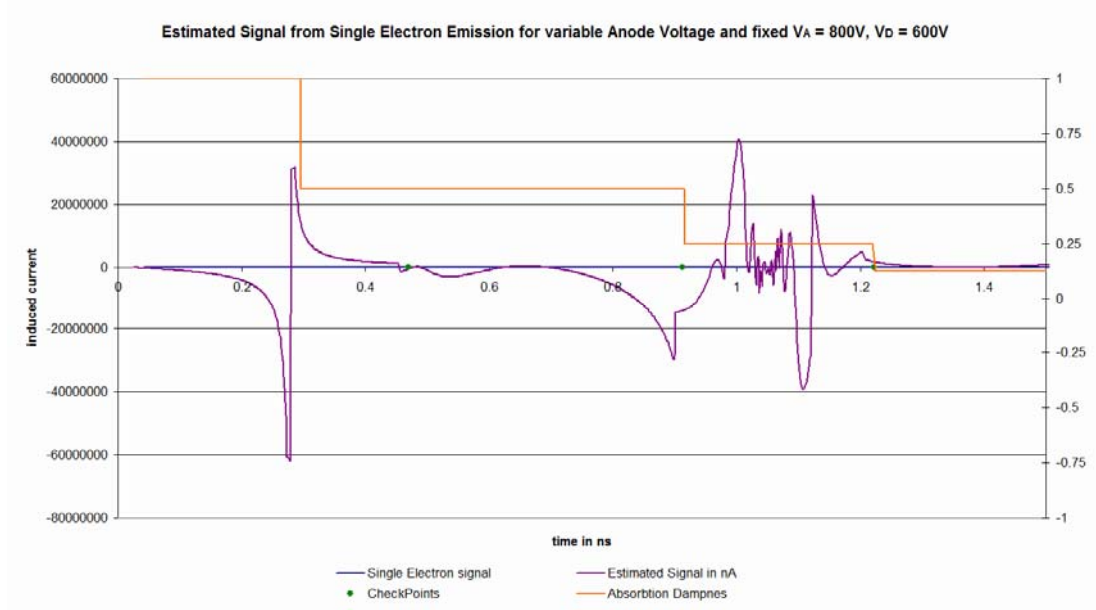
Figure 5-14 Signal estimation sample

The signal is finally multiplied by the number of photoelectrons so that the magnitude is comparable with experimental data. In order to do this, the laser manual [1] was consulted to obtain the details that would allow for the calculation of the approximate number of photoelectrons.

The energy of the laser pulse is proportional to the energy of each photon and given by:

$$E_{PULSE} = \#_{PHOTONS/PULSE} \cdot E_{\gamma} \tag{5-2}$$

The energy of a photon is given by $E_{\gamma} = \dfrac{h \cdot c}{\lambda}$ where **h** is Planck's constant, **c** is the speed of light, and **λ** is the photons wavelength. The laser used in the experiments in Chapter 6 has a wavelength $\lambda = 435$ nm so:

$$E_{\gamma} = \frac{h \cdot c}{\lambda} = \frac{\left(6.626 \times 10^{-34}\,J \cdot s\right) \times \left(3 \times 10^{8}\,m/s\right)}{435 \times 10^{-9}\,m} = 457 \times 10^{-21}\,J \tag{5-3}$$

The energy of a pulse is the ratio of its power and frequency. Therefore, using the technical data from the laser manufacturer (Figure 6-3), the power of the pulse at a repetition rate of 40 MHz is 0.36 mW, thus:

$$E_{PULSE} = \frac{P_{PULSE}}{f_{PULSE}} = \frac{0.36 \times 10^{-3}\,J \cdot s^{-1}}{40 \times 10^{6}\,s^{-1}} = 9\ pJ \tag{5-4}$$

So the number of photons in each pulse can finally be calculated by:

$$\#_{PHOTONS/PULSE} = \frac{E_{PULSE}}{E_\gamma} = \frac{9 \times 10^{-12} \text{ J}}{457 \times 10^{-21} \text{ J}} = 19.7 \times 10^6 \tag{5-5}$$

However, only a proportion of the incident photons release photoelectrons. As it was shown in Chapter 2, the ratio between photons and photoelectron is known as the Quantum Efficiency of the photocathode, which for the VPTs modelled in this thesis, the $QE = 18\%$.

Therefore, as $\#_{PHOTOELECTRONS} = QE \times \#_{PHOTONS/PULSE}$

Thus,

$$\#_{PHOTOELECTRONS} = 3.5 \times 10^6 \tag{5-6}$$

Response to a Variable Dynode Voltage

This study looks at the results from leaving the anode-cathode voltage constant but increasing the dynode voltage. By doing so, the effect of deceleration on the number of secondary electrons can be seen, as well as, why this number is not the only factor affecting the gain of the VPT. Figure 5-15 shows what is seen from SIMION7 when simulating the secondary electrons due to a single photoelectron[**]. This image shows the three electrodes (cathode, anode, and dynode) and the secondary electron trajectories for different dynode voltages when the $V_A = 1000 \text{ V}$ and $V_K = 0 \text{ V}$. What is obvious, is the direct relationship between the number of secondary electrons and V_D, but as V_D decreases the electron travels further away from the dynode due to the increasing acceleration from the anode-dynode potential difference. As the secondary electron increases in speeds, it would have to travel further from the anode, before reaching a stop, and reversing direction. The opposite is also true: as the dynode becomes more positive with respect to the anode, the

---

[**] Figure 5-15 shows a combination of the different simulations. They where joined in the same picture using Photoshop in order to illustrate the effect of different dynode Voltages.

electron feels an increasing attraction to the dynode, and as V_D increases, they find it harder to reach the anode.

This picture does not however, show the speed and time of flight of each electron so a picture of the signal should be inferred by other means. There were certain characteristics in the single electron signal shown in Figure 5-12 (above) that can be explained here. The part of the signal generated by the secondary electrons has two sign reversals, and the gap between these reversals depends on V_D. Figure 5-15 shows that as the secondary electron moves from right to left, they pass the anode and then decelerate to a stop at a distance "d" from the anode. Then they are attracted back by V_{KA} to the anode and continue to the dynode. 50% of the electrons are absorbed by the anode at each pass, but the secondary electrons that are not absorbed pass the anode twice.
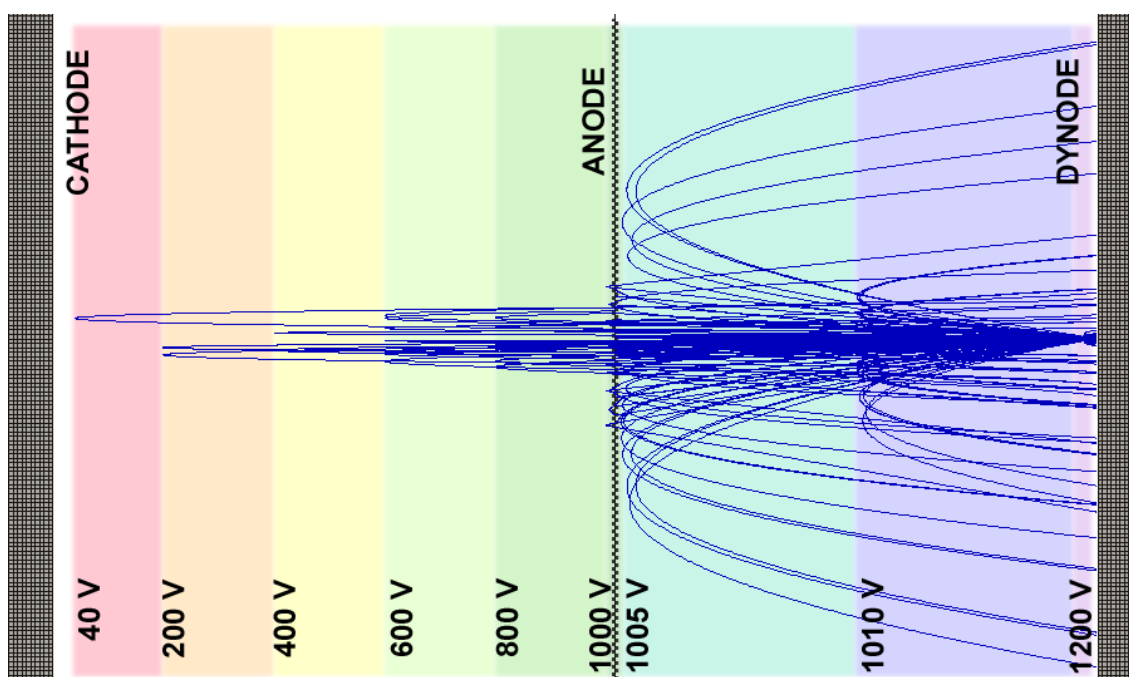

Figure 5-15 Variable dynode SIMION7 simulation for secondary electrons due to single photoelectron.

As was explained in Chapter 2, the induced current on the anode is proportional to $\vec{v}$. Therefore, the sign of the current depends on the relative direction of the electrons movement; i.e. it is negative for approaching electrons and positive otherwise. So even if the absolute velocity does not change

dramatically, once the electron passes the anode it stops moving towards it and starts moving away from it. This sudden change is the reason of the current sign reversal.

As the dynode voltage decreases the potential difference between anode and dynode increases, therefore the forces on the electrons (proportional to the electric field) increase. With bigger force, bigger is the acceleration and the speed of the electrons at the point they cross the anode. However the forces acting on the electrons on the cathode-anode region do not change, so neither does the deceleration of the electrons in this region. Because of this, the electrons travels further before reaching a stop, thus taking more time to return when accelerated back to the anode, hence increasing the gap between the signal reversals.

As was previously mentioned, the signal can only be inferred from the SIMION7 simulation window, due to that there is no information other than the distance travelled. When $V_A \leq V_D$ the secondary electrons drift at a constant speed from the dynode to the anode with their initial energy of 5 eV. Because of this low velocity (when the dynode is positive compared to the anode), the induced signal at the anode is very small.

Figure 5-16 shows the estimated signal for different dynode voltages.
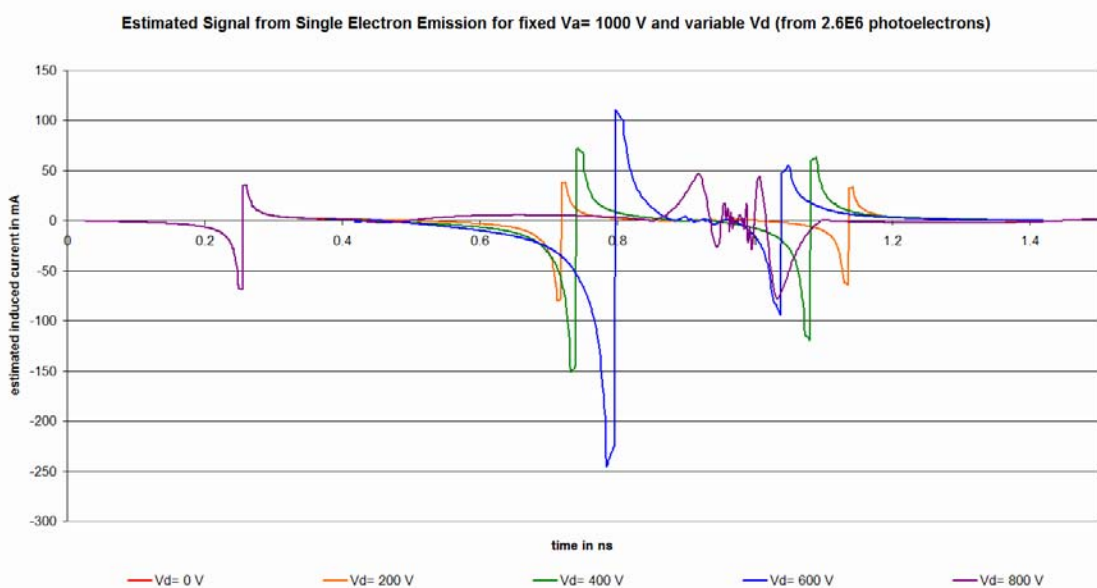

Figure 5-16 Estimated response to a variable dynode voltage

The rate of deceleration is also very important for the generation of secondary electrons, as the number of secondary electrons depend on the energy at which the photoelectron hit the dynode. However, this number can, at most, work as a multiplication factor to the signal shown in Figure 5-12. In other words, the amplitude of the signal due to the secondary contribution can not be solely dependent on their number but also depends on the magnitude of their individual contributions. Unfortunately, these two factors are inversely proportional to each other (the greater V_{AD}, the greater the signal contribution, but the smaller the amount of secondary electrons). Thus, one would expect the "gain" to reach an optimum, and then decline.

Response to a Variable Anode Voltage

This test looks at the results from increasing the V_{AK}, whilst keeping constant V_{AD} in order to simulate the effect of the acceleration of the photoelectrons on the gain.
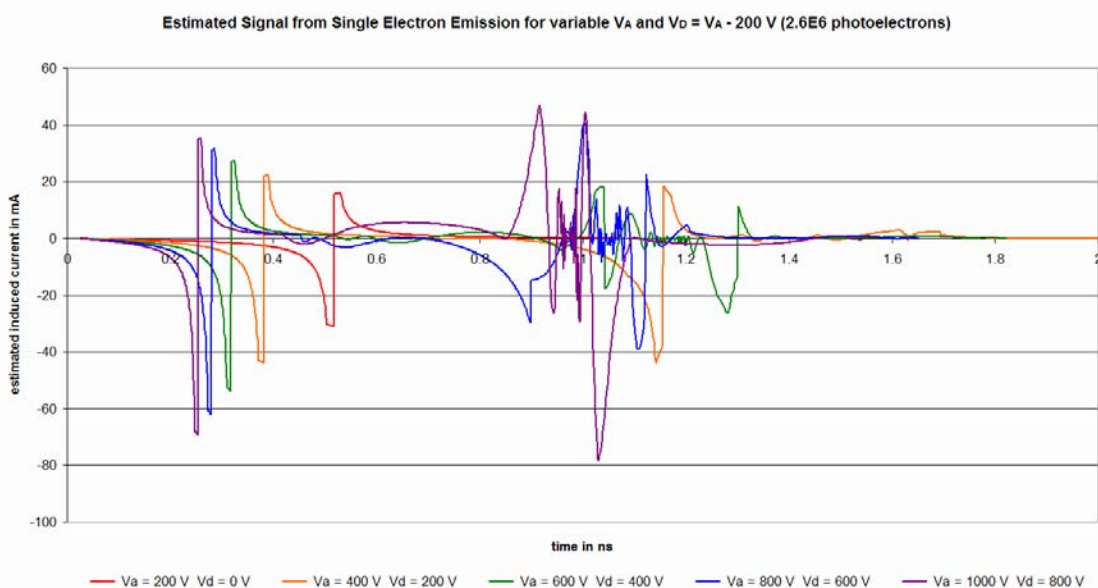

Figure 5-17 Estimated response to a variable anode voltage

Comparing Figure 5-13 and Figure 5-17 the main effect of the difference in the amplitude between the contributions due to the secondary electrons can be seen. The single electron contribution due to the secondary electrons should

not differ very much between the different anode voltages due to that V_{AD} is kept constant, thus keeping the same acceleration of the secondary electrons. In this case the number of secondary electrons has a direct influence on the magnitude of the signal, therefore, in order to increase the number of secondary electrons, one would need to increase the energy at which the photoelectrons hit the dynode. Since the rate of deceleration is the same whatever the anode voltage, then the greater V_A the more energy the photoelectron would have when hitting the dynode.

Diode Configuration Type II

The purpose of this configuration is to study the response of keeping the anode and the dynode at the same potential, i.e. V_{AD}=0 V . For this, the anode and the dynode were simultaneously increased from 0 V up to 1000 V . By doing so, the primary photoelectrons would not decelerate after passing the anode, and even if upon dynode impact they have the maximum possible energy (and therefore release of maximum secondary electrons) the acceleration for the secondary electrons would be minimal, in fact nil. The secondary electrons drift in the vacuum, and when inside the area of influence, they would have so little energy (their initial 5 eV) that their total induced current is also negligible. Having a greater dynode voltage would stop the secondary electrons reaching the area of influence altogether, before returning to the dynode. In addition, even if there are still electrons moving within the VPT, they do not induce a noticeable signal on the anode (even if multiplied by the great number of secondary electrons).
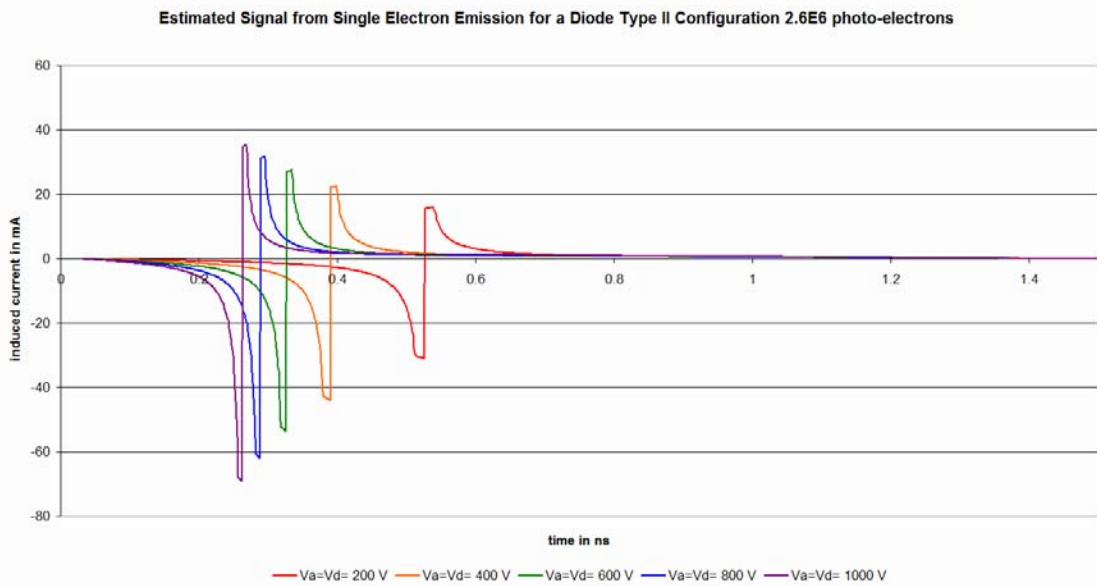
Figure 5-18 Estimated response to a varying anode voltage with the dynode at the same potential as the anode (Diode Type II)

The resulting signals are given by Figure 5-18. This figure looks like the reproduction of the Figure 5-17 signal due to the primary photoelectrons. That is to be expected since from the point of view of the photoelectrons there is very little difference and if any is registered it is only on the tail of each signal.

Diode Configuration Type III

This test looks at the effect of keeping the dynode at the same potential as the cathode while increasing the anode voltage. As opposed to the previous setting, this one tries to maximise V_{AD} so that the primary photoelectrons decelerate to an energy inadequate to allow the release of secondary electrons[††]. With no secondary electrons, there are no more contributions, so the story ends there.

[††] The photoelectrons do not decelerate to a standstill due to the geometry of the VPT, and the initial energy of the photoelectrons; for that, the dynode should be more negative than the cathode
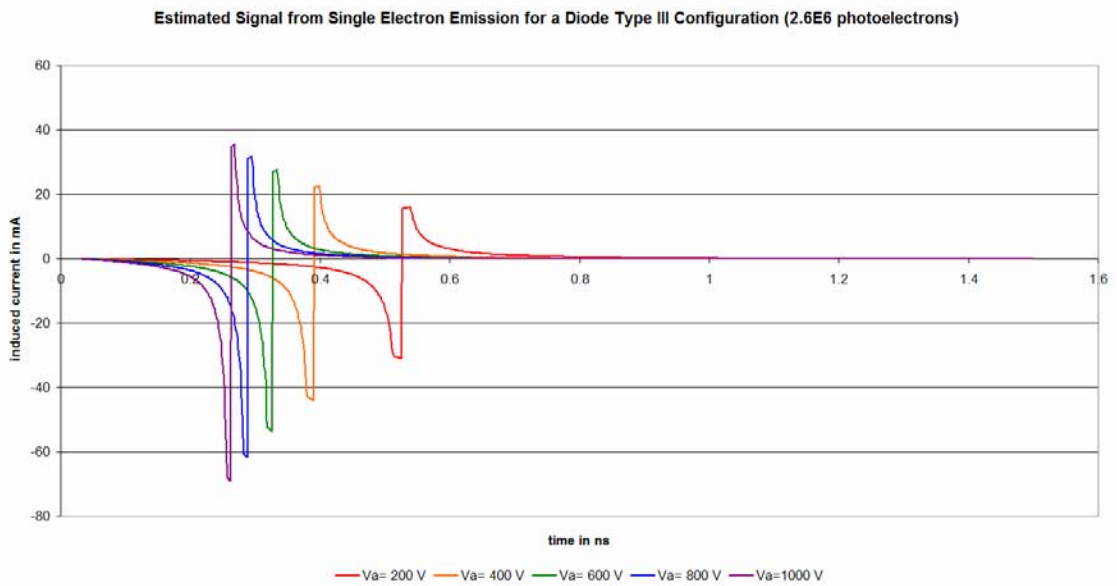
Figure 5-19 Estimated response to a varying anode voltage with the dynode at the same potential as the cathode (Diode Type III)

Figure 5-19 shows once again the signals due to the primary photoelectrons. As it can be seen, it resembles very much Figure 5-18, proving that this, as well as the previous method, is an acceptable for biasing an experiment for primary photoelectrons signal isolation.

Gain vs Voltage

The gain described here refers to the ratio of the negative peaks of the signals due to the primary photoelectrons and the secondary electrons. Note that as both peaks are affected in the same proportion by the number of photoelectrons, the gain would, therefore, be independent of the light intensity In the sample given in Figure 5-20 the gain would be

$$\text{Gain} = \frac{\text{Secondary Peak}}{\text{Primary Peak}} \qquad (5\text{-}7)$$
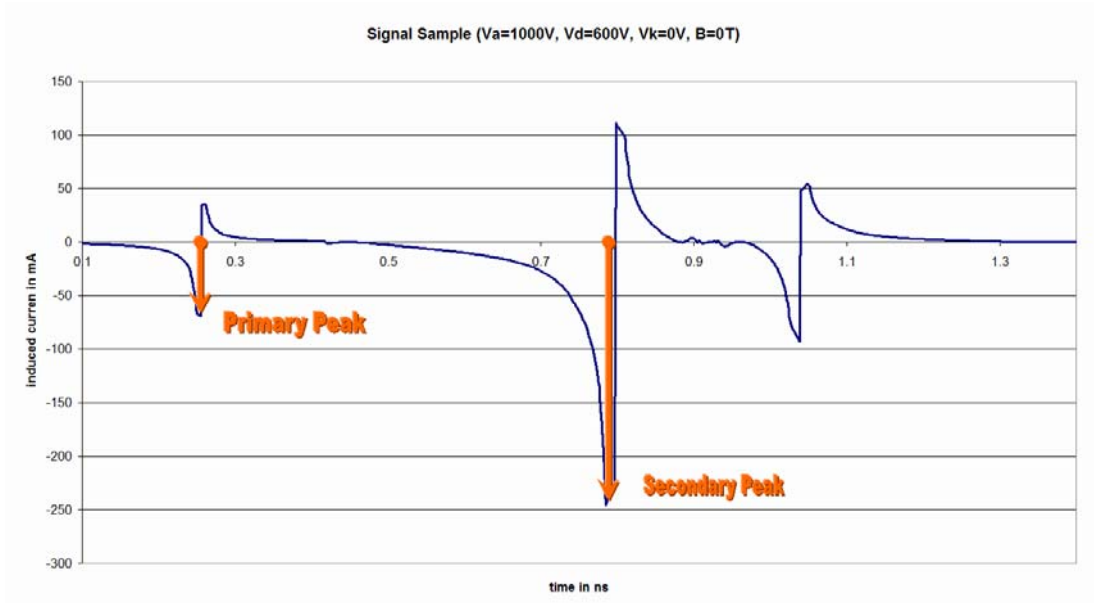
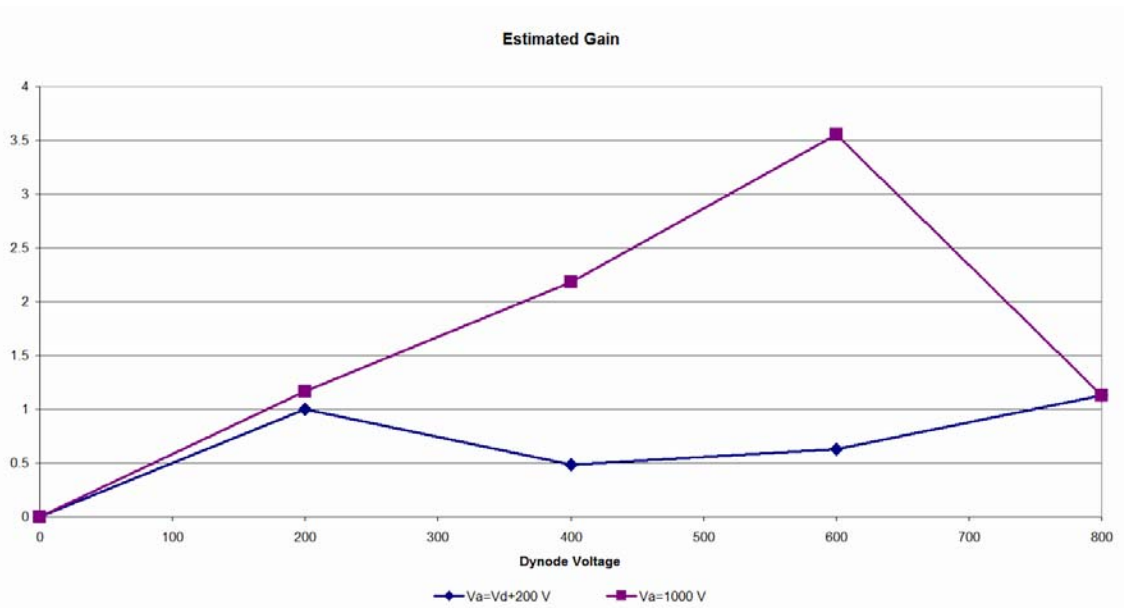**Figure 5-20 Signal sample for gain calculation**

Figure 5-21 Gain vs dynode voltage

Figure 5-21 shows the gain for two distinctive cases: in blue, when fixing the dynode such that $V_D = V_A - 200\ V$ and in purple for a varying dynode voltage. However, for convenience it was plotted with reference to the dynode.

This chart suggests that varying the dynode voltage has a greater effect on the signal if the anode is fixed at $V_A = 1000\ V$. Furthermore, as was predicted, the gain reaches a maximum before starting to decline. In the range of voltages studied, the maximum gain was at $V_A = 1000\ V$ and $V_D = 600\ V$.

Effect of the Magnetic Field Strength

This test looks at what happens when the VPT is in a uniform magnetic field orientated at 15° to the electric field[‡‡]. For this the magnetic field was increased from 0 up to 4 T (equivalent to the operating magnetic field at the ECAL of CMS).
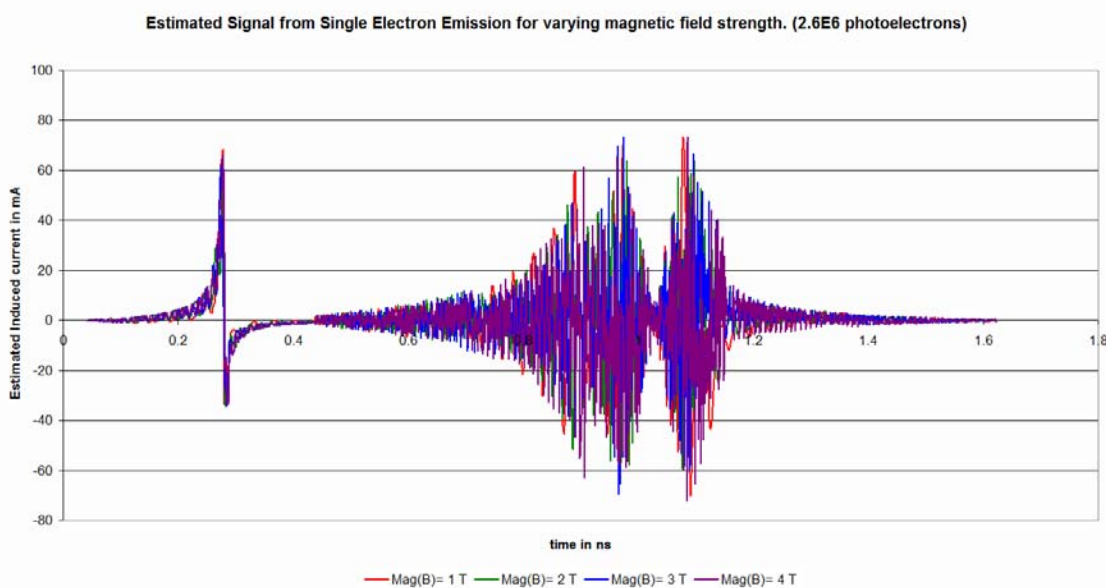

Figure 5-22 Estimated response from varying magnetic field strength

Figure 5-22 shows the signal at different magnetic field strengths at and angle of 15° for $V_A = 1000$ V and $V_D = 800$ V. It shows the now familiar shape of $V_{AD} = 200$ V with an added ringing, the frequency of which changes with the magnetic field strength. Figure 5-23 shows a zoomed version (from 1.26 to 1.34 ns) of the signals shown in Figure 5-22, where it can clearly be seen that the period of the ringing decreases as the magnetic field strength increases.

[‡‡] 15° would be the average angle between the magnetic field and the VPT in the endcap of CMS. Furthermore, this is the angle at which the VPT acceptance test are carried out at Brunel University with B=4 T.
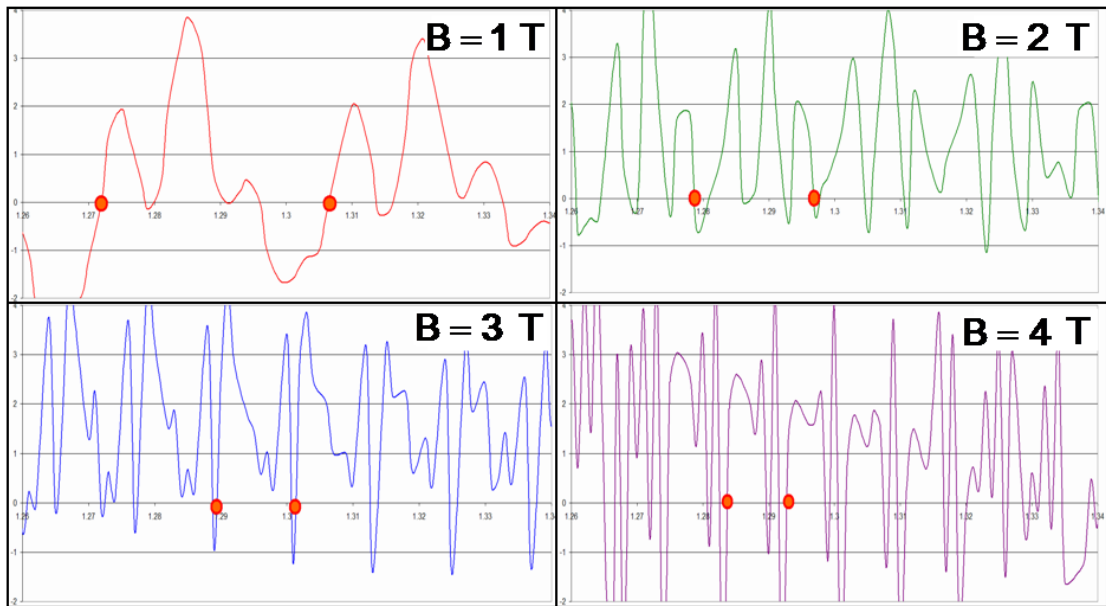
Figure 5-23 Effect of the magnetic field strength on the ringing frequency of the signal. All charts are at the same linear scale covering the range from 1.26 ns to 1.34 ns

These frequencies were measured at $27.77\,\text{GHz}$ for $B=1\,\text{T}$; $55.55\,\text{GHz}$ for $B=2\,\text{T}$; $83.33\,\text{GHz}$ for $B=3\,\text{T}$; and $111.11\,\text{GHz}$ for $B=4\,\text{T}$.

This ringing is due to the helical trajectory of the electron due to the magnetic field. Theoretically, the time it takes for the electron to complete a single turn is given by:

$$T = \frac{m_e \cdot 2 \cdot \pi}{q_e \cdot B} \tag{5-8}$$

where B is the magnitude of the magnetic field $(\vec{B})$, m_e and q_e are the mass and charge of the electron, respectively.

Therefore as

$$f(B) = \frac{1}{T} = \frac{q_e \cdot B}{m_e \cdot 2 \cdot \pi} = \frac{160.2 \times 10^{-21} \cdot B}{910.9^{-33} \cdot 2 \cdot \pi} = 27.99 \times 10^9 \cdot B \tag{5-9}$$

$f(1\,\text{T}) = 27.99\,\text{GHz}$, $f(2\,\text{T}) = 55.98\,\text{GHz}$

$f(3\,\text{T}) = 83.97\,\text{GHz}$, $f(4\,\text{T}) = 111.96\,\text{GHz}$

These values are in agreement with the measured data, where:

$$\frac{f(1T)}{1} = \frac{f(2T)}{2} = \frac{f(3T)}{3} = \frac{f(4T)}{4} \qquad \text{(5-10)}$$

Since the magnetic field $\vec{B}$ and the velocity of the electron $\vec{v}$ are at an angle, the electron circles about an axis not perpendicular to the anode. Because of this, from the anode perspective, the electron moves back and forwards as it approaches (something like, two steps forward one backward, then again two forwards and one backwards, etc.) therefore although the overall movement is in one direction, the v_x[§§] changes sign and with it the induced current.

Effect of the Magnetic Field Angle

This test looks at the effect of changing the magnetic field angle at a constant strength of 1.8 T
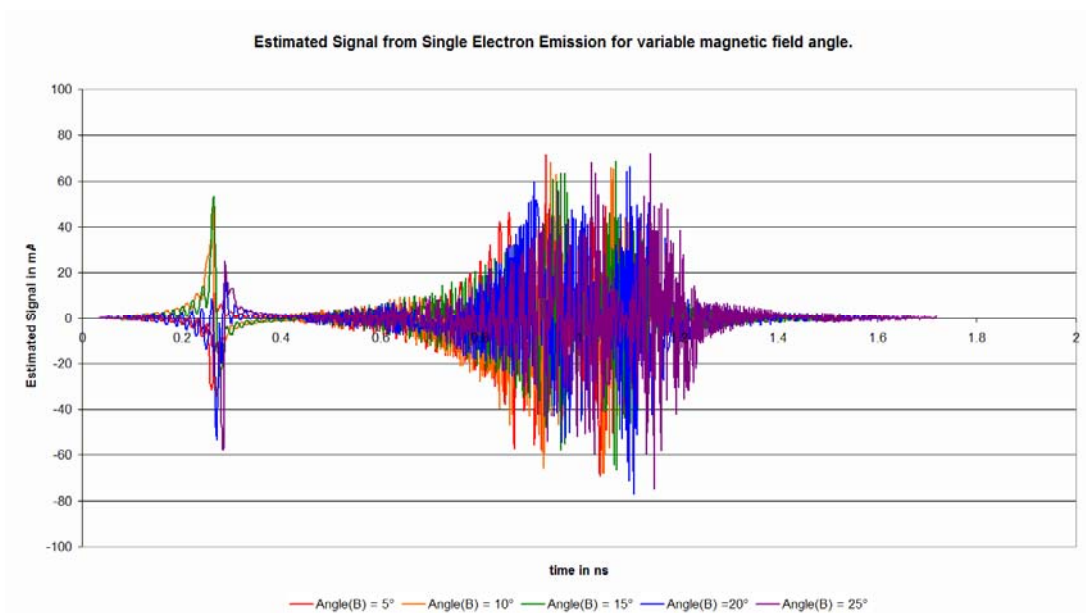

Figure 5-24 Estimated response from varying the magnetic field angle

Figure 5-24 shows a similar picture to Figure 5-22, but in this case, the ringing does not change frequency. The measured frequency remains constant at 50 GHz independently of the field angle as it can be seen from Figure 5-25.

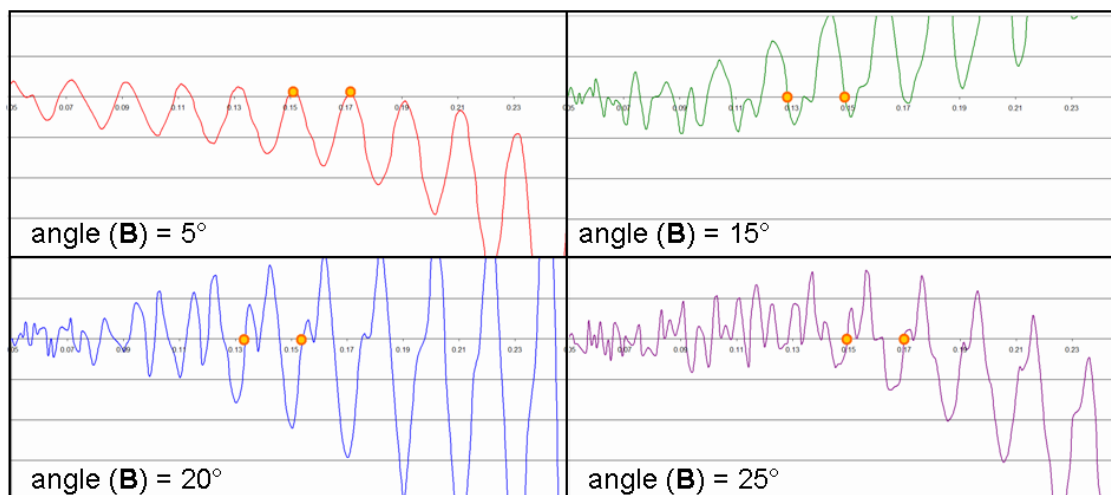[§§] v_x is the velocity component perpendicular to the anode.

Figure 5-25 Effect of magnetic field angle on the ringing frequency of the signal

The frequency calculated from the simulated signal agrees with the theoretical cyclotron frequencies as it satisfies that:

$$\frac{f(1T)}{1} = \frac{f(1.8T)}{1.8} \tag{5-11}$$

One should expect that the magnitude of the signal to be affected, but this is due to the estimation process that does not take into account the proportion of photoelectrons that do not reach the dynode because they forced out from the VPT by the magnetic field. This is a trade off from the previous simulation system, which allows for multiple photoelectron simulations, but lacks the resolution which adequately describes the signal induced at the anode.

Effect of Mesh Resolution on VPT Response at the Presence of Axial Magnetic Field

During the development of the model, different mesh resolutions were implemented in order to study the effect they had on the simulated signal. This was motivated by experimental work on prototype VPT which had shown that fine mesh tubes showed significantly less fall-off in gain with increasing field than those with coarser meshes [2]. Three different mesh sizes, each with 50% transparency, were simulated using the SIMION model.
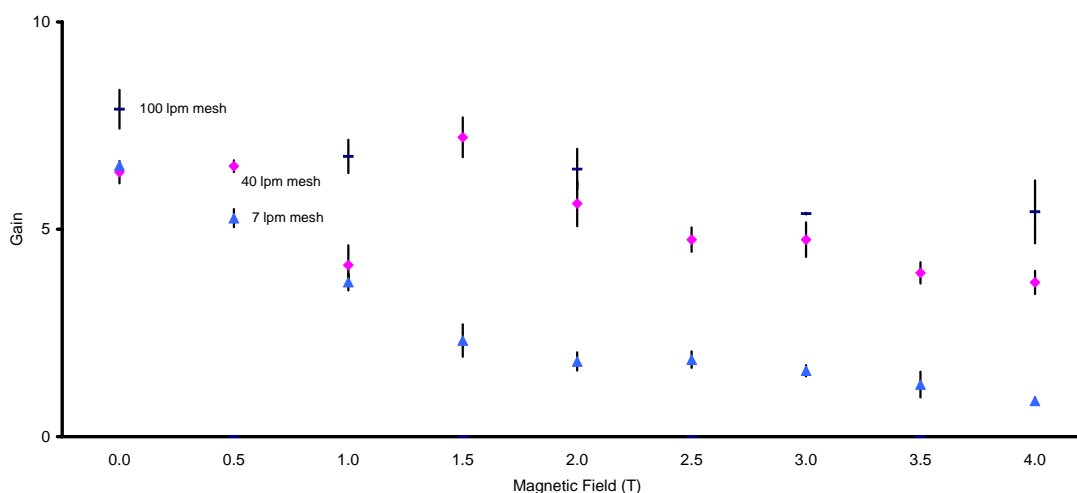
Figure 5-26 Simulated variation in gain as a function of magnetic field for a VPT with three different mesh sizes. The tube is at an angle of 15 degrees to the magnetic field. The standard errors on the mean are shown. The 100 lines/mm mesh data was only simulated at integer values of the field. This figure appears in reference [3].

The results from the simulation demonstrate that, as expected, the mesh resolution was only important when there was a magnetic field present. Fine mesh VPT cope better in magnetic fields than the coarse ones; the 100 lines/mm does not show the drastic decrease that the 7 lines/mm suffers; instead it varies little in comparison. The 40 lines/mm mesh behaved much better than the 7 lines/mm but not as well at 4 T as the 100 lines/mm.

This is because in a strong magnetic field the electron collection rate at the anode is affected due to the forced trajectory of the electron. In order to compensate for this, the mesh holes should be comparable in size with the radius of the helical path of the electron. Collection at the anode is important, because otherwise, as the electron moves back and forwards, the induced anode current integrates towards zero.

References

1 PDL 808 "SEPIA" PicoQuant: Multi-channel Pulsed Diode Laser System User Manual Version 1.0 (April 2002)

2 Apollonio M et al, "T*he performance of prototype vacuum phototriodes in the first full sized supercrystal array for the CMS ECAL endcaps*", Nuclear Instruments and Methods in Physics Research A **532** (2004) 566-574

3 Hobson, P R and Yaselli, I; "Simulation of a Vacuum Phototriode with SIMION 3D" Nuclear Instruments and Methods in Physics Research A **567** (2006) 226-229.

Chapter 6 Experiments on the VPT

T he three previous chapters described the implementation of a simulation system which allowed understanding (to some extent) of the operation of the VPT. It was shown that photoelectrons are initially accelerated towards the anode at the cathode-anode region and then decelerated at the anode-dynode region. The rate of these accelerations and decelerations depended on the cathode-anode and anode-dynode potential differences respectively. The photoelectrons that collided at the dynode released secondary electrons, the number of which depended on the incident photoelectrons energy. It was also shown that the signal of the VPT (anode current), was the consequence of the induced charge (at the anode) from the electrons moving across the VPT. In addition, the effect of the magnetic field was studied, and it was shown that it introduced a high frequency ringing to the signal which was proportional to the field strength; on the other hand, the angle of the magnetic had an effect on the signal amplitude by reducing the speed of the electrons on the VPT's axis component. Finally, different methods were shown where by the signal from the photoelectrons could be isolated so that it could be measured on the experimental apparatus. This resulted in three configurations which could be achieved by rewiring the current testing jig.

In this chapter the measurement apparatus which is used to verify the observations from the simulation is described. The experiments shown in this chapter were performed on three identical VPT with identification numbers: 971, 1485, and 2517. These VPT are from the same production batch to the one which was cut open and modelled in the previous chapters. The manufacturer of these VPT, Research Institute Electron (RIE), supplied the information given in Table 6-1 which lists the measured parameters specific to each of the VPT.

VPT	Gain	QE	Quality Factor
971	10.70	0.15	1.61
1485	13.90	0.18	2.50
2517	9.40	0.19	1.79

Table 6-1 List of VPT provided for the experiments.
The Quality Factor is the product of the Gain and the Quantum Efficiency (QE)
(Parameters measured by manufacturer)

The following pages present the equipment, methodology, and the experiments (under zero magnetic field) in which the timing characteristics of VPT were measured. The results presented in this chapter are for VPT 971, as for the results on VPT 1485 and VPT 2517, please refer to Appendix D.
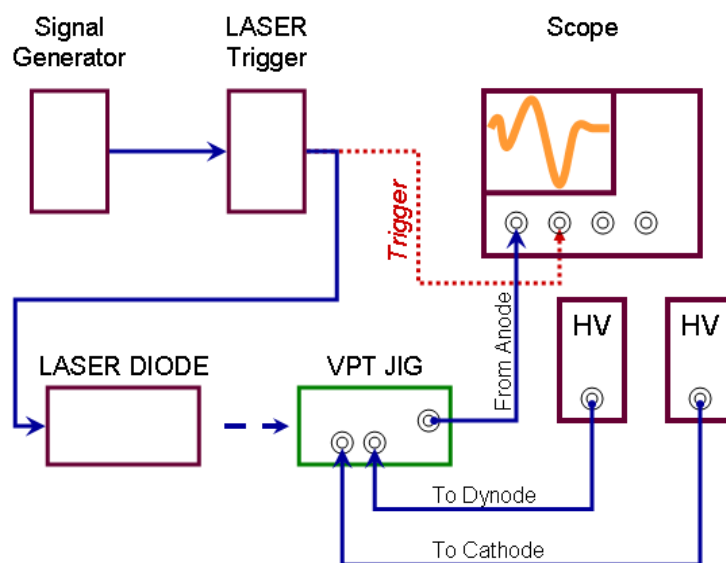
Methodology

Figure 6-1 Test System Diagram

The Vacuum Phototriode (VPT) is mounted on a jig (see Figure 6-6) and powered by two power supplies, which provide a negative DC voltage to the dynode and the cathode, while the anode is at ground potential. The Laser Diode is fired by the Laser Trigger at intervals set by the Signal Generator. The Scope reads the signal from the anode and the Laser Trigger to synchronise the signal with the laser pulse. The signal was then pre-processed and stored for later retrieval with a USB memory device.

In CMS the output signal of the VPT (the anode current) would be fed to a preamplifier before it is read out. By using a combination of low and high pass filters and a coupling capacitor, the HV DC components (and the noise) of the signal is eliminated to prevent damage to the pre-amplifier. All of these components have an adverse effect on the study of the time response of the VPT.

The purpose of the measurement experiment was to observe the anode signal with the least modifications as possible, so that future comparisons with the simulated data would be reliable. Because of this, it was crucial to eliminate as much of the CMS electronics as possible between the anode signal and the oscilloscope. This was done by changing the reference voltage (zero potential)

from the cathode to the anode. The potential differences between the anode and the other electrodes were kept by applying negative DC voltages to the cathode and to the dynode. Therefore, the experimental cathode voltage was set to $V_{KX}=V_K-V_A=-1000$ V, and the experimental dynode voltage was set to $V_{DX}=V_D-V_A=-200$ V.

Another reason for using the anode as the reference is due the fact that the scope is very sensitive, and its inputs can not tolerate voltages greater than 4 V; therefore, by having the anode voltage as the reference, the small anode current generates a small voltage across a 50 Ω resistor which is tolerable by the scope, thus minimizing the filters effect on the time response of the VPT.
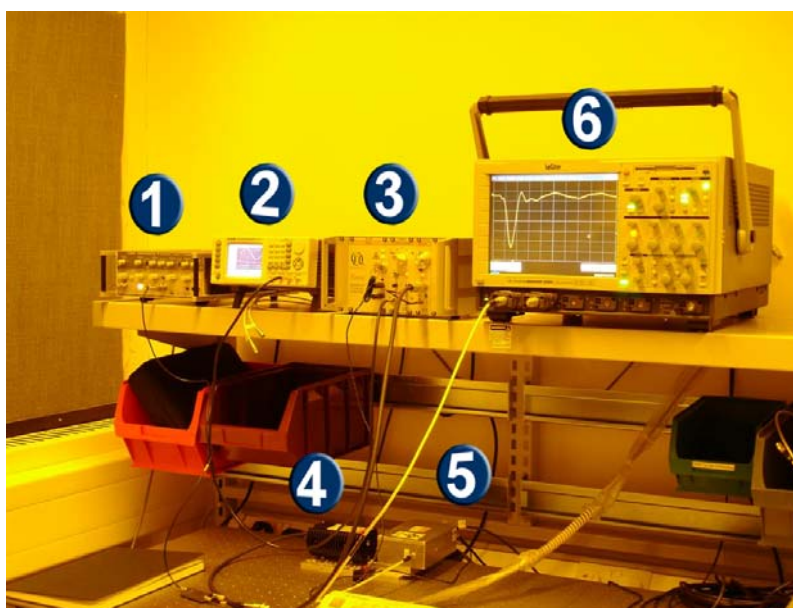
Lab Instruments and Equipment

Figure 6-2 Photo of the Testing System

(1) Signal Generator

Lyons Instruments PG 73N bipolar Pulse Generator

(2) Alternative Signal Generator (not used)

(3) Laser Driver Module

Pico Quant Sepia Multichannel Picosecond Diode Laser [1]

(4) Laser Head

Pico Quant Sepia Multichannel Picosecond Diode Laser [1]

Model No.   LHD-P-C-440

Serial No.:   LHD-C-4-340

Optics: Collimator

Wavelength: 435 – 436 nm

Average Optical Power:

Repetition Frequency	Max. optical power (10% calibre. error)
40 MHz	1.05 mW
20 MHz	0.59 mW
10 MHz	0.31 mW
5 MHz	0.16 mW
2.5 MHz	0.08 mW

Minimum Pulse Width: 59ps
(measured by manufacturer)

Figure 6-3, 6-4, and 6-5, show the characteristics of the laser head used for the experiments described in this chapter. Note that these figures are not general but actual data supplied by the manufacturer for this specific laser head. The laser head power was adjusted via the 10-turn potentiometer on the laser driver module.

Figure 6-3 shows the laser pulse at low power. As it can be seen from this chart, almost all of the light is concentrated on the pulse, peaking just over 86 mW at around 1.6 ns ; this part of the pulse is known as the fast component. The tail of this pulse (an elbow like shape) peaks almost 8 mW at 1.8 ns ; this part of the pulse is known as the slow component.
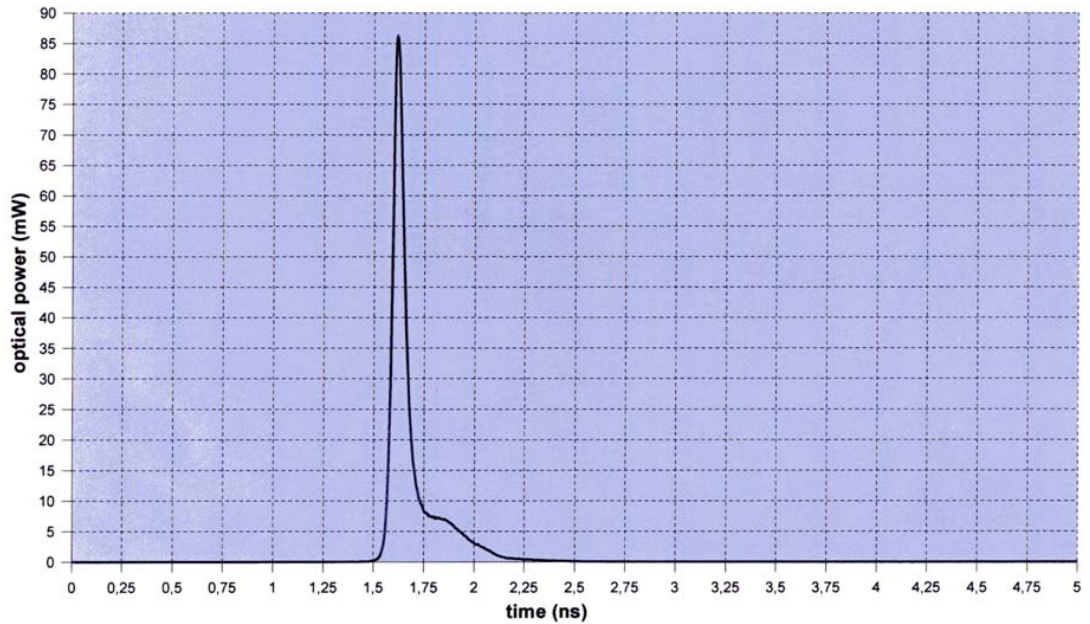
| Laser Head: | LDH-C-4-340 | wavelength: | 435 nm | peak power | 86 mW |
| PicoQuant GmbH 2004 | | average power @ rep. frequency | 0,36 mW 40 MHz | pulse energy: FWHM: IRF: | 9 pJ 68 ps 30 ps |

Figure 6-3 [1] Laser pulse characteristics for average power of 0.36 mW

As the power is increased, the fast component of the pulse also increases, but as Figure 6-4 shows, the slow component increases at a much greater rate. Increasing the pulse energy from 9 pJ to 27 pJ (300% increase), sees an increase of the peak power of the fast component from 86 mW to 147 mW (170%); while the slow component increased from 7.5 mW to 62 mW (830%).
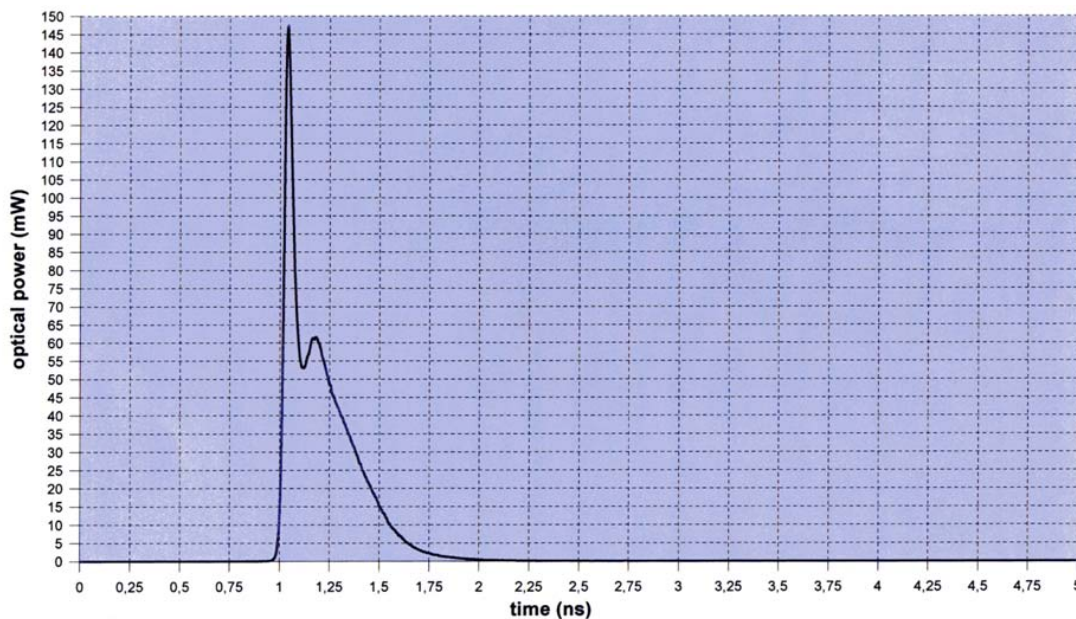
Laser Head:	LDH-C-4-340	wavelength:	436 nm	peak power	147 mW
		average power	1,1 mW	pulse energy:	27 pJ
		@ rep. frequency	40 MHz	FWHM:	63 ps
PicoQuant GmbH	2004			IRF:	30 ps

Figure 6-4 [1] Laser pulse characteristics for average power of 1.1 mW
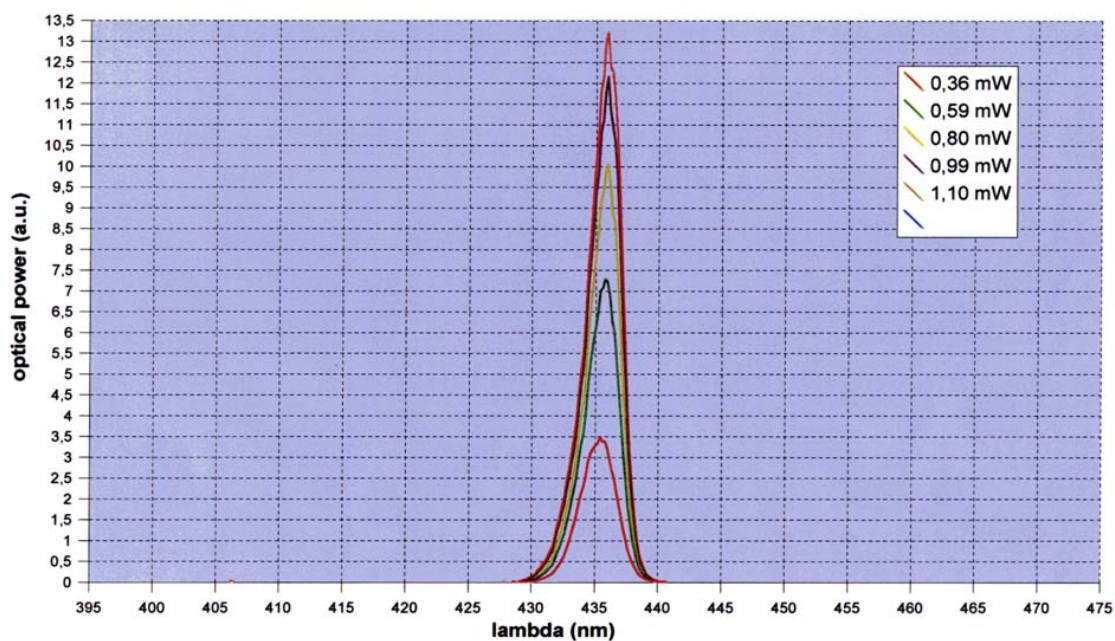
Laser Head:	LDH-C-4-340	avg. wavelength:	435,8 nm	min. spectral width:	2,8 nm
				max. spectral width:	3,3 nm
PicoQuant GmbH	2004				

Figure 6-5 [1] Laser optical power (in arbitrary units) vs wavelength (in nm)

(5) JIG
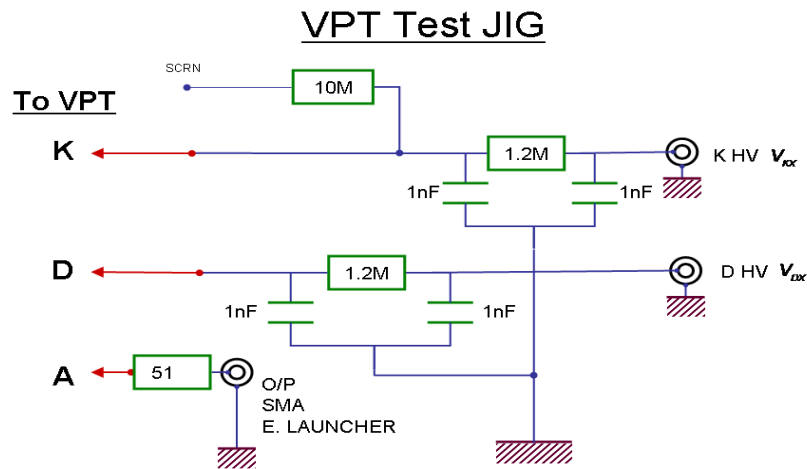
Figure 6-6 VPT Testing JIG.
(Design and build by Chris Selby)

Connection from anode to SMA connector is a 50 Ω strip line and the 51 Ω resistor is SOT1206 format.

(6) Scope

Le Croy WAVE MASTER 8300A

3 GHz Oscilloscope

Sampling Rate: 10 Gsamples/s or 10 samples/ns

System:

Microsoft Windows XP Professional Version 2002 Service Pack 2

Manufactured by LeCroy Corporation Test & Instrument

Pentium® 4 CPU 2.53 GHz

240 MB of RAM

(7) Power Supply

2x CANBERRA H.V. Power Supply model 3002

Tests

Normal Operation

The cathode-anode voltage differential was varied to show how the initial acceleration affected the gain of the signal. Similarly, the effect of deceleration due to the anode-dynode differential on the emission of secondary electrons was tested and also how this affects the gain.
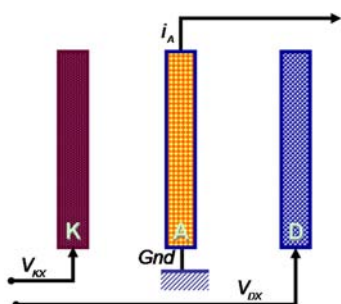
Figure 6-7 Normal Operation Connections

This mode of operation requires no modifications from the above description and includes the specific case which emulates the operating conditions in CMS, i.e. V_K=0 V , V_A=1000 V , V_D=800 V which would be referred as the Standard Bias, which in these experiments is replaced by V_{KX}=-1000 V , V_{AX}=0 V , V_{DX}=-200 V .

Diode Configuration

These tests tried to eliminate the contribution of the secondary electrons so that the signal due to the primary photoelectrons alone could be observed. There were three configurations proposed for this purpose, all of which required rewiring the jig. These configurations were:

Diode Type I

Figure 6-8 Diode Type I Connections

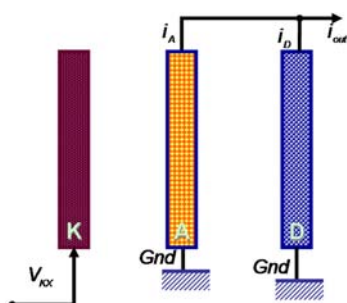In this configuration, the signal would be taken directly form the anode and dynode simultaneously. In addition, both electrodes would be held at ground (form the potential point of view). By adding the two signals, it was expected to obtain a larger signal from the photoelectrons, while the zero potential difference between anode and dynode would minimise the signal from the secondary electrons.

However, due to the fact that this configuration would require a rewiring of the PCB, it was decided to leave this experiment to be done at a later stage (time permitting).
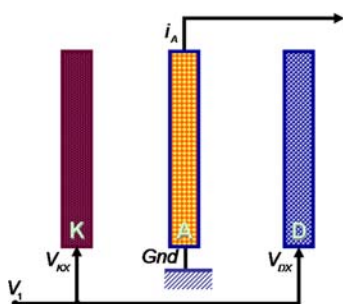
Diode Type II

Figure 6-9 Diode Type II Connections

The dynode was hardwired to the potential of the anode, which in our experiments was equivalent to GND ($V_A = V_D$). Because of this, the secondary electrons would not be accelerated towards the anode; therefore, the signal induced by them would be negligible.

Although this experiment would yield a slightly smaller signal than a Type I configuration, it was much simpler to implement.

Diode Type III
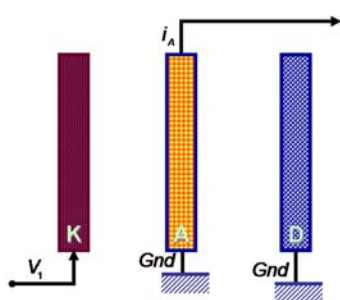
Figure 6-10 Diode Type III Connections

A HV splitter was used to provide the cathode and dynode with exactly the same potential ($V_K = V_D$). The objective was to decelerate the photoelectrons so that they reached the dynode with insufficient energy to release secondary electrons.

As well as a Type II, this configuration would yield a smaller signal than a Type I configuration, and furthermore, it requires an extra device to be attached to the testing jig.

Further Measurements

For reasons that will be described later, it was necessary to validate the results from the previous test by examining the testing principles themselves. In order to do this, the following issues were considered:

- **Repeatability**: It is important to determine the pulse-to-pulse repeatability as well as the fluctuations between the measurements so as to create trust on the signal observed from experiments.

- **Statistical Sufficiency**: Measurements where taken from an average of 2000 and 4000 sweeps in order to establish whether there were any statistical difference.

- **Effect of read out cable:** The anode cable was doubled in length to check its effects on the readings; such as: delay, attenuation, noise, reflection.

- **Shielding**: A frequency analysis of the measured signal was done in order to investigate if the outside world (mobile phones, transmitters, radio, WiFi, etc) was affecting the measurements.

- **Trigger Response**: This experiment was done as a response to the suggestion made by Professor Brown [2], where it is stated that the signal amplitude might be dependent on the trigger frequency.

- **Laser Intensity Dependency:** The laser intensity was changed to investigate whether the cathode was saturating, as well as any time delays associated with the tail of the laser pulse at high power.

Results from Basic Measurements

The experiments reported on this thesis were done on three identical production line VPT (within tolerance), manufactured by Research Institute Electron (RIE). These exact VPT were provided for the purpose of these experiments, and would otherwise be installed in CMS.

The results presented here are for VPT 971. For other tests, including VPT 1485 and VPT 2517, please refer to Appendix D. Moreover, the results given have been modified so that they had the cathode as the reference voltage.

Response to a Variable Anode Voltage

This test looks at the effect of increasing the anode voltage but keeping the voltage differential between the anode and dynode constant.
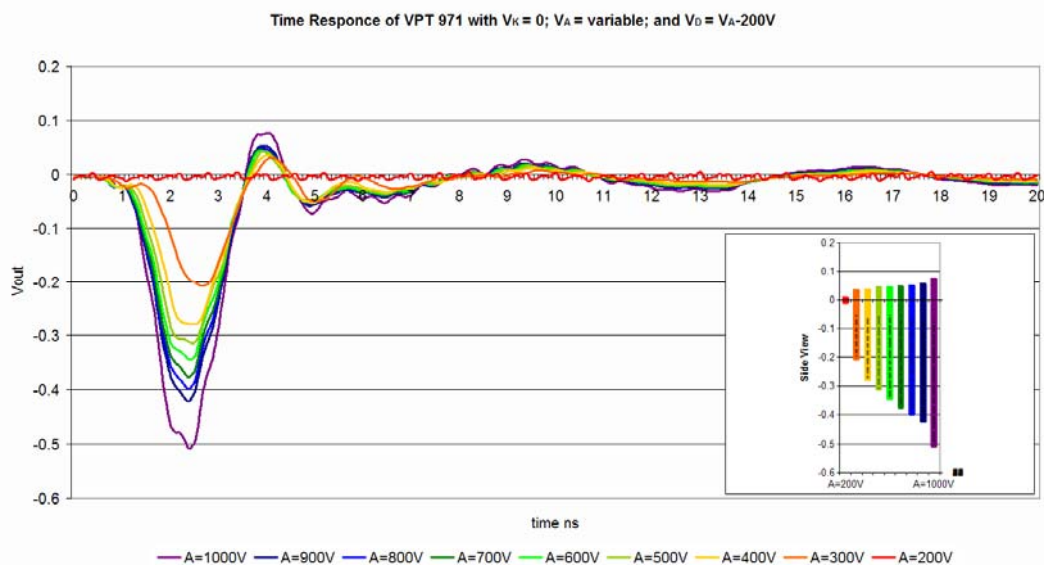
Figure 6-11 Time Response of the VPT 971 with a fixed anode-dynode voltage differential of -200 V and varying anode voltage from 0 to 1000 V

This test shows the effect of the initial acceleration from the photo cathode to the anode. Since for all the settings the deceleration at the anode-dynode region is constant, then one would expect that the energy at which the photoelectron hits the dynode would be directly proportional to the initial energy that the photoelectron had at the beginning of the anode-dynode region. This of course affects the gain, because the number of secondary electrons, as it was

defined before, is directly proportional to the energy of the incident electron on the dynode.

This chart clearly shows that by increasing the anode voltage (thus increasing the first stage acceleration), the gain of the VPT increases as it was expected.

The sub-plot at the lower right hand corner shows a perspective side view of the chart. Here, the peak voltages for each setting can be seen.

Response to a Variable Dynode Voltage

This test looks at the effect of changing the dynode voltage and hence, the anode–dynode voltage differential while keeping the anode at a constant 1000 V .
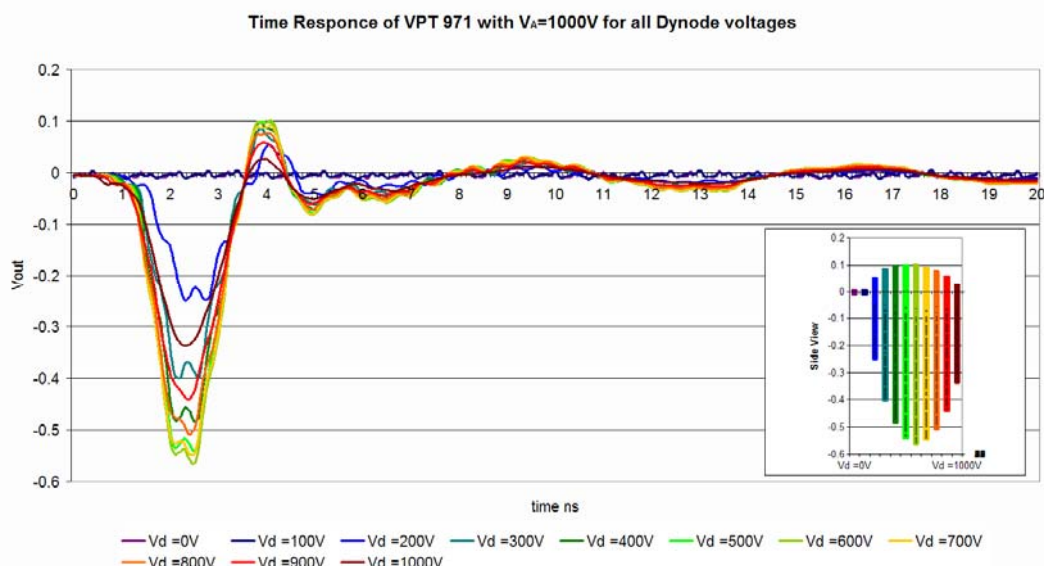
Figure 6-12 Time response of the VPT 971 with a fixed anode voltage and a varying dynode voltage from 0 V to 1000 V

The purpose of this test was to show the effect on the gain from the deceleration in the anode-dynode region. As opposed to the previous test, the constant here is the initial acceleration of all the photoelectrons at the cathode-anode region regardless of the dynode voltage, which may be the reason as to why the negative edge of the signals are synchronised. By increasing the dynode voltage, the anode-dynode voltage differential (V_{AD}) decreases and the deceleration coefficients with it. Although it is true that the higher the energy of the incident electron on the anode the greater the number of secondary electrons; it is not always true that the gain increases with the number of

secondary electrons. This is because the gain does not only depend on the number of electrons alone (which depends on the dynode voltage) but also on their speed (which is dependent on the anode-dynode differential); so even if the number of secondary electrons goes up, their speed dramatically decreases as $V_{AD} \rightarrow 0$, therefore, (and it can be seen from Figure 6-12) after reaching an optimum at $Vd = 600 \, V$, the gain of the VPT starts to drop.

Peak Voltages
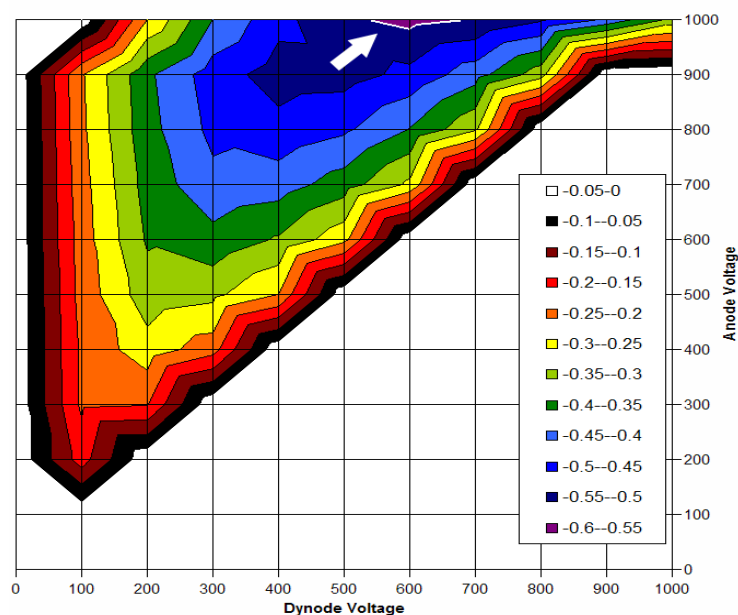
Figure 6-13 Peak voltages for every anode and dynode Voltage permutation

Figure 6-13 confirms the results shown in Figure 6-12, where the maximum gain was achieved with $V_{KX} = $ -1000 V and $V_{DX} = $ -400 V. For this, the anode-cathode voltage differential (V_{AK}) would be $1000 \, V$ and the dynode-cathode (V_{AD}) would be $600 \, V$ (indicated by the white arrow). Figure 6-13 shows the highest peak at such values. It also reveals that for a fixed anode-cathode voltage the gain depends on the dynode voltage, although not directly

proportional. On the other hand, for a fixed dynode voltage, the gain is directly proportional to the anode-cathode differential.

Furthermore, this chart summarises the gain for all different anode-dynode voltage combinations. As it can be seen from it, fixing the anode voltage and increasing the dynode voltage increases the gain to a maximum and then it declines (as it was previously shown in Figure 6-12). On the other hand, by fixing the anode-dynode differential, the gain is shown to increase as the anode voltage increases. Figure 6-14 shows the same data but from a different perspective: the gain increases to a maximum before decreasing again for each of the anode voltages. Furthermore, at every fixed dynode voltage (moving vertically) the gain increases with the anode voltage.
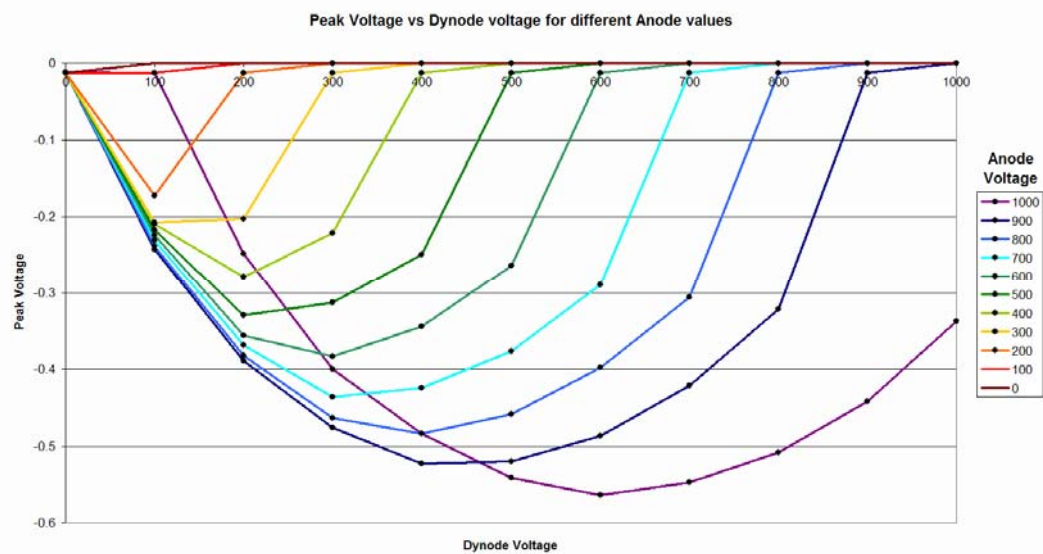

Figure 6-14 Peak voltages at every dynode voltage for varying anode voltage

Rise Times
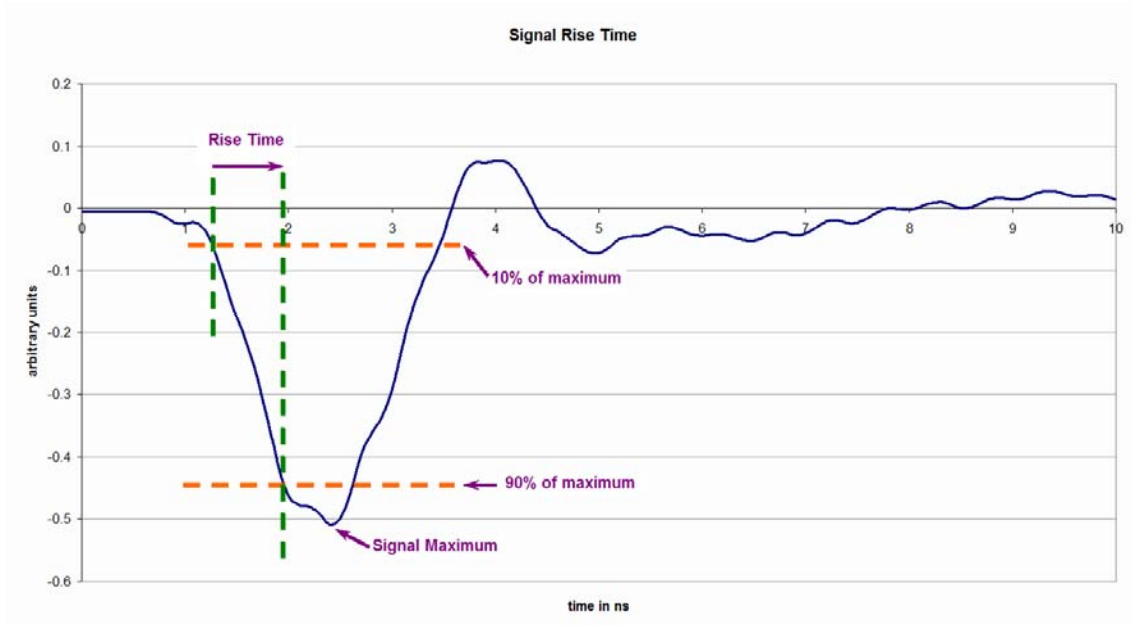
Figure 6-15 Signal rise time. Note that the signal is a negative pulse

The Rise Time is defined as the time it takes for the signal to increase from 10% to 90% of its maximum as shown in Figure 6-15. Note that as the signal is a negative pulse, the maximum is the negative maximum of the signal.

	Dynode Voltage									
	1000	900	800	700	600	500	400	300	200	100
200										0.9
300									1.0	0.9
400								1.1	0.8	0.9
500							1.1	0.9	0.8	0.9
600						1.0	0.9	0.8	0.8	0.8
700					1.0	1.0	0.8	0.8	0.8	0.8
800				1.0	1.0	0.8	0.8	0.7	0.7	0.8
900			1.0	1.0	0.8	0.8	0.7	0.7	0.8	0.8
1000	1.0	1.0	0.8	0.8	0.7	0.7	0.7	0.8	0.7	

(The left header column is labeled **Anode Voltage**)

Table 6-2 VPT 971 signal rise time in ns for VPT 971
(no data exists for V_A=100 V and V_D=100 V)

Table 6-2 shows the rise times for different anode and dynode voltages[*]. From this table, it can also be seen that the rise time increases with the dynode voltage (for a fixed V_A) and decreases as the anode voltage is increased (for a fixed V_D). This is due to the fact that the signal is dominated by the secondary electrons contribution, which depend on the acceleration of the secondary electron and therefore on the anode-dynode potential difference (V_{AD}). An increase in V_{AD} results on faster moving electrons and hence a faster signal, and vice versa, a decrease on V_{AD} results on a slower signal.

Fall Times

As oppose to the rise times, the fall time is the time it takes for the signal to fall from 90% down to 10% of its maximum. In the negative pulse, this fall time refers to the fall of the signal from the maximum negative peak towards zero (as shown in Figure 6-16).
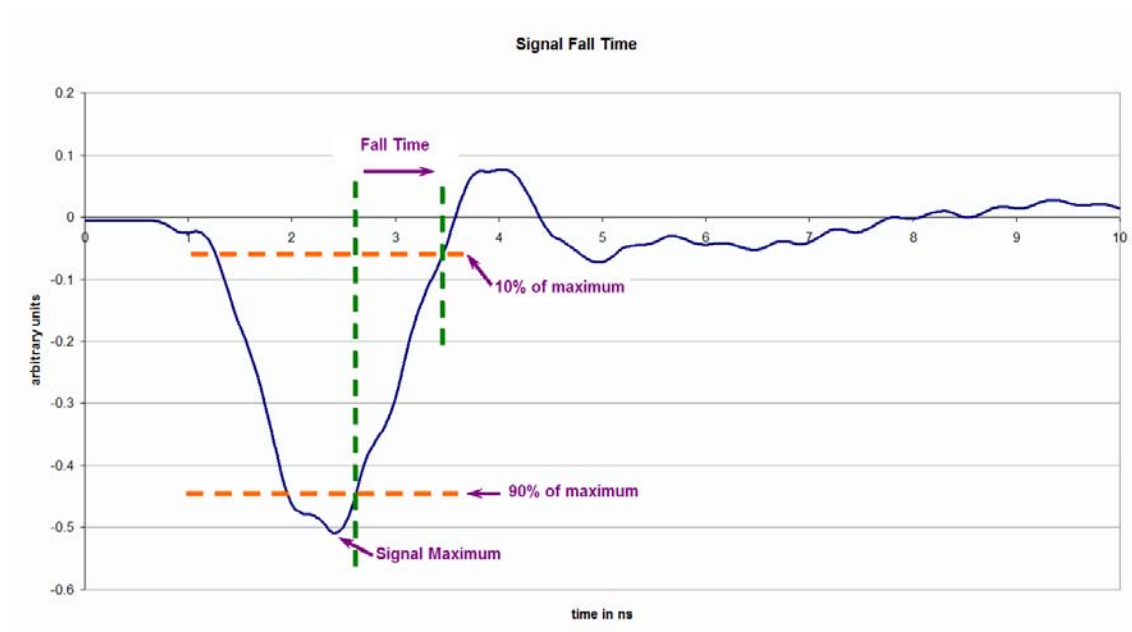

Figure 6-16 Signal Fall Time

---

[*] The voltages in this table are the equivalent to the range which could be tested on the lab, without changing the power supply to provide a dynode with a voltage more positive than the anode.

Anode Voltage	Dynode Voltage									
	1000	900	800	700	600	500	400	300	200	100
200										0.8
300									0.9	0.7
400								0.9	0.9	0.9
500							0.9	1.0	0.8	0.8
600						0.9	1.0	0.9	0.9	0.8
700					1.0	1.1	1.0	0.9	0.8	0.8
800				1.0	1.0	1.0	0.9	0.9	0.8	0.8
900			1.0	1.0	1.0	0.9	0.9	0.9	0.8	0.8
1000	1.0	1.0	1.0	0.9	0.9	0.9	0.9	0.9	0.8	

Table 6-3 Signal fall time in ns for VPT 971
(no data exists for V_A=100 V and V_D=100 V)

Diode Type II

This test looks at the result from making the dynode potential equal to that of the anode.

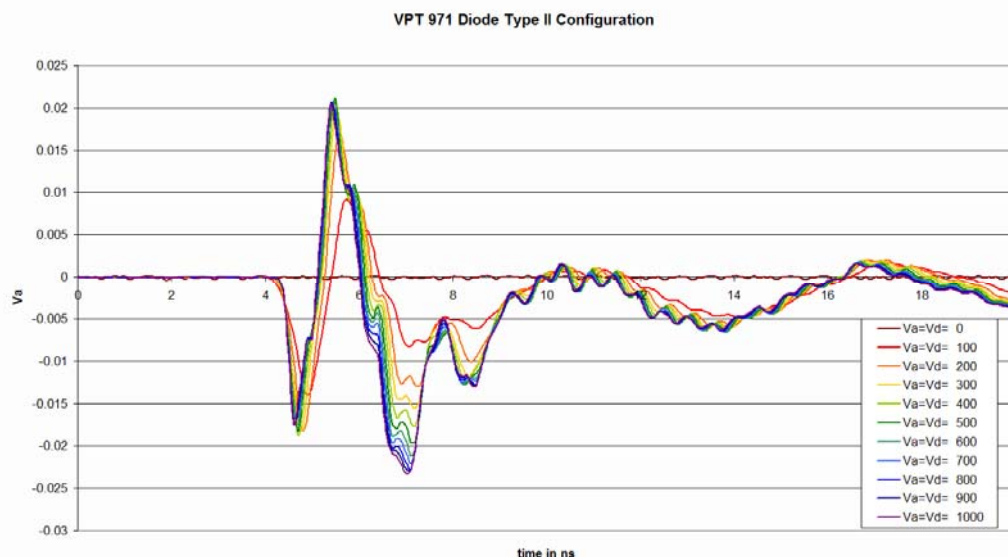The HV supplied to the cathode was varied with voltage increments of 100 V

Figure 6-17 Time Response for Diode Type II configuration ($V_A = V_D$)

This was done by hardwiring the dynode to ground and incrementally increasing the cathode voltage as shown in Figure 6-9. The idea was that if there were no potential difference between the anode and dynode, then the

secondary electrons would not be accelerated towards the anode. However, simulations showed that even on these conditions, the initial kinetic energy at which the secondary electrons were released was sufficient to carry them to the anode. In fact, in order to prevent secondary emissions from reaching the anode, the dynode should be set at more positive voltage than the anode.

The remaining properties, still apply: The acceleration of the photoelectrons are directly related to the anode voltage, thus, the greater anode voltage, the greater their energy. As the induced current depends on the speed of the inducing electron, one would expect the gain to increase with the anode voltage.

Because of this, one can infer from Figure 6-9 that the signal from the photoelectron is that which lasts from $4\,\text{ns}$ to $6\,\text{ns}$. As these are not decelerated in the anode-dynode region, one can expect that the number of secondary electrons to increase with V_A; however, the initial energy of the secondary electrons des not depend on the incident photoelectron's energy (as it was explained in chapter 2). This accounts for the variation on the magnitude for $t \geq 6\,\text{ns}$ which as expected is proportional to V_A.

If this is the case, it seems that the part of the signal which is due to the induction from the photoelectrons does not depend as much on their initial acceleration.

Diode Type III

A high voltage splitter was used to distribute the HV to the cathode and the dynode. By doing this, it was guaranteed that these electrodes would be at exactly the same potential. The HV supply was then increase incrementally in $100\,\text{V}$ steps, from $0\,\text{V}$ to $1000\,\text{V}$.

This test also tries to look at the response of the primary photoelectrons but using a different approach. By having the same potential as the cathode, the electrons would be decelerated in the anode-dynode region. Because of this, they would no have energy when they hit the dynode, and therefore, no secondary electrons would be emitted from it.
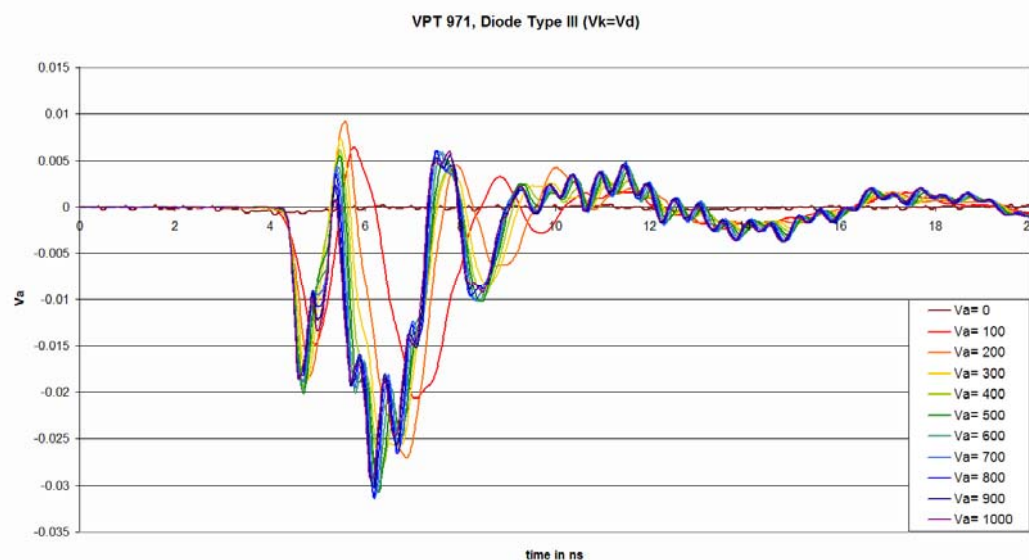
Figure 6-18 Time Response for Diode Type III configuration ($V_K = V_D$)

Figure 6-18 shows the results from this test, and it confirms the suggestion given on the previous configuration; i.e. the part of the signal which is due to the induction from the photoelectrons does not depend as much on their initial acceleration.

Using the same arguments describe before, one can infer from Figure 6-18, that decrease in magnitude of the first overshoot is due to the deceleration of the photoelectrons on the anode-dynode region. This differs from the Type II configuration where the photoelectrons were not decelerated on this region; hence the magnitude of the signal before the anode was similar to the magnitude of the signal after the anode.

It is also deduced, that the photoelectrons do not fully decelerate, and thus release a small number of secondary electrons when they hit the dynode. But if that is so, the number of the released secondary electron is not as proportional to the incident electrons energy, which goes against the principles described on chapter 2. One explanation is that the photoelectrons decelerate to a similar energy before hitting the dynode and therefore should produce a similar number of photoelectrons. However, there is no way of testing this theory with the equipment available at Brunel University.

Results from Further Measurements

Reproducibility

This test was proposed to show how much fluctuation the signal suffers. The scope was set to record the envelope over 2000 sweeps as well as the signal average. It was later re-tested averaging 4000 sweeps and no differences were noticed.
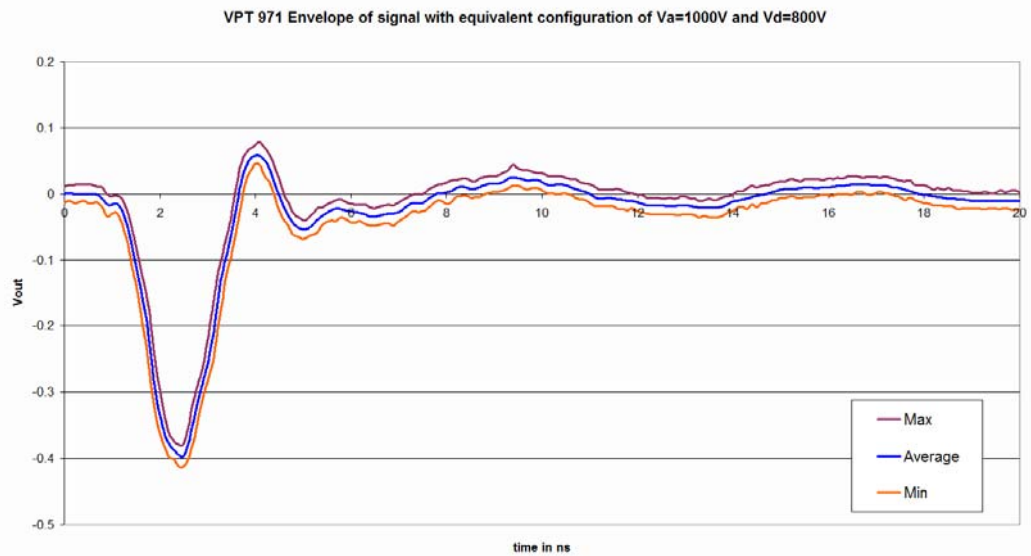

Figure 6-19 Signal Envelope

Figure 6-19 shows the averaged signal and its envelope, where the extremes are $\pm 15\,\text{mV}$ from the mean ($\pm 4\%$). As is clearly seen from this figure, the fluctuations are very small and consistent, suggesting that most of it is due to symmetrical electronic noise.

Anode Cable Dependency

This test tries to answer if the anode cable length coupled with imperfect termination was responsible for the ringing in the signal. It was thought that the ringing might be due to reflection and if the cable was increased in length, then there should be a corresponding difference between the signal read from a single length and a double length anode cable. In order to achieve this, an identical 1m cable to the current anode cable was attached to it, thus doubling its length, and then the measurements were repeated. The logic was based on the fact that if the ringing was due to the reflection on the 1 m anode cable, then

by doubling its length, the reflection would take twice as long to travel along the cable and therefore the ringing period should double.
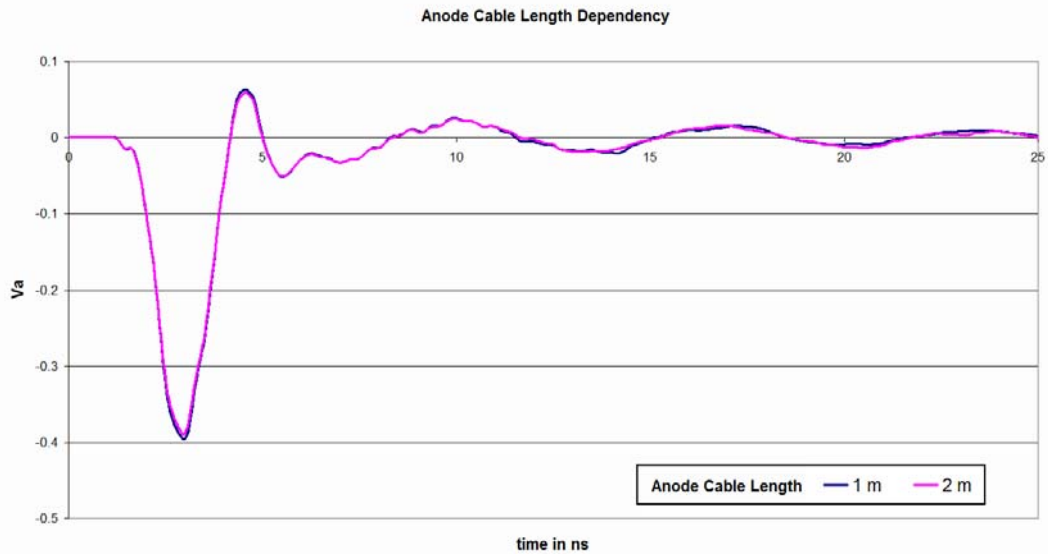

Figure 6-20 Comparison between the amplitudes two anode cables lengths
(Signals have been offset to compensate for time delays to enable comparison)

Figure 6-20 shows the result from these test and as it can be seen from it, there is almost no difference between the two measurements except for the expected slight attenuation due to the extra length of the cable.

Because of this, it was concluded that the anode cable length was not the cause of the ringing. These results should be expected, as coaxial cables are designed to be equivalent to $50\,\Omega$ impedance regardless of length, as long as the source is properly terminated. However, what is not shown in this figure is the delay of the signal due to that extra metre it had to travel. This delay was ignored to prove the superimposition of the signal due to both anode cable lengths.

In order to calculate the electrical length of the anode cable, it was divided the delay between the two signals[†] (4.5 ns) by the extra length of the anode cable

---

[†] The delay between the two signals is the time it takes for the signal to travel the extra length of the anode cable.

(1 m) thus 4.5 ns/m; meaning that the signal travels at 2/3 of the speed of light along the cable.

Signal FFT

Due to the unexplained differences between the simulated signal and the experimental measurements, as well as some characteristics such as ringing on the VPT measured signal, it was decided to run a Fast Fourier Transform (FFT) on the signal. The VPT was set to the standard bias and then, as corroboration to the previous test, the anode cable was extended to double its size in order to increase the effect of the anode cable.
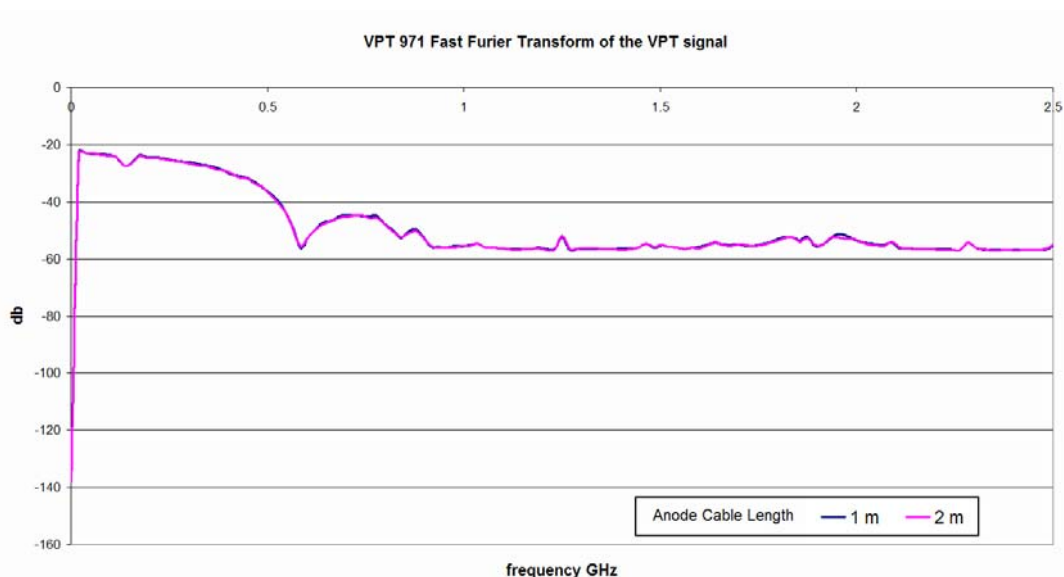
Figure 6-21 FFT of VPT 971 at normal operation bias and varying anode cable lengths

Amongst the many functions the LeCroy oscilloscope has, is the ability to FFT the signal from an input, and for this, it includes several settings to optimise this function according to the signal. In the case of our experiments, these settings were as follows:

Output Type: *Power Spectrum*

Window type: *Rectangular;* This window type is used when the signal is transient, which is the case of the VPT signal, due to the fact that it is a response from an impulse, and therefore is limited in the time domain.

Algorithm: *Least Prime*; This is the default algorithm for computing FFTs when the length of the sampled signal can be expressed as factors of $2^N \times 5^K$.

Furthermore, as shown in Figure 6-21, there was no significant variation on the frequency characteristics between the signals, suggesting therefore, that the anode cable length is not responsible for the ringing in the signal.

Trigger Period Dependency

It was suggested by Brown [2] that the signal might be dependent on the trigger frequency. In order to test if this was the case, especially with our equipment, the system was set to the Standard Bias (V_K=0 V , V_A=1000 V , V_D=800 V) and the trigger frequency of the laser was systematically changed.

Figure 6-22 shows the effect of varying the period of the trigger from 1.2 seconds down to 2 µs on the VPT signal. From this chart it can clearly be seen that the trigger period affected the maximum peak; but this effect was not that clear on the minimum peak.
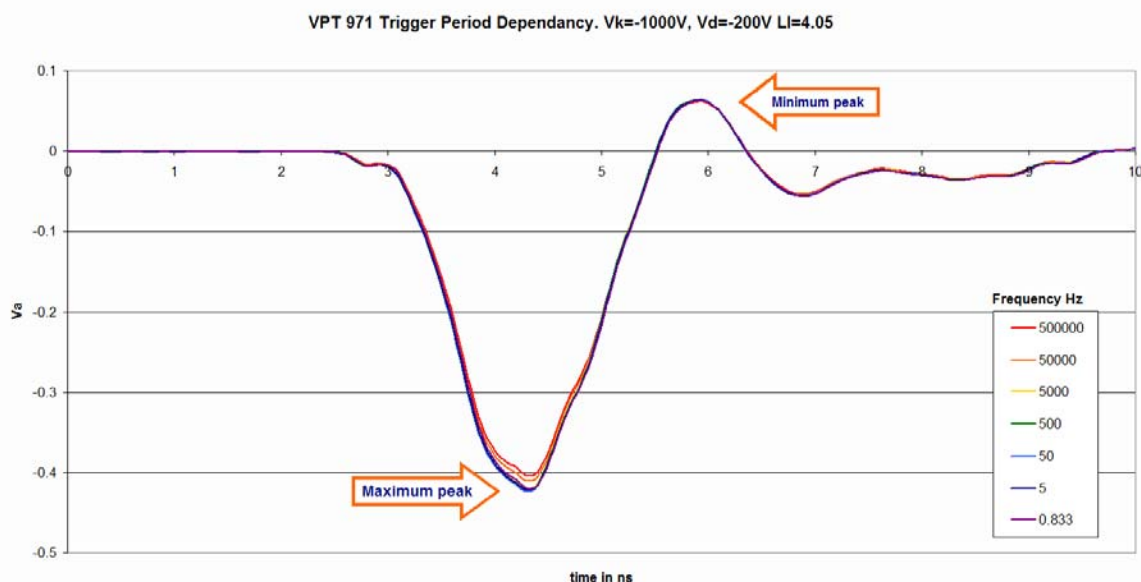

Figure 6-22 Comparison between different trigger periods at normal operation bias

The effect of the trigger period is shown to be proportional to the increase on the magnitude of the peak; and it could be attributed to the extra time the laser driver had to accumulate charge before triggering the laser. Since the charge of

the laser driver is proportional to the laser intensity, then as the laser intensity increases the magnitude of the signal increases (this is demonstrated on Figure 6-23).

From this argument, it should be expected that the magnitude of the minimum peak should also affected; however, this is not visible in Figure 6-22. On the other hand, the effect of the trigger period on the minimum peak is evident in Table 6-4, where is shown that changing the trigger frequency affects the positive peak as well as the negative peak.

Table 6-4 shows the percentage change of the maximum and minimum peak using the 50 Hz as the reference[‡] frequency. This table shows that the signal's greatest change at the minimum peak was 4.71%; this was just 1% more than the greatest changed observed on the maximum peak.

	Trigger Frequency Hz						
	500000	**50000**	**5000**	**500**	**50**	**5**	**0.833**
Minimum peak	4.71	3.20	0.69	0.13	0.00	0.42	1.06
Maximum peak	3.42	1.98	0.27	0.24	0.00	0.86	2.06

Table 6-4 Percentage change of peaks at various trigger frequencies with 50 Hz as the reference frequency

This experiment differs from Brown's in two aspects. The first is that Brown uses 4 LEDs which are used in pairs to provide a background and a signal. Secondly, his work focuses on the rate effect of the background and not of the signal. In contrast, this experiment has made use of a single laser head which provides the signal, and the aim was to observe how the VPT coped with light pulses at varying intervals.

[‡] There where two reasons for selecting 50 Hz as the reference frequency: a) it was the closest to the working frequency of 25 Hz; b) it registered the greatest amplitude in the positive peak.

Laser Intensity Dependency

The laser head power was adjusted via the 10-turn potentiometer on the laser driver module; but due to the variations of laser heads, there was not a direct relation between the dial setting (on the laser driver) and the output power (of the laser head) other than: the higher the setting number, the higher the laser power. Unfortunately, a calibrated power meter sensitive to low repetition rate fast pulses was not available. This could have been used to measure to power output at each of the dial settings.

One can only assume that the maximum setting (10) would correspond to the maximum power. However, as to how the laser power is scaled by the potentiometer, was not known from the laser manual.

Because of this, the settings described in this thesis would be relevant only for someone who used exactly the same equipment at Brunel University.

This test looks at what happens when turning the laser intensity (LI) dial from 0 to 10. The first observation was that there was no signal fro a dial setting less than 3. The laser manual explains that different leaser heads would begin to work at different dial settings from the laser driver. Thus, for this particular laser head and laser driver, the corresponding threshold setting is 3.
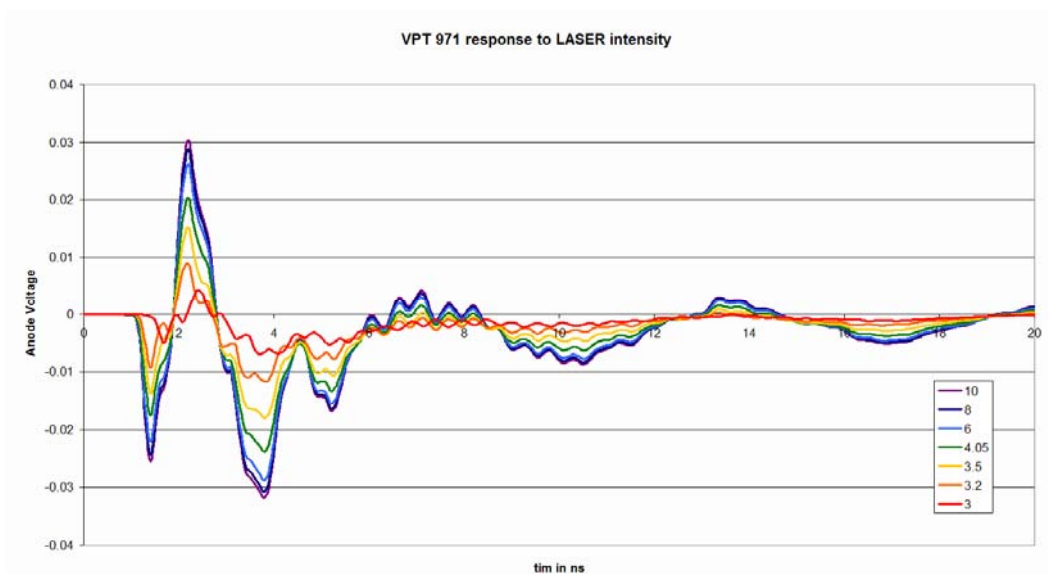

Figure 6-23 VPT response to a change on the laser intensity

Figure 6-23 shows the simple relationship between the laser intensity and the signal strength. This should be expected: as the laser intensity increases, the

number of photons which release photoelectrons increases and with it the number of secondary electrons. As the total induced current depends on the addition of all the individual contributions, then one can assume that the greater the number of electrons, the greater the induced current on the anode. Figure 6-21 also makes clear that the VPT and the electronics responded well to an increase as well as a decrease on the laser intensity, confirming that neither the VPT nor the electronics where being saturated.

This test also shows that the cathode does not saturate under the testing conditions. A saturated cathode would have a resistance effect creating a potential difference on its surface. This potential difference will drop the voltage between the cathode and anode, and therefore the acceleration of the photoelectrons. As a consequence, a saturated cathode would have been seen by a drop in the signal from the photoelectrons. Because of this reason, this experiment was performed on a diode configuration (described earlier) so that such a drop in the photoelectrons signal would be observed.

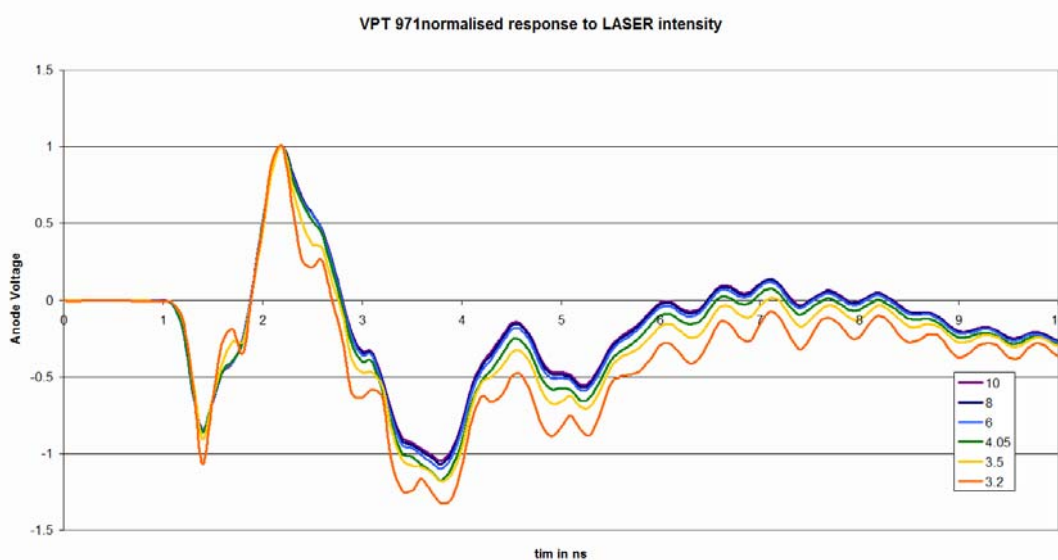**Figure 6-24 normalized VPT response to a change on the Laser Intensity**

As it was shown earlier in page 6-6, when the laser power is increased, most of that increase power is delivered by the slow component of the laser pulse; this can also be seen from Figure 6-24. As the laser power is increased, the signal is slightly widen proportionally to the increase in the magnitude of the laser pulse's slow component.

Comparison Between the Simulation Model and Experimental Results

Figure 6-25 shows the signals from the simulation system (in blue) and the experimental measurement (in magenta). The most obvious observation is that both results do not appear to match. While the simulated signal has the two components associated with primary and secondary electrons, the measured signal does not; in addition, the latter is much slower.
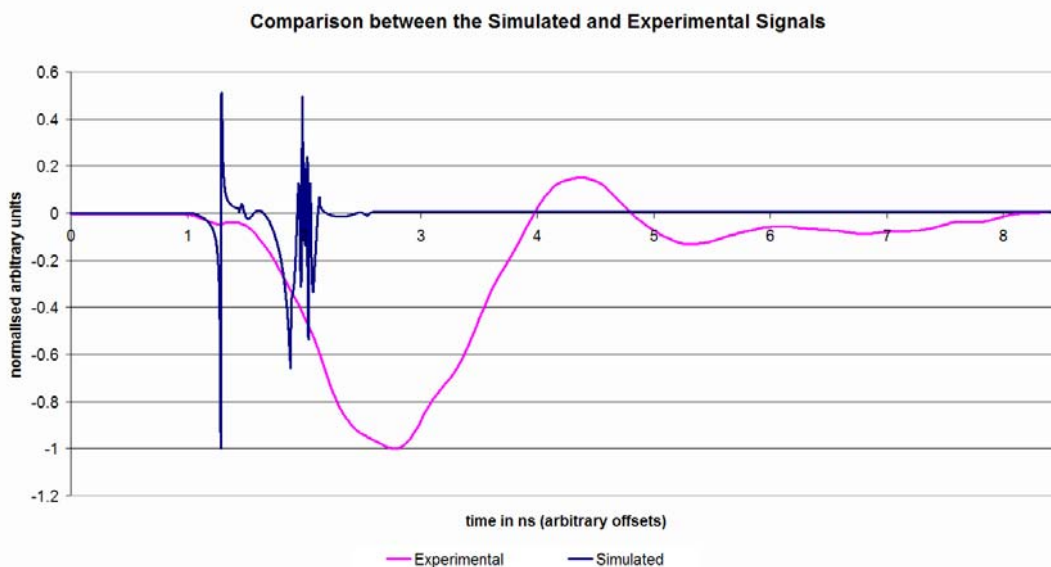
Figure 6-25 Comparison between experimental and simulated signal.
The equivalent bias was $V_K = 0\ V$, $V_A = 1000\ V$, $V_D = 800\ V$

Due to these differences, it was fundamental to test the measurement procedures in order to trust the results. These further experiments satisfied that:

- The measurements were repeatable

- The number of sweeps for the calculation of the average was sufficient

- The read out cable had no appreciable effect on the signal

- There was no electromagnetic interference affecting the measurements

- The cathode was not saturated

- The same effect on response by varying the trigger frequency as previously reported was observed.

- The measurements were consistent between the tested VPTs

At the same time, the code was re-examined. Moreover, the internal structure of the cut open VPT was re-measured using different instruments, yielding differences within 1% from the implemented dimensions[§], thus eliminating geometry of the simulations from the cause of the discrepancies.

As there was no theory to explain the differences (the simulation was theoretically plausible and the experiments were repeatable), it was hypothesised that maybe the signal was affected by the 3 GHz analogue bandwidth of the scope. However, as it can clearly be seen in Figure 6-21 this should not have been the case, as most of the power of the signal was concentrated at frequencies less than 1 GHz. Even though, the simulated signal was passed through a filter with a cut-off point at 3 GHz, in order to see what would happen to the signal during read out. The preliminary result confirmed that the VPT signal was too fast for the read out, and that therefore it was being integrated as it was sampled. However, the experimental evidence showed that the scope was not the cause of the integration.

Because of this reasons, it was decided to develop a Spice simulation of the electronics between the VPT's signal and the scope so that the differences between the simulated and experimental data could be better understood. In order to do this, the cut open VPT was re-examined, but in this time, the intention was to precisely measure its leads dimensions in order to calculate their inductive properties so that they could be taken into account. From this information, and with the internal capacitor values given in Chapter 2, Prof Peter Hobson developed the SPICE model shown in Figure 6-26. The response of this model to the simulated signal given in Figure 6-25 is shown in Figure 6-27 (in blue).

[§] The accuracy of the digital calliper is ±0.02 mm and the distance between the anode and the dynode is 2 mm
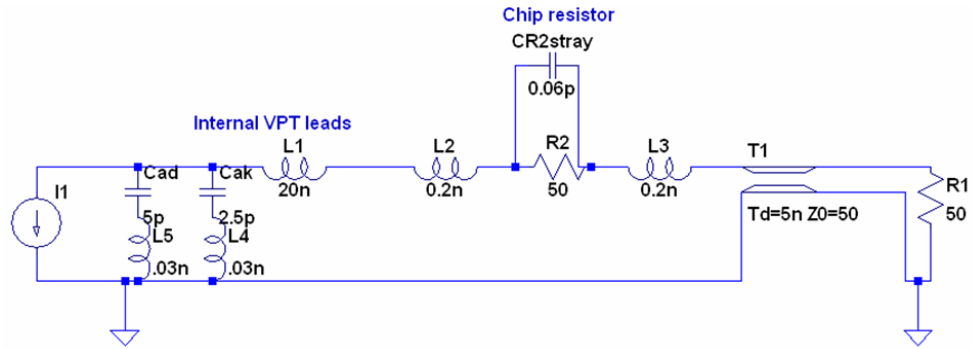
Figure 6-26 Representation of the electronic equivalent of the VPT readout.

Figure 6-26 shows the circuit of the passive components connecting the VPT to the oscilloscope. C_{AD} and C_{AK} are the anode-dynode capacitance and anode-cathode capacitance respectively, which were calculated from the electrode dimensions in Chapter 2. The values for L2, L3 CR2 and R2 represent a realistic SOT1206 chip resistor which matches the input impedance of the oscilloscope represented by R1. The inductances L1, L5 and L4 are an approximation of the lead impedance for wires of the dimensions of the anode, dynode and cathode wires respectively.

Figure 6-27 shows the simulated signal after filtering compared to the experimental measurements on VPT 971. In both cases, the equivalent bias was $V_K = 0\,V$, $V_A = 1000\,V$, $V_D = 800\,V$. Both signals have been offset such that their starts coincide.

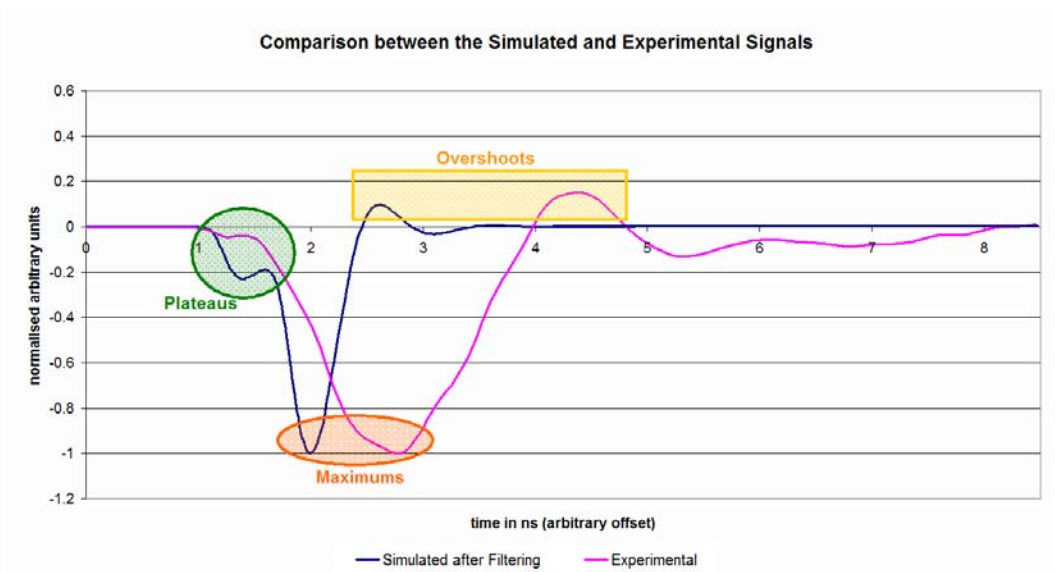**Figure 6-27 Comparison between experimental and simulated signal (after filtering).**
The equivalent bias was $V_K = 0\,V$, $V_A = 1000\,V$, $V_D = 800\,V$.

As it can be seen from this Figure 6-27, the simulated signal after filtering and the experimental measurements on VPT 971 share similar characteristics, such as the plateau[**] (shown between 1 and 1.5 ns), the fall and the overshoot. However, it is also clear that the experimental signal is still significantly slower than the simulated one. This is due to some factors which are still to be discovered. Even though some discrepancies remain, the fact that these two share similar characteristics confirms that the simulation and the experimental systems provide compatible results, and in addition, it proves that the signal from the anode has been integrated before it is displayed by the scope. Further work should focus on eliminating any unnecessary impedance from the experimental apparatus as well more accurately modelling the electric circuitry between the anode, and the scope's display.

[**] It was deduced from the experiments that this plateau was the part of the signal which is due to the primary photoelectrons. Figure 6-12 showed the signal due to various dynode Voltages. This chart also showed that the "plateau" was not affected, as it was predicted in the simulations. The Diode configuration showed signals with amplitudes which are in agreement with this; the signal shapes differences could be explained by the integration process of the whole signal.

VPT Comparisons

The three VPT evaluated showed almost identical characteristics, with the exception of the magnitude of the signal which is noticeably greater for VPT 971. The time responses agree between the different VPTs as can be seen from Figures 6-28, and 6-30.
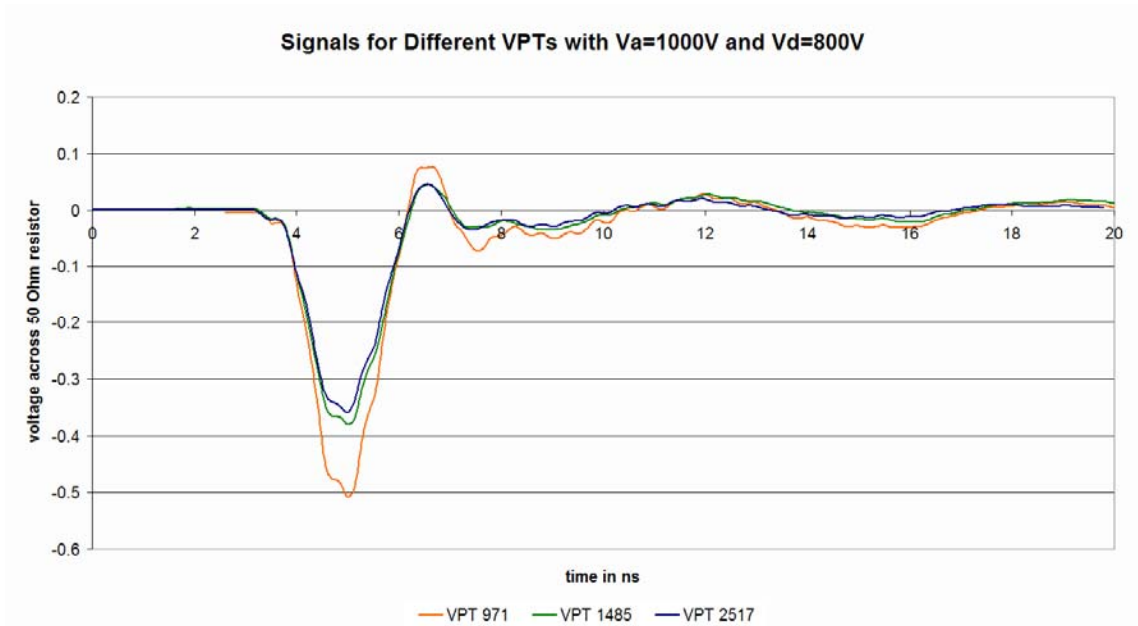

**Figure 6-28 Signals for VPT 971, VPT 1485 and VPT 2517
with V_K = 0 V , V_A = 1000 V , V_D = 800 V**

Table 6-5 shows that the measured rise times and fall times for the VPTs are identical with the exception of the slightly slower rise time of VPT 2517.

	VPT 971	VPT 1485	VPT 2517
Rise Time	0.8 ns	0.8 ns	0.9 ns
Fall Time	1.0 ns	1.0 ns	1.0 ns

**Table 6-5 Meassured signal rise time and fall time in ns for various VPT
with V_K = 0 V , V_A = 1000 V , V_D = 800 V**

Throughout this chapter, it has been noted a high frequency ringing from the measurements of VPT 971 and several experiments tried to explain this. However, this ringing is not as apparent on VPT 2517 and almost not present in

VPT 1485. This suggests that the high frequency ringing is a characteristic of the VPT and not of the experimental set-up. Figure 6-29 and 6-30 shows the diode test comparison, where the difference in the ringing between VPT 971 and VPT 1485 is more obvious.
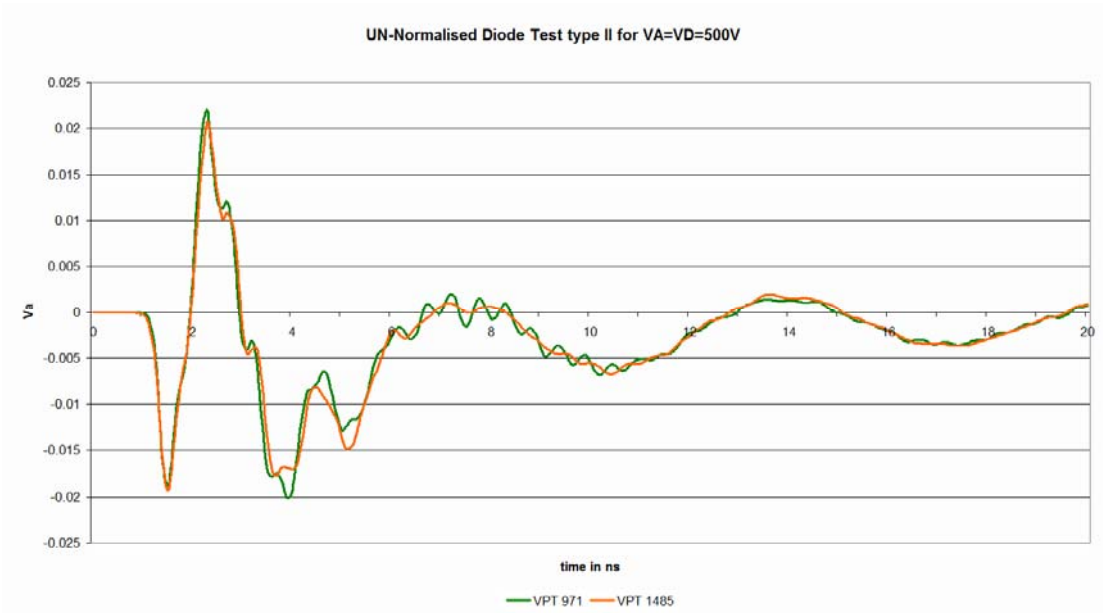
Figure 6-29 Diode test Type II comparison between VPT 971 and VPT 1485 with $V_A = V_D = 500$ V

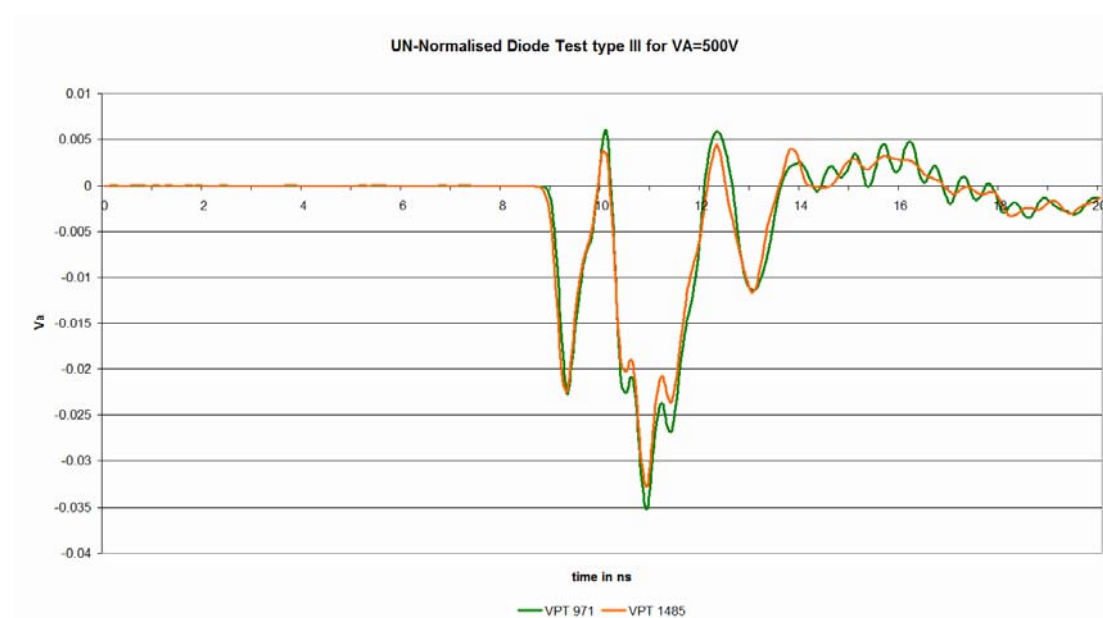**Figure 6-30 Diode Test type III comparison between VPT 971 and VPT 1485 with $V_A = 500$ V**

References

1 PDL 808 "SEPIA" PicoQuant: Multi-channel Pulsed Diode Laser System User Manual Version 1.0 (April 2002)

2 RM Brown, et al., "VPT Rate Dependence, measurements and discussion" [online]. Available: http://hepwww.rl.ac.uk/CMSecal/VPTs.htm [accessed on the 09th of September 2008]

Chapter 7 Radiation effect on HV filter components, Part I

First Set of Components

For the correct operation of the VPT, a low noise HV DC biasing is needed. This is done by filtering the HV lines using filter circuit shown in Figure 7-1[*]. These filter cards serve two purposes: firstly, it acts as a low pass filter from the biasing voltage to the VPT (eliminating noise at the HV lines); and secondly, it protects the preamplifier from discharges from the VPT as well as blocking the HV from biasing lines.

At the time of the start of the work for this thesis, the HV filter cards where the last components of CMS which had their design to be finalized; therefore, creating the need to evaluate the filter components for the irradiation tolerance which they were required to satisfy. The radiation tolerance of the HV filter components is critical because if the capacitor or the resistor changes or if the capacitors have a high leakage current, they would either introduce a new source of noise or become less effective in filtering noise on the HV lines.

There are also financial implications: as opposed to space launched equipment, where they benefit from a huge budget, and therefore, being able to spend for expensive components, the CMS experiment could not spend as much for the purpose made radiation hard component supplied by specialist manufacturers. Therefore, it raises the importance of finding an economic alternative suitable for electronic systems used in the harsh radiation environment of the CMS ECAL endcaps. However, it was known that certain type of commercial of the shelf components may be radiation tolerant, but as

---

[*] The HV filter cards were designed by M. Torbert from the Rutherford Alperton Laboratory (RAL) Electronics group

they are not manufactured on strict guidelines, the radiation tolerance could be different from batch to batch.

Therefore, this part of the project was time critical, as from this work, the components for each of the 5 channels of each of the 3100 filter cards were going to be selected.

The impedance of a capacitor is inversely proportional to frequency. High frequency components from the HV lines are not impeded by C_1 or C_2, making them the easiest way for these components to ground instead than through the rest of the circuit. On the other hand, low frequency components (DC voltage which biases the VPT) would see a very large barrier from C_3 as it appears as an open circuit, while (similarly as C_1 and C_2) the high frequency signal from the anode is allowed to pass through to the Pre-Amp.
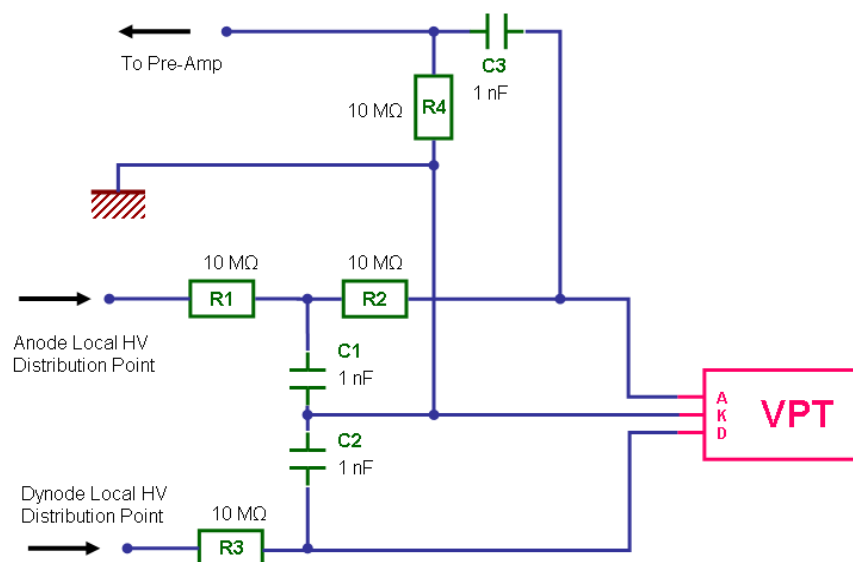
Figure 7-1 High Voltage Filter Schematics

This chapter looks at the effects of gamma radiation on the VPT high voltage filter components; namely: RS 176-7956 10 MΩ 0.25 W resistors (for use on R1, R2, R3, and R4 of Figure 7-1), and the Farnell 498-385 1nF 2 kV capacitors (for use on C1, C2 and C3 of Figure 7-1). The aim of these experiments was to record the change in performance, so as to determine their suitability for their use in the HV filter for the VPT in the ECAL endcaps.

Since these components would be tested destructively, it was imperative to obtain as much data as possible. This information was obtained using two different techniques:

- The capacitance and conductivity of the capacitors as well as the resistance and parasitic capacitance of the resistors was measured with an impedance meter

- Leakage current of the capacitor at 1000 V, measured with a purpose build jig.

This chapter describes in its first part the methodology used for the measurements, and subsequently, the degree of radiation received by the components, after which a comparison between the results will be made. Finally, the leakage current of a sample capacitor while under irradiation will be dynamically tested.

In order to carry out the experiments, two facilities at Brunel University capable of delivering gamma radiation using ^{60}Co were used. For the first part, due to the need for irradiating the components to an equivalent of ten years of operation within CMS (~345 kGy) in a relatively short time, a high-rate source was used. The second low-rate facility was used for the studies under a irradiation rate to similar to the operation conditions. The source of this last facility is smaller (approximated to a point source) and nearly 100 times weaker than the previous one. This provided the extra advantage of allowing electronic equipments to be left in the cell during source exposure, without the risk of getting them damaged in the short term.

Methodology

In order to study the trends, a set of 10 nominally identical capacitors and 9 resistors were tested. However, this raised the problem of providing the correct method for identification.

It was important therefore, that the method in which each sample should be identified, complied with the following requirements:

- The method should not be intrusive, i.e. adding or removing anything that could, under some condition, affect the performance of the component before or after the irradiation has taken place.

- The identification should be clear, unique and permanent (at least for the duration of the study), i.e. the method of identification should not degrade with radiation, to the point that identification between samples becomes impossible.

With this in mind, it was concluded that the samples should be contained in individual recipients with their identification. The identification was written with graphite pencils on pieces of paper (all the same size). This method provided not only the compliance for the restrictions above, but also the means of protection against loss or accidental damage during transport, storing, and handling.

The circuit shown in Figure 7-2 was designed for assisting in the measurements of the leakage current on the capacitors. The power supply was set to provide 1000 V, and a digital voltmeter was set to measure the voltage across R2. Ideally, after 5τ this voltage should be nearly zero, but in practice this is not the case, so any value displayed by the digital voltmeter corresponds to a current which leaks from the capacitor. The resistor R1 has two purposes: firstly for safety reasons, as it allows the capacitor to discharge when the HV cables are disconnected before the capacitor is changed; and secondly it guarantees a minimum current for the HV power supply which ensures stability.
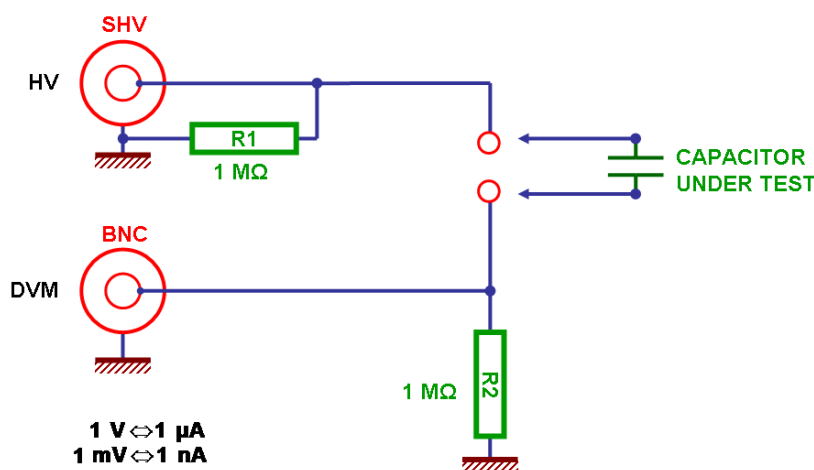

Figure 7-2: Capacitor leakage measuring circuit.

Figure 7-2 shows the circuit diagram for the measurement of the current through the capacitor. However, it is important to note that, since the voltmeter (Keithley 191 Digital Multimeter) has an input resistance of 10 MΩ, the calculation of the current had to account for the systematic affects this introduces.

The circuit was installed in a metal box for shielding against electromagnetic waves on the environment (lighting, communication signals, etc). This box also contained a bag of silica gel to reduce the humidity and thus surface leakage inside it.

Each capacitor was loaded to 1000 V DC using a CANBERRA HV Power Supply (Model 3002). Measurements were then recorded each minute from time 0 to 10'. Thus, allowing the charging time to greatly exceed five RC time constants ($\tau = 0.91$ ms $\Rightarrow 5\tau = 4.54$ ms).

The impedance characteristic of each component was measured with an impedance analyser from HP (model 4192A LF). This apparatus has two displays which were set to display the conductance and capacitance of a device connected at its probe input. The testing frequency was changed to allow a study of the frequency response of the tested device. To ensure the values measured were repeatable, it was decided to test each component ten times. The level of this repeatability is demonstrated in the Figure 7-4.

In order to obtain as much consistency as possible, measurements were done when the lab temperature ranged between 19 to 21 °C.

For the identification, storing, and manipulation of the samples, borosilicate tubes of approximately 2.5 cm in diameter and length 10 cm were used. They were transparent, allowing the identification label written with graphite pencils on a piece of paper stored inside it to be seen.

The metal box containing the components was placed at a distance of 70 mm from the source, such as is shown in Figure 7-3.
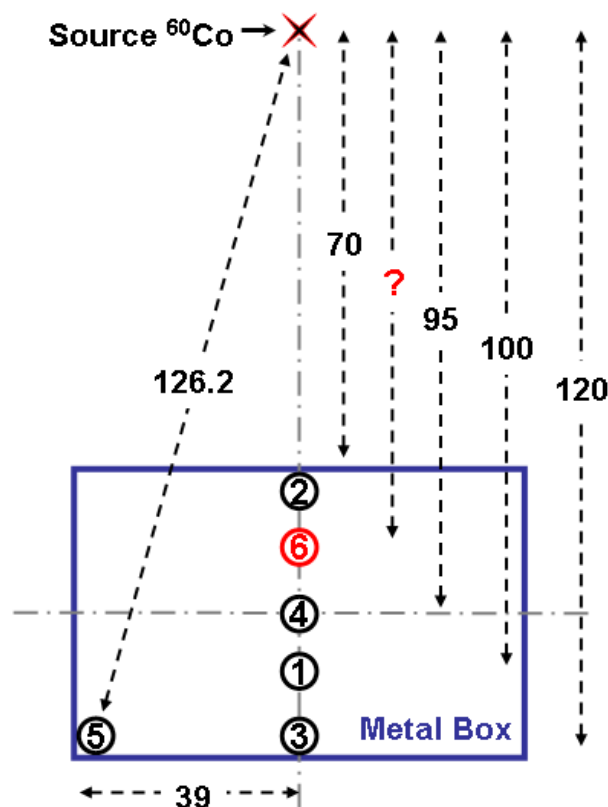
Figure 7-3 Relative distance of components to source in mm. 1- reference point at 100 mm, 2- shortest distance, 3- longest distance along the box axis, 4- box centre point, 5- furthest component from the source, 6- is the point at which there is a symmetric maximum variation.

In order to calculate the radiation rate at any point from the source, it is used a reference base rate (BR) at a known distance (in Figure 7-3 this would be d1). The rate decreases proportionally to $1/d^2$, therefore, the irradiation dose rate (DR) at a distance d_z from the source is calculated by:

$$DR(d_z)=\left(\frac{d_1}{d_z}\right)^2 \cdot BR \tag{7-1}$$

Let z be the point at which the radiation dose is X Gy/h with a symmetric maximum variation of ±Y% so that:

$$X+\frac{X \cdot Y}{100} = MAX \, dose \, rate \tag{7-2}$$

$$X-\frac{X \cdot Y}{100} = MIN \, dose \, rate \tag{7-3}$$

Expressing X and Y in terms of the maximum and minimum dose rates

$$X = \frac{MAX+MIN}{2} \tag{7-4}$$

$$Y = 100\left(\frac{MAX-MIN}{MAX+MIN}\right) \tag{7-5}$$

From Figure 7-3 the maximum dose rate is that at the point closest to the source (d_2), while the minimum dose rate is that at the furthest point form the source (d_5). These they are calculated from the reference base rate (BR) at a distance d_1 from the source by:

$$MAX = DR(d_2) = \left(\frac{d_1}{d_2}\right)^2 BR \tag{7-6}$$

$$MIN = DR(d_5) = \left(\frac{d_1}{d_5}\right)^2 BR \tag{7-7}$$

Substituting equations 7-6 and 7-7 in 7-5:

$$Y = 100\left(\frac{\left(\frac{d_1}{d_2}\right)^2 BR - \left(\frac{d_1}{d_5}\right)^2 BR}{\left(\frac{d_1}{d_2}\right)^2 BR + \left(\frac{d_1}{d_5}\right)^2 BR}\right) \tag{7-8}$$

And therefore:

$$Y = 100\left(\frac{d_5{}^2 - d_2{}^2}{d_5{}^2 + d_2{}^2}\right) \tag{7-9}$$

 so the percentage of variation does not depend on the source but only on the geometry of the distribution of the samples. From the measurements given in Figure 7-3

$$Y = 100\left(\frac{126.2^2 - 70^2}{126.2^2 + 70^2}\right) = 52.94\% \tag{7-10}$$

From equation 7-1, the dose rate X at a distance d_6 from the source is related to the base rate by:

$$X = DR(d_6) = \left(\frac{d_1}{d_6}\right)^2 BR \tag{7-11}$$

Substituting 7-6 and 7-7 in 7-4 and equating to 7-11:

$$\left(\frac{d_1}{d_6}\right)^2 BR = \frac{\left(\frac{d_1}{d_2}\right)^2 BR + \left(\frac{d_1}{d_5}\right)^2 BR}{2} \qquad (7\text{-}12)$$

$$d_6{}^2 = 2 \times \frac{d_2{}^2 \times d_5{}^2}{d_2{}^2 + d_5{}^2} \qquad (7\text{-}13)$$

Therefore the distance from the source for a symmetric variation does not depend on the source either, and using the measurements from Figure 7-3, this point is located at:

$$d_6{}^2 = 2 \times \frac{70^2 \times 126.2^2}{70^2 + 126.2^2} = 86.57 \text{ mm} \qquad (7\text{-}14)$$

The radiation dose is finally calculated at d_6 by using the base rate known at d1 and multiplying the result by the amount of time the components are exposed to the source.

Data presentation

Finally, the results are displayed in marginal bands obtained from the measurements. For example, Figure 7-4 shows the complete set of measurements for the capacitors after the first dose of radiation, including the ten tests per capacitor, for all ten capacitors. The maximum and minimum measurement recorded forms the margins referred as the **high band** and the **low band** (shown in black thick lines enveloping all the measurements). By taking a detailed look at the graph it is also possible to notice that the measurements are divided in close groups. These groups correspond to individual capacitors showing also that the instrumental errors are very small, except for some exceptional peaks by some capacitors at some specific test. All in all, this graph is representative of the repeatability of the tests
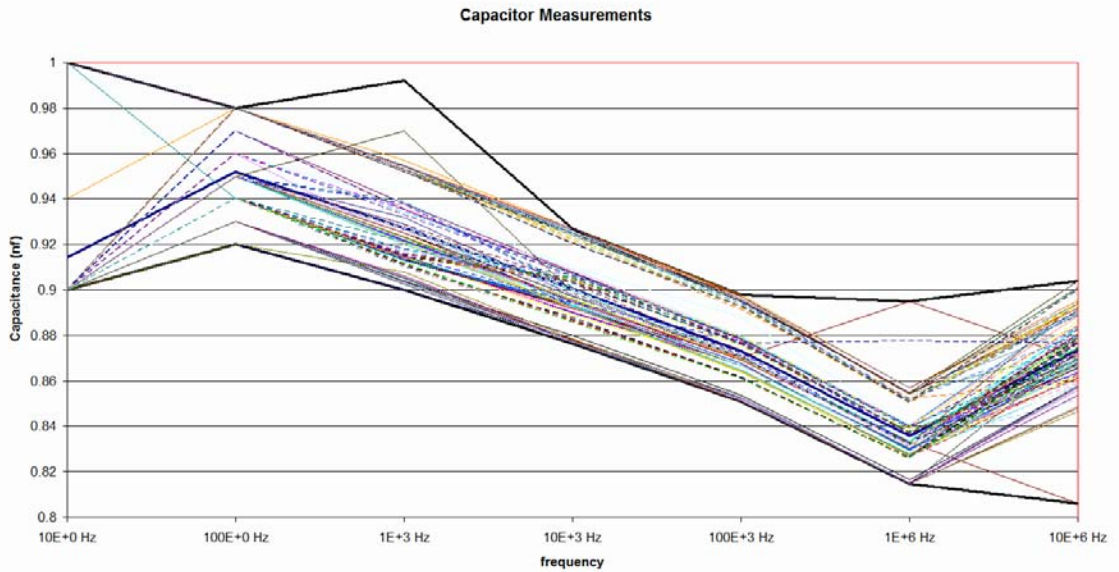
Figure 7-4 Complete set of capacitance measurements on the capacitors after 26 kGy at various frequencies

When substituting all the measurements from Figure 7-4 with their average, one would have a graph as shown in Figure 7-5, where the high band and low band are replaced by blue and magenta lines (respectively) and the average shown in dotted black.
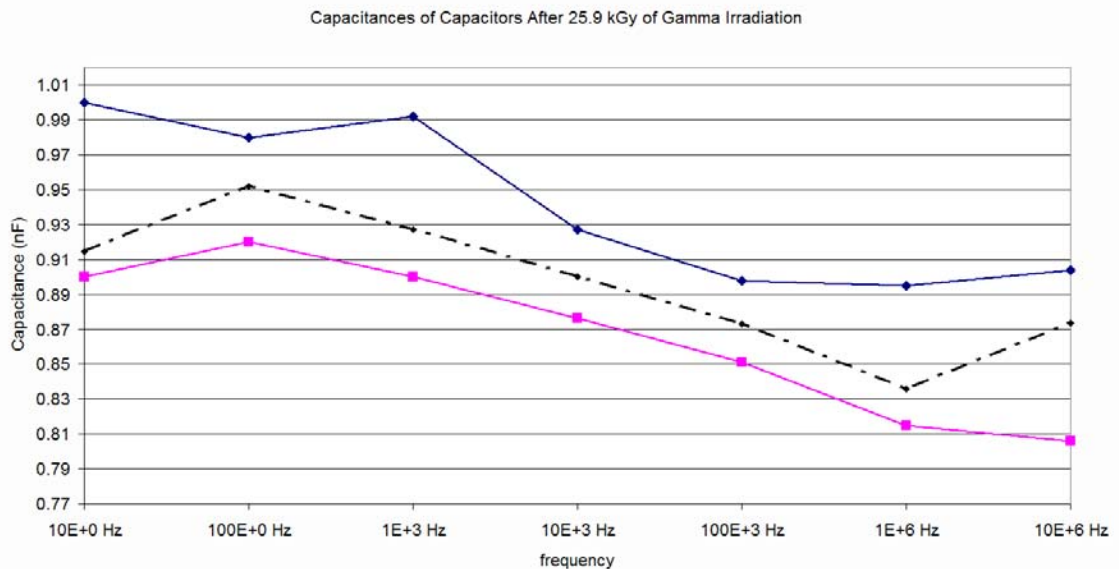

Figure 7-5 Reduced set of capacitance measurements on the capacitors after 26 kGy at various frequencies
The high band (in blue) and low band (in magenta) show the absolute maximum and minimum recorded measurement (respectively), while the black line shows the average for all measurements.

The reasons for presenting the measured data as in Figure 7-5 are:

a) It shows the maximum variation from the average data,

b) Less implicitly, it gives an idea of the distribution of the data measurements. e.g. at 1 kHz the high band peaks while there is nothing special on the average and low band, suggesting that this peak is anomalous. This is confirmed by Figure 7-4 at same frequency, where only a couple of measurements were off the trend.

c) From an engineering perspective, it shows the measurements which are the worst case at each frequency. If these measurements showed that the devices were not good enough, they would not be used. This is critical as no system failures can be afforded, so the component tested should all be within the specified tolerance.

Unirradiated Component Data

Since the aim of this report was to study the effects of radiation on the components, the need to perform the measurements on the components before any damage is done to them is clear.

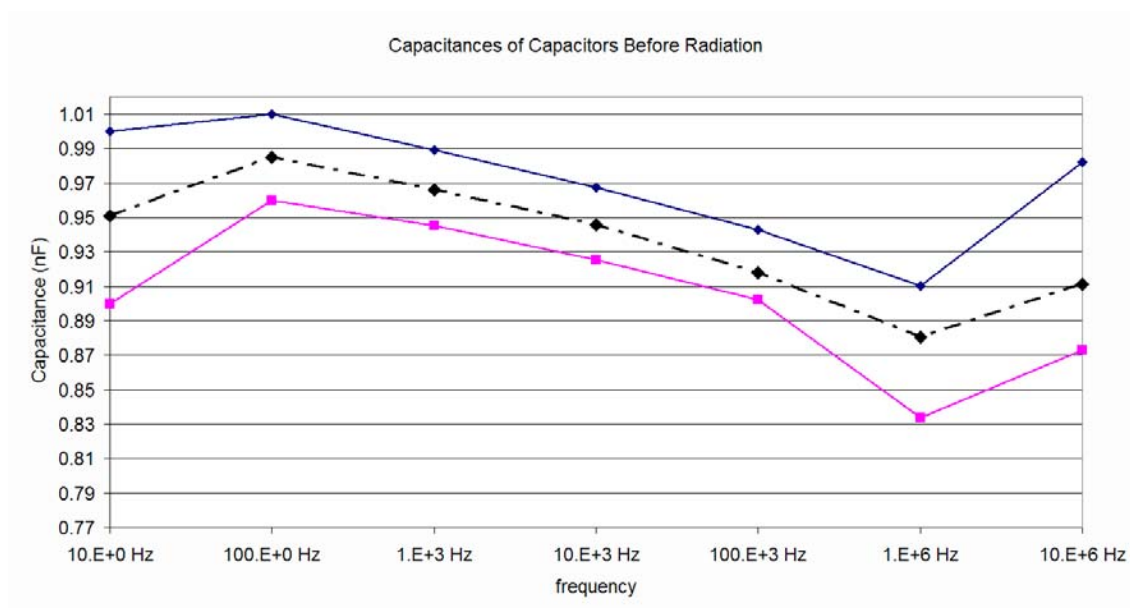Capacitances of Capacitors Before Radiation

Figure 7-6 Capacitance of the capacitors before irradiation at various frequencies
The high band (in blue) and low band (in magenta) show the absolute maximum and minimum recorded measurement (respectively), while the black line shows the average for all measurements.

Figure 7-6 and Figure 7-7, shows the characteristics of the capacitors in the frequency domain. It should be pointed out, that all the samples follow roughly the same trend, and even if they diverge on a vertical translation, this is clearly shown on the behaviour of the bands, where it can be seen that the effect of the frequency was very similar.

On the other hand, the conductance from these capacitors increased with frequency. This was expected, due to the fact that the impedance of a capacitor is inversely proportional to the frequency, hence, as the frequency rises, the impedance should decrease, or in this case, the conductivity (the real part of the impedance, and inversely proportional to the resistance) would rise with the frequency.
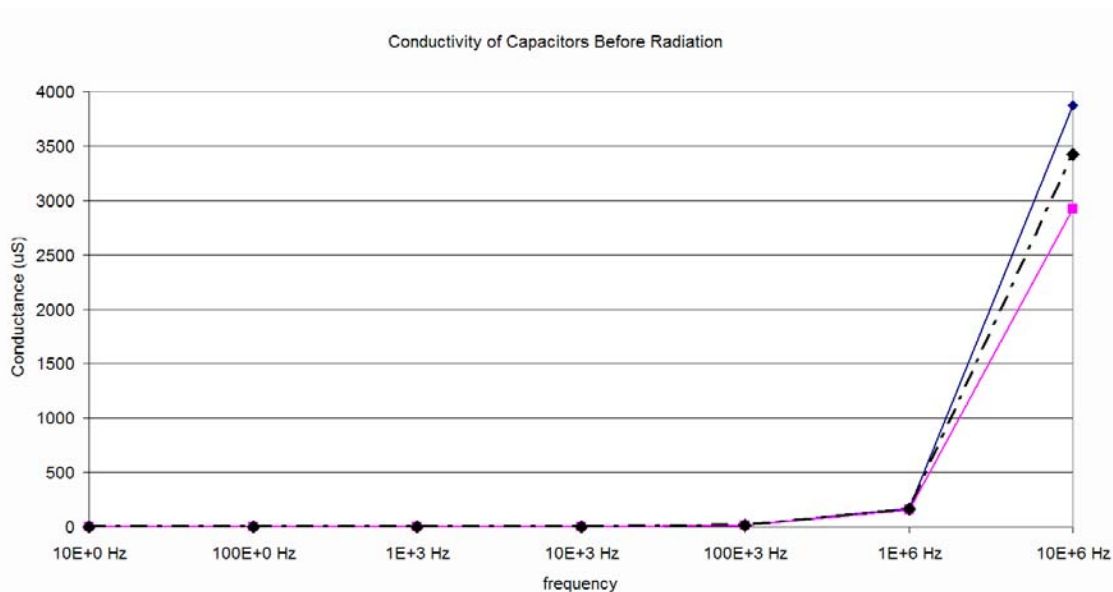

Figure 7-7 Conductivity of capacitors before irradiation at various frequencies
The high band (in blue) and low band (in magenta) show the absolute maximum and minimum recorded measurement (respectively), while the black line shows the average for all measurements.

For the studies of the leakage current, the circuit shown above in Figure 7-2 was used; when powered, a jump was noticed in the voltage registered on the DVM, which dropped rapidly over a short period of time, and after the 5th minute, the fall of the voltage gradually changed to an asymptotic behaviour. It is safe to mention that the time elapsed was considerably greater than the RC constant ($\tau \approx 9 \times 10^{-4}$ s), so as to say that the voltage registered on the DVM was

indeed due to the leakage current of the capacitor. Figure 7-8 shows the leakage current of the unirradiated capacitors, as well as the leakage current of the circuit when no capacitors were connected.
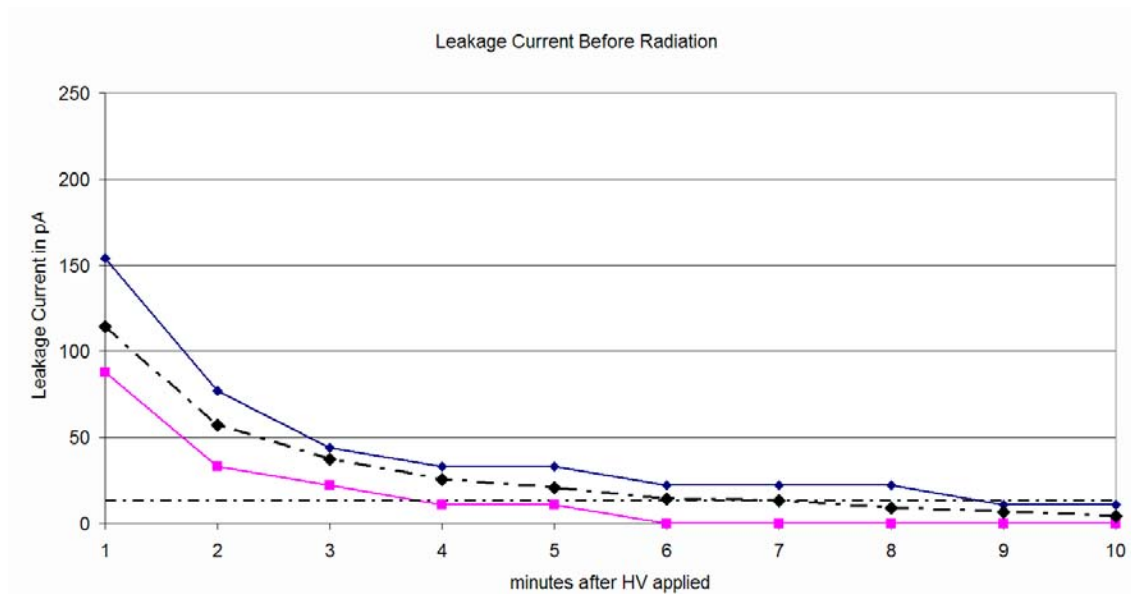
Figure 7-8 Leakage current at 1000 V of capacitors before irradiation at various frequencies
The high band (in blue) and low band (in magenta) show the absolute maximum and minimum recorded measurement (respectively), while the black line shows the average for all measurements.

Finally, it should also be mentioned, that the minimum voltage detected, was comparable to the noise level of the DVM, and it was suggested that part of the voltage observed was due to the intrinsic noise of the resistors on the circuit. However, it could prove useful to compare how these measurements change depending on the radiation dose the components receive.

First Irradiation

After the first dose of radiation was completed, it was calculated that the components received 25.9 kGy of gamma radiation at rate of 116 Gy/hour. The cell temperature was constant at 18 °C.

The components were then subject to the same experiments described in the previous section, so as to compare the effects of such dose.

Capacitor

After the first dose of radiation, measurements were taken and the results are shown below:

Figure 7-9 Capacitance of the capacitors after first irradiation (26 kGy total) at various frequencies
The high band (in blue) and low band (in magenta) show the absolute maximum and minimum recorded measurement (respectively), while the black line shows the average for all measurements.

Figure 7-9 shows that, even if the capacitance of the capacitors differs slightly from the control model (the model obtained from the measurements before radiation), they do share the same trend.

	10 Hz	100 Hz	1 kHz	10 kHz	100 kHz	1 MHz	10 MHz
AV	3.80	3.36	4.02	4.79	4.89	5.07	4.05
Worst Case	9.00	5.05	5.83	6.72	5.72	6.33	9.23

Table 7-1 Average and worst case percentage change after 26 kGy of irradiation

Table 7-1 shows the average percentage change of the capacitances after a total dose of 26 kGy. Note that the in average, the capacitor changes almost by the same amount. Moreover, this change is close to the worst case registered except for 10 Hz and 10 MHz where it was almost 10%; even though, these exceptions were all below the tolerance given by the manufacturer. From these results, it could be agreed that after the first dose of radiation, the capacitors have suffered very little change to their capacitances. These measurements take into account the type of event shown in Figure 7-10, where ten measurements were done on the same capacitor at various frequencies. Note that occasionally a measurement does not fall within a small percent of the average such as shown by the peak at 1 MHz.

Figure 7-10: Results of repeated measurement of capacitor C1 at various frequencies after irradiation dose of 26 kGy

The same argument could be applied to the conductivity of these capacitors as shown in Figure 7-11. However, even if they have increased, it does not rise for over 10%, so in the average, the conductance has not change appreciably.

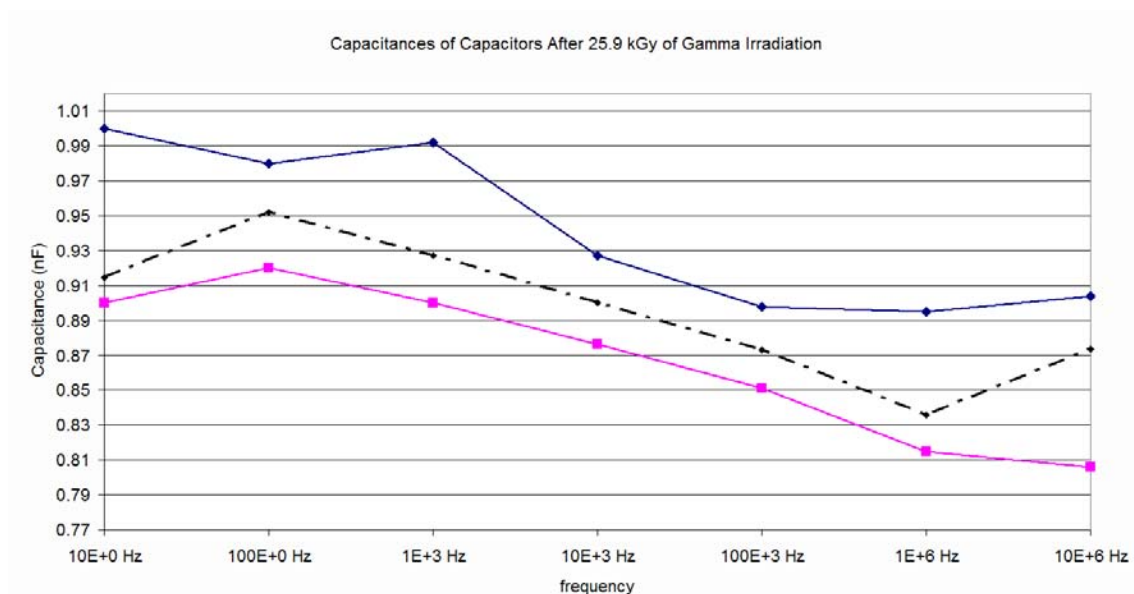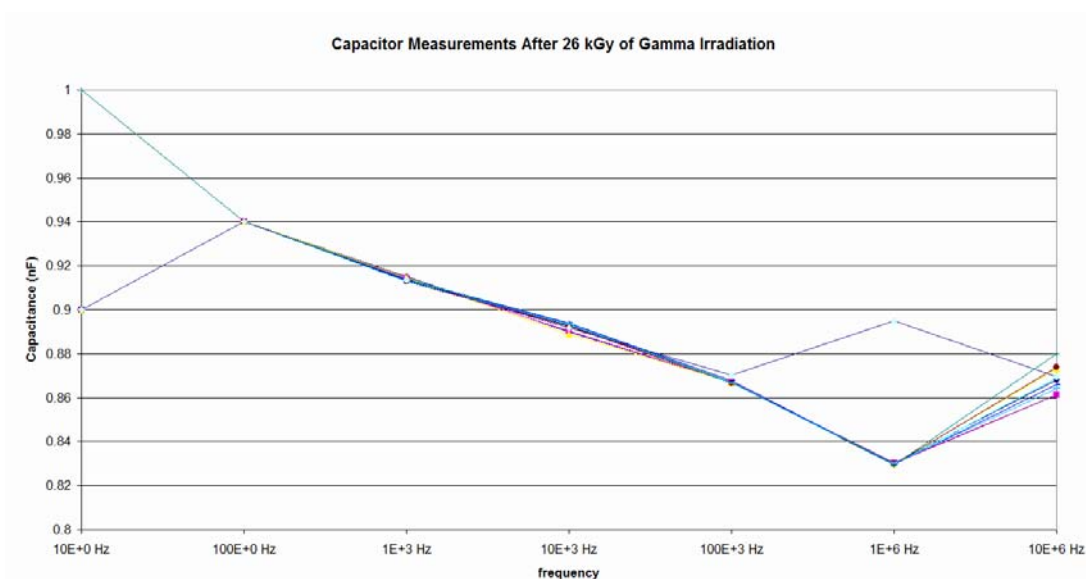**Figure 7-11 Conductivity of capacitors after first dose of irradiation (26 kGy total) at various frequencies**
The high band (in blue) and low band (in magenta) show the absolute maximum and minimum recorded measurement (respectively), while the black line shows the average for all measurements.

When comparing the leakage current after the first dose of radiation (shown in Figure 7-12) with the leakage before radiation, the preservation of the behaviour of the components can be seen. This could be due to that the first radiation dose was, in fact, within the radiation tolerance of the capacitors.

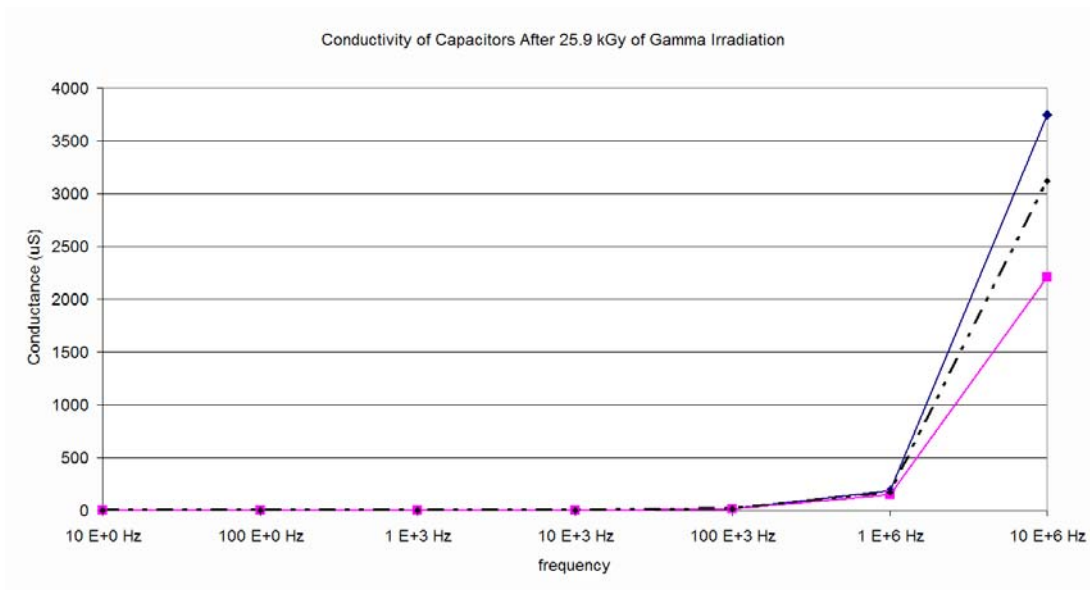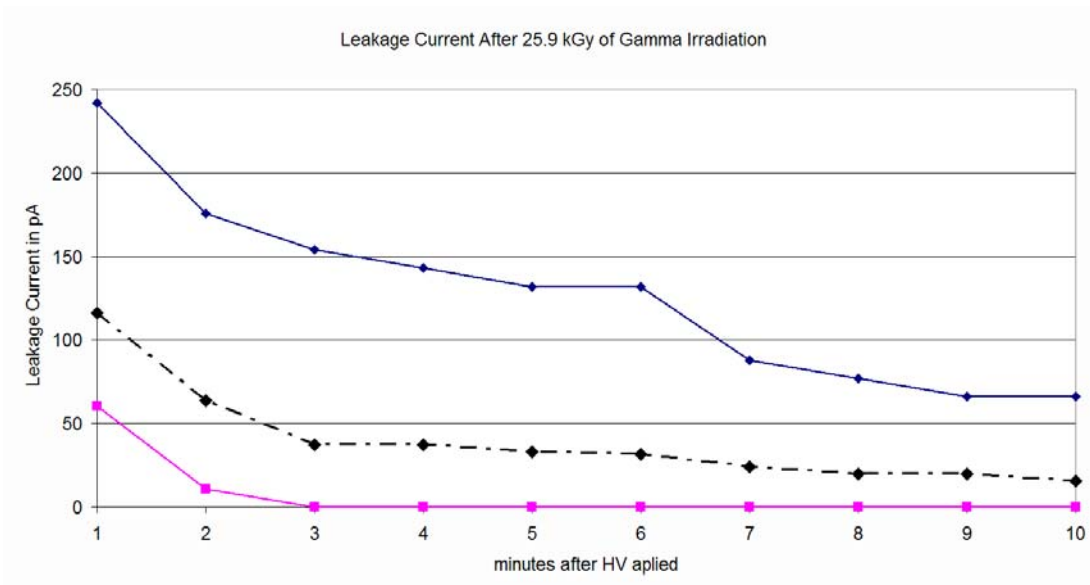**Figure 7-12 Leakage current at 1000 V after first dose of irradiation (26 kGy total) at various frequencies**
The high band (in blue) and low band (in magenta) show the absolute maximum and minimum recorded measurement (respectively), while the black line shows the average for all measurements.

Resistors

Once the capacitors were tested, it was agreed that the resistors should have the same rigorous testing, and in spite of not having previous control data with which to compare these results, it would prove useful for future comparisons with higher irradiation dose experiments.

This decision was taken after observing that the characteristics of the resistor varied with frequency. Figure 7-13 shows the parasitic shunt capacitance of the resistors, which, after 100 Hz, rises from a nominal 0 to a maximum of 0.2 pF and then at 10 kHz it declines to an almost constant value of 0.15 pF. These capacitive effects are very small, but it might explain why the conductance of resistors also changes with frequency. As the frequency increases, the impedance due to the shunt capacitances reduces, which in effect increases the conductivity of the resistor at high frequencies.
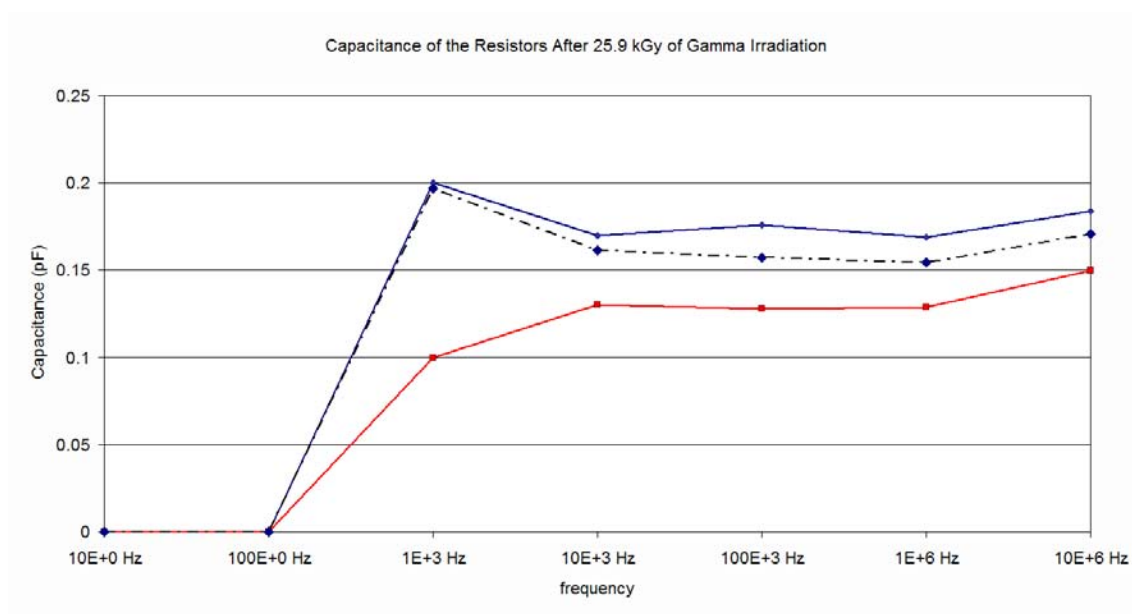

Figure 7-13 Shunt capacitance of resistors after first dose of irradiation (26 kGy total)at various frequencies
The high band (in blue) and low band (in magenta) show the absolute maximum and minimum recorded measurement (respectively), while the black line shows the average for all measurements.

Figure 7-14 Conductance of the resistors after first dose of irradiation (26 kGy total) at various frequencies.
The high band (in blue) and low band (in magenta) show the absolute maximum and minimum recorded measurement (respectively), while the black line shows the average for all measurements.
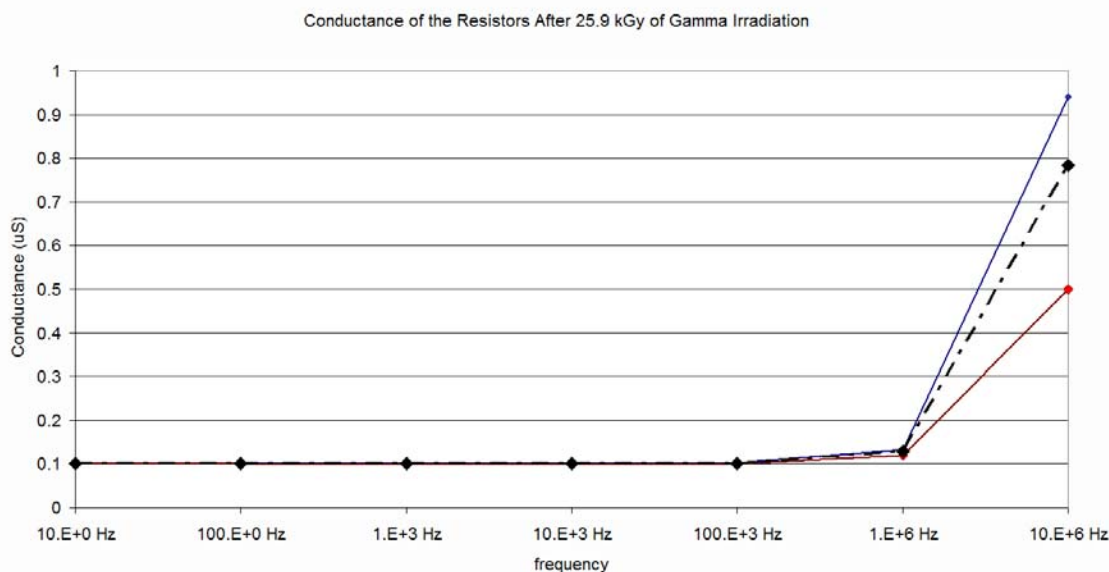
Figure 7-14 shows this change as a rise of the conductance of the resistors with frequency, in other words, as the frequency rose, the impedance decreased. As it has been seen on previous charts, the conductivity of these components and frequency are directly dependant.

Second Irradiation

On the preparation for the second does of radiation, it was estimated that, due to the volume of the metal box, in which the individual containers held the components, the timer required for achieving a high dose of radiation was going to be impractical. To solve this problem, it was concluded to change the containers to ones of a much smaller size.

This new cylindrical containers (made of borosilicate glass), had an approximate diameter of ½ cm and were 5 cm in length. Therefore, it was possible to provide accommodation for a better distributed irradiation. It was also suggested to separate the containers containing the resistors from the capacitors in two metal boxes. This will allow a greater number of components

to be closer to the source, and thus minimising the variation on the dose due to geometric reasons.

After the second and final dose of radiation was completed, it was calculated that the components received 319 kGy of Gamma radiation at a rate of 1.04 kGy/hour and room temperature of 17 °C, raising the total dose to 345 kGy.

The components were then re-measured to see the effects of a large dose on their properties.

Capacitor.

From Figure 7-15, the maximum and minimum limits of the capacitance of the capacitors may be seen. This limit reflects a reduction in such capacitances due to the radiation that the components were subject to. This reduction was of the order 10% at 10 Hz on the lower limit, with no change on the maximum limit; however, at higher limits, this differences drop to less than 5% in both limits. On the other hand, the conductance of the capacitors shown in Figure 7-16 reflects big differences but only at very high frequencies

Figure 7-15: Capacitance of capacitors after second irradiation (345 kGy total) at various frequencies.
The high band (in blue) and low band (in magenta) show the absolute maximum and minimum recorded measurement (respectively), while the black line shows the average for all measurements.

These differences were rated at 25% at 10 MHz for the high band and 66% on the lower band. However, it is advised to remember, that these bands are only indicative of the values measured, and has no relation to the frequency of occurrence.
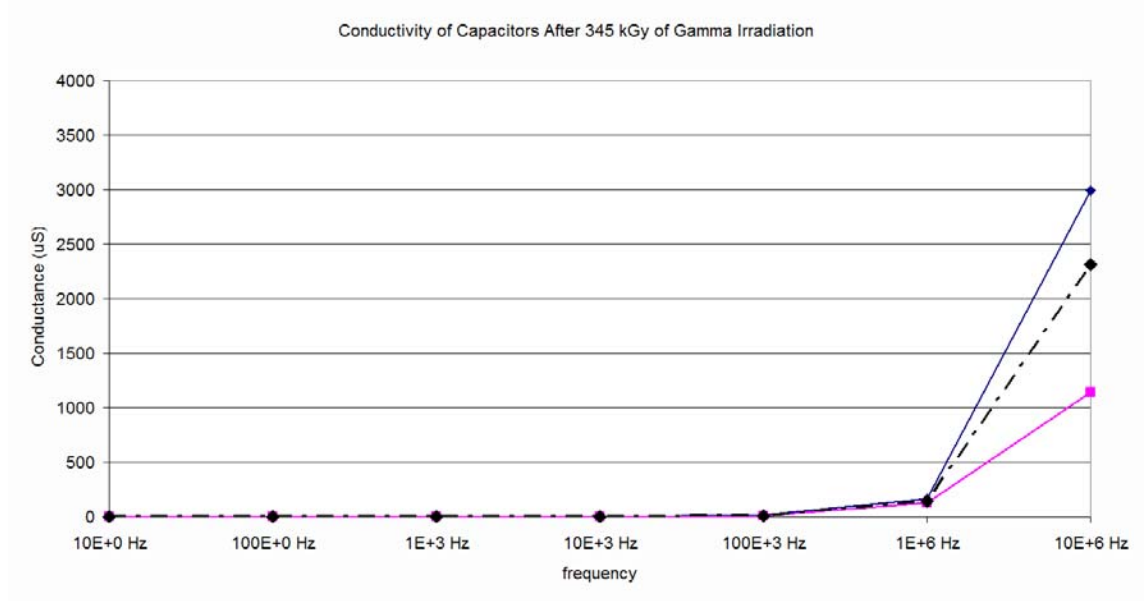
Figure 7-16: Conductivity of capacitors after second dose of radiation (345 kGy total) at various frequencies.
The high band (in blue) and low band (in magenta) show the absolute maximum and minimum recorded measurement (respectively), while the black line shows the average for all measurements.

Figure 7-17: Leakage current after second dose of radiation. (345 kGy total)
The high band (in blue) and low band (in magenta) show the absolute maximum and minimum recorded measurement (respectively), while the black line shows the average for all measurements.

Even if it has been shown that the parameters of the initial values of the components have been adversely affected, Figure 7-17 shows an improvement with a decrease of the leakage current.

	10 Hz	100 Hz	1 kHz	10 kHz	100 kHz	1 MHz	10 MHz
C 1	9.00	7.07	8.12	8.44	8.37	9.54	9.57
C 2	0.00	8.33	8.53	8.87	8.77	9.35	4.50
C 3	10.00	9.90	9.74	9.80	9.83	10.23	12.45
C 4	4.26	10.11	9.94	11.86	9.73	10.01	11.00
C 5	3.23	9.94	10.20	10.07	9.89	10.15	6.02
C 6	6.25	9.55	10.01	9.96	9.88	10.77	8.27
C 7	15.79	10.75	10.55	10.33	10.03	10.33	6.96
C 8	9.09	9.54	9.86	9.78	9.68	9.92	9.24
C 9	2.17	8.62	9.59	9.62	9.37	9.77	8.91
C 10	2.17	8.72	9.20	9.36	9.36	4.32	6.44
Average	6.20	9.25	9.57	9.81	9.49	9.44	8.34
Worst Case	15.79	10.75	10.55	11.86	10.03	10.77	12.45

Table 7-2 Percentage change of capacitances, average and the worst case after radiation dose of 345 kGy

Resistors

In contrast with the capacitors, the shunt capacitance of the resistors in Figure 7-18 shows a narrowing of the tolerance band at intermediate and high frequencies.

What it is considered as interesting, is that the effect of the shunt capacitances flattens along the frequency axis, thus allowing a manageable model of the component for the studies of the frequency response of the HV filter. However, reference to the conclusion is recommended for further explanation of these results. On the other hand, the differences in the capacitances did not reflect the similarities that the resistors and capacitors shared on their conductivities.

Figure 7-19 shows, once again, a similar behaviour of the resistor to the capacitors. The lower and high bands suffered a widening as a function of the

frequency; however, these bands have decreased their values by 5% for the higher band and 20% for the lower band at 10 MHz.

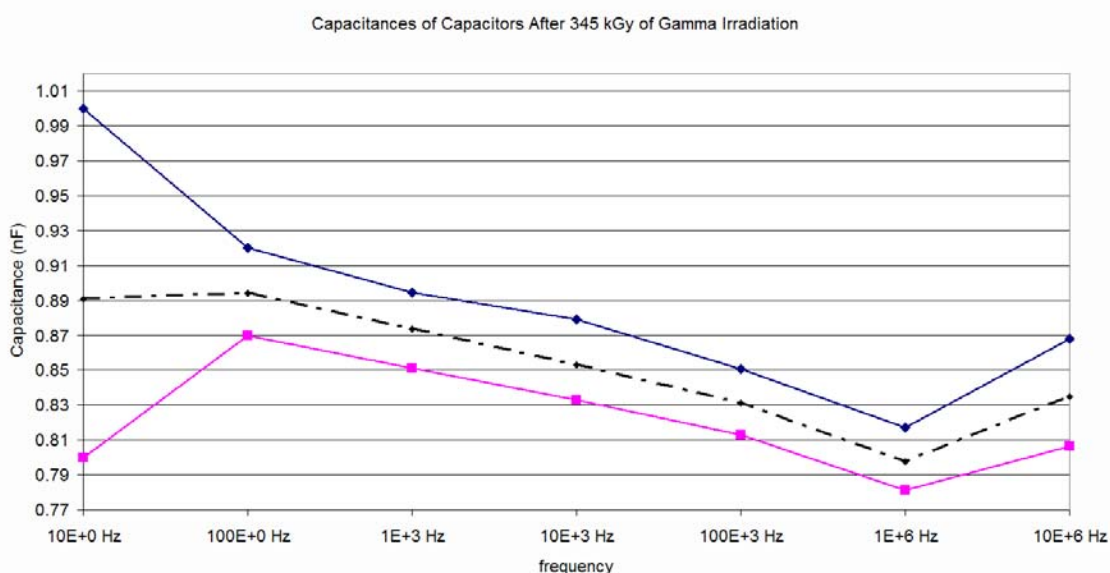**Figure 7-18: Capacitance of resistors after second dose of radiation at various frequencies.**
The high band (in blue) and low band (in magenta) show the absolute maximum and minimum recorded measurement (respectively), while the black line shows the average for all measurements.
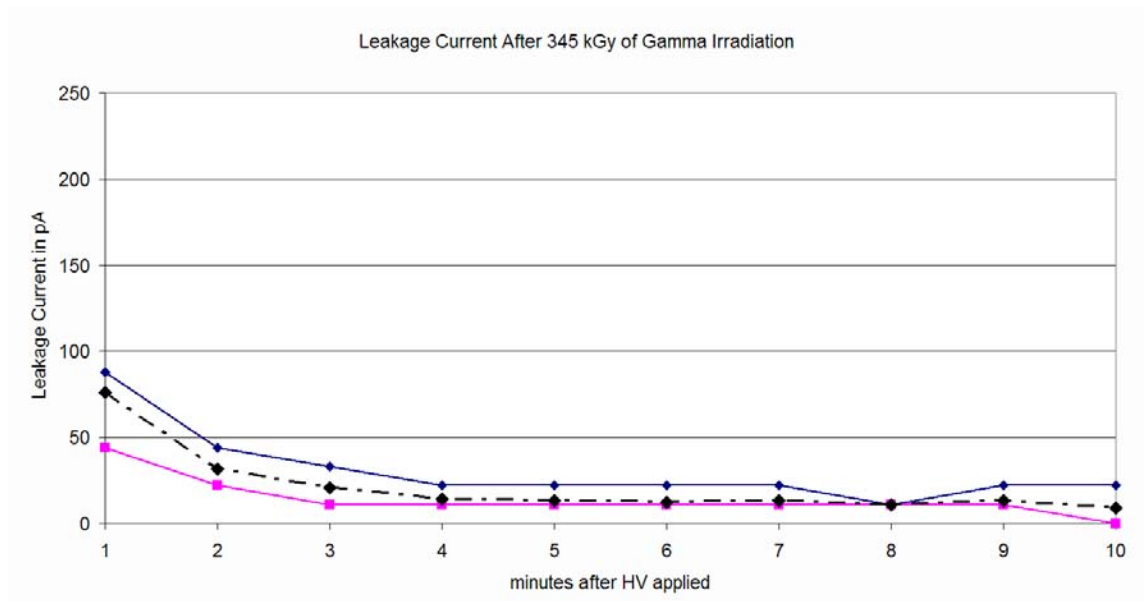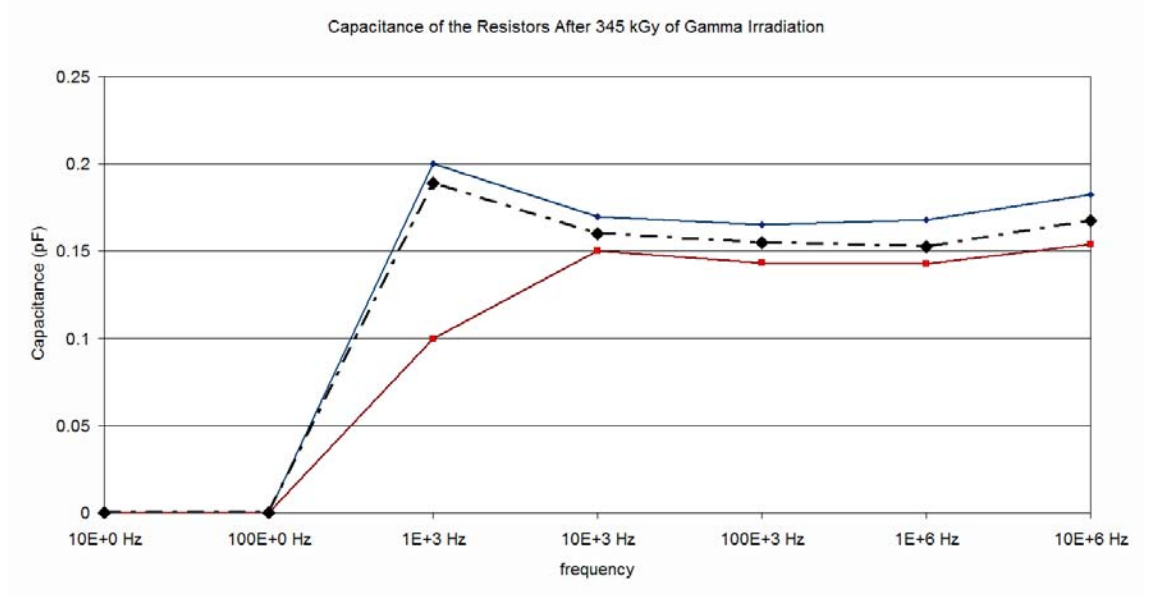

Figure 7-19: Conductivity of resistors after second dose of radiation at various frequencies
The high band (in blue) and low band (in magenta) show the absolute maximum and minimum recorded measurement (respectively), while the black line shows the average for all measurements.
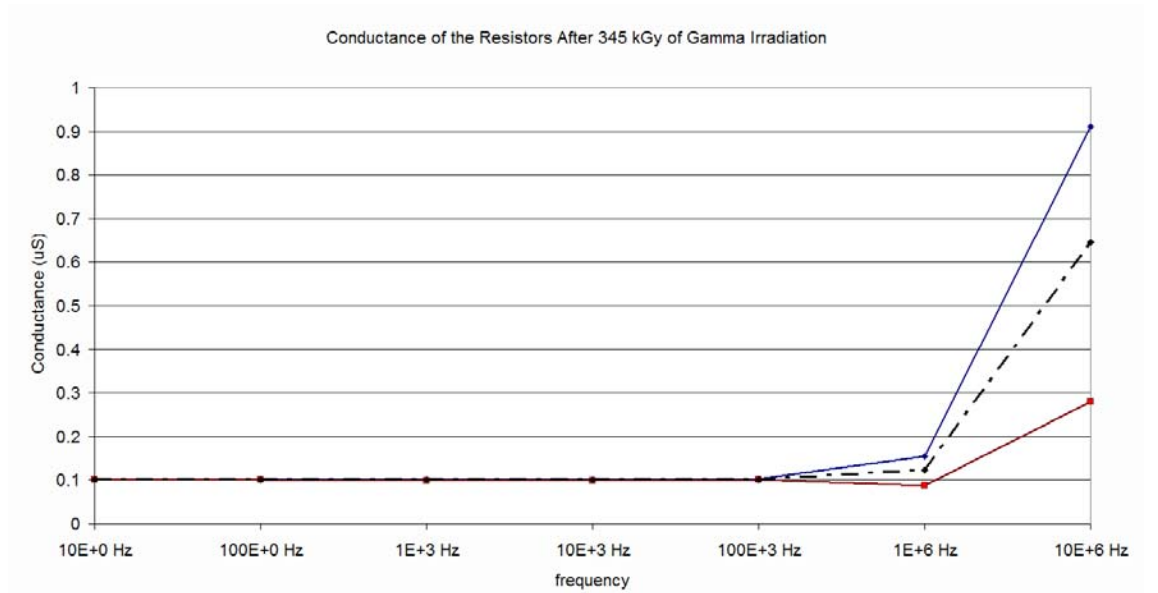
Leakage Current During Irradiation

This section discusses the measurement of the leakage current of a Farnell 498-385 1 nF 2 kV capacitor during irradiation.

Experiment

The leakage current on the capacitors was measured using the circuit shown in Figure 7-2 and mounted as shown in Figure 7-20.
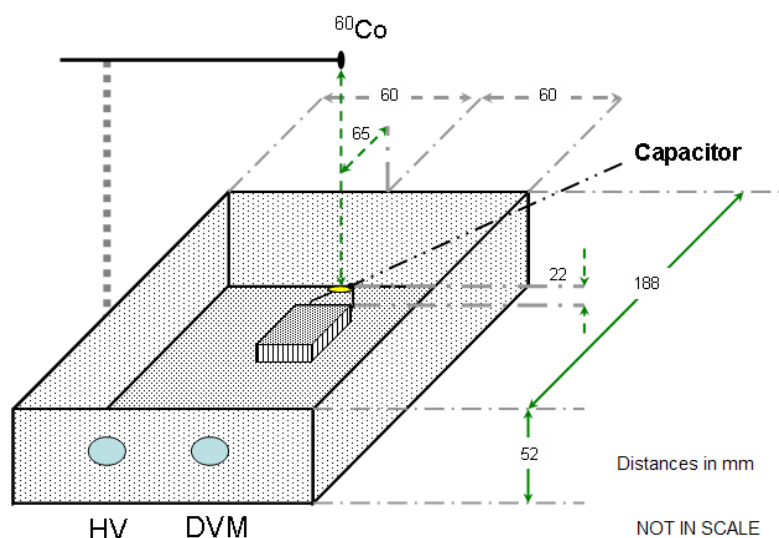
Figure 7-20: Jig Setup for Dynamic Testing

The source was taken to the testing place by a manual winding mechanism. After a set amount of time, the source was winded back. A chronograph was used to aim for a consistent amount of irradiation and winding rate

As in the previous experiment, the capacitor was loaded to 1000 V DC using a CANBERRA HV Power Supply, Model 3002. An "Intelligent Digital Multimeter" Thurlby 1905a was programmed to record measurements every 15 seconds.

The experiment was divided in to three tests. The first test consisted of studying the leakage current during irradiation without a capacitor. In the second, the capacitor was installed. Finally, the third test consisted of replacing the capacitor with wires of the same characteristics as the capacitor leads.

Once each test was ready to start, the circuit was powered and left to stabilise for at least ten minutes. Then the program on the DVM was run to start recording, and after an estimated time (or number of measurements) the

mechanism that winds the source was activated.   Finally, after approximately three minutes, the mechanism was wound back in order to remove the source.

Confirmation of some effect of radiation, was observed, when there was a coherent change in the measurements at the estimated time

Results

As it can be seen from Figure 7-21, the first obvious result was a sudden rise in the leakage current when the source was exposed, proving that radiation and leakage current do have a relation. The second observation was the time delay between the reactions of the three different modes. This was due to the human mechanical effect: although using a chronograph to know when to start winding the mechanism which took the source to the testing area and vice-versa, the speed at which this was done could not be controlled precisely, and hence synchronising the time-position of the source for all the tests was not possible.

Because of this, and in order to appreciate better the effect of radiation, some irrelevant data was omitted in favour of time synchronisation; as it can be seen in Figure 7-21. Secondly, due to the same reasons explained above, it is suggested to omit the analysis of the "transient" i.e. during the processes of winding and unwinding the source is omitted.
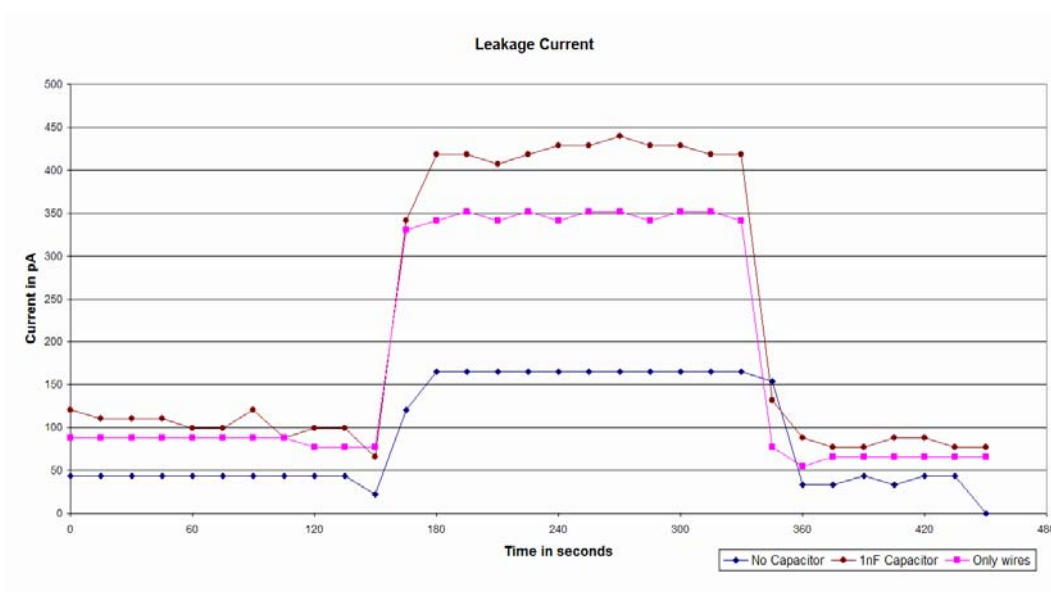
Figure 7-21 Dynamic testing of capacitor under irradiation

As mentioned above, it is clear that radiation does have an effect on the current passing through the circuit; however, this current should not be attributed only to the increased leakage of the capacitor. Figure 7-21 shows the contributions of the capacitor and the wires, when the base measurements have been subtracted.

Figure 7-21 also shows that the leakage is greater with the capacitor than in any other case; however, it also shows that the wires of the capacitor contribute significantly to the leakage current. It has been hypothesize that this is due to that the air around the wires are being ionised by the radiation, and hence producing another route for the current to flow. Therefore, the contribution of the capacitor alone could be extracted from the two charts and it is shown on Figure 7-22.

Finally, Figure 7-22 shows contribution of the capacitor alone; the average per region in the continuous line; and the sampled values in dots.

Figure 7-22 Additional leakage current due to capacitor alone

Studies of Recovery

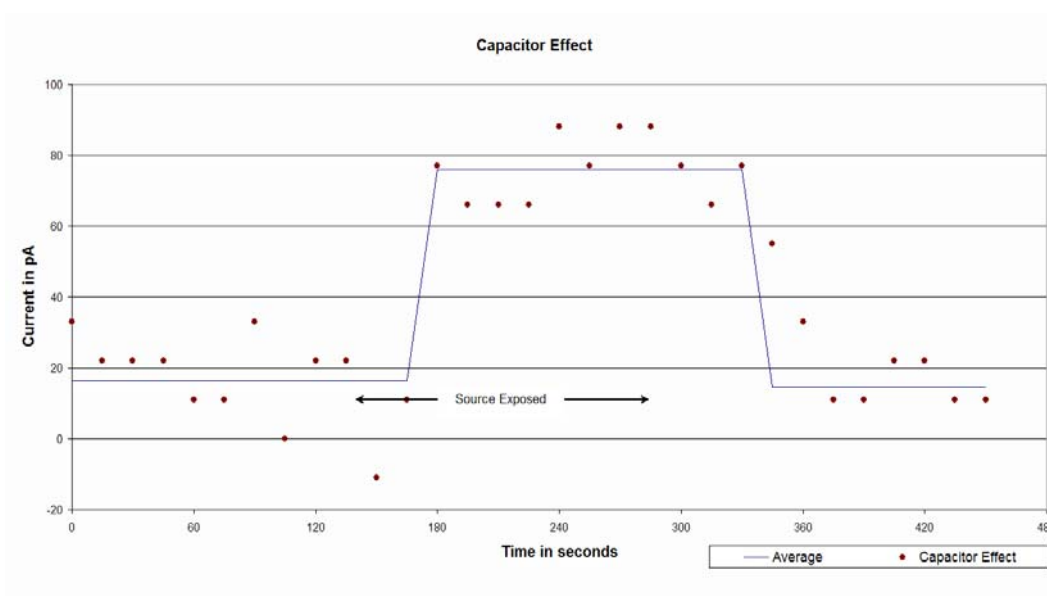This part studied a phenomenon raised by Osmokrovic [1], where it was mentioned that a capacitor would recover from irradiation. These theories were very interesting, so it was decided to conduct experiments to prove whether the theories applied to the capacitors studied in this report or not.

The capacitances were measured 3 and 15 weeks after the final full dose of radiation, and the results were compared to the values obtained from the measurements just after the second dose of irradiation.
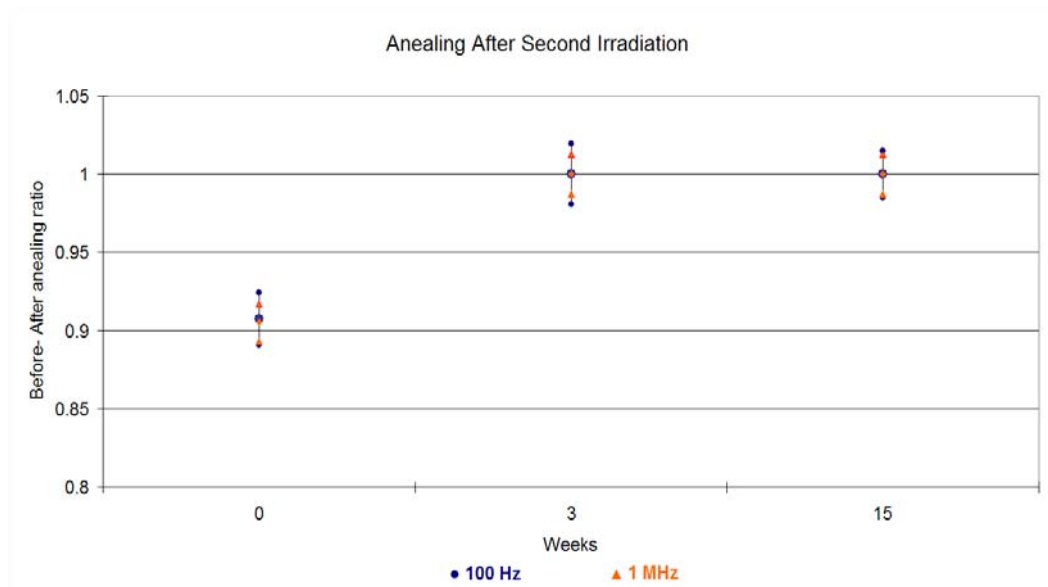
Figure 7-23 Measured recovery of capacitors some time after being exposed to irradiation

Figure 7-23 shows the process of recovery of the capacitance after being subject to 345 kGy of gamma radiation. The data plotted on this figure are the mean values ($mean \pm 1\sigma$) of all the capacitors. It shows that most of the recovery takes place during the first three weeks, with very little change during the subsequent weeks. The frequencies studied (100 Hz and 1 MHz) were selected for this analysis due to the fact that they are reasonably distant to each other, as well as being the points with more variations observed in the measurements.

This analysis concludes that these capacitors do recover after irradiation, and that any significant recovery takes place during the first three weeks.

General Observations

The Higher and Lower Bands

The benefits of this method for displaying the measurements obtained, arises from the simplification of the information shown. However, this simplification omits the frequency of a particular result, and hence reflecting the average, which was rarely the average of the bands, but some value between them. Even though, in some cases it showed that the margin of error was very slim, and that the data acquired varied very little with respect to the particular test of a component across the other components.

The values considered for these bands, were not from a particular sample, but from the maximum and minimum values measured; i.e. these bands enveloped the whole experimental data, enclosing the totality of the measurements.

Observation on the effects of the radiation

The results are very encouraging in the fact that even if there was a 20% difference in some cases, the overall change does not reach an order of magnitude; therefore, the stability and tolerance of theses components to radiation could be concluded.

Reliability of the experiments and data acquired

It is a fact that gradual radiation over a period of time has effects different to those from strong radiation on a shorter period, even if the total radiation dose is the same. However, the length of time needed for the gradual radiation to which the components will be subject, would makes the experiment unviable. Therefore, the results obtained from this chapter should only be considered as a guide.

External factors

It is important to mention again, that measurements of the impedance were dependant on variables outside of control, such as temperature, humidity, and even the temperature of the impedance meter. These factors might have altered

considerably the results from the measurements, explaining the appearance of widening on the gaps between the bands.

Leakage current corrections

Corrections were taken to compensate for the leakage current observed without a capacitor due to instrumental error, noise and leakage on the circuit. This current generally approximated to 20 pA, but the actual value was taken just before each testing each sample, to ensure consistency.

Comparison with Previous Studies

Comparing the results obtained from these experiments to those of Torbet [2], it could be concluded that:

1. In the case of the resistors conductance, there was no difference for a frequency range of 0-300 kHz. However, Torbet's report did not study the effects of frequency on the measurements of the conductance, thus making it impossible to compare the effects on the conductance or shunt capacitance, at intermediate and high frequencies, for the 10 MΩ resistor.

2. Similarly, comparison of the effects of frequency on the capacitance and conductance of the capacitors, were not possible due to the lack of a base to compare them with. Even though, the evidence seen in this paper reinforces Torbet 's report on not only the changes seen between components, but the effects radiation has on the capacitances, as well as how much some capacitors are changed by radiation. In addition, his measurements at 300 kHz have a mean across the capacitor range of 0.925 nF approximating the results of this investigation, which were 0.91 nF at that same frequency before radiation. Furthermore, after the full dose of radiation, the results were even closer, matching to 0.87 nF.

3. Finally, there was a good correlation between Torbet's report and the present one, on the study of leakage currents at 1 kV each. The difference being that this report focused on the first ten minutes of the

experiments and the former one for the next 20 minutes. Thus, the comparison could be made for t=10 minutes, at which, both reports show the same results.

Other sources were investigated to complete the comparisons with this paper. However, since Lambert et al [3], in 1975, no other publication was found. The group shows in their report a very comprehensive study of the effect of radiation across a wide range of components; however, Lamberts' report lacks the frequency analysis exposed in this paper, thus, making comparison impractical.

P. Osmokrovic et al. [1], explain in their paper that the decrease of the capacitance was due to the formation of ionised structures on the dielectric, which somehow affects the partial screening of the electric field. With time, these structures recombine producing a recovery of the Capacitance. Although Osmokrovic's experiments were based on poly-carbon capacitors, this effect was too interesting to ignore. After three weeks the capacitances were measured again and a slight recovery was noticed; further readings were taken 12 weeks later, and when compared with the previous data, it was concluded that most of the recovery happened during the first three weeks.

Other Measurements

Comparison of the effect of irradiation between capacitors.

The following charts show the normalized capacitance of the capacitors calculated by:

$$C'_i(f_k, R) = \frac{C_i(f_k, R)}{C_i(f_k, R_0)}$$

(7-15)

where F_K is the testing frequency, R is the radiation level and R_0 refers to the test before radiation.

Figure 7-24 Measured effect of gamma irradiation on the capacitors at 10 Hz

Figure 7-25 Measured effect of gamma irradiation on the capacitors at 100 Hz
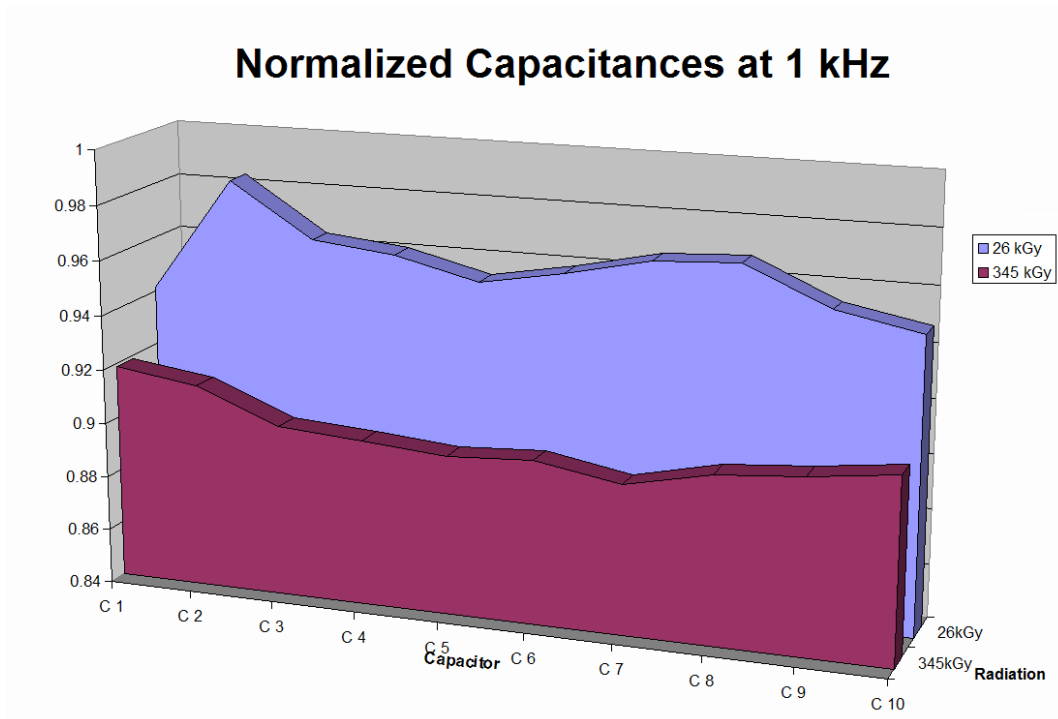
Figure 7-26 Measured effect of gamma irradiation on the capacitors at 1 kHz

Normalized Capacitances at 10 kHz
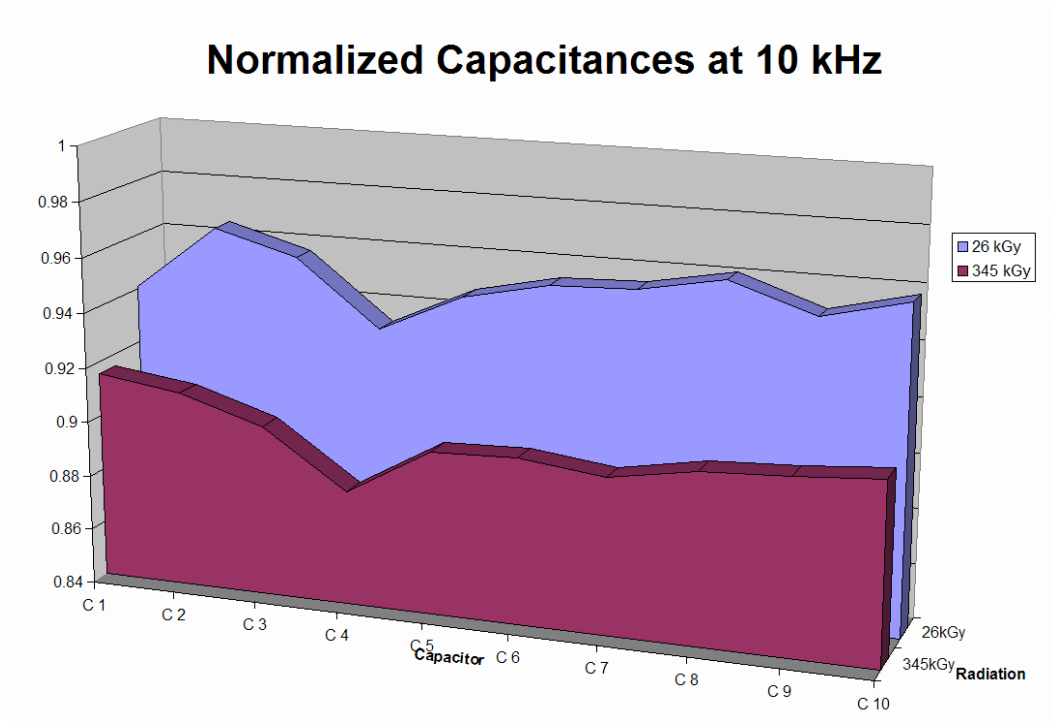
Figure 7-27 Measured effect of gamma irradiation on the capacitors at 10 kHz

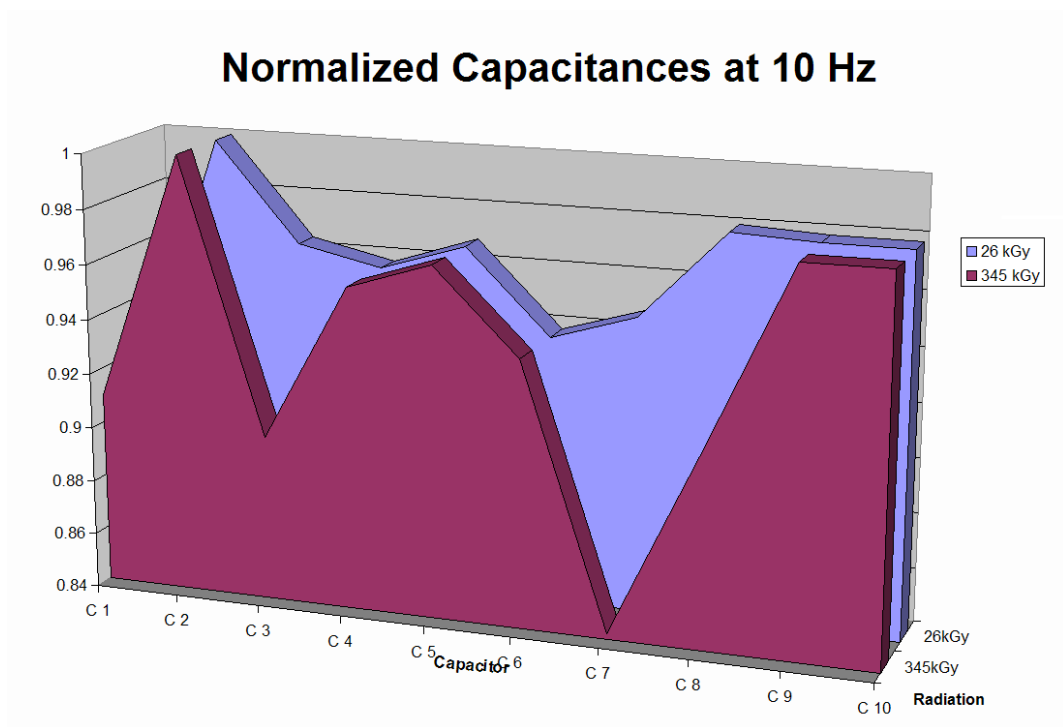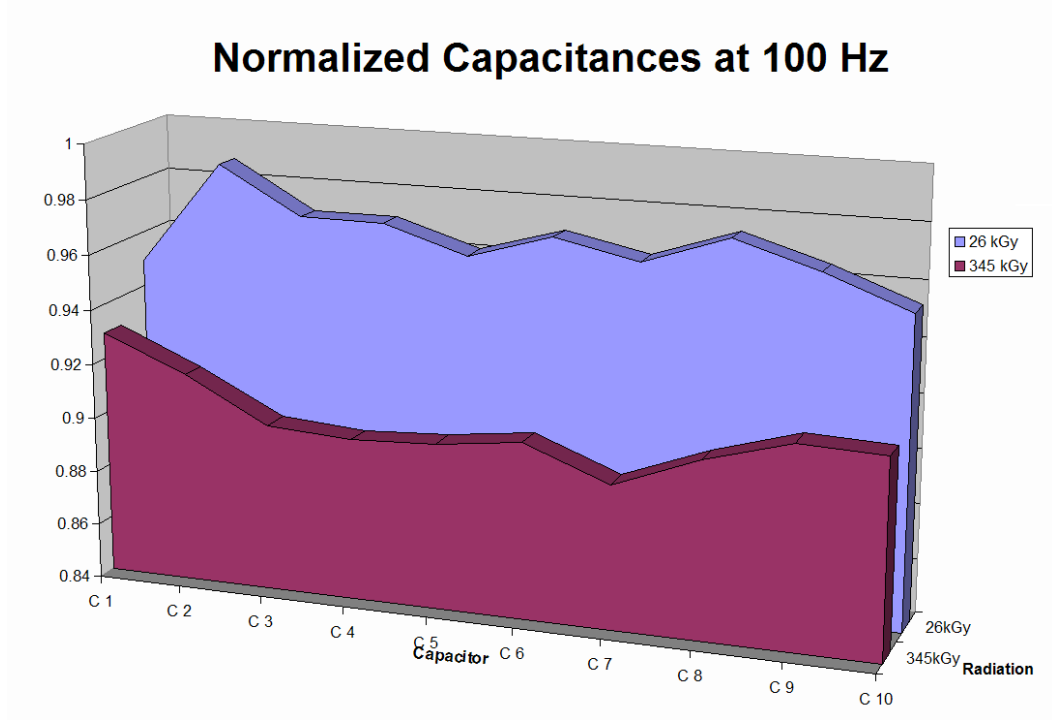## Normalized Capacitances at 100 kHz
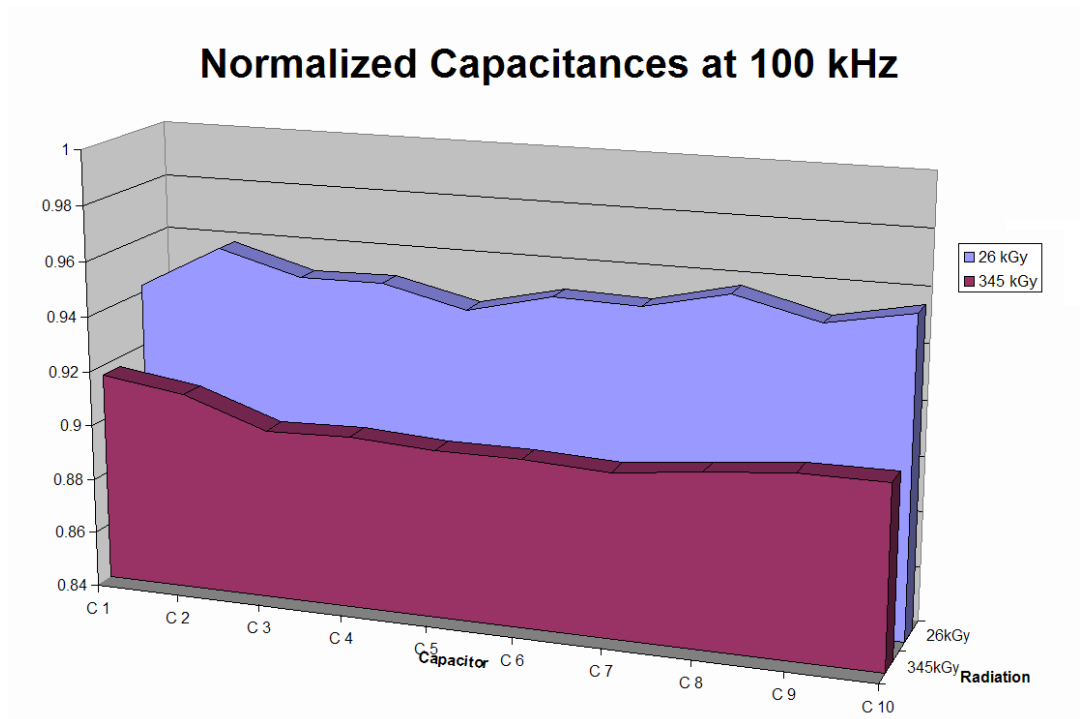
Figure 7-28 Measured effect of gamma irradiation on the capacitors at 100 kHz
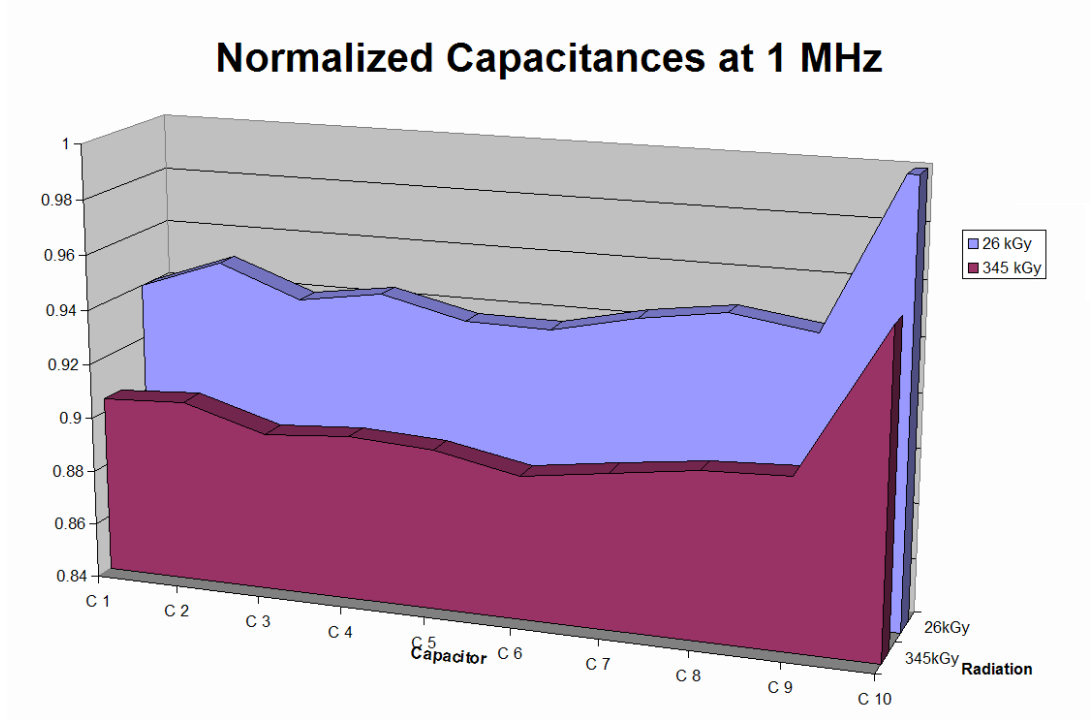
Figure 7-29 Measured effect of gamma irradiation on the capacitors at 1 MHz
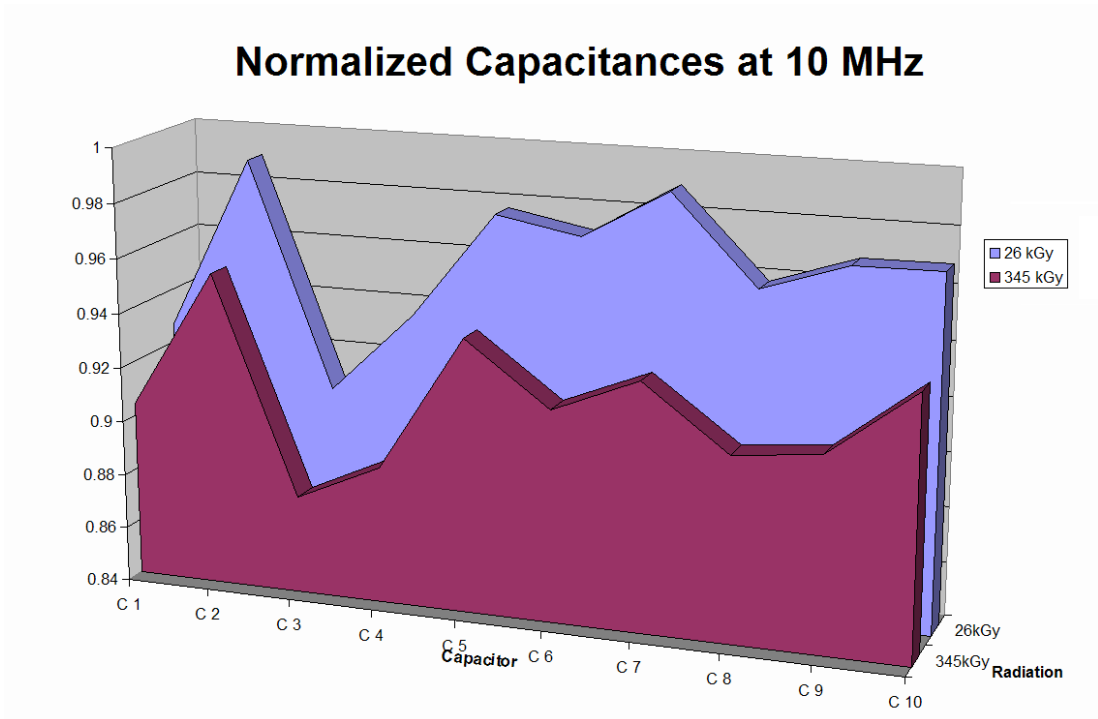
Figure 7-30 Measured effect of gamma irradiation on the capacitors at 10 MHz

References

1 P. Osmokrovic et al, "*Radioactive resistance of elements for over-voltage protection of low-voltage systems*", <u>Nuclear Instruments and Methods in Physics Research Section B: Beam Interactions with Materials and Atoms</u>, **140**, Issues 1-2, (April 1998), Pages 143-151

2 Torbet, M.; "*Irradiation tests on HV filter components - Unbiased leaded components*" <u>CMS   ECAL   Endcap</u> (2000): <u>http://www.eng-external.rl.ac.uk/cms-gen/Project_papers/EE231/irradiation_results_3.ps</u>

3 K. P. Lambert, H. Schönbacher and M. Van de Voorde, "*A comparison of the radiation damage of electronic components irradiated in different radiation fields*", <u>Nuclear Instruments and Methods</u>, **130.1**, (1 December 1975), Pp 291-300

Chapter 8 Radiation effect on HV filter components, Part II

Second Set of Components

ue to concerns that a spark at the anode of the VPT may cause the coupling capacitor C3 to discharge into the pre-amplifier, the design of the HV filter was modified. These modifications include the reduction of the capacitance of (C3) so as to reduce the stored charge, the introduction of a 100 Ω resistor (R6) between C3 and the preamplifier to increase the transient time of the possible discharge. In addition to these R3 was doubled to 22 MΩ. Figure 8-2 shows the modified circuit diagram.
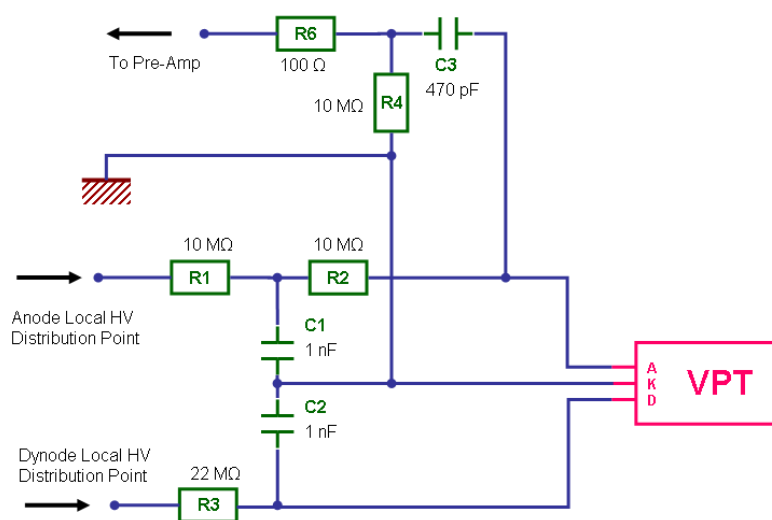
Figure 8-1 Modified circuit diagram

Following the results from the previous chapter where it was proven that commercial off the shelve components may be suitable for their use in the HV filter cards for the CMS ECAL endcaps, this chapter extend these test to include the values of the new components.

Furthermore, due to the fact that the manufacturer (RS) does not guarantee anything about the radiation tolerance of the components, each batch should be

tested before a decision of purchase. This is because components from different batches may have the same dielectric, same value of capacitance, same voltage ratings, same tolerance, but who knows if the manufacturer has introduced something in the manufacturing process that would make the components behave differently.

Because of this, a new set of components were received which required testing. These include 10 samples for each of the 4 different types of resistors, and 10 samples for each of the 2 types of capacitors (total of 60 components). For the purpose of classifying them, they were given serial numbers of the type

X.T.Y- S.ZZ

- X is either "R" (for resistors) or "C" for (capacitors)

- T.Y is the type ID of the component: e.g. T1 T2 T3… TN for "N" different components

- S.ZZ is the sample ID. In the case of 10 samples then ZZ will range from 01 to 10

- Example: RT4 S06 is the resistor with the type ID 04 and sample ID 06

This provided easy identification, unique to each particular component. This identification was written on paper with graphite pencils and placed with the component on individual borosilicate glass vials. This allowed for storing, manipulation and irradiation, without the risk of mixing the components.

The identification of these components was assigned as follows. (Please note that the RS number shown is the full catalogue reference number for the year 2005.)

RS Number	XTY ID	Comp. Type	Nom. Value	Rating
RS – 117 – 316	CT1	SMT Disc Ceramics	1 nF	2 kV
RS – 117 – 300	CT2	SMT Disc Ceramics	470 pF	2 kV
RS – 484 – 4602	RT1	VR25 HV Resistor	22 MΩ	2 kV
RS – 135 – 667	RT2	CFR25 Carbon Film	10 MΩ	0.125 W
RS – 131 – 132	RT3	CFR25 Carbon Film	100 Ω	0.125 W
RS – 484 - 4595	RT4	VR25 HV Resistor	10M Ω	2 kV

Table 8-1 Updated series of components for the HV filter cards

Irradiation

As the number of components was large in comparison with the previous set, the total time required to do the measurements was at least three times greater. In order to save time due to the urgency of these test, it was decided to split the whole set into two groups so that it could be possible to irradiate some components while others were being tested, and vice versa.

The groups were then placed on a metal box for EM shielding, in a random distribution such as the one displayed on Figure 8-2.

- The first group (RT1, RT2, RT4) received a dose of radiation of 179 kGy with a variation of ±52.9% due to geometric factors.

- The second group (RT3, CT1, and CT2) received a dose of radiation of 174.83 kGy with a variation of ±52.9% due to geometric factors.

These variations are caused by the fact that the dose of radiation for each of the components will depend on where they are situated within the metal box. As radiation falls by $1/d^2$, the further behind the component is, the less radiation it will receive. Therefore, the variations are purely due to geometric factors.
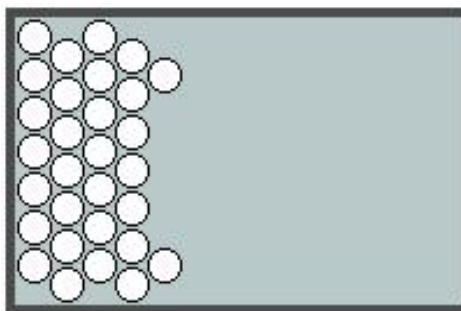

Figure 8-2 Vials Array

Testing Methodology

The same methods as with the previous set of components (as discussed in Chapter 7) were used, with the addition that this time, the effect of frequency on the resistors was measured before the resistors were irradiated.

For this, the same impedance analyser (HP, model 4192A LF) was used, set to measure the passive component, in parallel with the reactive component. In almost every case, this was a resistor in parallel with a capacitor. The exception was RT3, which will be explained later.

For this setting, the impedance analyser provides the readings in fractions of farads and fractions of siemens. Because of this, this chapter reports our findings in these units, so as to show the reader the same values (and units) observed on the instruments.

The second change in the methodology was concerned with how many repeated measurements should be taken. In the previous chapter, each component sample was measured ten times at each frequency. The previous chapter also proved that in general, each component do not vary between repeated measurements (except for very few occasions). However, a meticulous test such as that, will mean a total of 4200[*] measurements will be have to be made (and theses exclude the leakage current measurements) before the components were irradiated, and a equal number of measurements would have to be made after irradiation. Due to the time constrains for the measurement of these new components it was necessary to drop the number of measurements to at least half. In order to achieve this, each measurement was repeated 5 times (not 10) if the observations were consistent (i.e. same values within a small tolerance), if not, then the repetition of the measurement would be as before (10 repetitions).

- Therefore, every sample of every component was tested 5 times at each individual frequency.

---

[*] 60 components $\times$ 10 measurements/component $\times$ 7 frequencies to meassure = 4200 meassurements

- The measurement frequencies were: $10\,Hz$, $100\,Hz$, $1\,kHz$, $10\,kHz$, $100\,kHz$, $1\,MHz$, and $10\,MHz$. Thus providing a test at every decade that the impedance analyser could supply. These include either side of the main frequency (50 Hz) up to the high frequency signals.

- The leakage current was calculated by measuring the voltage across a resistor, using the same jig as used before for this purpose.

- The charts presented below follow the same format as in Chapter 7; i.e. The high band and low band are the absolute recorded maximum and minimum (respectively) for each component number. The average is that of the 50 tests (5 tests on each of the 10 samples).

For measuring the leakage current, the same jig was used as previously and is shown in Figure 8-3. However, due to availability, the high voltage power supply used for this experiment was the SRS (Stanford Research System), Model PS310/1250V – 25 W.
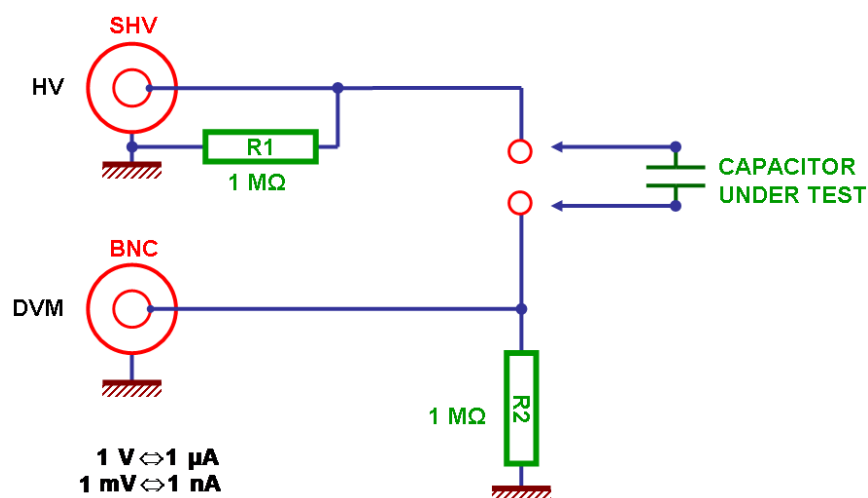
Figure 8-3 Capacitor Leakage Current jig

It was observed that when using this power supply, the voltmeter showed a reading of 0 V when no capacitor was connected. The voltmeter also showed a reading of 0 V before the voltage was applied and a capacitor was connected. This confirmed that the DVM was showing the expected voltages under the most basic condition.

CT1:   Capacitor of Type 1 (RS – 117 – 316) 1 nF

Capacitance

Figure 8-4 Capacitance of CT1 before irradiation at various frequencies
The high band (in blue) and low band (in magenta) show the absolute maximum and minimum recorded measurement (respectively), while the black line shows the average for all measurements.
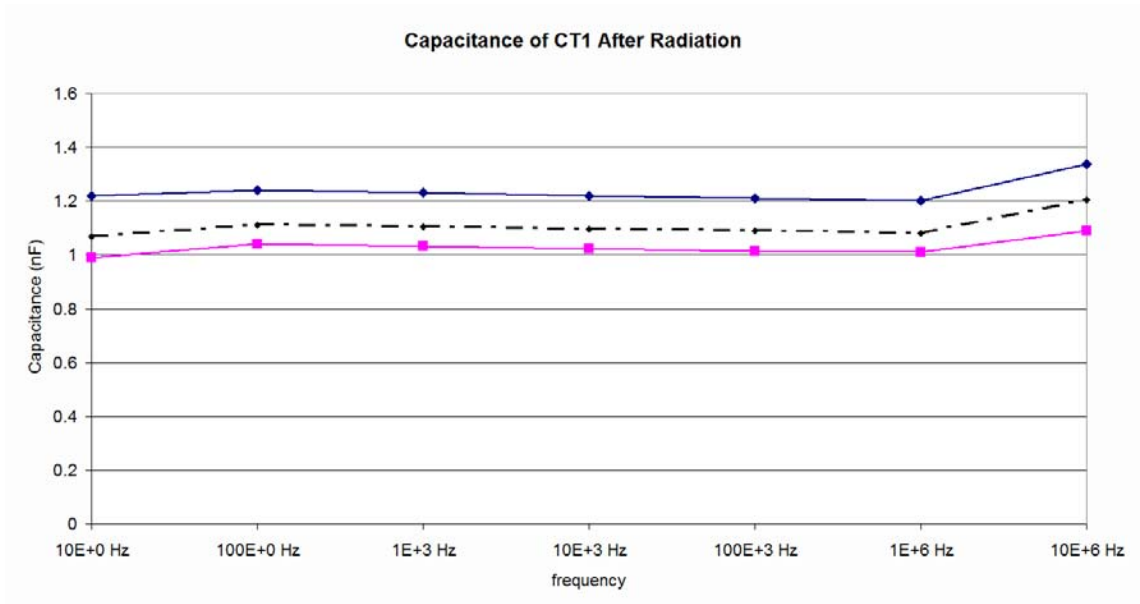
Figure 8-5 Capacitance of CT1 after a radiation dose of 136 kGy at various frequencies
The high band (in blue) and low band (in magenta) show the absolute maximum and minimum recorded measurement (respectively), while the black line shows the average for all measurements

Conductance

Figure 8-6 Conductance of CT1 before irradiation at various frequencies
The high band (in blue) and low band (in magenta) show the absolute maximum and minimum recorded measurement (respectively), while the black line shows the average for all measurements

Figure 8-7 Conductance of CT1 after a radiation dose of 136 kGy at various frequencies
The high band (in blue) and low band (in magenta) show the absolute maximum and minimum recorded measurement (respectively), while the black line shows the average for all measurements

Leakage Current
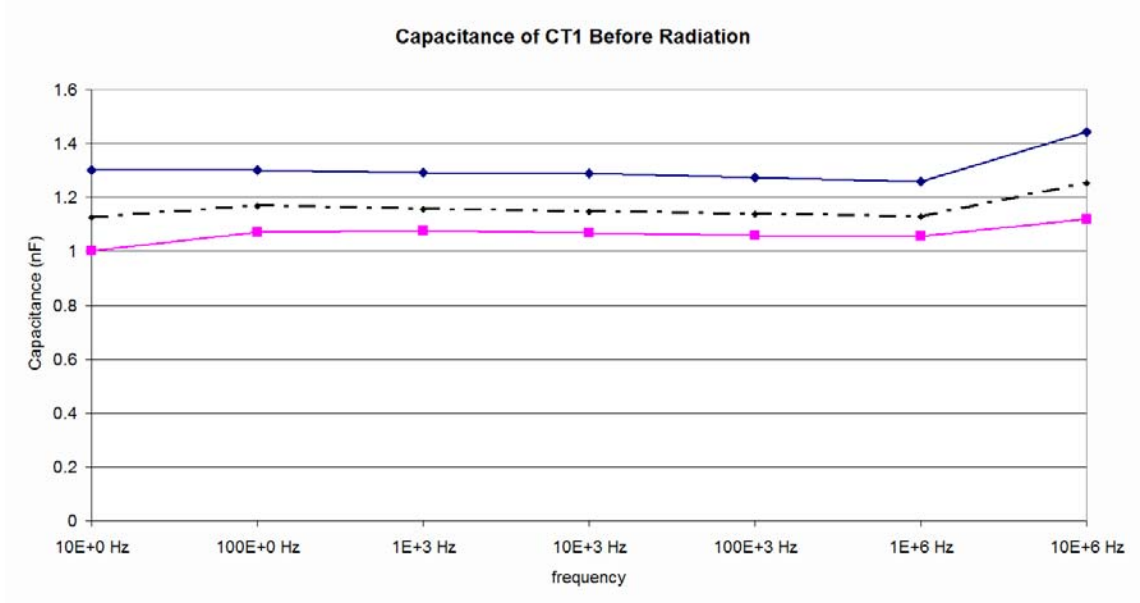
Current Leakage for CT1 Before Radiation

Figure 8-8 Leakage current of CT1 before irradiation at various frequencies
The high band (in blue) and low band (in magenta) show the absolute maximum and minimum recorded measurement (respectively), while the black line shows the average for all measurements

Current Leakage of CT1 After Radiation

Figure 8-9 Leakage current of CT1 after a radiation dose of 136 kGy at various frequencies
The high band (in blue) and low band (in magenta) show the absolute maximum and minimum recorded measurement (respectively), while the black line shows the average for all measurements

As it can be seen from Figure 8-4 and Figure 8-5, the capacitor samples varied very little between before and after irradiation, assuring that this type of capacitor are sufficiently hard to radiation and thus suitable for their use in an environment such as CMS.

Figure 8-8 and Figure 8-9 show that the magnitude of the leakage current seems to also reduce with irradiation as it has been reported in previous chapter.

The leakage current is shown to decrease as well by reducing the time it takes to stabilise at 1 pA .

This is confirmed by Table 8-2, where it can be seen an average of almost 5% change on the capacitances, and the worse case just above 10% at 10 MHz.

	10 Hz	100 Hz	1 kHz	10 kHz	100 kHz	1 MHz	10 MHz
Average	4.97	4.90	4.47	4.44	4.24	4.15	3.79
Worst Case	9.17	7.33	7.08	7.32	7.40	7.02	10.37

Table 8-2 Average and worst case percentage change of capacitance for CT1 after a radiation dose of 136 kGy at various frequencies

CT2:   Capacitor of Type 2 (RS – 117 – 300) 470pF

Capacitance

Figure 8-10 Capacitance of CT2 before irradiation at various frequencies
The high band (in blue) and low band (in magenta) show the absolute maximum and minimum recorded measurement (respectively), while the black line shows the average for all measurements

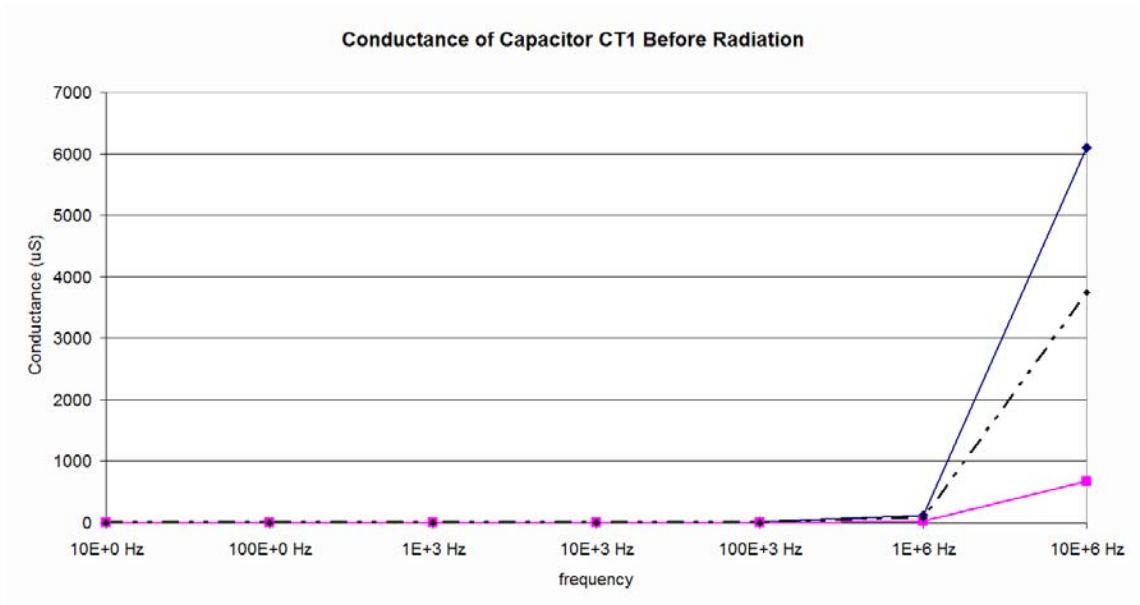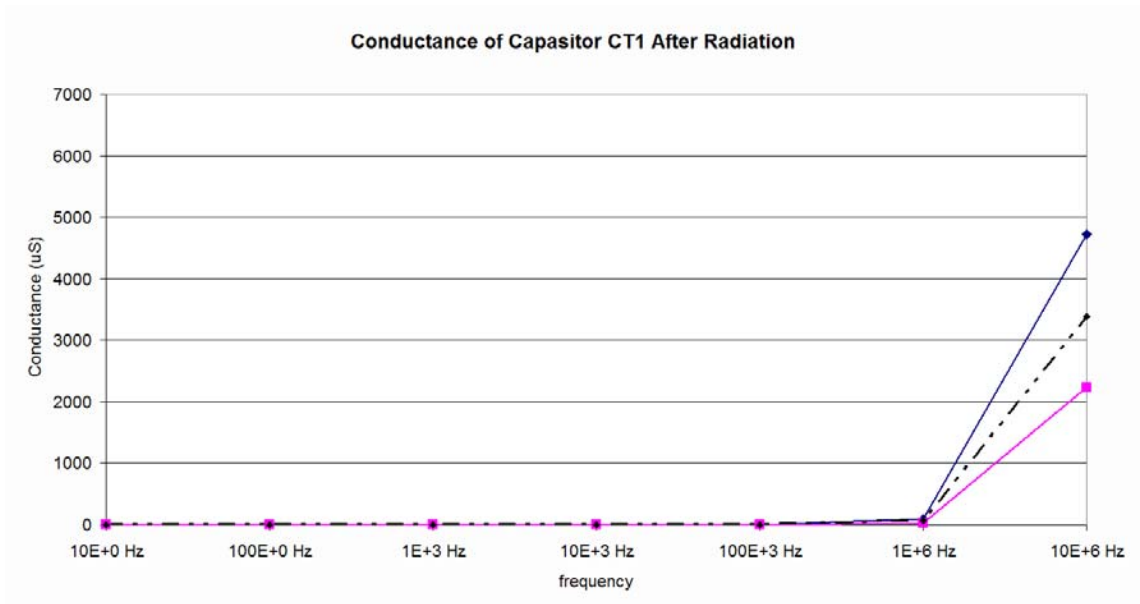**Figure 8-11 Capacitance of CT2 after a radiation dose of 136 kGy at various frequencies**
The high band (in blue) and low band (in magenta) show the absolute maximum and minimum recorded measurement (respectively), while the black line shows the average for all measurements
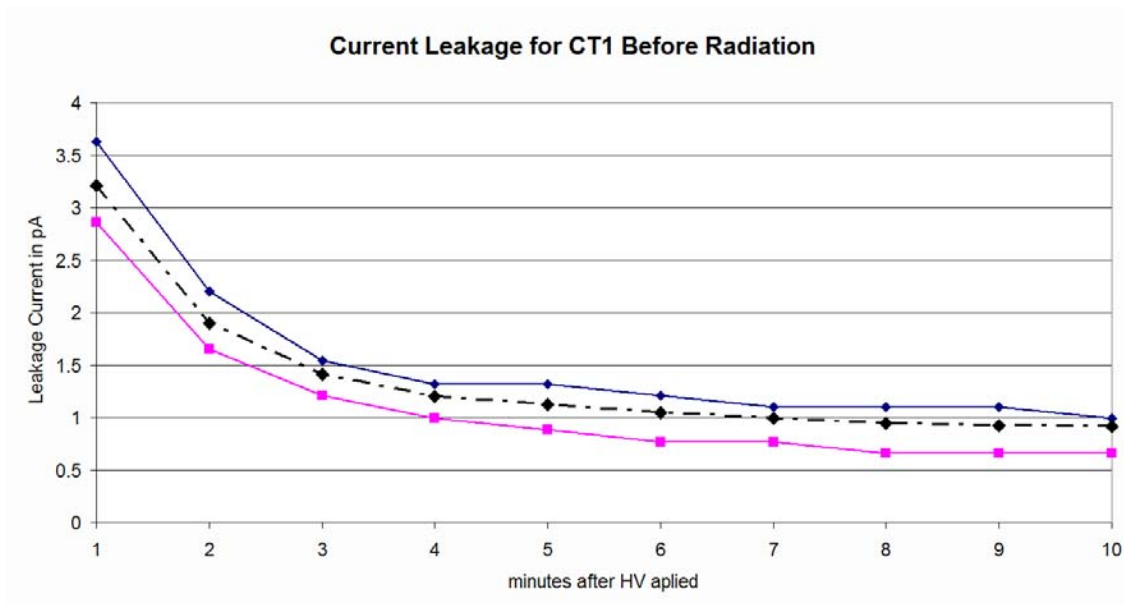
Conductance

Conductance of Capacitor CT2 Before Radiation

Figure 8-12 Conductance of CT2 before irradiation at various frequencies
The high band (in blue) and low band (in magenta) show the absolute maximum and minimum recorded measurement (respectively), while the black line shows the average for all measurements
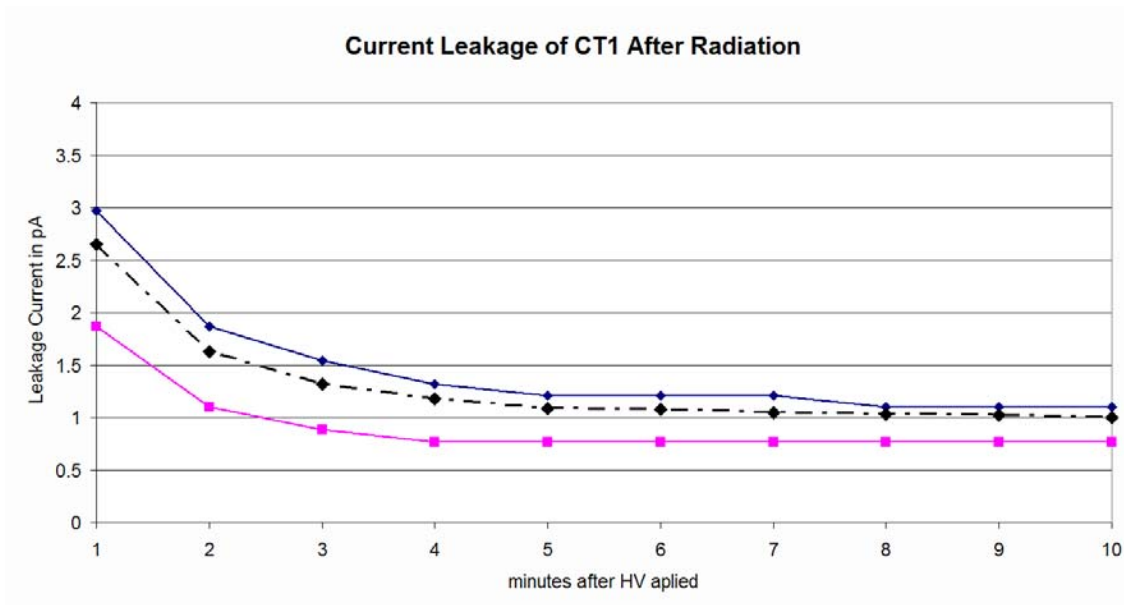
Conductance of Capasitor CT2 After Radiation

Figure 8-13 Conductance of CT2 after a radiation dose of 136 kGy at various frequencies
The high band (in blue) and low band (in magenta) show the absolute maximum and minimum recorded measurement (respectively), while the black line shows the average for all measurements

Leakage Current

Current Leakage for CT2 Before Radiation

Figure 8-14 Leakage current of CT2 before iradiation at various frequencies
The high band (in blue) and low band (in magenta) show the absolute maximum and minimum recorded measurement (respectively), while the black line shows the average for all measurements

Current Leakage of CT2 After Radiation
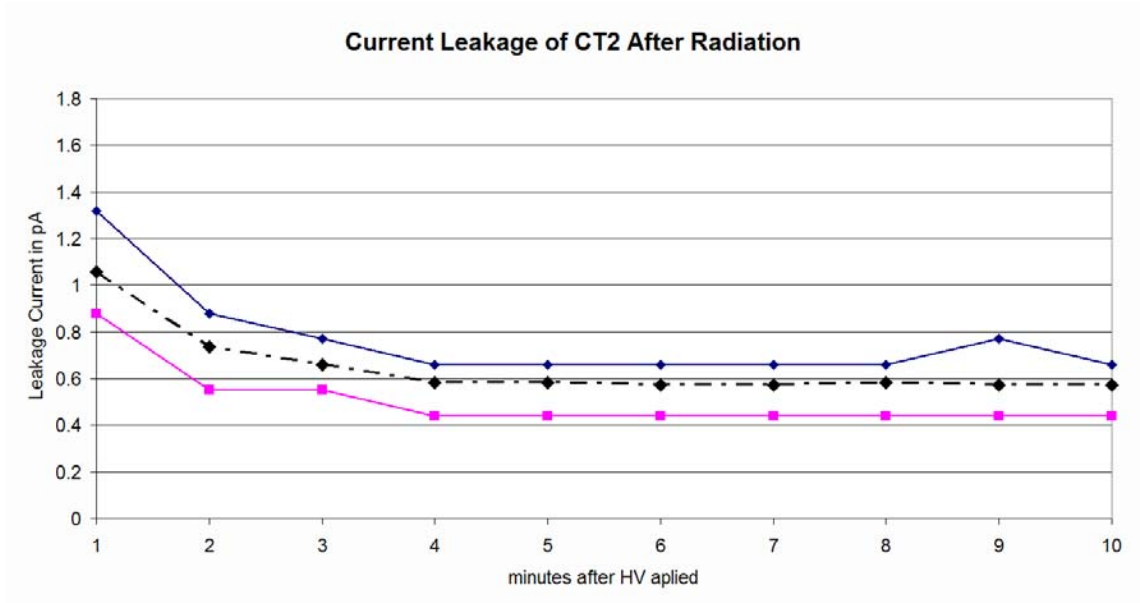
Figure 8-15 Leakage current of CT2 after a radiation dose of 136 kGy at various frequencies
The high band (in blue) and low band (in magenta) show the absolute maximum and minimum recorded measurement (respectively), while the black line shows the average for all measurements

CT2 shows to be a bit less stable with frequency as it does not remain as constant as CT1. However, as it can be seen from Figure 8-10 and Figure 8-11, there has not been substantial change in the capacitance due to irradiation.

Figure 8-12 and Figure 8-13 show that the conductivity of the capacitor has not changed substantially for frequencies less that 1 MHz, and for high frequencies, a slight fall has been noticed.

The leakage current has also an improvement taking 4 minutes instead of 7 to stabilise at 0.6 pA as it can be seen from Figure 8-14 and Figure 8-15

The percentage change can be seen from Table 8-3. The percentage change is more or less constant throughout the spectrum. Although these percentages are on the edge of 10% with the worst case at 10 Hz, the capacitances do not drop below 400 pF, which keep them within the parameters set by the designer of the HV filter.

	10 Hz	100 Hz	1 kHz	10 kHz	100 kHz	1 MHz	10 MHz
Average	17.04	8.67	8.70	8.61	8.35	8.19	8.87
Worst Case	20.00	10.20	9.62	9.58	9.24	9.01	10.56

Table 8-3 Average and worst case percentage change of capacitance for CT2 after a radiation dose of 136 kGy at various frequencies

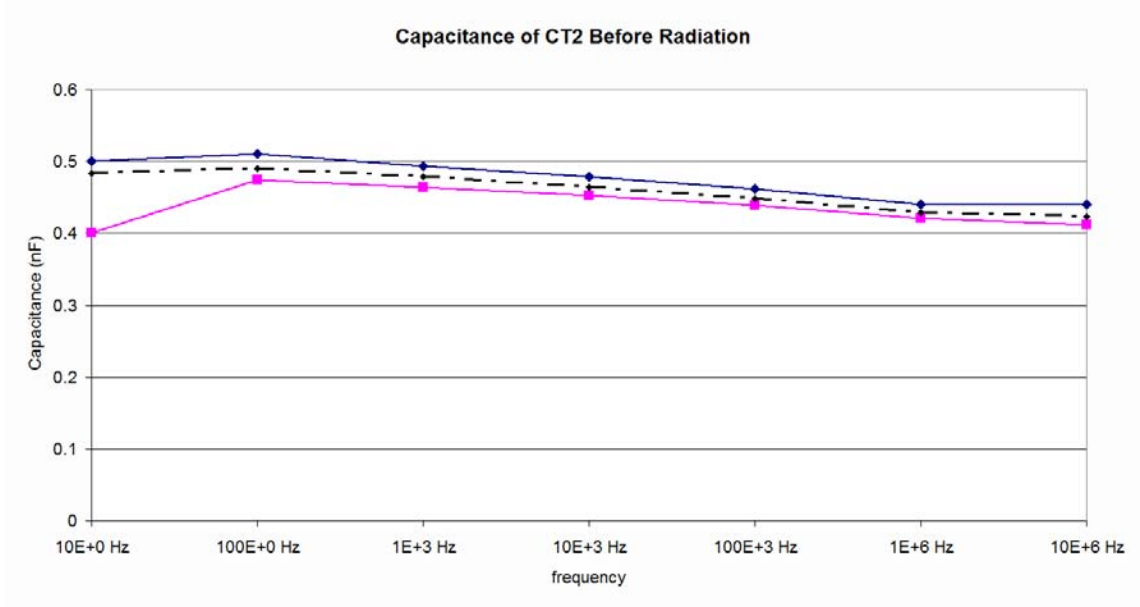# RT1:   Resistor of Type 1 (RS – 484 – 4602) 22MΩ

Capacitance

Figure 8-16 Capacitance of RT1 before irradiation at various frequencies
The high band (in blue) and low band (in magenta) show the absolute maximum and minimum recorded measurement (respectively), while the black line shows the average for all measurements
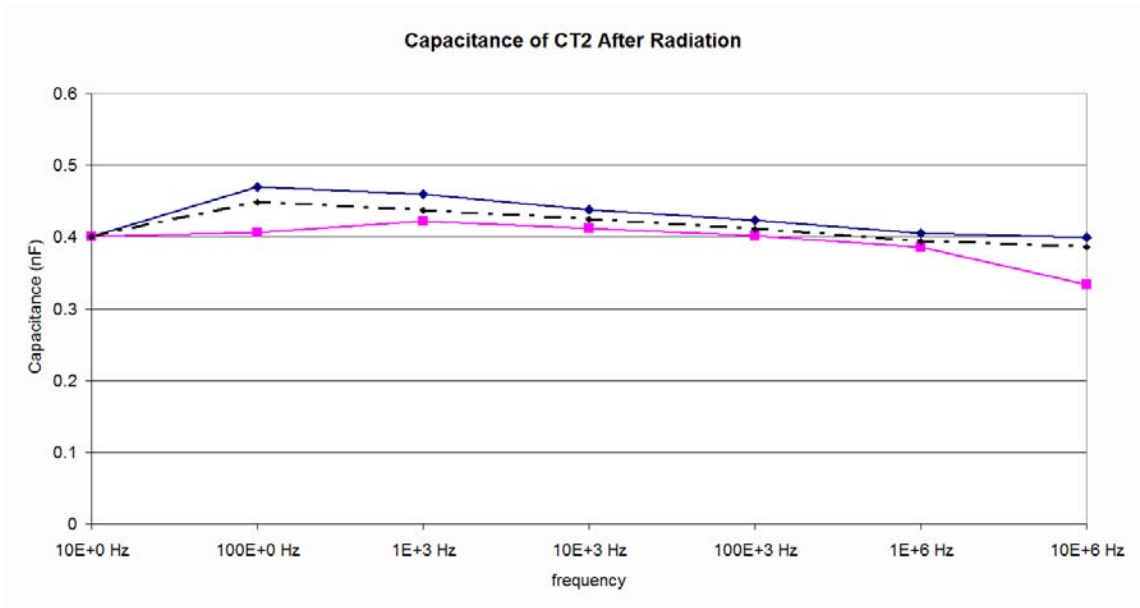

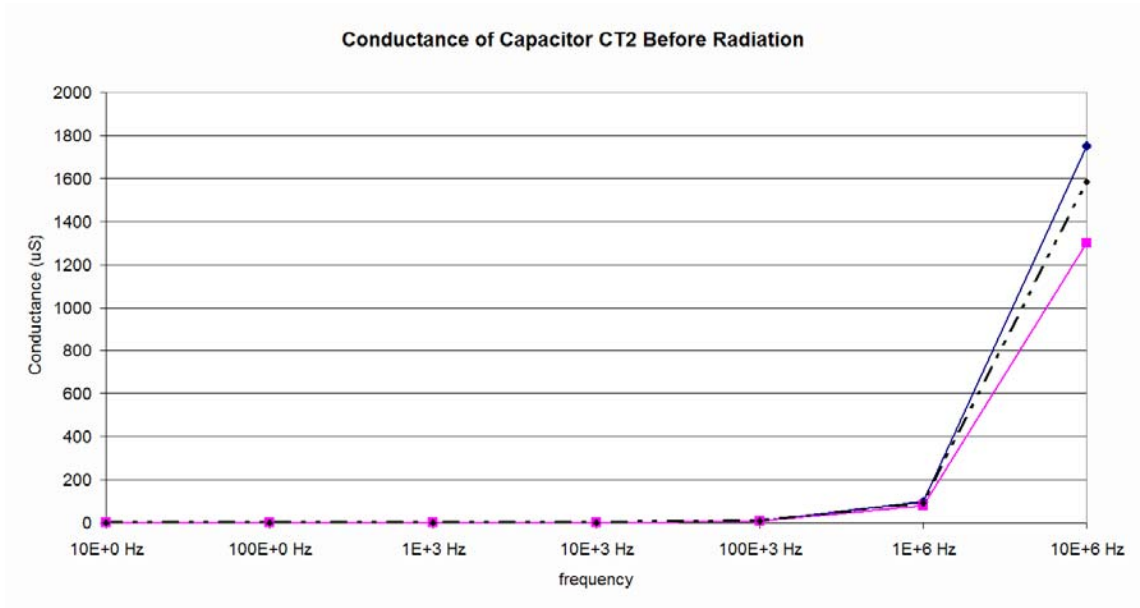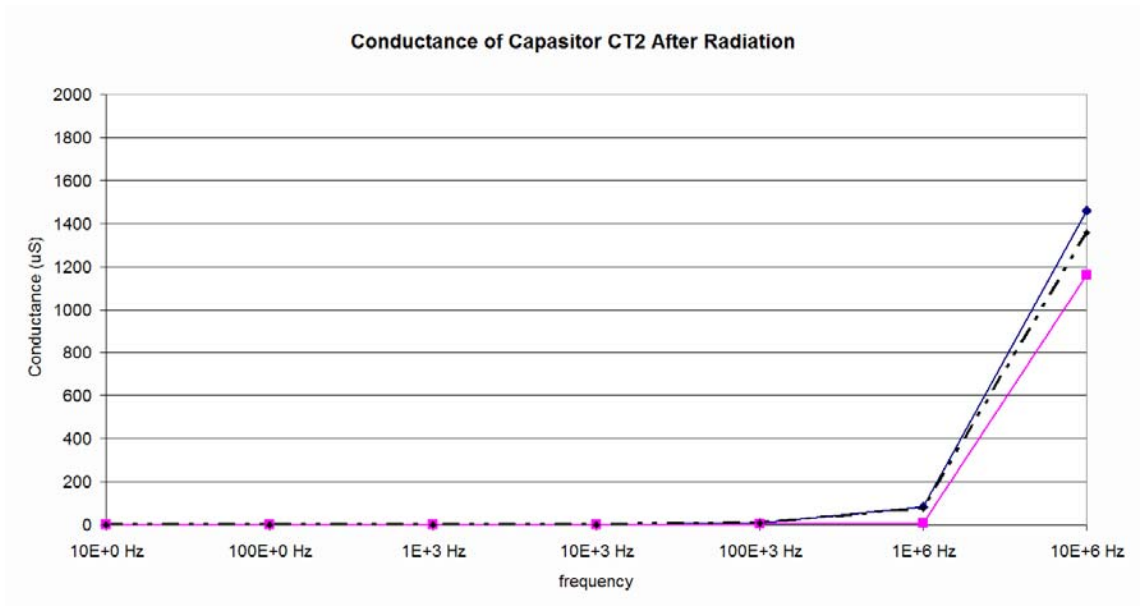**Figure 8-17 Capacitance of RT1 after a radiation dose of 134 kGy at various frequencies**
The high band (in blue) and low band (in magenta) show the absolute maximum and minimum recorded measurement (respectively), while the black line shows the average for all measurements

Conductance

Figure 8-18 Conductance of RT1 before irradiation at various frequencies
The high band (in blue) and low band (in magenta) show the absolute maximum and minimum recorded measurement (respectively), while the black line shows the average for all measurements
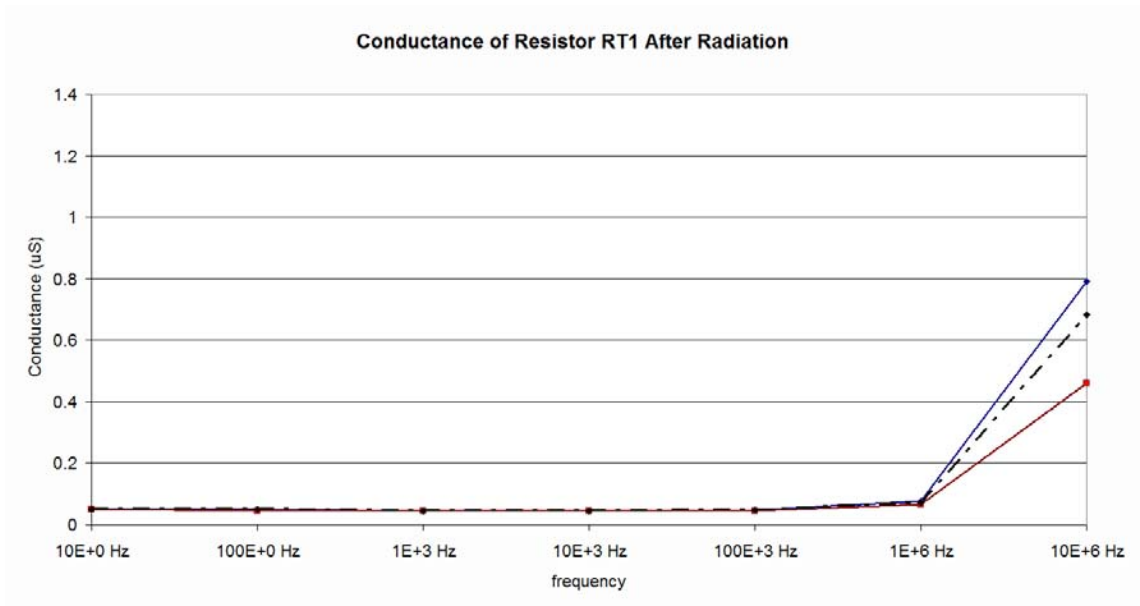
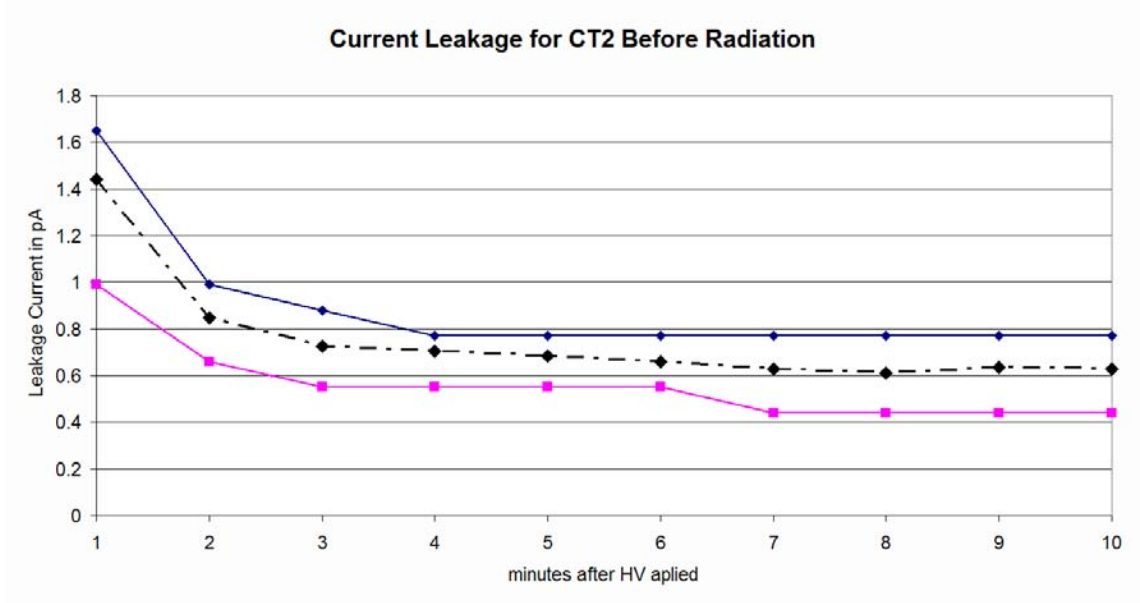**Figure 8-19 Conductance of RT1 after a radiation dose of 134 kGy at various frequencies**
The high band (in blue) and low band (in magenta) show the absolute maximum and minimum recorded measurement (respectively), while the black line shows the average for all measurements

Figure 8-16 and Figure 8-17 show the shunt capacitance across the resistor. Obviously, this component is negligible at very small frequencies since the capacitive impedance behaves effectively as an open circuit. However, at intermediate and high frequencies, the capacitances of these components appear to be constant.

From Figure 8-18 and Figure 8-19 it can be seen that the resistor's conductance has not changed significantly due to irradiation, in addition, Figure 8-16 and Figure 8-17 shows that the small change of the shunt capacitance tends to an improvement. This is confirmed by Table 8-4, which shows that in average the conductance of the 22 MΩ resistor does not change beyond 1% for frequencies less than 1 MHz. The worst case is very similar, except for a single measurement at 100 Hz where it dropped by 10%. Even so, these values are within the specifications and tolerances of the HV filter.

	10 Hz	100 Hz	1 kHz	10 kHz	100 kHz	1 MHz	10 MHz
Average	0.00	1.00	-0.04	0.00	0.00	0.48	3.53
Worst Case	0.00	10.00	0.88	-0.89	0.00	1.15	9.04

Table 8-4 Average and worst case percentage change of conductance for RT1 after a radiation dose of 134 kGy at various frequencies

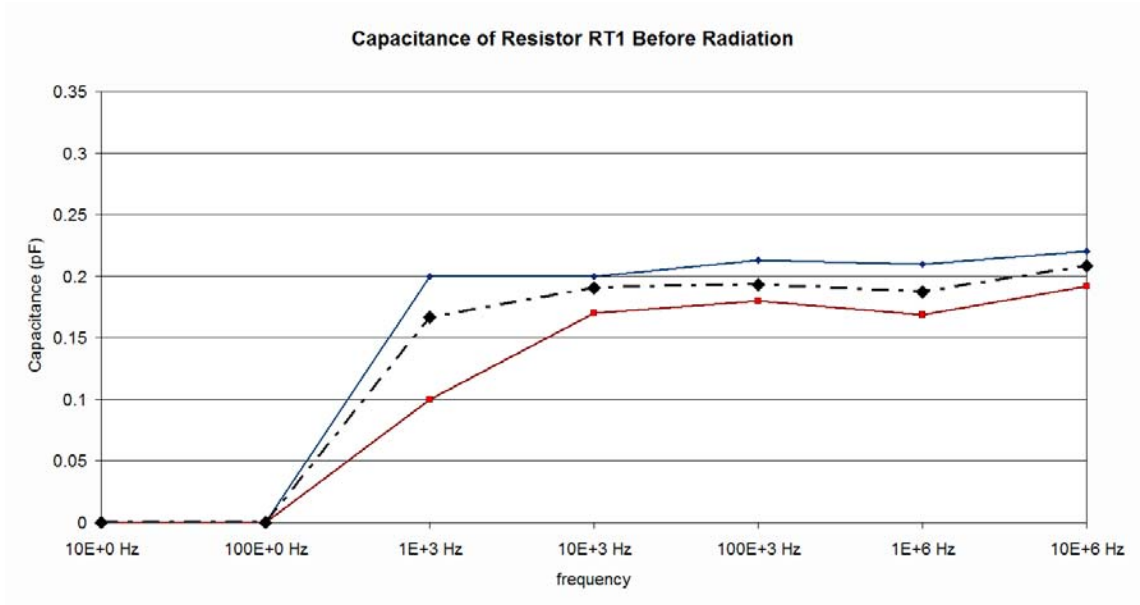# RT2:   Resistor of Type 2 (RS – 135 – 667) 10MΩ

Capacitance

Figure 8-20 Capacitance of RT2 before irradiation at various frequencies
The high band (in blue) and low band (in magenta) show the absolute maximum and minimum recorded measurement (respectively), while the black line shows the average for all measurements
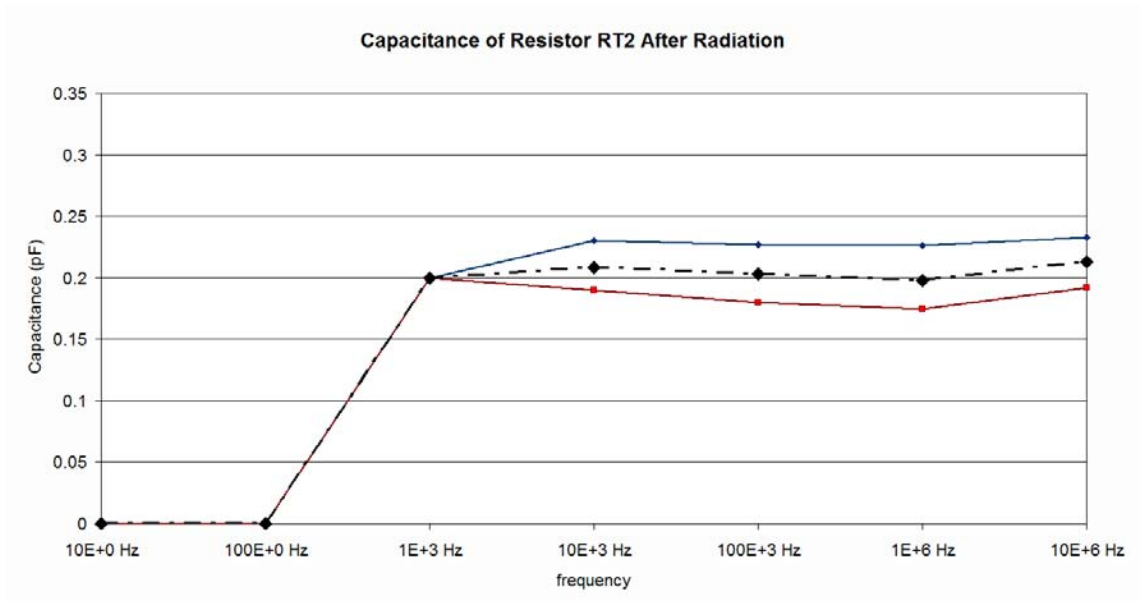
Figure 8-21 Capacitance of RT2 after a radiation dose of 134 kGy at various frequencies
The high band (in blue) and low band (in magenta) show the absolute maximum and minimum recorded measurement (respectively), while the black line shows the average for all measurements
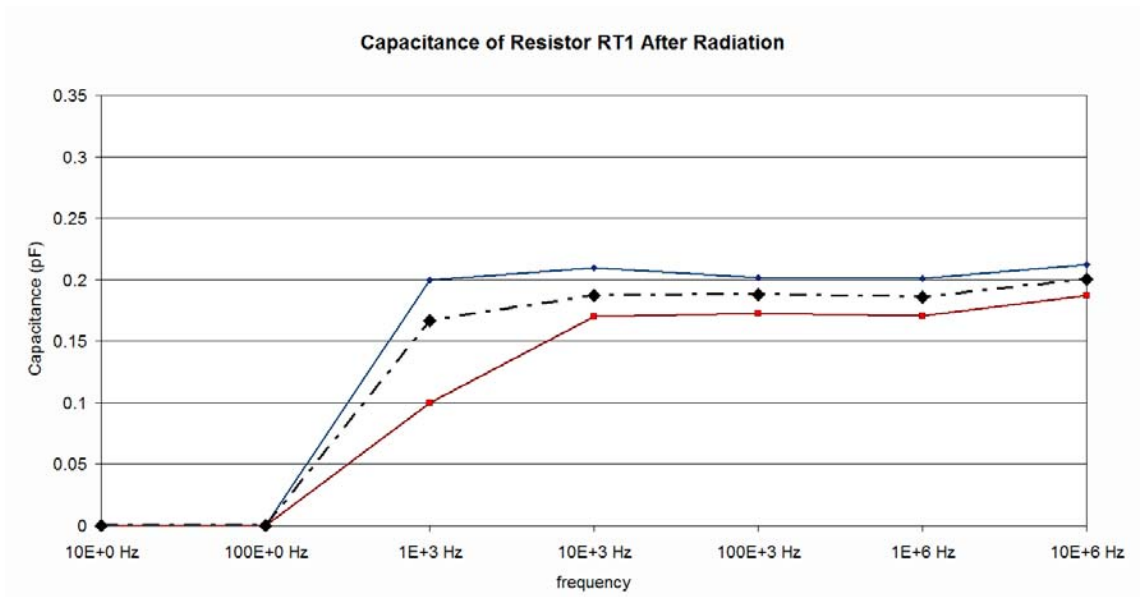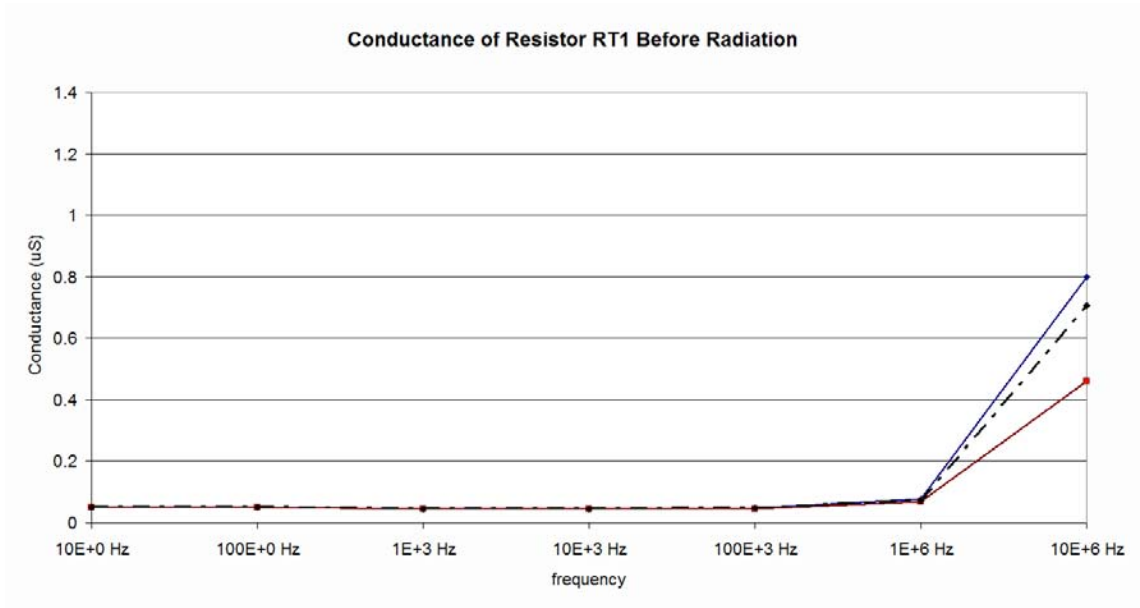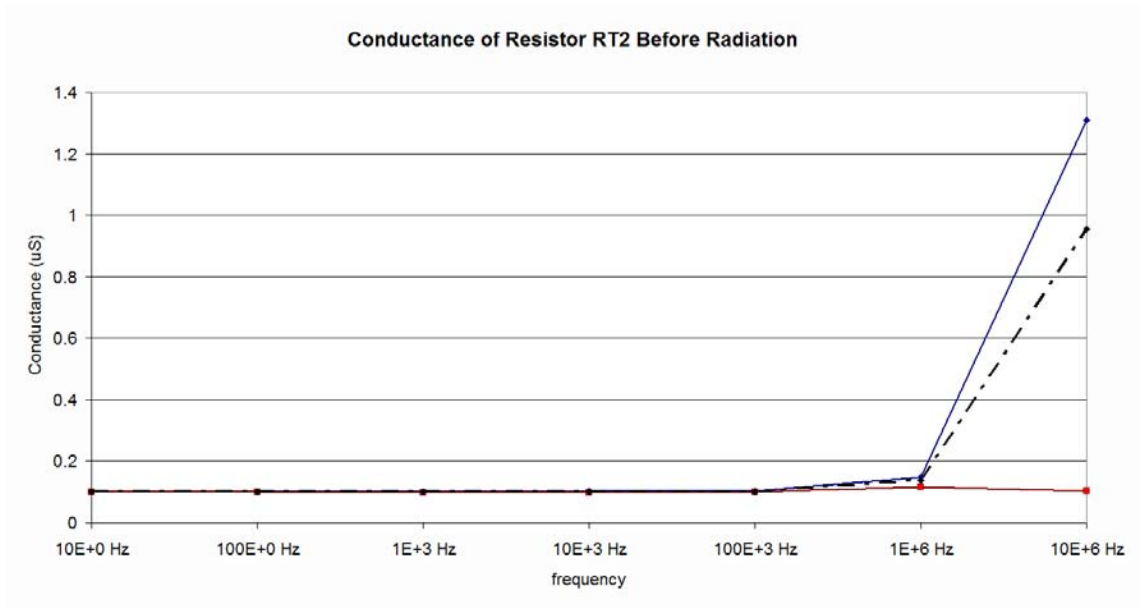
Conductance

Figure 8-22 Conductance of RT2 before irradiation at various frequencies
The high band (in blue) and low band (in magenta) show the absolute maximum and minimum recorded measurement (respectively), while the black line shows the average for all measurements

Figure 8-23 Conductance of RT2 after a radiation dose of 134 kGy at various frequencies
The high band (in blue) and low band (in magenta) show the absolute maximum and minimum recorded measurement (respectively), while the black line shows the average for all measurements

From Figure 8-20 and Figure 8-21 a slight decrease in the shunt capacitance can be seen following irradiation. In addition, if it would not have been because of an anomalous measurement at 1 kHz before irradiation, both charts would be almost identical to each other, proving the consistency of the samples of these resistors.

Figure 8-22 and Figure 8-23 shows the same behaviour on the conductive side of the story. The mean in chart Figure 8-22 clearly shows that the minimum at 10 MHz must have been an anomalous measurement which should be on the line observed in Figure 8-23. This is proven from Table 8-5 where it shows that even the worst case does not exceed 2.06% fro frequencies under 10 MHz. Therefore, it is concluded that these types of resistors are well suited for harsh environments such as the CMS ECAL endcaps.

	10 Hz	100 Hz	1 kHz	10 kHz	100 kHz	1 MHz	10 MHz
Average	0.00	0.00	0.76	0.66	0.65	-0.09	-2.13
Worst Case	0.00	0.00	1.79	1.20	1.75	-2.06	-20.27

Table 8-5 Average and worst case percentage change of conductance for RT2 after a radiation dose of 134 kGy at various frequencies

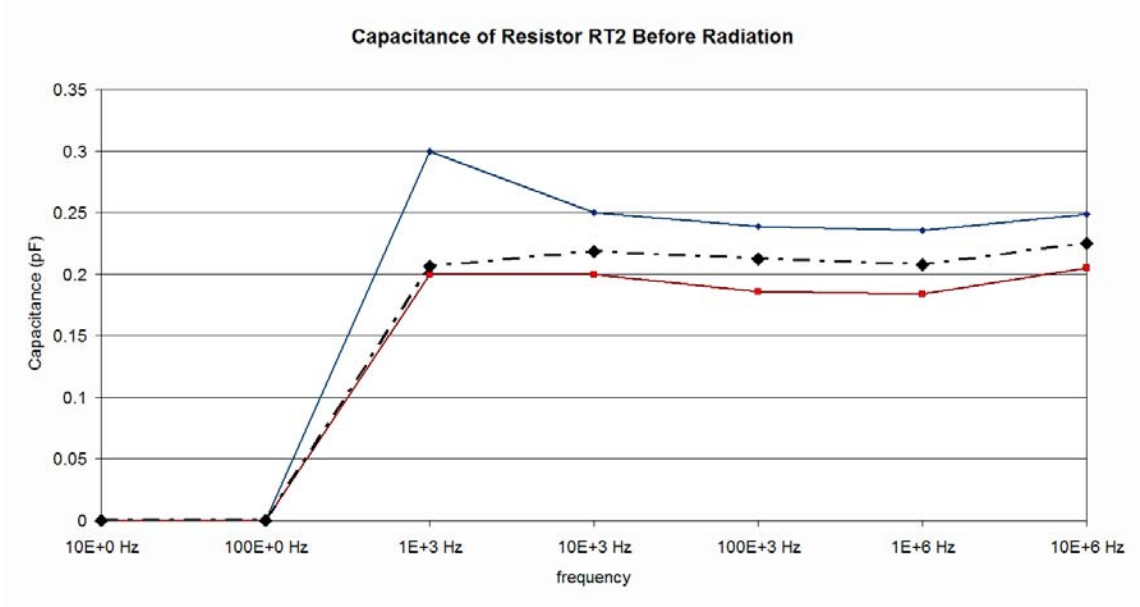# RT3:   Resistor of Type 3 (RS – 131 – 132) 100Ω

Figure 8-24 Conductance of RT3 before irradiation at various frequencies
The high band (in blue) and low band (in magenta) show the absolute maximum and minimum recorded measurement (respectively), while the black line shows the average for all measurements
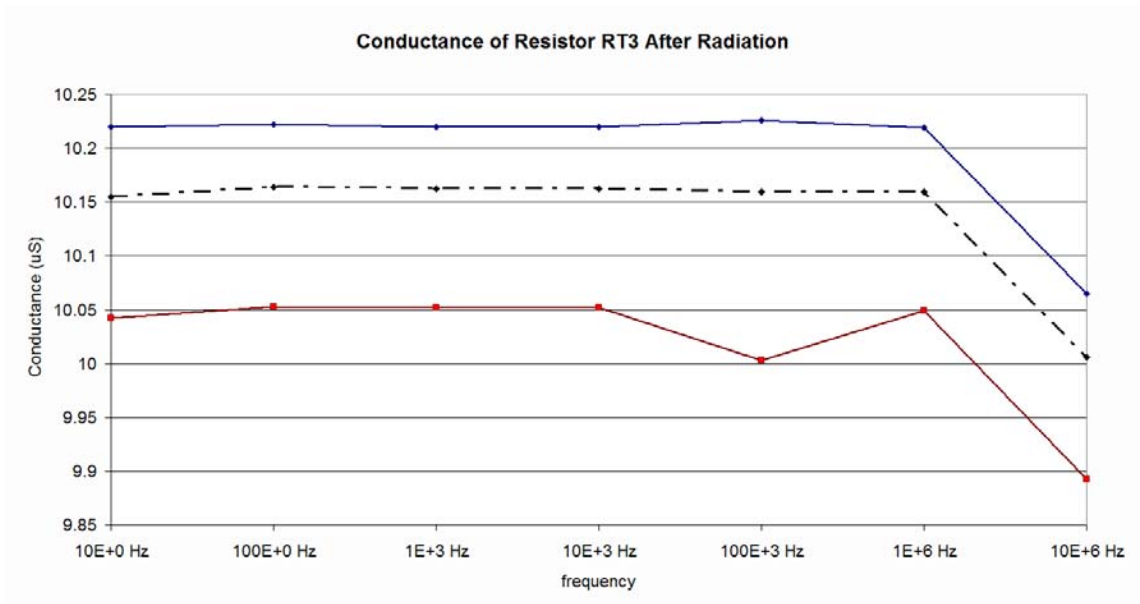
Figure 8-25 Conductance of RT3 after a radiation dose of 136 kGy at various frequencies
The high band (in blue) and low band (in magenta) show the absolute maximum and minimum recorded measurement (respectively), while the black line shows the average for all measurements

As mentioned before, RT3 was an exception to the other resistors. Although for slow frequencies, the impedance model had the reactive component dominated by a parallel capacitance, for frequencies over 10 kHz the reactive component was dominated by a serial inductance.

The measurements in ohms from the serial model were inverted to siemens for consistency.

One of the focal points of the graphs shown is what happens at high frequencies. All the previous cases show that conductance should increase with frequency, which is true for a parallel RC configuration. Whereas frequencies increase, the impedance due to C decreases to a short circuit making the model "more conductive". Since at high frequencies RT3 is more inductive, the impedance increases to an open circuit and hence the model is "less conductive"

The resistors have not change appreciably; and this can be seen from Table 8-6 where even at the worst case the percentage of change does not reach a 0.5%.

	10 Hz	100 Hz	1 kHz	10 kHz	100 kHz	1 MHz	10 MHz
Average	-0.02	-0.03	-0.02	-0.05	0.03	-0.02	-0.01
Worst Case	0.08	-0.05	0.05	-0.34	0.37	0.09	-0.05

Table 8-6 Average and worst case percentage change of conductance for RT3 after a radiation dose of 136 kGy at various frequencies

RT4:   Resistor of Type 4 (RS – 484 - 4595) 10MΩ

Capacitance
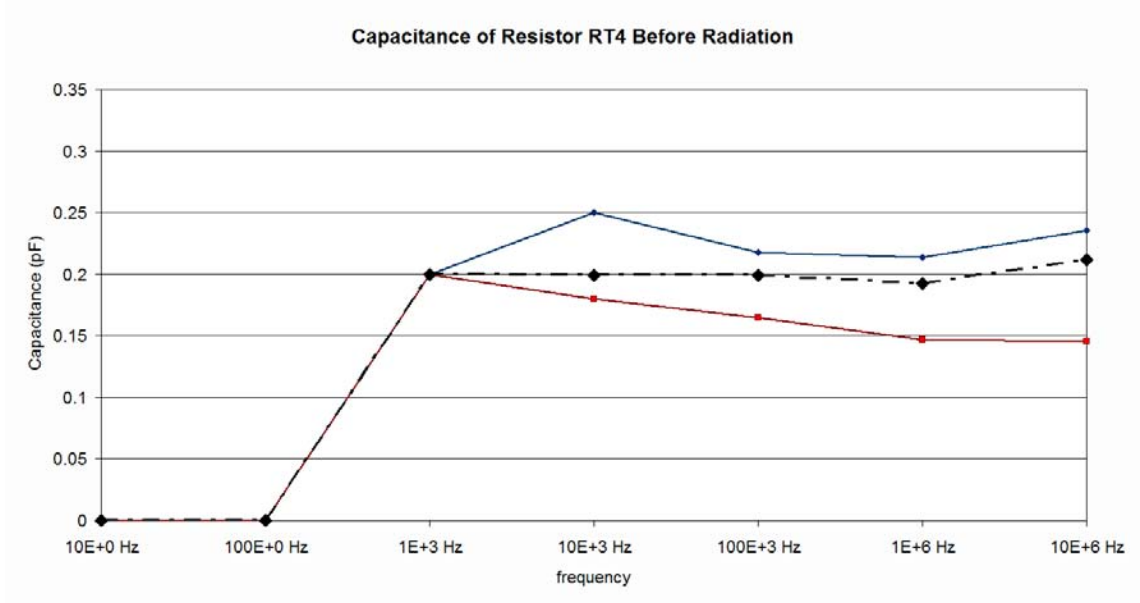
Figure 8-26 Capacitance of RT4 before irradiation at various frequencies
The high band (in blue) and low band (in magenta) show the absolute maximum and minimum recorded measurement (respectively), while the black line shows the average for all measurements
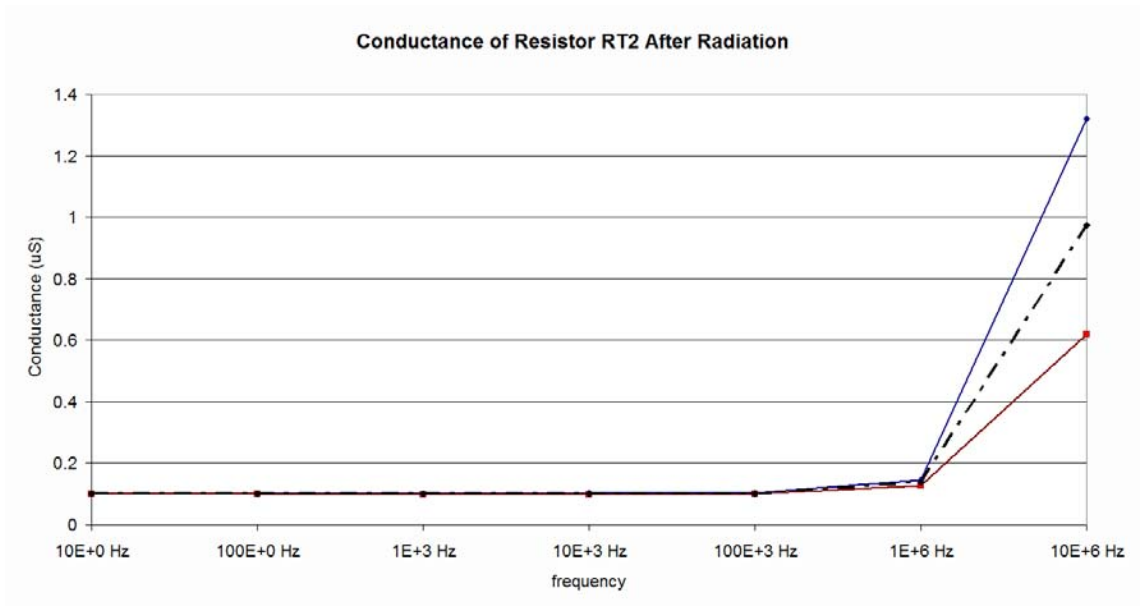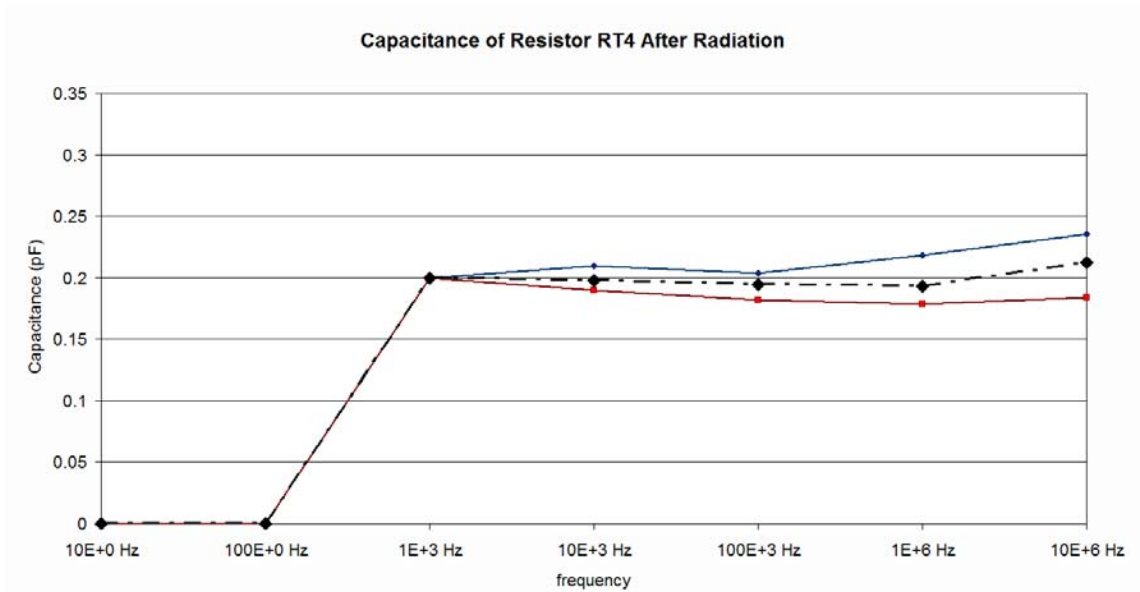

Figure 8-27 Capacitance of RT4 after a radiation dose of 134 kGy at various frequencies
The high band (in blue) and low band (in magenta) show the absolute maximum and minimum recorded measurement (respectively), while the black line shows the average for all measurements

Conductance

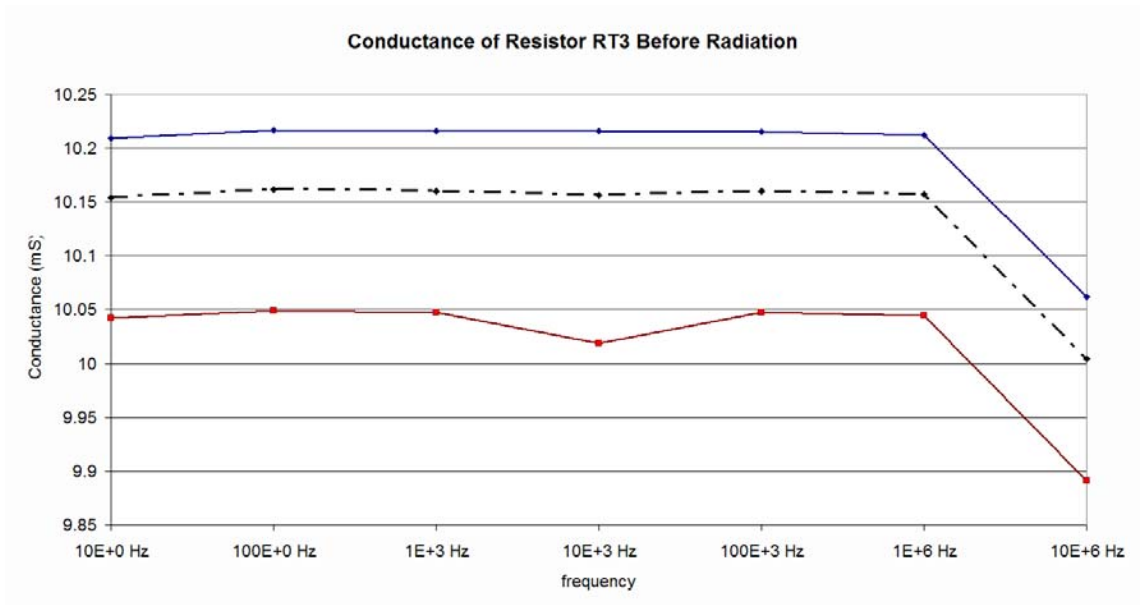**Conductance of Resistor RT4 Before Radiation**
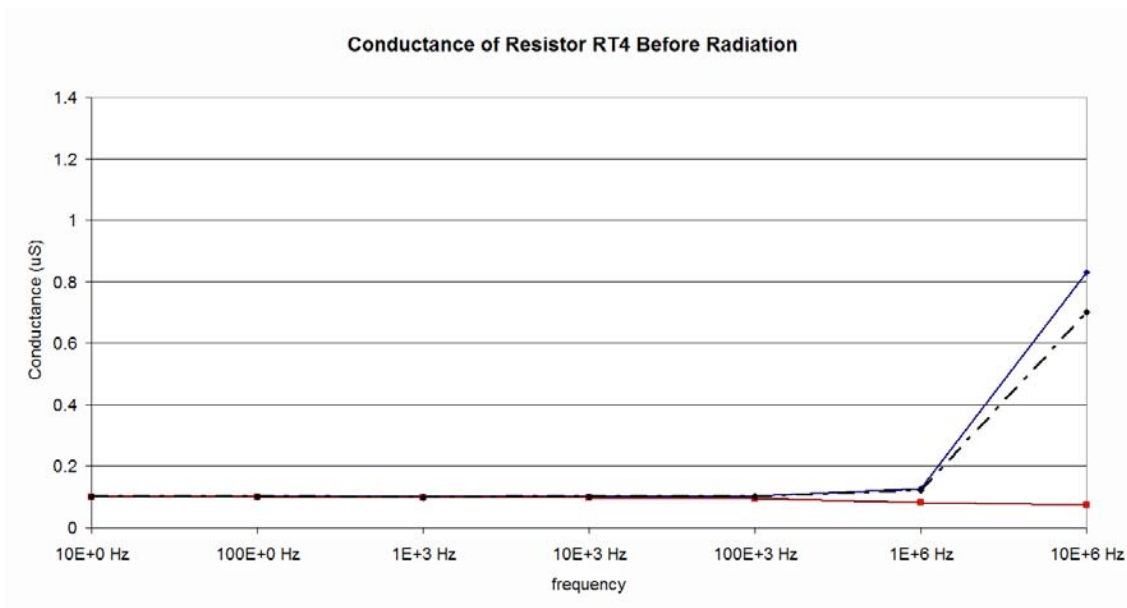
Figure 8-28 Conductance of RT4 before irradiation at various frequencies
The high band (in blue) and low band (in magenta) show the absolute maximum and minimum recorded measurement (respectively), while the black line shows the average for all measurements

Conductance of Resistor RT4 After Radiation
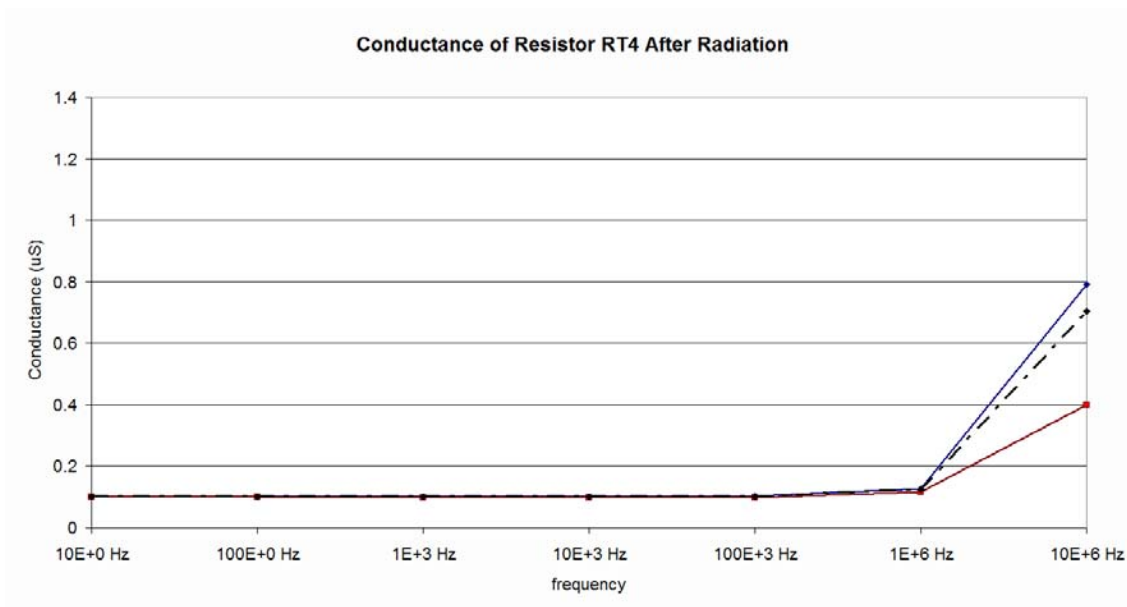
Figure 8-29 Conductance of RT4 after a radiation dose of 134 kGy at various frequencies
The high band (in blue) and low band (in magenta) show the absolute maximum and minimum recorded measurement (respectively), while the black line shows the average for all measurements

RT4 shows also its hardness to radiation as it can be seen from Figure 8-26 and Figure 8-27 where the shunt capacitance is almost unaffected.

The same can be said about the conductance shown in Figure 8-28 and Figure 8-29. This charts show, very little differences between before and after radiation for frequencies less than 1 MHz. By following the relationship of the average with respect off the limiting bands, one can appreciate that due to that the average is very close to the maximum band the minimum band should too. The fact that it does not, means that there were anomalous measurements, which were off the trend. Even though, as it can be seen from Table 8-7 the average percentage change does not reach 2%. For the worst case however, it reaches 10% at high frequencies (1 MHz and 10MHz), other than that, it does not even reach a 1%.

	10 Hz	100 Hz	1 kHz	10 kHz	100 kHz	1 MHz	10 MHz
Average	0.00	0.00	-0.08	0.10	-0.01	-1.27	-1.04
Worst Case	0.00	0.00	-0.82	0.60	-0.50	-10.11	10.33

Table 8-7 Average and worst case percentage change of conductance for RT4 after a radiation dose of 134 kGy at various frequencies

Chapter 9 Conclusions and further work

The work presented in this thesis reports on the development and application of a computer model which simulates the time response of a vacuum phototriode which was developed for the electromagnetic calorimeter of CMS. This thesis also reports on a detailed study of the effect of gamma irradiation on high voltage capacitors and resistors for the VPT HV filter.

The main conclusions from this work are:

SIMION7 as purchased can not fully model a VPT due to its inability to simulate the generation of secondary electrons at a dynode. It also does not simulate the induced current on any electrode caused by charges moving within it. This was overcome by writing an add-on, named SADYS, which was specifically designed to simulate the secondary emission from the dynode and to calculate the anode current induced by the electrons moving through the VPT.

The simulation developed in this work reproduced the basic features of the DC operation of the VPT such as the variation of gain with dynode and anode potential and external magnetic field strength. The simulation also confirmed the previously known experimental result that a fine anode mesh is needed for the device to operate at magnetic fields, in excess of 1 T since the gain is seen to decrease dramatically with the mesh resolution.

The work presented in the experimental chapter represents the first measurements of the response from this type of VPT when excited with a very fast laser pulse. The measured response from the VPT was observed to be fast and quite complex, in spite of the simple geometry of the VPT structure. However, from the simulation one can conclude that the intrinsic speed of the VPT is about a factor of 3 faster than the experimental data. Using a SPICE model which took into account the lead inductances and the inter-electrode

capacitances provided a better agreement between the simulation and the experimental data.

SADYS was developed as a SIMION7 add-on and would be useful in the modelling of photo-tubes with different electrode geometries.

From the measurements made of the effect of gamma radiation on the HV filter components, we can conclude that there are economical alternatives to purpose made radiation hard electronic components. This work demonstrated that low cost commercial off the shelf components can be suitable for electronic systems used in environments where the dose is as high as 300 kGy. As a consequence of these experiments, the batch from which the components were tested was bought and these were used in the 3100 HV filters which were installed in the endcaps of the Electromagnetic Calorimeters of CMS.

Further development of the simulation is desirable since there are still unknown factors which caused the experimentally measured signal to be slower than expected. The following improvements to the simulation should be made:

- Accurately model the electronics from the anode to the scope display in order to obtain the transfer function.

- Model the laser pulse to reproduce the waveform provided by the laser manufacturer (shown in Figures 6-3, 6-4 and 6-5) which corresponds to the actual laser head used in the experiments.

- Port the simulation system to SIMION8. This new version replaces the PRG user program language for LUA[*] and offers greater capabilities. One of these is it can handle multiple files for input/outputs. This will allow separation of the flying electrons for calculation of the signal, from the ones used for the generation of secondary electrons. Because of this, electrons could be flown concurrently (as oppose to one after the other) which means that samples could be taken at the same time, this in turn

---

[*] Capabilities and features of SIMION ™ v 8

would eliminate the complex procedures for interpolating individuals contributions so that they could be added together. Furthermore, this would drastically reduce the data size because it would no longer be required to store each individual sample for each individual electron. The other advantage is that the second generation of electrons could be implemented within SIMION8 as they could be saved on the respective ION file. Allowing the simulation to write to several files, reduces the computer power required to store, read and keep in memory an excessive amount of data which prohibits the producing of a statistically significant high resolution signal.

Appendix A Mesh User Program

; SECONDARY EMISSIONS
; Ignacio Yaselli
; This program Analyses the conditions at which an Ion hits an electrode, in order to
; produce secondary ions.

              ;.........................Variable Definition........................

          defa Counter   0
          defa Lower_T   0.28
          defa Upper_T   0.48
          defa Delta_T   0.000001
          defa Counter   0
          defa IonID   0
;..

;_____
____
              ;//////////////////// Tstep_Ajust \\\\\\\\\\\\\\\\\\\\\\\

;seg Tstep_Adjust

; 2e-3 sto Ion_Time_Step

;exit

;_____
____
              ;//////////////////// OTHER_ACTIONS \\\\\\\\\\\\\\\\\\\\\\\
Seg Other_Actions

          ;------------- Selecting When to record Ions in Flight --------------
          rcl Ion_Splat
          X!=0 goto StopTracking   ; If Splat is not 0 the Ion is not
                                          ; flying.

; This segment will check if the current coordinates in the X axis falls
; within two limits. Previous_X, and Next_X the aim is to establish
; recordings at each Delta_X and to avoid over sampling

      rcl Ion_Time_of_Flight   ; Check if Previous_T < TOF < Next_T
      rcl Upper_T X<Y exit   ; if not in region then exit
      RLUP
      rcl Lower_T X>Y exit

```
        RLUP ;RLUP                              ; Px is within Region

   lbl CalcRegion

RLUP ; RLUP
rcl Upper_T rcl Delta_T + sto Upper_T RLUP   ;Calculate the next Region:
                                             ;Upper_T' = Upper_T + Delta_T


rcl Lower_T rcl Delta_T + sto Lower_T RLUP
;Lower_T' = Lower_T + Delta_T
0 sto ElectrodeHit RLUP

rcl Counter 1 + sto Counter RLUP
;mess ; # #  ****
goto Analysis                                ;Start Analysis.

;end of inflight selection

;--------------------------------- The Electron has hit an Electrode  ---------------------
-------
lbl StopTracking
         rcl Ion_Splat
         1 CHS X=Y goto Hit_Electrode   ; Has hitted an electrode
         0 sto ElectrodeHit RLUP        ;No Electrode HIt
         goto Analysis
         exit

         lbl Hit_Electrode
                 ;Mess ;Anode
                 1 sto ElectrodeHit RLUP


         lbl Analysis
         Go_Subroutine Calc_Energy      ; Also Calculates Azimuth and
Elevation
                                        ; angles
         Go_Subroutine WriteIon         ;Write description of Ion
         goto End_Other_Actions         ;finish
         ; end of Hit_Electrode
;_____
____

                          ;SUB-ROUTINES
;_____
____
             ;...........................Calculate Ion's Current Energy........................
lbl Calc_Energy
         RLUP
         RLUP
          rcl Ion_Vz_mm                 ; Recall Speed Vectors
          rcl Ion_Vy_mm
```

```
                rcl Ion_Vx_mm
                >P3D
                sto Speed RLUP                  ; Save Speed
                sto Azimuth RLUP                ; Save Azimuth Angle
                sto Elevation RLUP              ; Save Elevation Angle
                rcl Ion_Mass
                rcl Speed
                Speed_to_Kinetic_Energy         ;Transform Mass and Speed to
                                                ;Kinetic_Energy
                sto Current_Energy RLUP

                RLUP                            ; Clear Stack
             rtn
             ;end Calc_Energy
.**********************************************************************************
'                                      *
              ;.............................Recording Format.........................
; There are only 10 RPN Registers so the output which has more than 10 values
has
; to be split
; What is Important is that the order of the output follows as:
; TOB  MASS   CHA  X  Y   Z  AZ  EL  KE  CWF  COLOR  TOF
ELECTRODE
;so that ION-ator reads the correct value

      lbl WriteIon
             ;Mess                           ;%
             rcl Azimuth                     ;AZ
             rcl Ion_Pz_mm                   ;Z
             rcl Ion_Py_mm                   ;Y
             rcl Ion_Px_mm                   ;X
             rcl Ion_Time_of_Birth           ;TOB

                      ;TOB      X         Y          Z          AZ
             Mess ;      #       #        #          #          #

             rcl Ion_Vx_mm                   ; Vx
             rcl Ion_Number                  ;IonID
             rcl ElectrodeHit                ;Which was the electrode hit?
             rcl Ion_Time_of_Flight          ;TOF
             rcl Current_Energy              ;KE
             rcl Elevation                   ;EL

                      ;EL     KE      TOF      ELECTRODE      IonID
             Mess       ;#      #       #          #             #

             ;rcl ElectrodeHit
             ;MARK
      rtn
```

```
;*************************************************************************************
                                                          *
lbl End_Other_Actions
exit
;by Ignacio Yaselli
```

```
;*************************************************************************************
                                                          *
lbl End_Other_Actions
exit
;by Ignacio Yaselli
```

Appendix B Pseudo VPT User Program

; SECONDARY EMISSIONS
; Ignacio Yaselli
; This program Analyses the conditions at which an Ion hits an electrode, in order to
; produce secondary ions.

;.........................Variable Definition........................

```
defa Counter        0
defa Lower_T        0.28
defa Upper_T        0.48
defa Delta_T        0.000001
defa Counter        0
defa IonID          0
```

;_____

*;//////////////////// Tstep_Ajust *

;seg Tstep_Adjust

; 2e-3 sto Ion_Time_Step

;exit

;_____

*;//////////////////// OTHER_ACTIONS *

Seg Other_Actions

;----------------------- ------ Set Initial Parametres for flight Recording ---------------------

```
    rcl IonID                ; Compater The current Ion number with last
used
    rcl Ion_Number           ;if they are equal, do not reset the recording
steps
    x=y goto StartSelecting   ;if current Ion number is not the one in use,
    sto IonID rlup           ; then use the current Ion and reset recording
step


    rcl Ion_Time_of_Flight   ;TOF
```

```
        rcl Delta_T 2 / + sto          Upper_T
        rcl Delta_T -  sto             Lower_T
        RLUP
        ;mess            ;# # #
```

lbl Continue rlup rlup

```
        ;------------- Selecting When to record Ions in Flight --------------
            rcl Ion_Splat
            X!=0 goto StopTracking             ; If Splat is not 0 the Ion is not
                                               ; flying.
```

; This segment will check if the current coordinates in the X axis falls
; within two limits. Previous_X, and Next_X the aim is to establish
; recordings at each Delta_X and to avoid over sampling

```
        rcl Ion_Time_of_Flight                 ; Check if Previous_T < TOF <
Next_T
        rcl Upper_T X<Y exit                   ; if not in region then exit
        RLUP
        rcl Lower_T X>Y exit
        RLUP ;RLUP                              ; Px is within Region
```

  lbl CalcRegion

RLUP ; RLUP
rcl Upper_T rcl Delta_T + sto Upper_T RLUP   *;Calculate the next Region:*
                                             ;Upper_T' = Upper_T + Delta_T

rcl Lower_T rcl Delta_T + sto Lower_T RLUP
;Lower_T' = Lower_T + Delta_T
0 sto ElectrodeHit RLUP

rcl Counter 1 + sto Counter RLUP
;mess ; # # ****
goto Analysis   *;Start Analysis.*

;end of inflight selection

;---------------------------------- The Electron has hit an Electrode ---------------------
----
lbl StopTracking
```
        rcl Ion_Splat
        1 CHS X=Y goto Hit_Electrode   ; Has hitted an electrode
        0 sto ElectrodeHit RLUP        ;No Electrode HIt
        goto Analysis
        exit
```

```
        lbl Hit_Electrode
                ;Mess ;Anode
                1 sto ElectrodeHit RLUP

        lbl Analysis
        Go_Subroutine Calc_Energy        ; Also Calculates Azimuth and
Elevation
                                         ; angles
        Go_Subroutine WriteIon           ;Write description of Ion
        goto End_Other_Actions           ;finish
        ; end of Hit_Electrode
;_____
____

                            ;SUB-ROUTINES
;_____
____
            ;...........................Calculate Ion's Current Energy.........................
lbl Calc_Energy
        RLUP
        RLUP
         rcl Ion_Vz_mm                   ; Recall Speed Vectors
         rcl Ion_Vy_mm
         rcl Ion_Vx_mm
         >P3D
         sto Speed RLUP                  ; Save Speed
         sto Azimuth RLUP                ; Save Azimuth Angle
         sto Elevation RLUP              ; Save Elevation Angle
         rcl Ion_Mass
         rcl Speed
         Speed_to_Kinetic_Energy         ;Transform Mass and Speed to
                                         ;Kinetic_Energy
         sto Current_Energy RLUP

         RLUP                            ; Clear Stack
        rtn
        ;end Calc_Energy
;************************************************************************************
                                      *
            ;...........................Recording Format.........................
; There are only 10 RPN Registers so the output which has more than 10 values
has
; to be split
; What is Important is that the order of the output follows as:
; TOB  MASS   CHA  X  Y   Z  AZ  EL  KE  CWF  COLOR TOF
ELECTRODE
;so that ION-ator reads the correct value

    lbl WriteIon
        ;Mess                           ;%
```

```
        rcl Azimuth                    ;AZ
        rcl Ion_Pz_mm                  ;Z
        rcl Ion_Py_mm                  ;Y
        rcl Ion_Px_mm                  ;X
        rcl Ion_Time_of_Birth          ;TOB


                ;TOB      X        Y        Z        AZ
        Mess ;    #       #        #        #        #


        rcl Ion_Vx_mm                  ; Vx
        rcl Ion_Number                 ;IonID
        rcl ElectrodeHit               ;Which was the electrode hit?
        rcl Ion_Time_of_Flight         ;TOF
        rcl Current_Energy             ;KE
        rcl Elevation                  ;EL


              ;EL     KE      TOF     ELECTRODE    IonID
        Mess    ;#      #       #          #           #


        ;rcl ElectrodeHit
        ;MARK
    rtn
.**********************************************************************************
'                                       *

lbl End_Other_Actions
exit
;by Ignacio Yaselli
```

Appendix C How to use the SIMION7 VPT Simulation

This chapter aims to help the reader to successfully operate the SIMION7 software for simulating the VPT. Please note that this is an application specific guide and that if further developments are required, then I would advice you to read the SIMION7 user guide.

Main Simulation Settings

SIMION7 Starts with a "Main Menu Screen".

The first thing to do here is to allocate memory for all the possible electrons that will be generated. If we consider 100 initial photoelectrons and a dynode with a mean gain of 20, then we can assume that a decent estimate of the number of electrons that will be flown is around 1500 at maximum. (It is not impossible to exceed this number, but as they use space, the trade off is between memory consumption and performance.) Should this maximum be exceeded, the extra Ions will be discarded, thus the signal will not be in accordance with the initial number of hits.
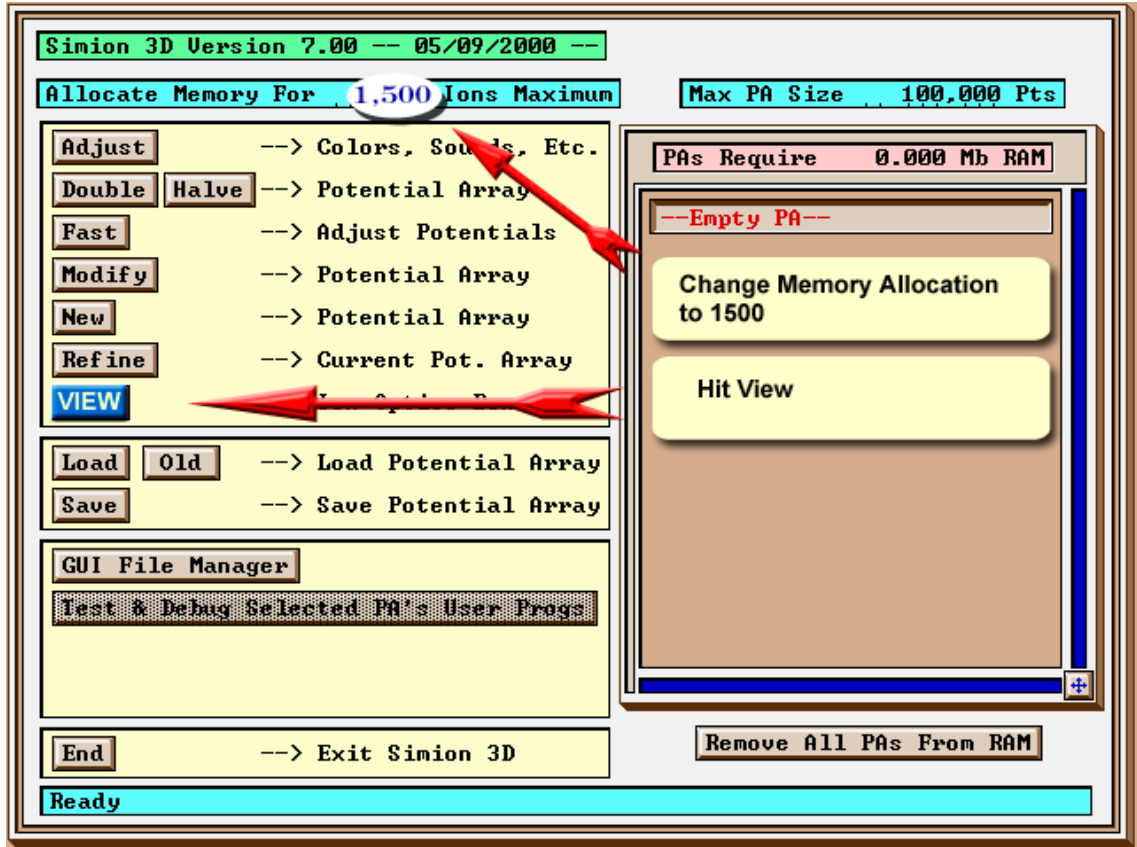
Once, ready, depress the View button, to load the file with all the potential arrays known as the Ion Optics Workbench File .IOB.

The GUI file manager will open and load all the folders on the drive. (This might take some time, depending on the amount of folders you have in your drive.)

A note about this: SIMIION7 attempts to read every folder in your drive, however, as it is in most cases, the number of folder exceeds the amount SIMION7 can handle, and therefore it will not read from certain point. I had to compensate for this by creating a folder on the root directory in which to pout my SIMION7 files into. Most Importantly, this folder had to have a name I was

sure it would be within the first folders, so I prefixed my SIMION7 project folder with the number 0, thus my working folder was: "c:\0 My SIMION7 Projects".

The GUI File Manager looks like the figure below. Select the working directory fro the "Root Tree" and then select the simulation mode for the VPT (RealVPT for non magnetic simulations, and RealVPTMagnetic for Magnetic Simulation). The difference on the modes is of course the presence of a magnetic field. Let's assume for the moment, that we are not interested on a magnetic field interaction; therefore, by choosing the non magnetic mode, we save memory as oppose to selecting the magnetic mode and setting the B field to 0.
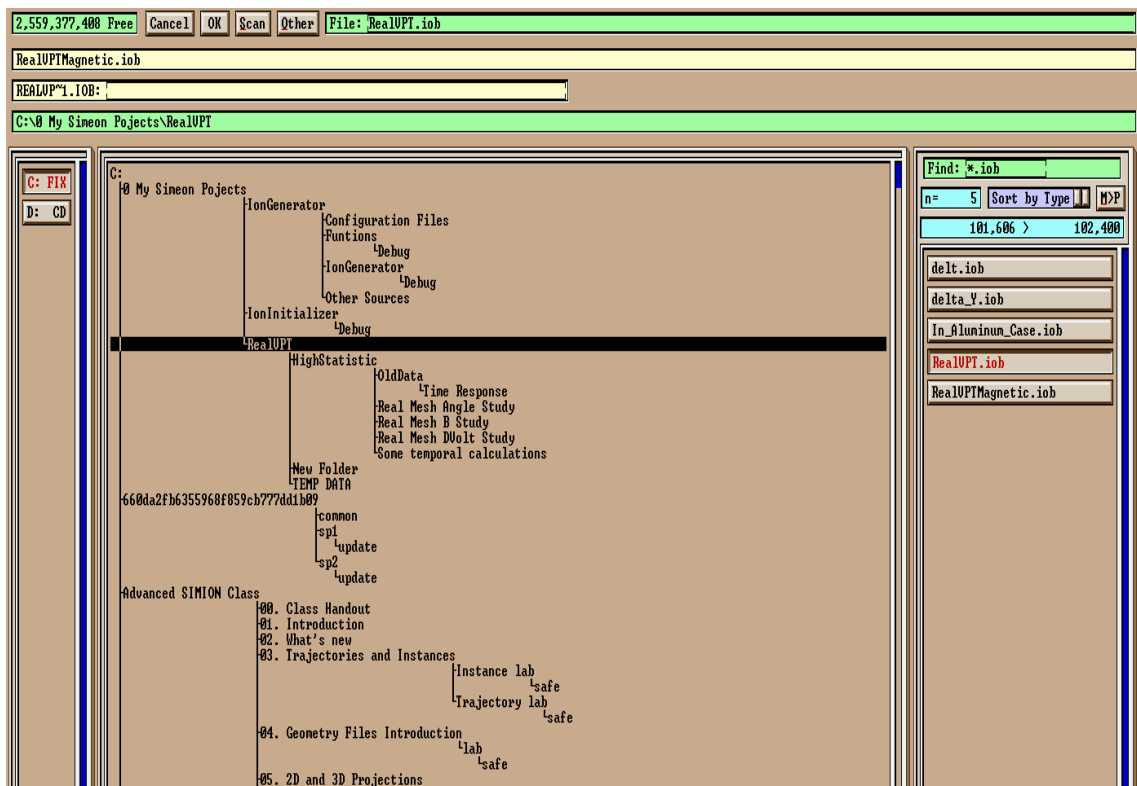
After pressing "OK" all the necessary files and potential arrays will open, and so will so the "View Screen".
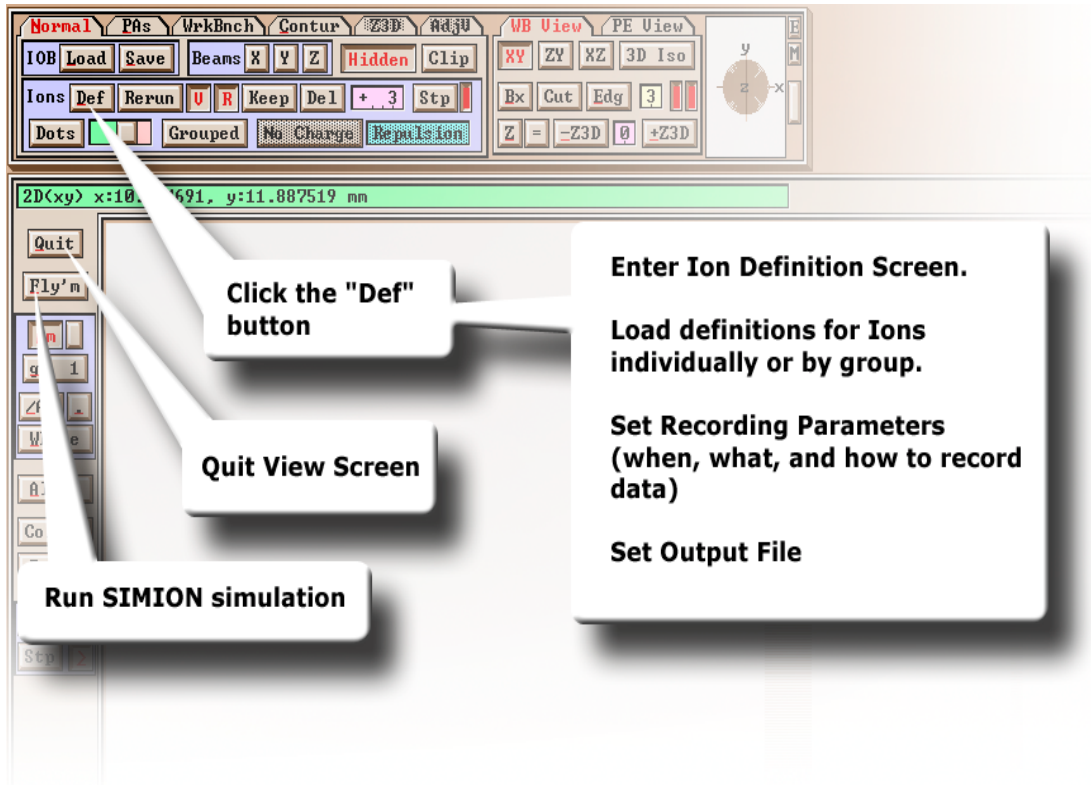

In this screen there are 3 main buttons to control the simulation. The Ion Definition, for setting and loading Ions definition, as well as controlling data recording; the Fly'm button which starts the simulation (requires preloading of ions) and the Quit button for, when simulation is finished.

Depress the "Def" button to enter the Ion Definition Screen, which looks like the figure below.
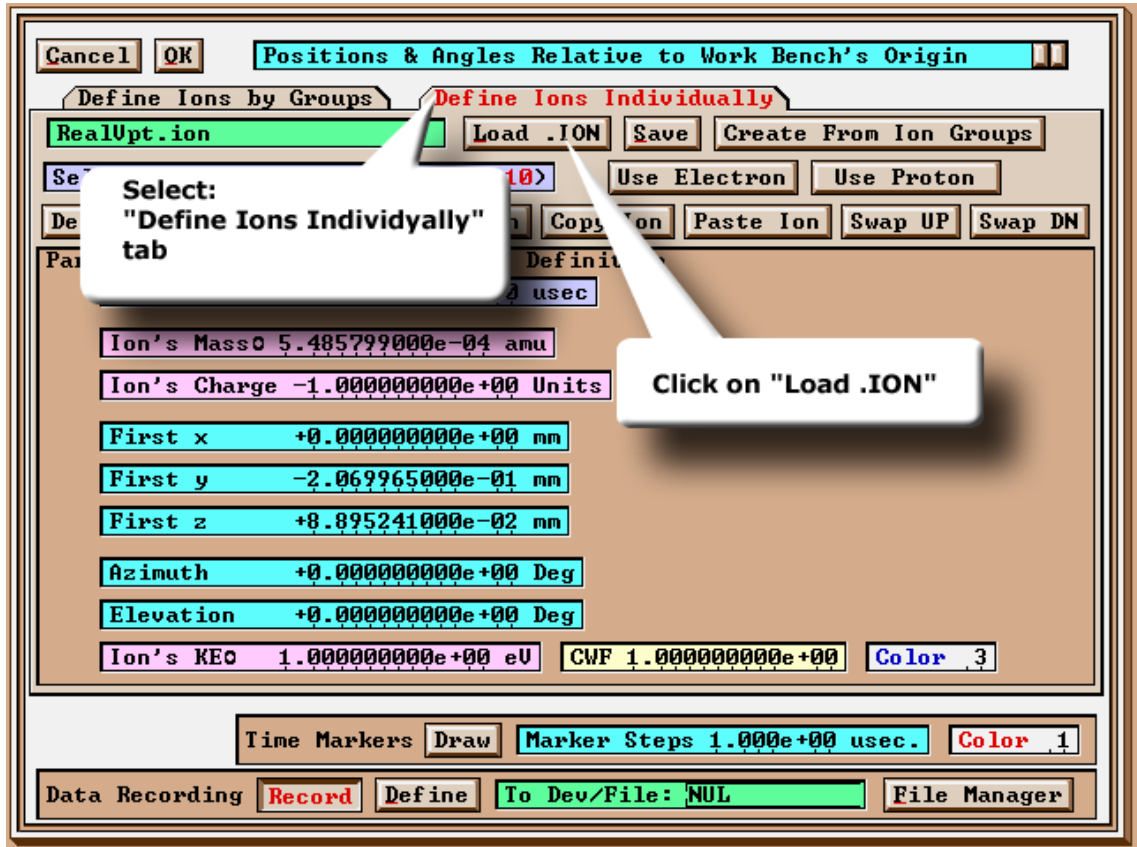
There are two ways of how to define a set of ions; the first one is to define a group of related ions, and the second for defining the ions, unrelated to each other. The chosen method is the latter, as it allows a third party program to generate the ion definition file.

Make sure the "Define Ions Individually" tab is selected, and depress the "Load .ION" button to load a previously generated .ion file.
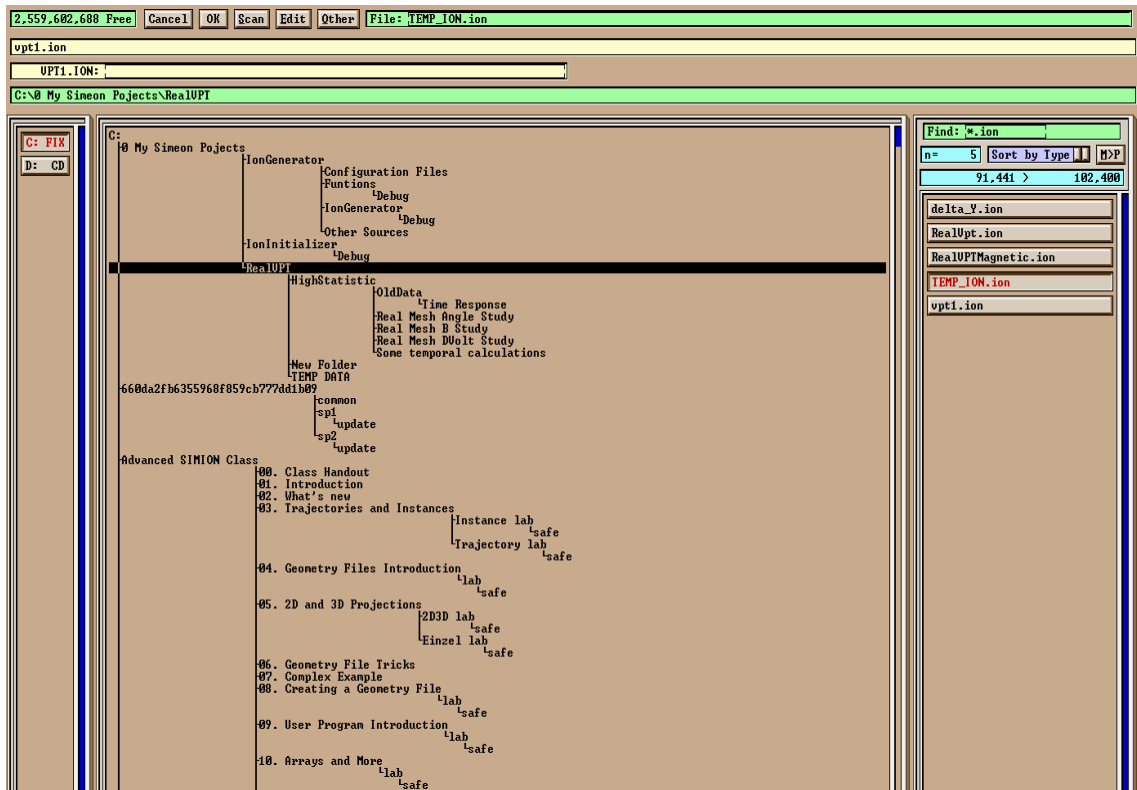
Select the running project using the same principles as when choosing the IOB file. This example is using a project called "TEMP" which creates a file called TEMP_ION.ion. As it will be explain later, the whole simulation system uses different naming for different projects, mainly because SIMION7 files must all be kept on the same folder as the working folder.
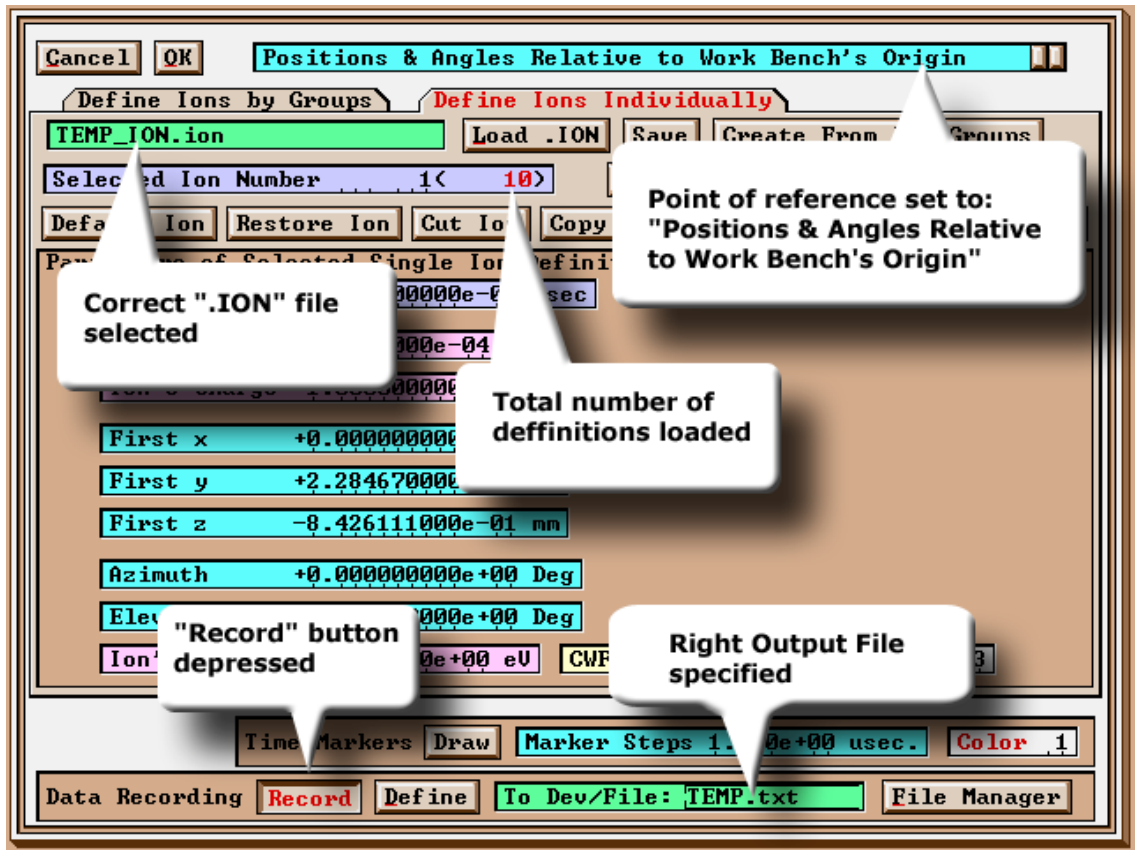
On returning to the Ion Definition Screen, it should make sure that:

- The point of reference is Work Bench Origin. (Each PA could act as a point of reference; however, this should be set prior the definition of the ions.)
- The correct .ion file was loaded
- The Record Button is depressed
- An output file has been entered, and matches the file to be read by the third party program.

Once all this have been satisfied press "OK" to return to the VIEW screen.

SIMION7 is now ready for flying the defined IONS, and it will do so when the

"Fly'm" button gets depressed.

At this points, the "PA User Programs" get compiled, and a variable window, as bellows, opens awaiting for confirmation of the predefine values.
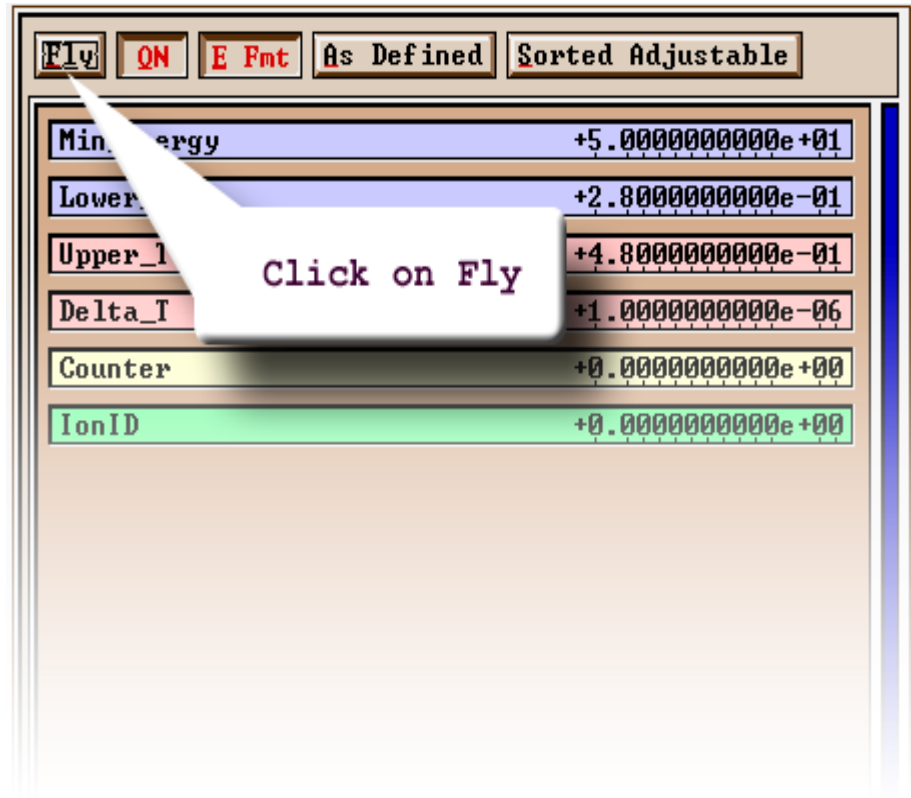
Hit the "Fly" button on the variable windows to accept these values and it will possible to see the ions flying from the Cathode.
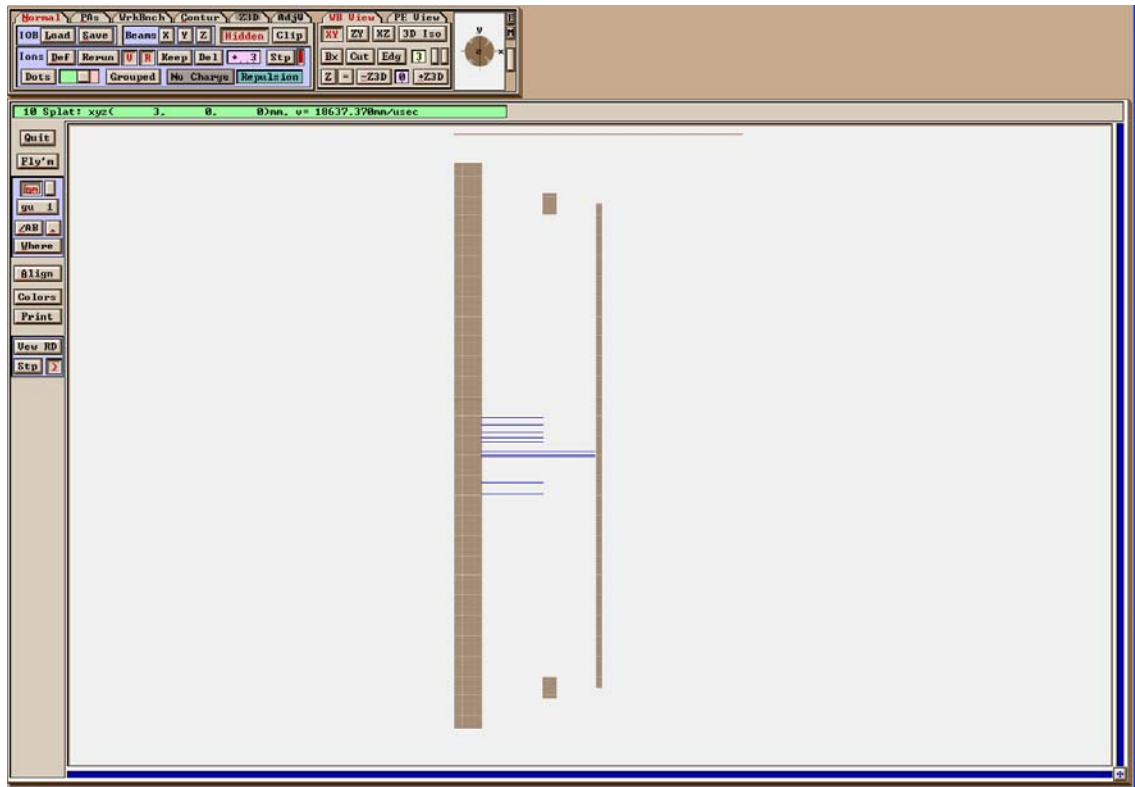
While the simulation is running, the number of splats will increase to that of the total ions simulated. When it stops, the third party software should be made to run, so as to analyse the data gained form the SIMION7 Simulation, and generate further set of Ions if appropriate.

After this, the operations should be repeated from step x, until no further ions are to be flown.

How to use the SIMION VPT SIMULATION

Modify Biasing Voltage

Studying the effects of changes in the electric field between the electrodes of the VPT it is just a case of Adjusting the Potential Arrays (PA), for this SIMION7 has a convenient function called "Fast Adjust" (conveniently enough). This function is tied to each of the instances independently (modifies the potential of one instance without affecting the others).
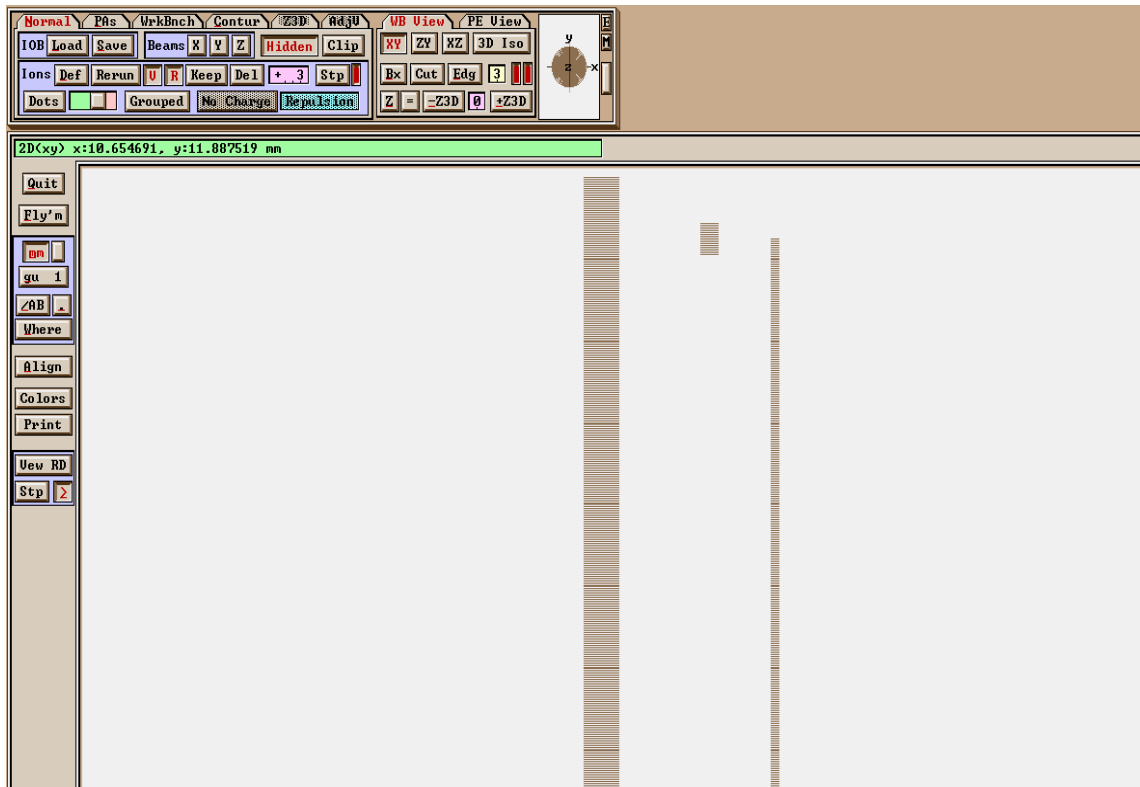
On the View Screen, click on the PAs tab and select the instance to modify[*] , and then click on the "Fadj" button. That will make the Fast Adjust screen to open.

---

[*] Refer to using the mouse
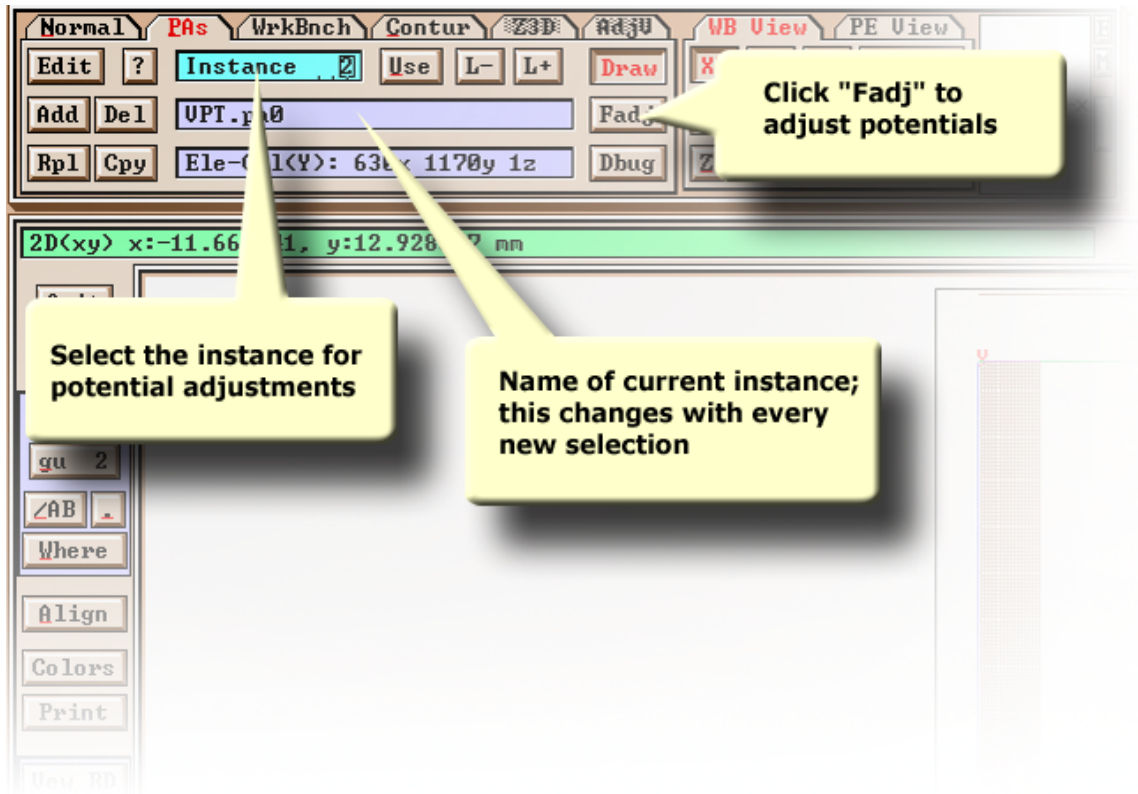
This screen shows the electrode that the instance has, and a respective box with the identification number and the value of the potential (in Volts) of the corresponding electrode. Changing the value in the box will result on the box to change colour.   Click the "Fast Adjust PA" button to make the changes permanent; otherwise, click on "cancel"[†]. SIMION7 will then return to the View screen.

[†] Note: Fast Adjust will only be accepted if there is a change on the values (at least one of the boxes are red) and it will result in an error message if these values have not been modified.
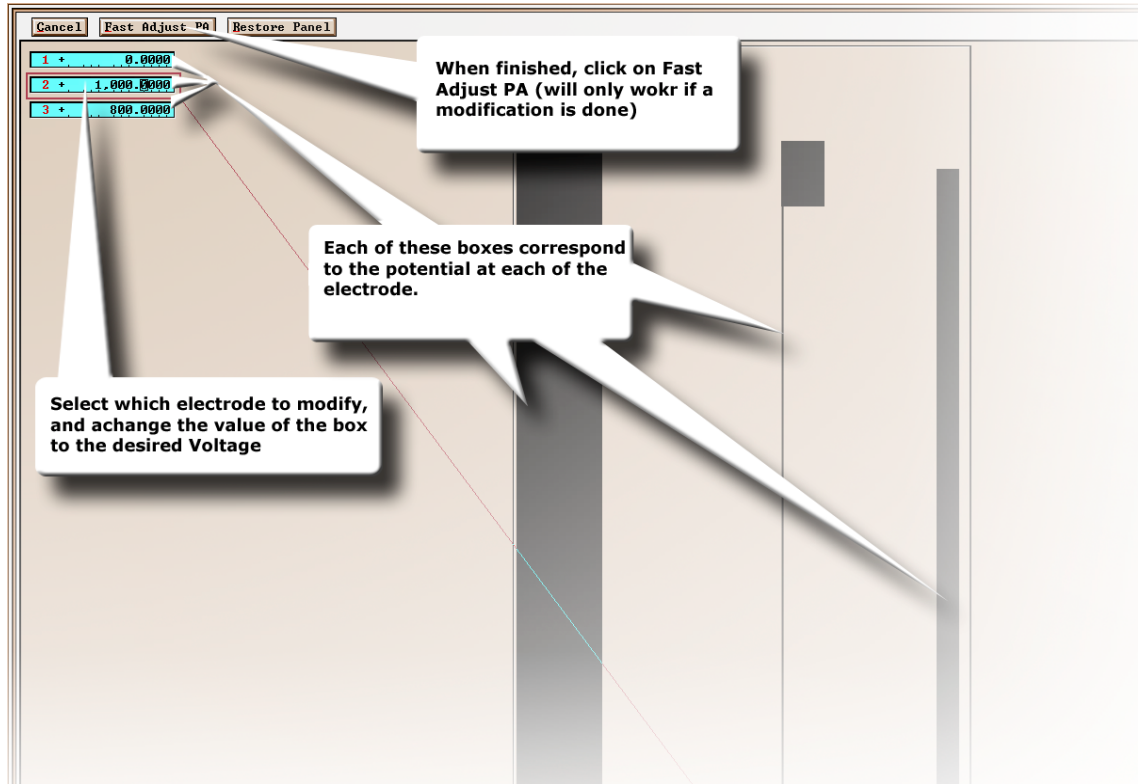
A reminder

- The VPT has three electrodes: cathode, anode, and dynode.
- The anode is a mesh 50% transparent, with a resolution of 100 lines/mm.
- The implementation of the complex geometry was done on separate instances. With the "realistic" mesh overlapping an "ideal" one (a mesh 100% transparent).

Because of this, modifying the anode in one of the instances must be followed by a corresponding modification on the other instance. I.e. if changing the potential of the anode at the instance labelled "VPT" to a voltage "X" then the potential of the anode on the instance labelled "MESH" must also be changed to "X".

How to use the SIMION VPT SIMULATION

Modify Magnetic Field Angle

Apart of studying the effect of the magnetic field strength on the VPT, it is also important to know how the field angle will affect the VPT performance. The importance of this study is due to the fact that all the VPTs will not have the same orientation when installed on CMS.
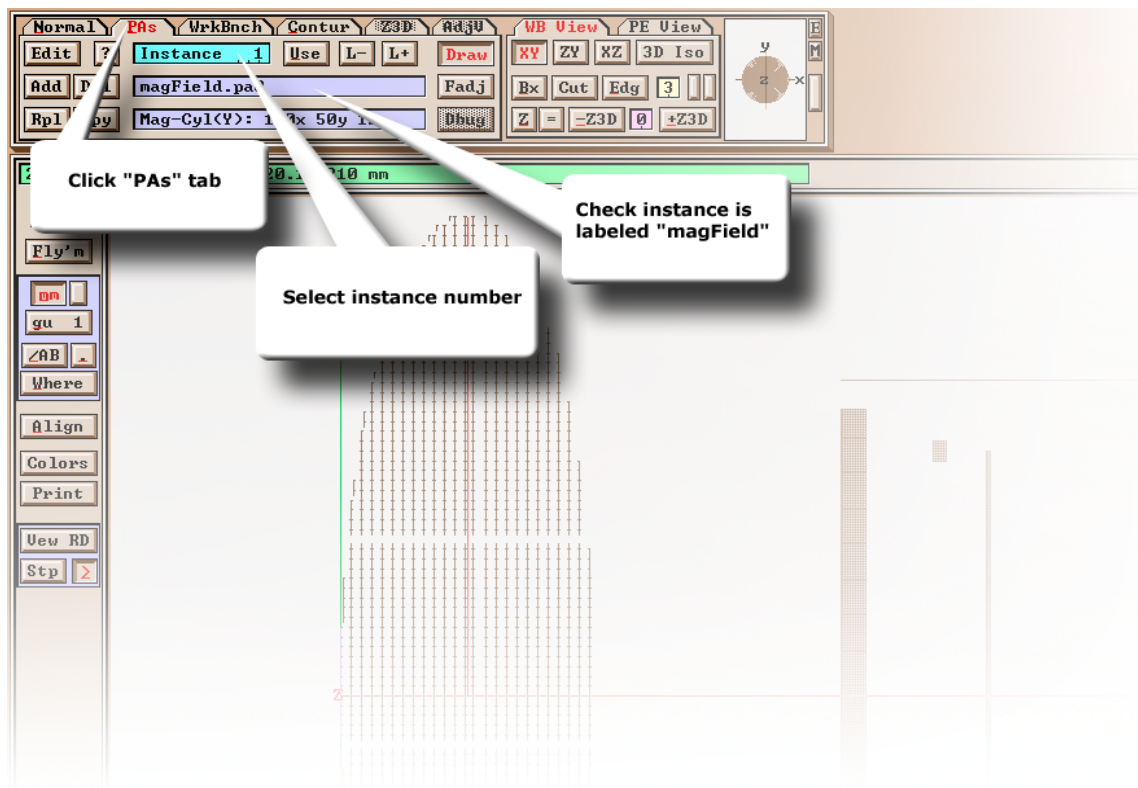

On the View Screen, click to select the "PAs" tab, select the magnetic field instance labelled "magField"

Click on the "Edit" button to change the instance setting. The first sat of settings help to change the location in (XYZ) of the Instance with respect of the work bench. Also, there is a control that regulates the scaling of the instance itself.

However, in order see how the angle of the instance could be change, one would have to click on "MORE".
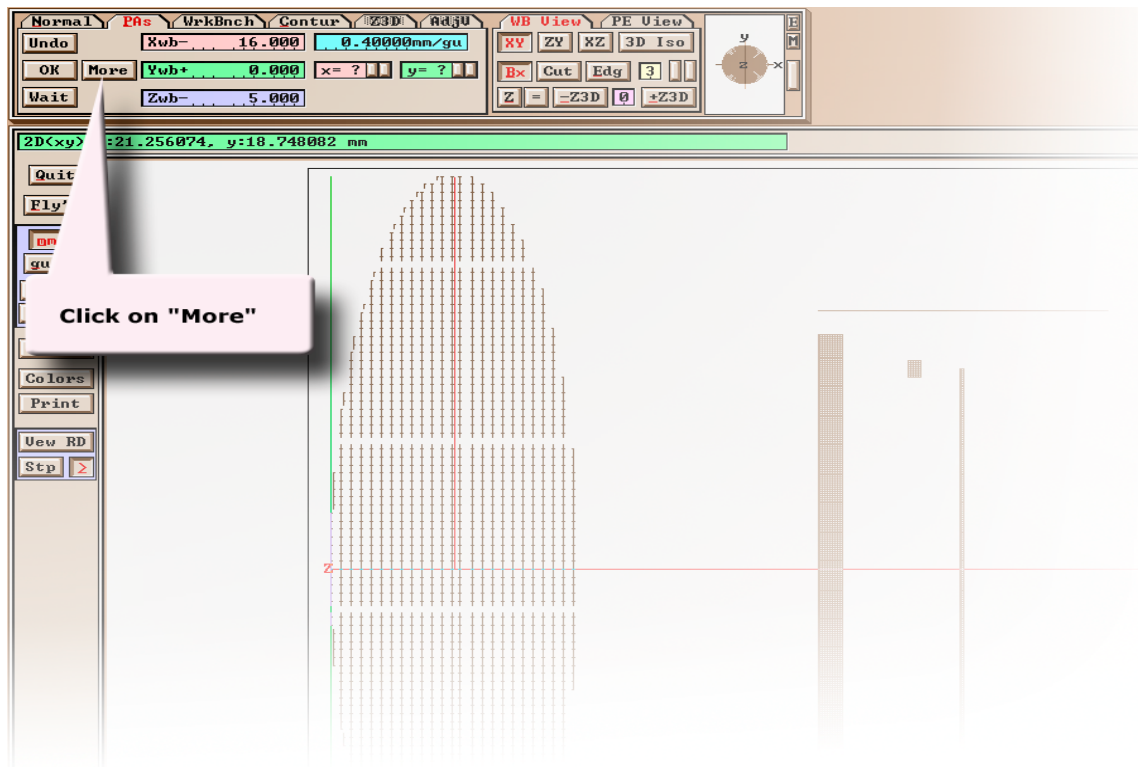
Due to the geometry of the VPT which is cylindrical, it does not really mater in which direction the field is rotated (Azimuthally or Elevation wise) yet alone if the rotation is on the "x" axis. Change the Azimuth angle (in degrees) to rotate the magnetic field in the XZ plane or change the Elevation angle (in degrees as well) for a rotation on the XY plane (always considering the X direction to be along the axis of the VPT.
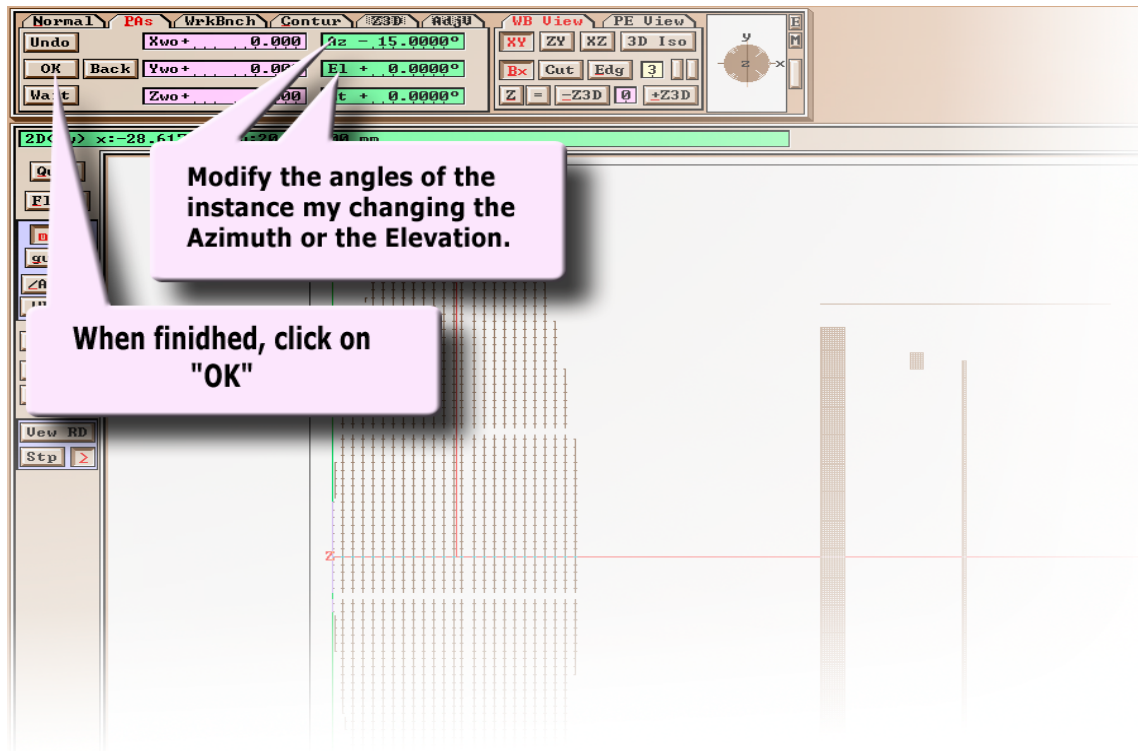
Once satisfied with the changes, click "Ok"

Modify Magnetic Field Strength

It is also very useful to understand how the VPT would behave under different magnetic field conditions. One of these conditions is the strength of the field itself, which can be changed by a process similar to the described on modifying the biasing potentials.

In order to do this analysis, the magnetic "iob" setup must have been loaded. If this is not the case, then refer to "changing the IOB setup" to load the appropriate one.
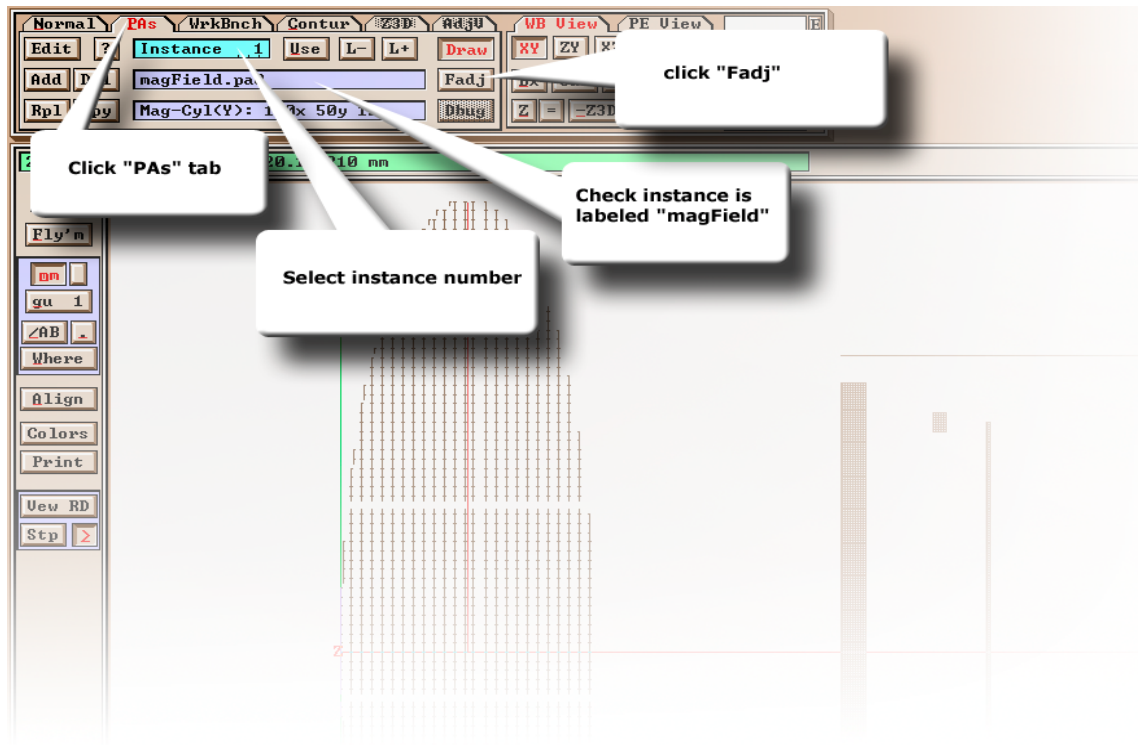
On the view screen select the "PAs" tab, and select the instance labelled "magField". Click on "Fadj" and the Fast Adjust Screen will open.

In contrast to the other instances, the magnetic arrays have poles instead of electrodes. Consequently, their interaction with the surrounding is different.

One of the differences (also attributed to the geometry) is that the magnetic field is uniform (well… almost), and does not depend on the coordinates on space.

The units here are Gauss, so conversion from Teslas must be performed before any change is done. Fortunately, this conversion is quite simple, with $1T = 10,000 Gauss$ so for example, $4T = 40,000 Gauss$ and $1.8T = 18,000 Gauss$.
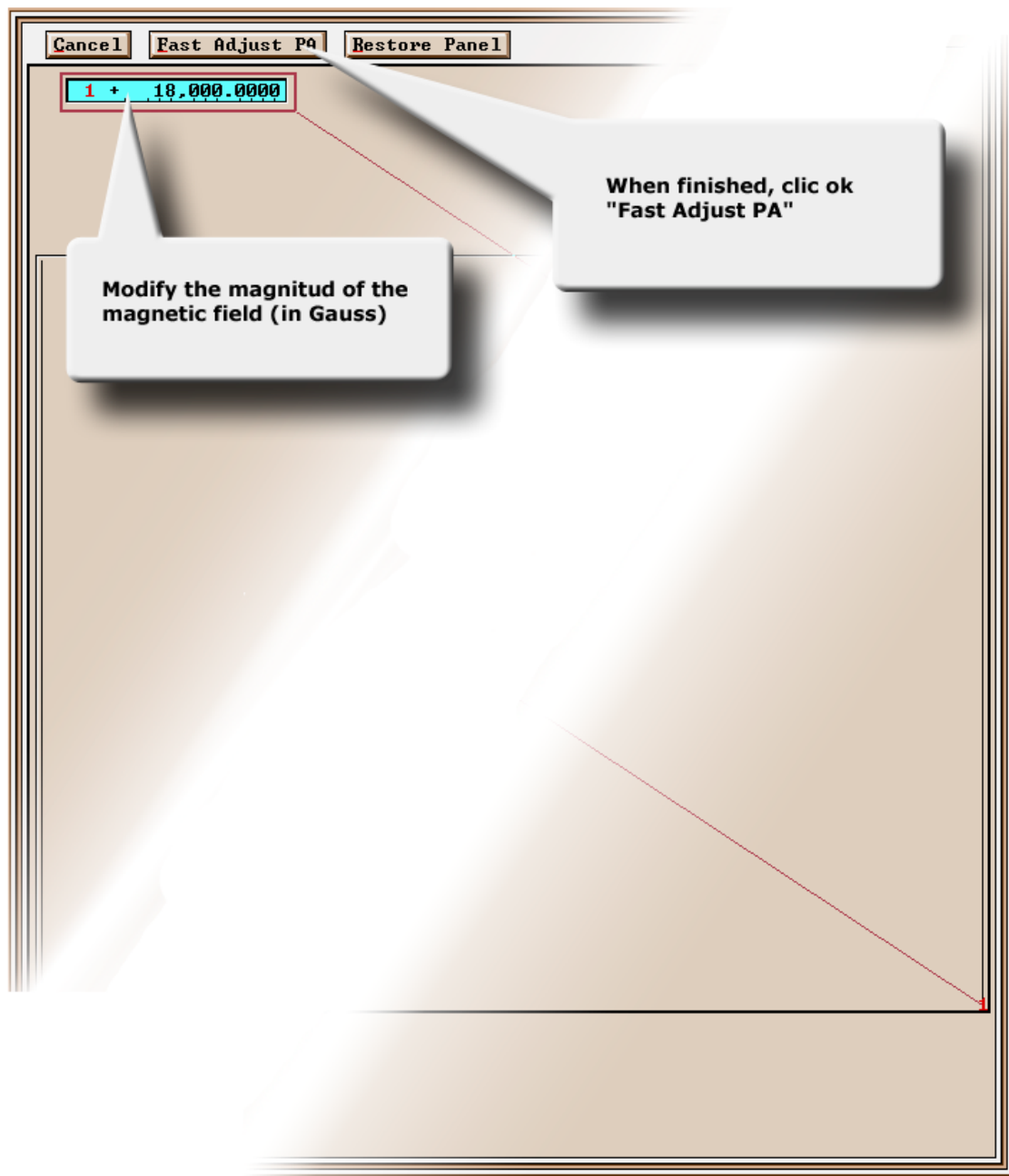
Confirm and changes by clicking on "Fast Adjust PA".

FAQ

SIMION7 often communicates in forms of error messages. I have collected some of them and explain why they happen and how to solve the issue.

> **Directory File Too Big To Totally Load**
>
> **Directories Missed: More Than a total of 3000 in Drive**

This error is quite normal, and should not be worried of. It is natural that big drives will eventually contain more than 3000 folders, and most of the time unavoidable.

SIMION7 will load the first 3000 folders alphabetically and hierarchically. From the folder 3001 onwards loading will be omitted; therefore, a SIMION7 working folder should be made sure to within the loading set.

In order to do this, I recommend creating a projects folder on the root directory which name starts by a number, e.g. "c\0 My SIMION7 Projects". By doing this, it is guaranteed not only that the working folder will be between the first loaded, but also, that the content of the drive could keep growing without affecting the location of the working project folder.

> **Too Many Ions for List Size… Ion Definition Missed**

This error is related to loading an ion file with more definitions that than the currently allocated memory allowance.

There reasons for this could be divided in two main categories:

- **Stochastic**
    - The gain of the Dynode is a Poisson Distributed Random Variable with a mean of approximately 20. However, since the probabilities of a large gain for some random group of electrons is not zero, it is possible for an overloading of secondary electrons to randomly occur. This could be minimized by increasing the allocation size, but at what expense? And to what extend? However, my

recommendation is to ignore the set of results that generated this error (including the primary hits), and rerun the simulation. If this fails, see the other probable causes.

- **Deterministic**
    - o **Failing to increase at all the allocation size** from that of the default value, to compensate for secondary emissions numbers.
    - o **Underestimating the gain of the Dynode**. As explained, the gain is a Poisson distributed random variable with a mean of 20. Considering that the mesh is about 50% transparent (allowing half the electrons to go through) then roughly it could be estimated that the mean amount of secondary emissions to that of the first photoelectron is of a ration of 10:1.

To Solve these, go to the ""Main Menu" screen, remove all the PAs form RAM, and then allocating memory for a realistic amount of electrons (in this case, the worst case scenario is that of the number of secondary emissions, so it will be useful to allocate enough memory to deal, at least, with the most frequent gain values). Finally, reload the ".iob" file, and the ".ion" file to rerun the simulations.

File Loading Aborted

This error appears when trying to load an empty ion definition file. Try rerunning the ion definition initialising program, or selecting a non empty ".ion" file.

Abort: You Didn't Request Any Potential Changes

This error message appears when clicking "Fast Adjust PA" button on the "Fast

Adjust" screen without having modified any of the potentials. Do one of the

followings:

- Click on cancel if no modifications are to be saved
- Modify any of the potential voltages to a desired value, then click on the "Fast Adjust PA" button

How to use the SIMION VPT SIMULATION

Appendix D Experiments on the VPTs

VPT 1485
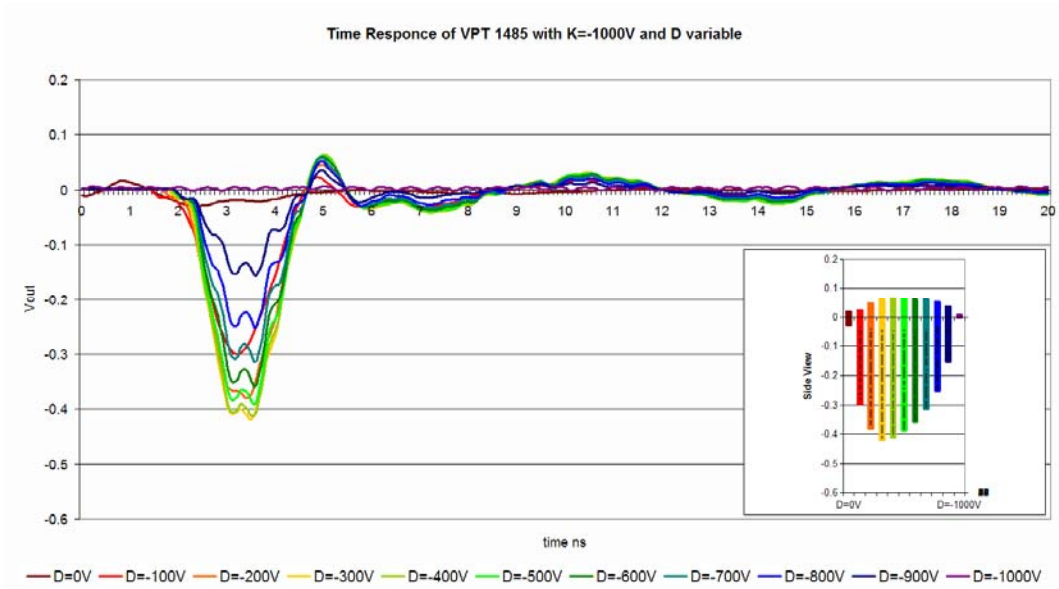
Figure D-1
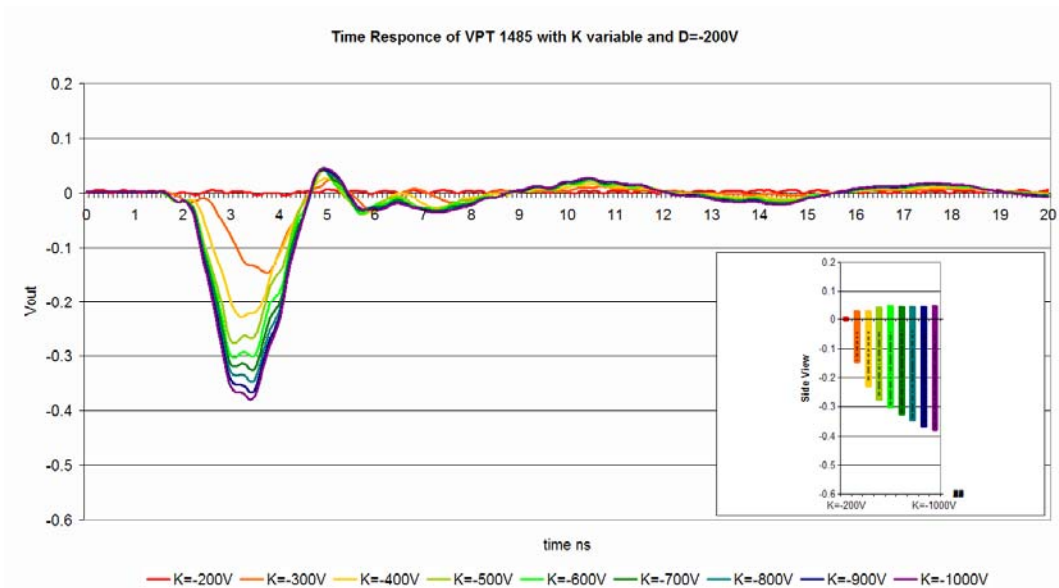
Figure D-2
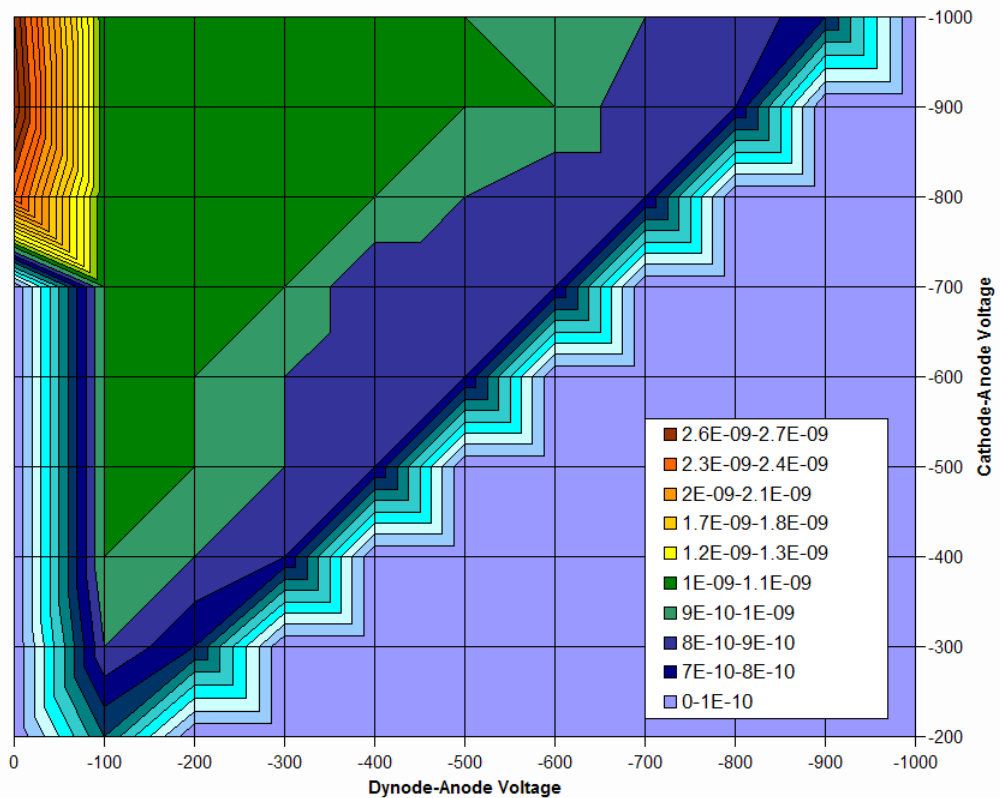
Figure D-3

Signal Rise Time of VPT 1485 depending on Dynode-Anode voltage and Cathode-Anode Voltage

Legend:
- 9E-10-1E-09
- 8E-10-9E-10
- 7E-10-8E-10
- 0-1E-10
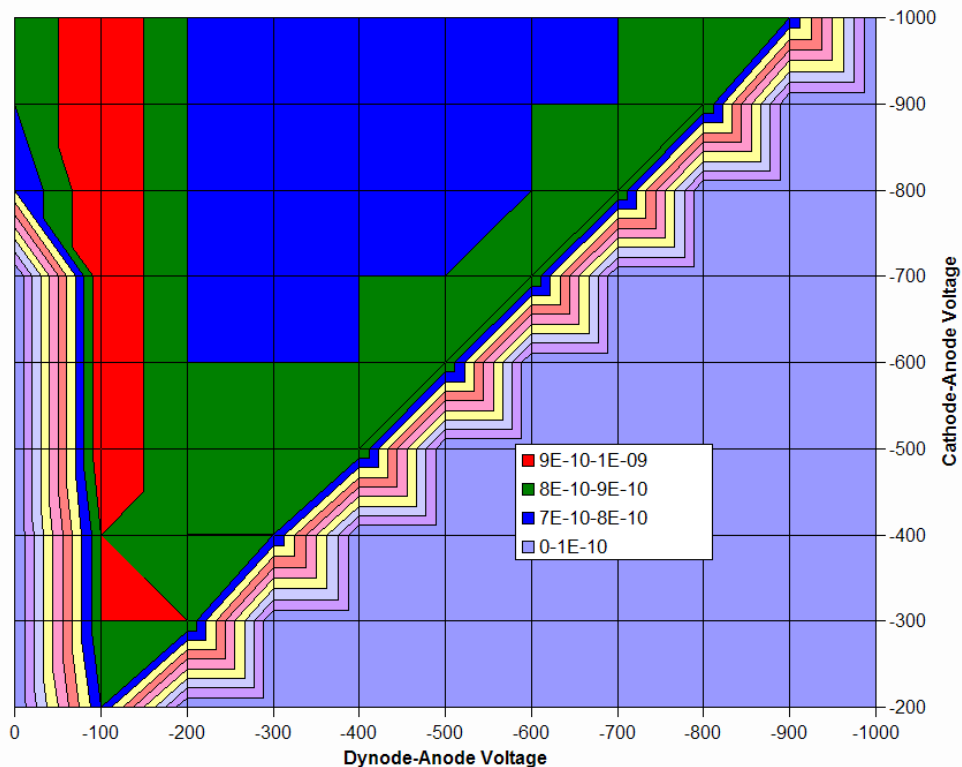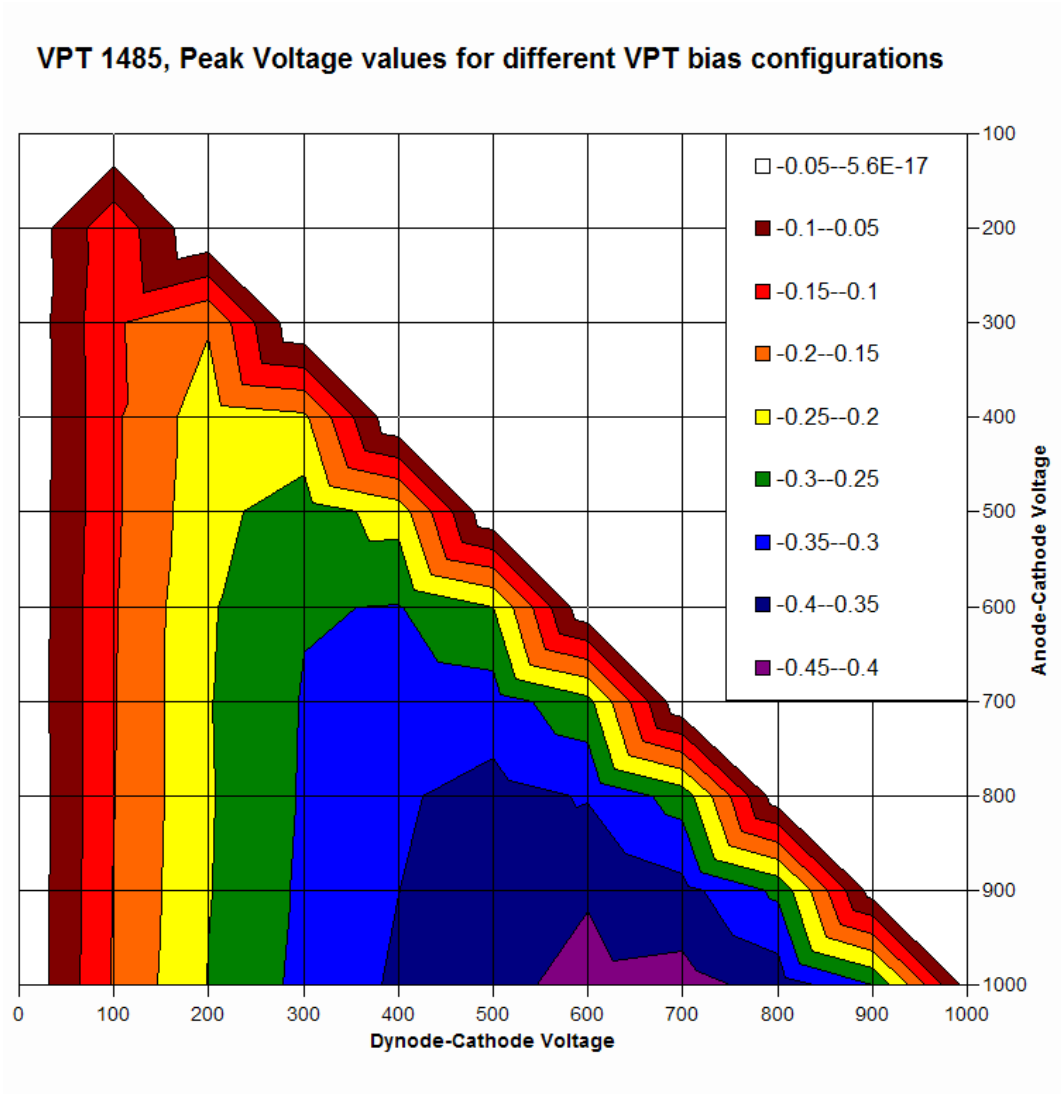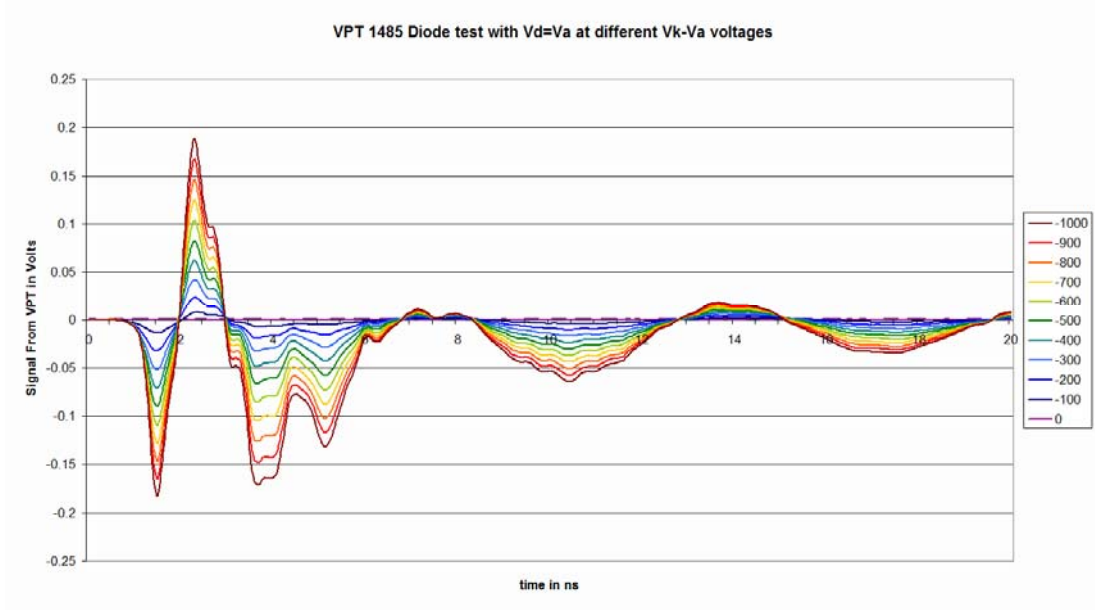
Figure D-4

Figure D-5

Figure D-6

Figure D-7

VPT 2517

VPT 2517 Signal comparison between different cathode voltage configuration for Vd=-200V

Figure D-8

VPT 2517 Signals for Vk=-1000V and Variable Dynode
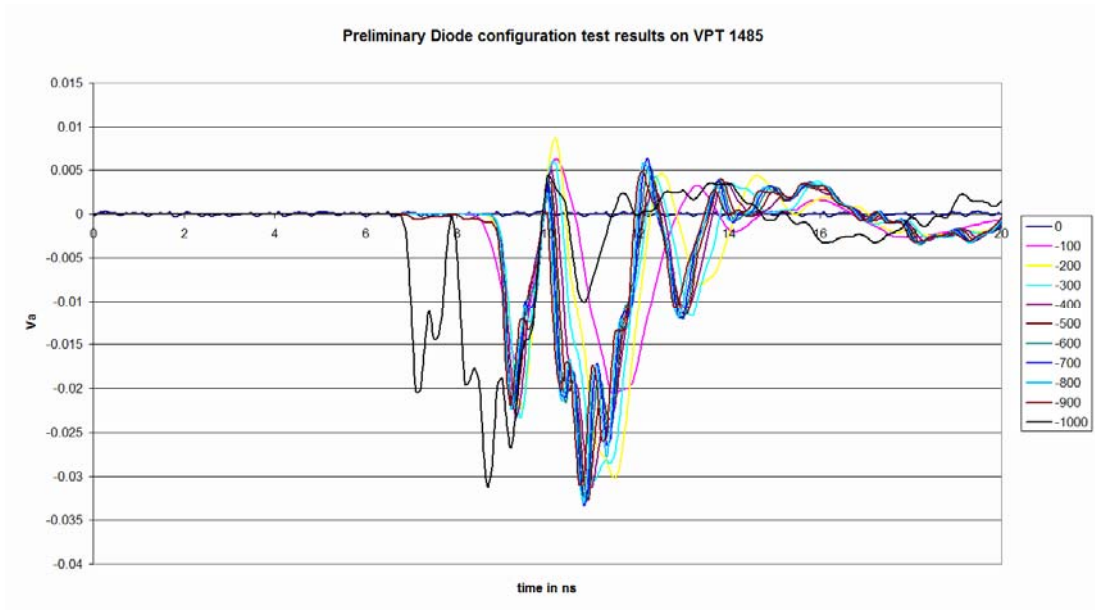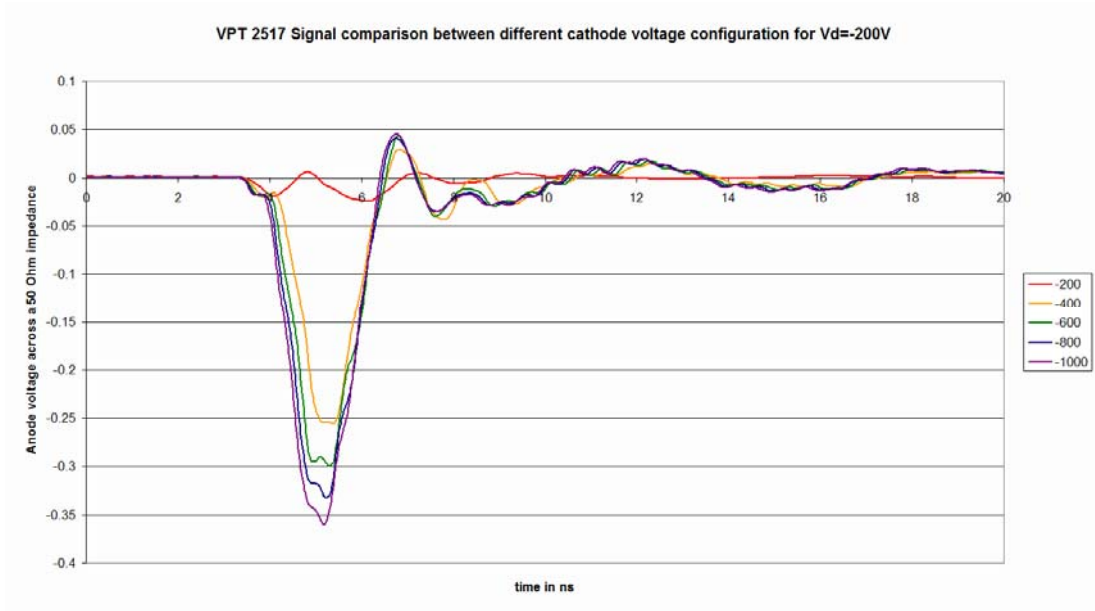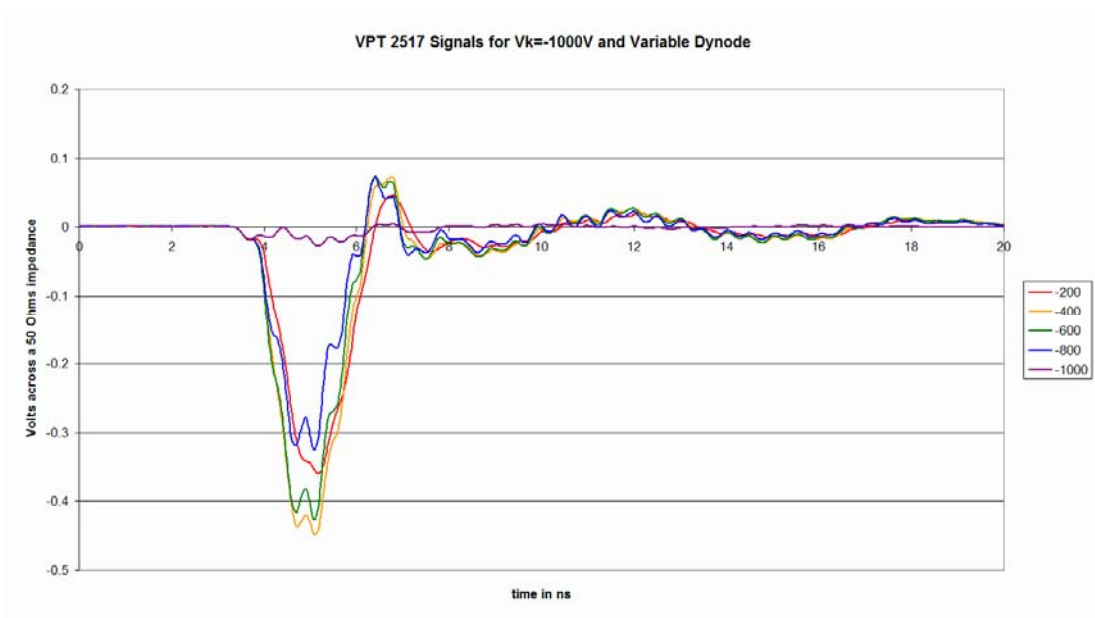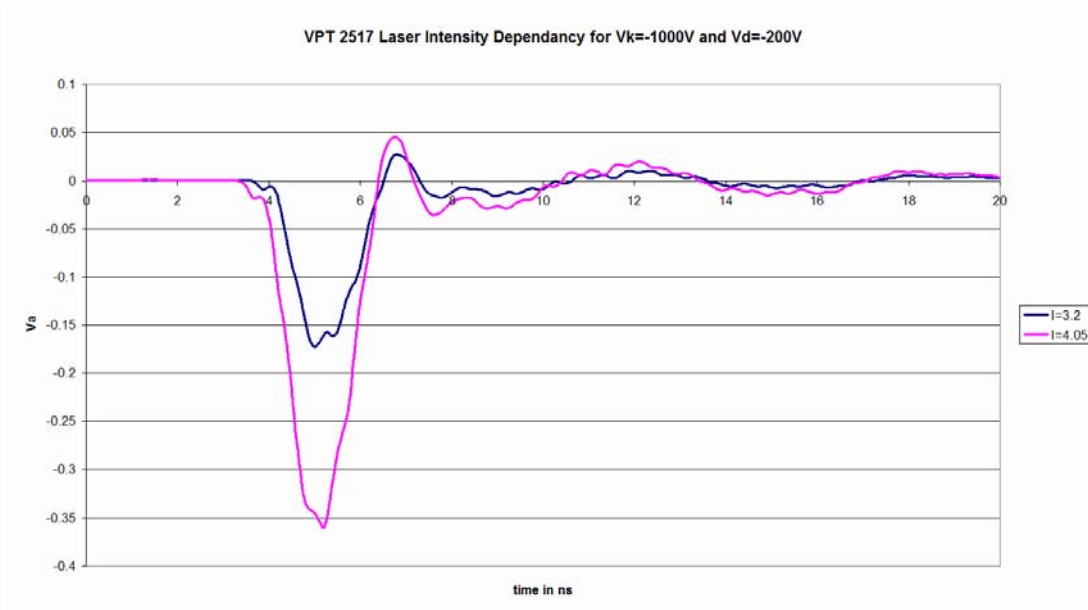
Figure D-9

Figure D-10

Appendix E Relevant Publications

The following pages correspond to previous publications which are relevant to this work and in which I am an author.

The CMS Electromagnetic Calorimeter Group; "Results of the first performance tests of the CMS electromagnetic calorimeter" The European Physical Journal C 44, s02, (2006): 1–10

Hobson, P R and Yaselli, I; "Simulation of a Vacuum Phototriode with SIMION 3D" Nuclear Instruments and Methods in Physics Research A 567 (2006): 226-229. This work was presented at the 4th Beaune Conference on New Development in Photodetection (Beaune, France 19-24 June 2005)

 "Timing Performance of a Vacuum Phototriode"

Work presented by Dr D E Leslie at the 10th ICATPP Conference on Astroparticle, Particle, Space Physics, Detectors and Medical Physics Applications (Como, Italy 8-12 October 2007), and submitted for publication in the conference proceedings (World Scientific).

The CMS Collaboration, S Chatrchyan *et al.,* "*The CMS experiment at the CERN LHC*" Journal of Instrumentation **3** (2008) S08004

EPJ C direct

electronic only

Scientific Note

Results of the first performance tests of the CMS electromagnetic calorimeter

The CMS Electromagnetic Calorimeter Group

P. Adzic[3], R. Alemany-Fernandez[13], C.B. Almeida[13,14], N.M. Almeida[13], G. Anagnostou[2], M.G. Anfreville[11], I. Anicin[3], Z. Antunovic[30], A. Asimidis[12], E. Auffray[10], S. Baccaro[28,29], D. Barney[10], L.M. Barone[29], P. Barrillon[15], A. Bartoloni[29], S. Beauceron[11], F. Beaudette[10], K.W. Bell[8], R. Benetta[10], M.J. Bercher[25], B. Betev[37], R. Beuselinck[15], A. Bhardwaj[7], C. Biino[33], S. Bimbot[25], P. Bloch[10], S. Blyth[6], M. Bonesini[17], P. Bordalo[13], A. Bornheim[26], J.M. Bourotte[10,25], D. Britton[15], R.M. Brown[8], R. Bruneliere[10,34], P. Busson[25], T. Camporesi[10], N. Cartiglia[33], F. Cavallari[29], D. Chamont[25], P. Chang[32], Y.H. Chang[6], C. Charlot[25], E.A. Chen[6], R. Chipaux[11], D.J. Cockerill[8], C. Collard[25], C. Combaret[34], S. Costantini[29], J.C. Da Silva[13], I. Dafinei[29], G. Daskalakis[10], G. Davatz[37], A. De Min[17], K. Deiters[35], M. Dejardin[11], R. Della Negra[34], P. Depasse[34], J. Descamp[11], G. Dewhirst[15], S. Dhawan[23], M. Diemoz[29], G. Dissertori[37], M. Dittmar[37], L. Djambazov[37], L. Dobrzynski[25], S. Drndarevic[3], M. Dupanloup[34], M. Dzelalija[30], J. Ehlers[37], H. El Mamouni[34], A. Elliott-Peisert[10], I. Evangelou[12], B. Fabbro[11], J.L. Faure[11], J. Fay[34], F. Ferri[17], P.S. Flower[8], G. Franzoni[17], W. Funk[10], A. Gaillac[25], C. Gargiulo[29], S. Gascon Shotkin[34], Y. Geerebaert[25], F.X. Gentit[11], A. Ghezzi[17], J. Gilly[25], A.S. Giolo-Nicollerat[37], A. Givernaud[11], S. Gninenko[20], A. Go[6], N. Godinovic[31], N. Golubev[20], R. Gomez-Reino[10], P. Govoni[17], J. Grahl[18], P. Gras[11], J. Greenhalgh[8], J.P. Guillaud[1], M. Haguenauer[25], G. Hamel De Montechenault[11], M. Hansen[10], H.F. Heath[5], J.A. Hill[8], P.R. Hobson[16], D. Holmes[5], A.G. Holzner[37], G.W. Hou[32], B. Ille[34], Q. Ingram[35], A. Jain[13], P. Janot[10], P. Jarry[11], M.A. Karar[25], S.K. Kataria[22], V. Katchanov[27], B.W. Kennedy[8], K. Kloukinas[10], B. Koblitz[25], P. Kokkas[12], M. Korjik[19], N. Krasnikov[20], D. Krpic[3], A. Kyriakis[2], M. Lebeau[10], P. Lecomte[37], P. Lecoq[10], M.C. Lemaire[11], M. Lethuillier[34], W. Lin[6], A.L. Lintern[8], A. Lister[37], E. Locci[11], A.B. Lodge[8], E. Longo[29,a], D. Loukas[2], W. Lustermann[37], C. Lynch[5], C.K. Mackay[5], D. Maletic[3], I. Mandjavidze[11], N. Manthos[12], A. Markou[2], H. Mathez[34], V. Matveev[20], G. Maurelli[34], E. Menichetti[33], P. Meridiani[29], P. Milenovic[3], G. Milleret[25], P. Mine[25], M. Montecchi[28,29], M. Mur[11], Y. Musienko[4,19], A. Nardulli[37], J. Nash[10,15], H. Neal[23], P. Nedelec[1], P. Negri[17], F. Nessi-Tedaldi[37], H.B. Newman[26], A. Nikitenko[15], M.M. Obertino[18,33], R.A. Ofierzynski[37], G.C. Organtini[29], P. Paganini[25], M. Paganoni[17], I. Papadopoulos[12], R. Paramatti[10,29], N. Pastrone[33], F. Pauss[37], P. Poilleux[25], I. Puljak[31], A. Pullia[17], J. Puzovic[3], S. Ragazzi[17], S. Ramos[13], J. Rander[11], O. Ravat[34], M. Raymond[15], P.A. Razis[24], N. Redaelli[17], N. Regnault[25], D. Renker[35], S. Reucroft[4], J.M. Reymond[11], M. Reynaud[34], S. Reynaud[10], T. Romanteau[25], F. Rondeaux[11], A. Rosowsky[11], C. Rovelli[17], R. Rusack[18], S.V. Rusakov[21], M.J. Ryan[15], H. Rykaczewski[37], T. Sakhelashvili[35,*], R. Salerno[17], M. Santos[13,14], D. Schinzel[10], C. Seez[15], I. Semeniouk[25], P. Sempere Roldan[10], O. Sharif[16], P. Sharp[10], C. Shepherd-Themistocleous[8], S. Shevchenko[26], R.K. Shivpuri[7], G. Sidiropoulos[12], D. Sillou[1], A. Singovski[18], Y Sirois[25], A.M. Sirunyan[36], B. Smith[8], V.J. Smith[5], M. Sproston[8], H. Suter[37], J. Swain[4], T. Tabarelli De Fatis[17], M. Takahashi[15], R.J. Tapper[5], A. Tcheremoukhine[9], I. Teixeira[13,14], J.P. Teixeira[13,14], O. Teller[10], F.A. Triantis[12], S. Troshin[27], N. Tyurin[27], S. Udriot[37], K. Ueno[32], A. Uzunian[27], I. Van Vulpen[10], J. Varela[10,13], N. Vaz Cardoso[13], P. Verrecchia[11], P. Vichoudis[10,12], G. Viertel[37], T. Virdee[10,15], M. Wang[32], J.H. Williams[8], I. Yaselli[16], N. Zamiatin[9], S. Zelepoukine[27], M. Zeller[23], L.Y. Zhang[26], K. Zhu[26], R.Y. Zhu[26]

[1] Laboratoire d'Annecy-le-Vieux de Physique des Particules, 74941 Annecy-le-Vieux, France
[2] Institute of Nuclear Physics "Demokritos", 153 10 Attiki, Greece
[3] "Vinca" Institute of Nuclear Sciences and Faculty of Physics of University of Belgrade, 11000 Belgrade, Serbia and Montenegro
[4] Northeastern University, Boston MA 02115-5096, USA
[5] Bristol University, Bristol BS8 1TL, United Kingdom
[6] National Central University, Chung-Li, Taiwan, ROC
[7] Delhi University, Delhi 110 007, India
[8] CCLRC, Rutherford Appleton Laboratory, Didcot OX11 0QX, United Kingdom
[9] Joint Institute for Nuclear Research, 141980 Dubna (Moscow Region), Russia
[10] European Organization for Nuclear Research, CERN, 1211 Geneva 23, Switzerland

[a] e-mail: egidio.longo@roma1.infn.it

[11] Centre d'Etudes Nucleaires de Saclay, 91191 Gif-sur-Yvette Cedex, France
[12] University of Ioannina, 451 10 Ioannina, Greece
[13] Laboratório de Instrumentação e Física Experimental de Partículas, 1000-149 Lisboa, Portugal
[14] Instituto de Engenharia de Sistemas e Computadores, 1000-029 Lisboa, Portugal
[15] Imperial College, London SW7 2BZ, United Kingdom
[16] Brunel University, Middlesex UB8 3PH, United Kingdom
[17] Università degli Studi Milano-Bicocca and INFN-Sezione di Milano, 20126 Milano, Italy
[18] Minnesota University, Minneapolis MN 55455, USA
[19] Research Institute for Nuclear Problems, Byelorussian State University, 220050 Minsk, Byelorussia
[20] Institute for Nuclear Research, Russian Academy of Sciences, 117312 Moscow, Russia
[21] Lebedev Physical Institute, Russian Academy of Sciences, 117924 Moscow, Russia
[22] Bhabha Atomic Research Centre, Mumbai 400 085, India
[23] Yale University, New Haven CT 06520-8121, USA
[24] Cyprus University, 1678 Nicosia, Cyprus
[25] Laboratoire Leprince-Ringuet, Ecole Polytechnique, 91128 Palaiseau Cedex, France
[26] California Institute of Technology, Charles C. Lauritsen Laboratory, Pasadena CA91125, USA
[27] State Research Center, 142284 Protvino (Moscow Region), Russia
[28] ENEA - CR Casaccia, 00060 S. Maria di Galeria, Roma, Italy
[29] Università "La Sapienza", Dipartimento di Fisica and INFN-Sezione di Roma, 00185 Roma, Italy
[30] Split University, PMF, 21000 Split, Croatia
[31] Technical University of Split, FESB, 21000 Split, Croatia
[32] National Taiwan University, 106 Taipei, Taiwan ROC
[33] Università di Torino, Dipartimento di Fisica and INFN-Sezione di Torino, 10125 Torino, Italy
[34] Institut de Physique Nucléaire, IN2P3-CNRS and Université C. Bernard Lyon I, 69622 Villeurbanne, France
[35] Paul Scherrer Institut, 5232 Villigen, Switzerland
[36] Yerevan Physics Institute, 375036 Yerevan 36, Armenia
[37] Eidgenössische Technische Hochschule, ETH, 8093 Zürich, Switzerland

Abstract. Performance tests of some aspects of the CMS ECAL were carried out on modules of the "barrel" sub-system in 2002 and 2003. A brief test with high energy electron beams was made in late 2003 to validate prototypes of the new Very Front End electronics. The final versions of the monitoring and cooling systems, and of the high and low voltage regulation were used in these tests. The results are consistent with the performance targets including those for noise and overall energy resolution, required to fulfil the physics programme of CMS at the LHC.

1 Introduction

The Compact Muon Solenoid (CMS) [1] detector is a general purpose detector to be installed at the 14 TeV proton-proton collider, LHC, under construction at CERN and due to start operation in 2007. The Electromagnetic Calorimeter (ECAL) [2] of the detector is a hermetic homogeneous calorimeter made of 61,200 lead tungstate ($PbWO_4$) crystals mounted in the central "barrel" part, closed by 7,324 crystals in each of the two end-caps. Avalanche photodiodes (APDs) are used as photodetectors in the barrel and vacuum phototriodes in the end-caps. The use of high density $PbWO_4$ crystals [3] has allowed the design of a calorimeter which is fast, has fine granularity and is radiation resistant, all important characteristics in the LHC environment. One of the driving criteria in the design was the capability to detect the decay to two photons of the postulated Higgs boson. This capability is enhanced by the superior energy resolution provided by a homogeneous crystal calorimeter. The intrinsic performance of components of the calorimeter has been demonstrated in previous publications [4].

One of the key requirements, needed to be able to realise the potential excellent energy resolution in operation, is stability of the calibration and inter-calibration over extended periods of time. The temperature of the crystals needs to be maintained constant to high precision. The variation of the crystal transparency under irradiation must be tracked with precision monitoring and corrected for. In addition, the gains of the APDs used in the barrel part are strongly sensitive to both temperature and bias voltage, placing further constraints on thermal stability and power supply regulation. With the construction of final elements of the barrel calorimeter underway, it became possible to verify the performance of these system aspects of the calorimeter. This paper reports on tests of these aspects carried out in 2002 and 2003.

In recent years a major redesign of the electronics system architecture was made to reduce the number of optical links and hence the cost and complexity of the overall system. This required the generation of trigger primitives to be moved from the off-detector to the on-detector electronics, which was made possible by designing on-detector ASICS using the recently developed 0.25 μm IBM CMOS technol-

---

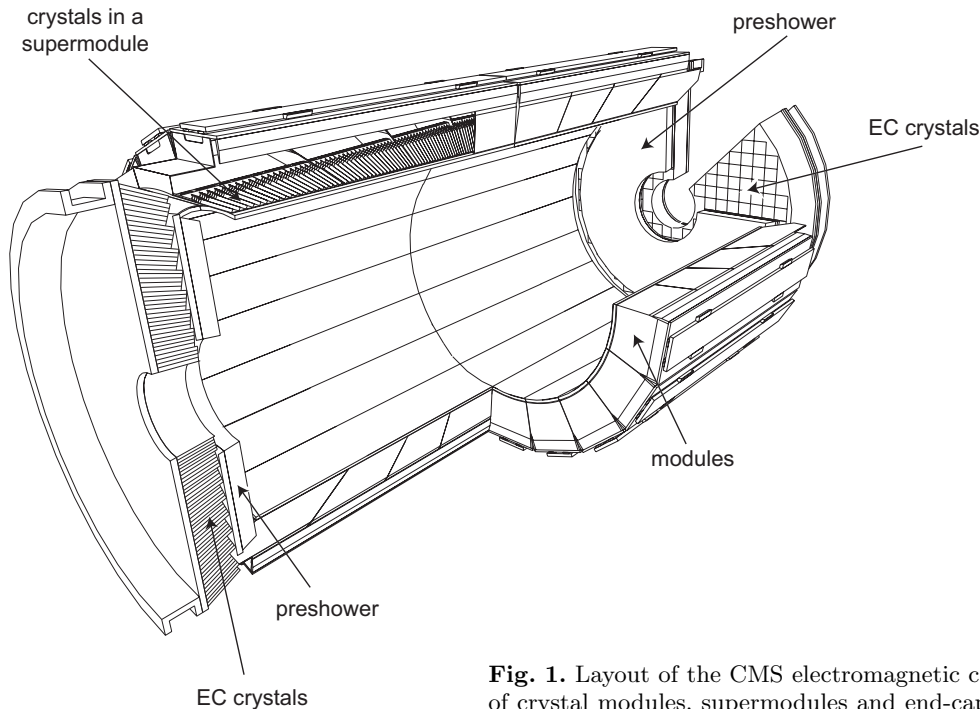   * On leave from High Energy Physics Institute, Tblisi, Georgia

Fig. 1. Layout of the CMS electromagnetic calorimeter showing the arrangement of crystal modules, supermodules and end-caps

ogy. This paper reports on a high energy electron beam test made in late 2003 to validate prototypes of the new electronics. The noise level and the ability to reconstruct the signal amplitude from the digitised time-samples of the pulses were tested, and the impact of the overall electronics performance on energy resolution was determined.

The light yield of each crystal is measured in the laboratory before being installed in the calorimeter. The variations in the yield can be used to predict differences in response of the individual channels in the calorimeter. Results are presented on the extent to which this can be used to inter-calibrate their response before the start of the experiment.

In November 2004, tests of a supermodule fully equipped with the final electronics in an electron beam confirmed the stability and performance reported here; these results will be presented in detail in a future publication.

2 The CMS barrel electromagnetic calorimeter

The crystals in the barrel part of the calorimeter have a tapered shape, slightly varying along the polar angle with respect to the beam axis. The front face dimensions are approximately $2.2 \times 2.2 \, \text{cm}^2$, and the crystal length of 23 cm corresponds to 25.8 radiation lengths. To avoid cracks aligned with particle trajectories, the axes of the crystals are tilted by $3°$ in both polar and azimuthal angles with respect to the direction of the nominal interaction point. The crystals are grouped into 5×2 matrices, held in a glass fibre alveolar submodule, of which 40 or 50 are then mounted into a module. The modules are held by an aluminium grid, which supports their weight from the rear. Four modules (of different types according to the position in pseudo-rapidity η are assembled together in a supermodule, which

thus contains 1,700 crystals. Eighteen supermodules form a half barrel covering the range of $|\eta|$ from 0 to 1.48 (Fig. 1).

Scintillation light from the crystals is detected by the APDs of type S8148 developed by Hamamatsu Photonics in collaboration with CMS for the ECAL [5]. Two APDs, embedded in a plastic capsule, are glued to the back of each crystal. They are connected in parallel to the read-out electronics, which is mounted on the outside of the aluminium grid. The electronic read-out chain follows a modular structure whose basic elements are matrices of 5×5 crystals corresponding to a trigger tower. Five APD pairs are connected to one Very Front End (VFE) board, and five of these are mounted on one motherboard. Each motherboard is also connected to one Front End (FE) board where the trigger tower primitives are generated. The VFE boards preamplify and shape, then further amplify, and finally digitise the signals from the APDs. The first two steps are performed by a chip (MGPA) with three parallel amplification stages (1, 6 and 12). The three analogue output signals are digitised in parallel by a multi-channel, 40 MHz, 12-bit ADC (AD41240), whose integrated logic selects the highest non-saturated signal. The digitised data are then stored in the FE board and the trigger primitives, which are elementary quantities such as the energy sum in a trigger tower, are generated and transmitted to the trigger electronics. On receipt of a level-1 trigger, with a latency of $\sim 3 \, \mu\text{s}$, the data are transmitted to the off-detector electronics by a 800 Mbit/s optical link system. The link is based on a Giga-bit Optical Hybrid consisting of a data serialiser, a laser driver chip and a laser diode.

Each VFE motherboard also hosts a Low Voltage Regulator board (LVR), which supplies a common voltage of 2.5 V (required by the $0.25 \, \mu\text{m}$ IBM CMOS technology) to both the analogue and digital parts of the electronics. Four LVRs receive the power from one low voltage distribution
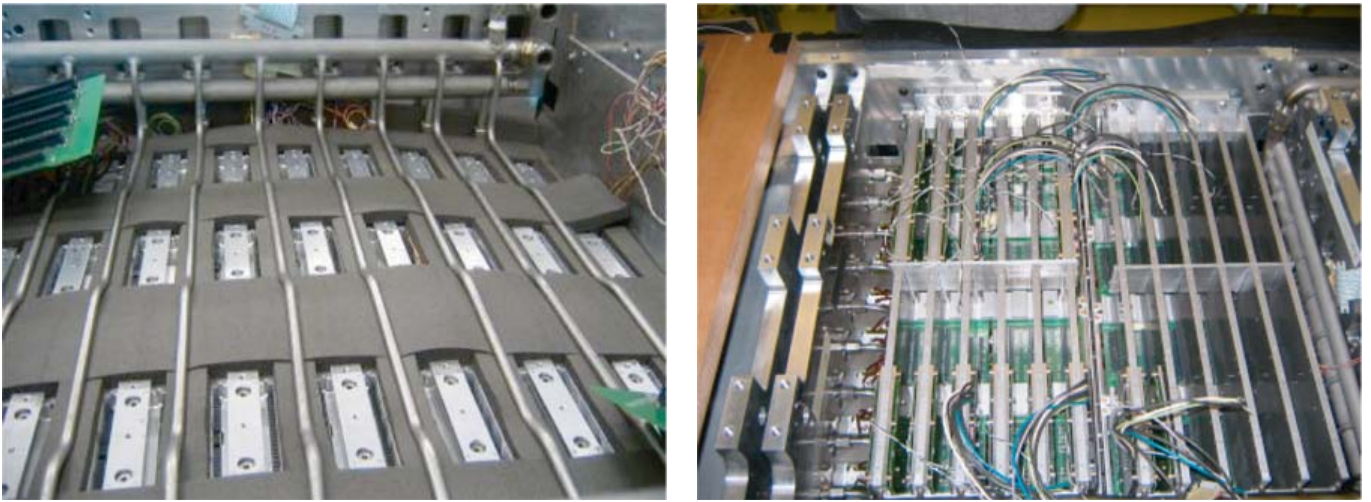
Fig. 2. ECAL cooling scheme. On the left, the layer of insulating foam is shown on top of the grid. On the right, the cooling bars are shown with some of the cards inserted

panel (LVD). The LVDs are supplied by low voltage power supplies with remote sensing. High voltage ($\sim$390 V) for the APDs is supplied through the motherboards, with one channel providing a common bias for the 100 APDs of two motherboards.

3 Experimental set-up

In the summer of 2002 and 2003, several parts of the barrel system were tested in the H4 test beam facility at CERN, consisting of a secondary beam line capable to supply electron beams with a narrow momentum bite and high rates ($>$ 2000 electrons per burst) between 20 and 250 GeV/c. Modules or supermodules were mounted on a rotating table, allowing the beam to be directed into the centre of the front face of each crystal. In 2002, a module of type 2, designated M0', was installed, with 100 crystals fully equipped with the previous version of the electronics [6]. In 2003, a supermodule, designated SM0, was installed on the table with 100 crystals read out. Following this a second supermodule, SM1, was put in place with 50 channels equipped with prototypes of the new on-detector electronics. Other tests were performed on modules and supermodules during the assembly procedure, during the same two years.

4 Validation of the cooling system

The number of scintillation photons emitted by the crystals and the amplification of the APD are both temperature dependent. Both variations are negative when the temperature increases. Changes in response due to both effects were studied in test beams at CERN on module M0' during summer 2002 and on supermodule SM1 in 2003. The signal from crystals responding to incident electrons was studied while the temperature of the set-up was changed from 18 to 19°C. The variation with temperature of the response (due to changes of both light yield of the crystal and APD gain) was measured to be $-4.1\%°\text{C}^{-1}$ for

M0' and $-3.8\%°\text{C}^{-1}$ for SM1, with a spread among the channels of 0.6 and $0.4\%°\text{C}^{-1}$, respectively. During the same thermal step, a study was also made of the channel response to laser light injected into each crystal. In this case, assigning all the observed changes in response to a change in the APD gain, its variation with temperature was determined to be $-2.4\%°\text{C}^{-1}$ for M0' and $-2.1\%°\text{C}^{-1}$ for SM1, with a spread among the channels of 0.06 and $0.07\%°\text{C}^{-1}$, respectively.

The nominal operating temperature of the CMS ECAL is 18°C. Keeping the constant term of the energy resolution (the contribution to the fractional energy resolution which is independent of energy) below a few permil requires the temperature to be stabilised to within 0.05°C. In recent years, a large effort [7] has been put into the design of the cooling system so as to comply with this severe thermal requirement. The system employs water flow to stabilise the detector. In the barrel, each supermodule is independently supplied with water at 18°C. The water runs through a thermal screen placed in front of the crystals which thermally decouples them from the silicon tracker, and through pipes embedded in the aluminium grid, connected in parallel. Between the grid and the motherboards, a 10 mm thick layer of insulating foam (Armaflex®) is placed to minimise the heat flowing towards the crystals by convection (Fig. 2, on the left). Return pipes distribute the water through a manifold to a set of aluminium cooling bars. These bars are in close contact with the VFE cards and the LVR cards (Fig. 2, on the right) and have been designed to absorb the heat dissipated by the electronics components mounted on these cards. A thermally conductive paste (gap filler 2000, produced by Bergquist™) is used to provide a good contact between the electronic components and a metal plate facing each board. This plate is coupled to the cooling bar by a conductive pad (ultrasoft gap pad A2000, also produced by Bergquist™). Both the gap pad and the gap filler have been irradiated with twice the dose expected in the ECAL endcaps after 10 years at the LHC and have shown no change in character or loss of performance.
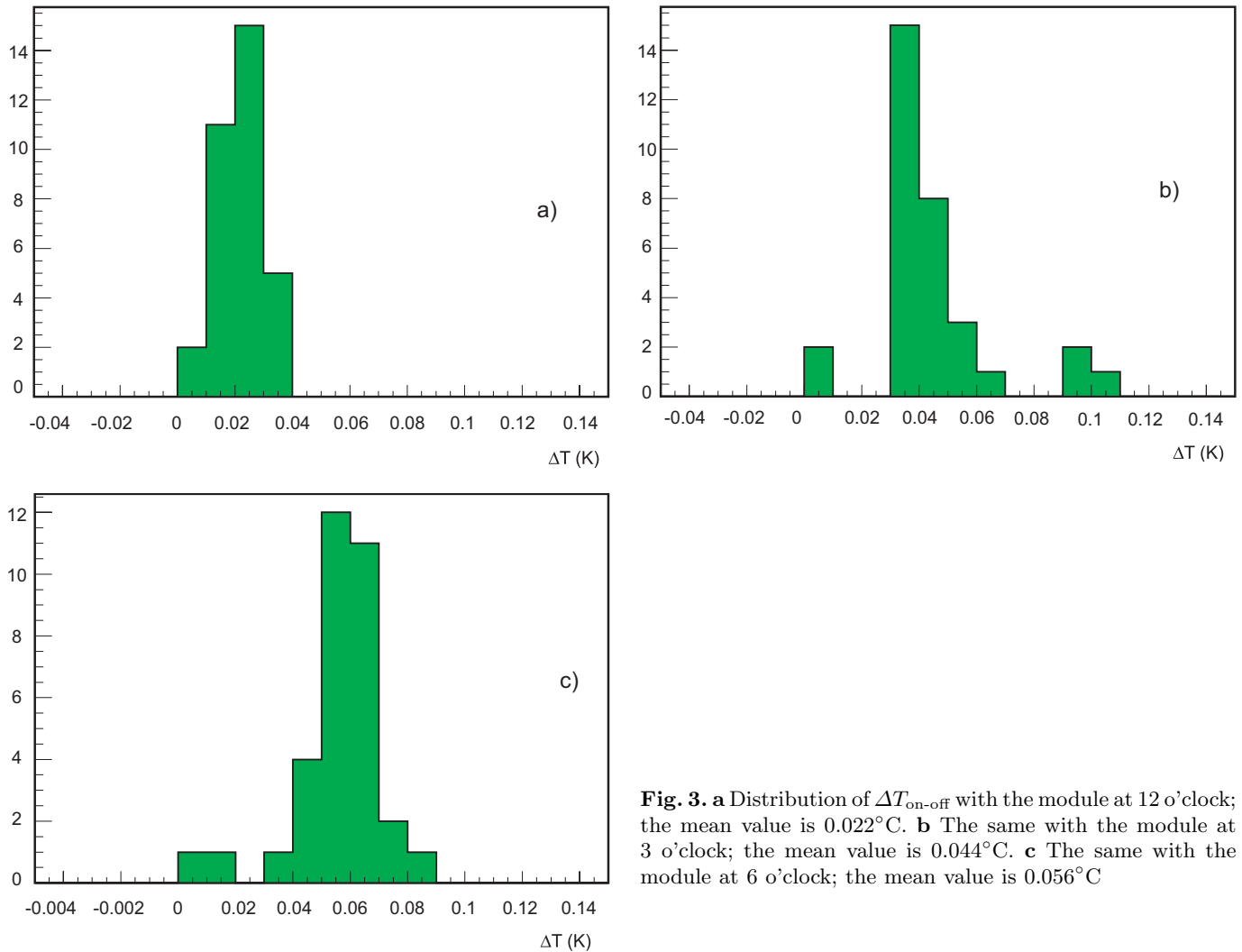
Fig. 3. a Distribution of $\Delta T_{\text{on-off}}$ with the module at 12 o'clock; the mean value is $0.022°$C. **b** The same with the module at 3 o'clock; the mean value is $0.044°$C. **c** The same with the module at 6 o'clock; the mean value is $0.056°$C

On the right, the cooling bars are shown with some of the cards inserted.

In summer 2003 thermal tests were carried out at CERN in the assembly laboratory on a type 2 module containing 400 crystals and equipped with dummy VFE and LVR electronics cards. The components of the read-out circuits were replaced with special power resistors MP725 and MP930, produced by Caddock Electronics. These allowed the same thermal contact with the housing and dissipated the same amount of heat as expected for the components on the real electronics cards. These dummy electronics cards were supplied by eight power units dissipating 72.7 W per trigger tower, 1160 W for the whole module, which corresponds to about 3 W per channel. Subsequent measurements on a completed supermodule have shown that the actual dissipation is slightly lower, 2.6 W per channel.

A total of 110 sensors were read out, including 40 NTC Betatherm thermistors, embedded in every tenth APD capsule. Other sensors monitored the eight high voltage supplies and the flux and temperature of the cooling water. The remaining sensors were temperature probes (PT100 or AD590) distributed around the module on the grid, the

cooling bars and the electronics boards. The cooling water was chilled and stabilised to $0.01°$C by a cooling unit produced by Lauda, and the flow set to 0.30 l/s to reproduce the operating conditions of CMS. An extra cooling unit was employed to supply an auxiliary water circuit running across the sides of the module in order to have the best possible insulation from changes of temperature in the laboratory (in CMS, each module will be surrounded by other modules at the same nominal temperature, so that no lateral insulation will be necessary). The module was mounted in a metal cradle which could rotate around the ϕ direction.

Given the stability of the cooling water and the ECAL's external thermal screening, the only source of temperature variation within the ECAL is possible variation of the power dissipated by the electronics. To investigate the sensitivity to this, the temperatures of the thermistors in the APD capsules were measured with the electronics switched on and switched off. The change in temperature, $\Delta T_{\text{on-off}}$, was determined from sets of measurements in each state. Each set consisted of about 1000 measurements taken over a few hours. This procedure ensured that the statistical uncer-

tainty on a single thermal excursion $\Delta T_{\text{on-off}}$ was negligible. The remaining, systematic, uncertainty was due to the calibration procedure of the sensors and was estimated to be less than 0.01°C. Since convection might play an important role in the heat transmission, the measurements were repeated in three orientations: with the electronics on top of the module (12 o'clock in CMS), at a side (3 and 9 o'clock) and below (6 o'clock). (In CMS the electronics is positioned at all azimuthal angles.) The results for $\Delta T_{\text{on-off}}$ in these positions are shown in Figs. 3a–c. Each entry in the histograms corresponds to a measured temperature excursion, $\Delta T_{\text{on-off}}$, for one of the thermistors used. The maximum measured change was 0.1°C, with a mean change of 0.056°C for the worst position (6 o'clock, where the APDs are above the electronics). However, the electronics will remain switched on during the experiment with little variation in power dissipation and so the temperature variations should be much smaller than these values. Therefore the contribution to the constant term of the energy resolution due to thermal fluctuations will be negligible, even without temperature corrections.

5 HV stability

The APDs are silicon avalanche photodiodes, which are operated with an internal amplification, M, of 50. Since the gain has a strong dependence on the bias voltage $(1/M \, dM/dV \approx 3.2\%/\text{V} \text{ at } M = 50)$, the APDs require a bias voltage supply system with a stability of few tens of mV (including long term stability, regulation, noise and ripple, and reproducibility) in order to give a negligible contribution to the constant term of the energy resolution. For this reason a special HV system has been developed for the CMS ECAL in collaboration with the CAEN company. It is made of a control crate (SY1527) hosting several boards (A1520E). Each board has nine channels and each channel supplies 50 crystals (100 APDs, grouped to have the same bias voltage requirement). Each channel can give a bias voltage from 0 to 500 V with a maximum current of 15 mA. Laboratory measurements [8] have shown that the stability is better than 20 mV.

A prototype of this system was tested in the summer of 2002, with 200 APDs supplied by two HV channels. The HV crate was connected to the module via a cable of 120 m, as it will be after installation in the experiment. The HV system was controlled and continuously monitored using a Labview program and the CAEN OPC server to access the crate. The program allowed the setting of HV values, and the monitoring of the voltage and the current for each channel. The stability of the crystals was monitored with the laser system described in the next section. The APD bias voltage was permanently monitored by a sense wire close to the load. Figure 4 shows the stability of this voltage, as monitored by the HV crate for the two channels over several days. Calibration measurements performed in the laboratory show that the fluctuations measured over the sense wires correspond to a dispersion of the voltage at the load of less than ±20 mV, as required by the specifications.
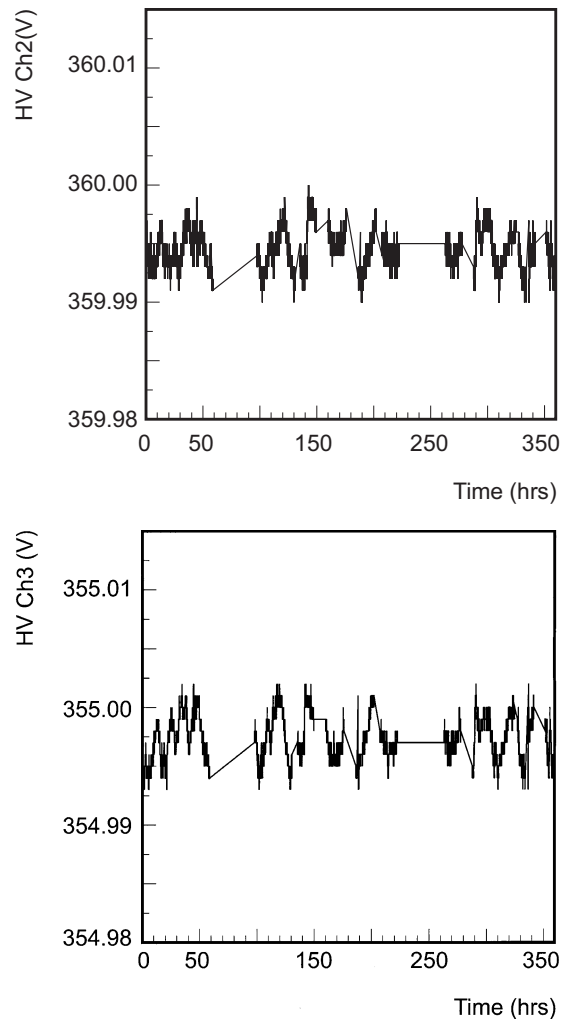

Fig. 4. Stability of the high voltage monitored by the sense wire for two channels

6 Crystal transparency monitoring

Variations in the light transmission of the crystals are expected at the LHC due to radiation damage and recovery. The damage has been shown [9] to be the creation of colour centres, which then partly disappear due to self annealing. In the high luminosity regime, the response of the barrel crystals is expected to drop by a few percent in the first few hours of operation with colliding beams. Due to the competition between damage and recovery the light loss then saturates at a level that depends on the dose rate. Frequent optical transmission measurements of all the ECAL crystals are thus required in order to obtain short-term corrections to the calorimeter response. An optical monitoring system has been developed consisting of a laser source and an optical fibre distribution system. The system is described in detail elsewhere [10] and a schematic overview is shown in Fig. 5. The final system consists of two lasers operating at four different wavelengths (440, 495, 706 and 796 nm) but in these tests only the blue (440 nm) laser was used, whose wavelength is close to the scintillation emission peak of the crystals. This laser light is distributed through optical fibres and injected simultaneously into 850 crystals
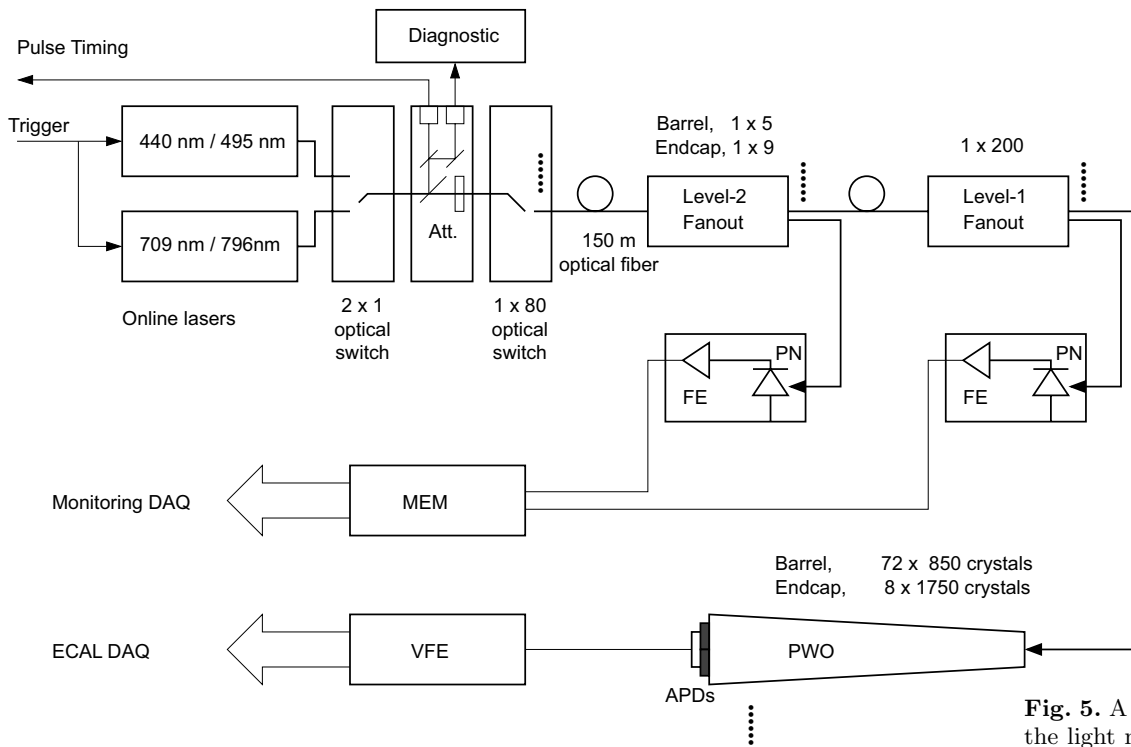
Fig. 5. A schematic overview of the light monitoring system

(half a supermodule). PN diodes measure the amplitude of the laser pulses as received by groups of 200 crystals, and provide a normalisation of the magnitude of the injected light pulse. The system, including PN diodes and fibres, has been shown to be radiation hard for doses up to those expected for 10 years of high luminosity LHC running [10].

The change in amplitude of the APD signal, due to a change in the transparency of the crystal, is not the same for an electromagnetic shower as for laser light injected through the front of the crystal. An important reason for this is that the mean light path lengths through the crystal are different in the two cases. For small variations of the response the relationship between the two responses can be modelled as $\frac{S}{S_0} = \left(\frac{R}{R_0}\right)^\alpha$, where S/S_0 and R/R_0 are the variations of the response to scintillation and laser light respectively.

The validation of the light injection system with its final laser and read-out electronics and the feasibility of determining the short-term corrections were the main goals of dedicated beam tests during 2002 and 2003. The channel response to laser light without any incident beam, normalised to a PN diode, was stable to 0.15% for all 100 channels over a period of 18 days, fully meeting the specifications. During the tests with beam, 24 crystals were exposed to a high intensity 120 GeV electron beam in H4. A typical irradiation run lasted for 10 hours with dose rates from 0.2 to 0.4 Gy/h at the shower maximum, larger than that expected in the barrel at high luminosity (0.15 Gy/h at $10^{34}\,\mathrm{cm}^{-2}s^{-1}$). Under these conditions, the signal loss is expected to saturate at around 5%. During a 0.2 Gy/h irradiation the flux of beam electrons entering the front of the crystal was about 30,000 particles per SPS spill. Each irradiation period was followed by a recovery period

of comparable duration, during which the beam intensity was reduced by an order of magnitude. Incident electrons passing through a $5\times5\,\mathrm{mm}^2$ plastic scintillator device in front of the centre of the crystal being irradiated triggered the read out of the detector. These electron runs, of about 40 SPS spills, were alternated with short laser runs with about 1,500 laser pulse triggers. Signals from electrons and from the laser from consecutive runs were then compared. Figure 6a shows data for 120 GeV electrons and the laser collected from a crystal during irradiation and recovery. The damage and the recovery are clearly seen. To get the correlation between electron and laser data at equal times, the latter are first interpolated, according to the radiation-damage model described in [11]. Figure 6b shows the resulting correlation, and its fit with $\alpha = 1.6$. In the procedure, some arbitrariness is left in the choice of the starting points S_0 and R_0. This uncertainty does not affect the correlation.

In Fig. 7, the distribution of α is presented for the 24 crystals measured over the two years. The dispersion of the values is about 6.5%. The precision on the determination of α is about 3%, so that the intrinsic dispersion of its value is deduced to be about 6%. Thus for crystals showing a decrease in signal size of 5% a single value of α can be used to correct the loss, with a precision of 0.3%.

7 Very Front End electronics performance

For the last two weeks of available beam time in 2003, the 50 crystals of two trigger towers of supermodule SM1 were equipped with prototypes of the new VFE electronics. After amplification, the signal, shaped to peak after about
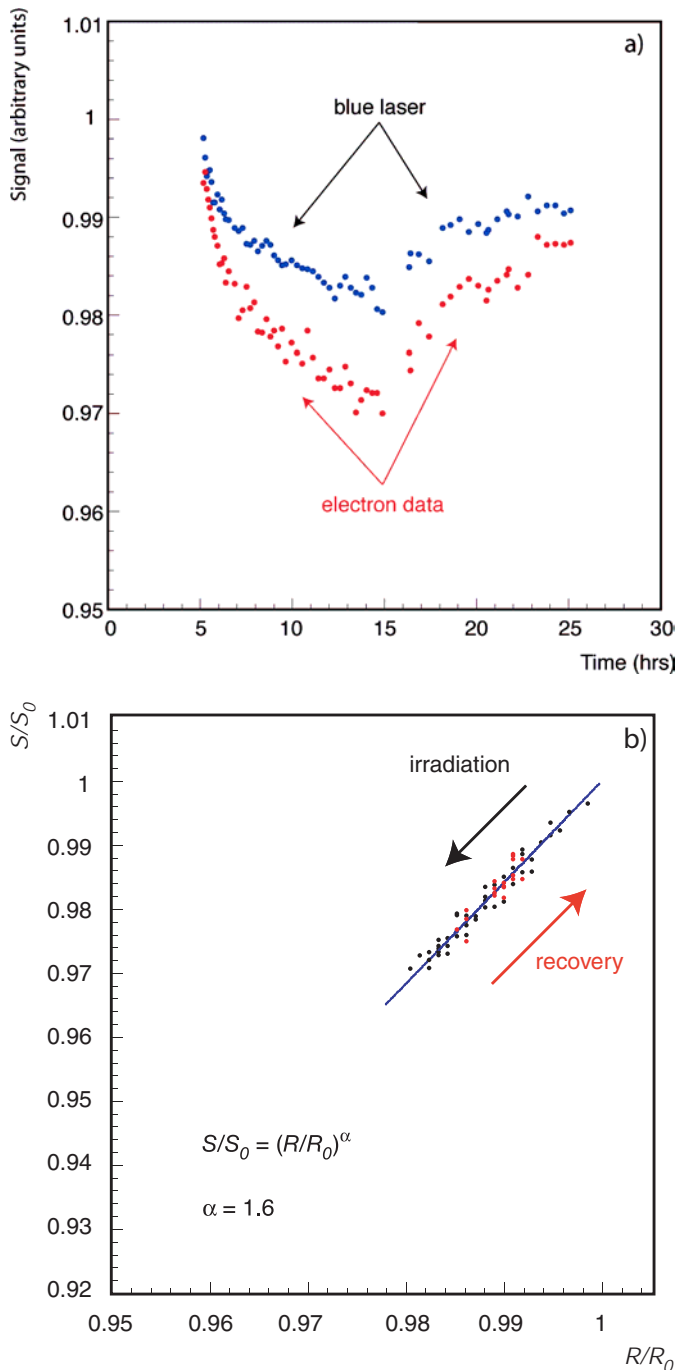
Fig. 6. a Data for 120 GeV electrons and 440 nm laser pulses shown as a function of time during irradiation and recovery periods. **b** S/S_0 plotted against R/R_0 for the same data and the fit for $\alpha = 1.6$

Fig. 7. Distribution of the coefficient α for the 24 crystals

50 ns, is sampled and digitised at 40 MHz. For each trigger the consecutive digitisations within a defined time frame (250 ns) were read out.

In order to obtain the amplitude of a digitised pulse, the samples within the time frame were weighted and summed as $A = \sum w_i s_i$ where w_i and s_i are the weight and value of the sample for digitisation i, respectively. The weights were determined by a procedure that minimises the noise contribution to the signal, and is described elsewhere [12].
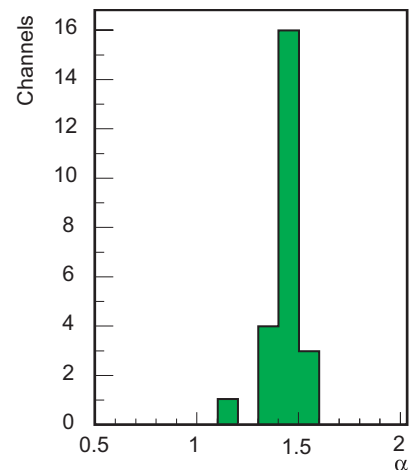
At a given time after the start of the pulse the corresponding weight is common to all data. During CMS operation, the 40 MHz sampling clock will be synchronous with the LHC beam crossing, and thus with the signals from the crystals. Hence the sampling times will be fixed relative to the start of the pulse. In the test beam, however, the signal pulses were asynchronous and so a TDC was used to measure their phases with respect to the clock. Then a separate set of weights was determined for each 1 ns of the 25 ns phase and the appropriate set used for each event according to its measured phase. In order to calculate the optimum weights, a description of the pulse shape is needed. For these data an analytic description [12] of the pulse shape, fitted to the average pulse shape from all crystals, was used. However, this analytic function does not describe the leading edge of the pulse reliably and hence the first sample on its rising edge was excluded. Six samples were used for the analysis: two before the pulse (sampling the baseline) and four on the pulse, covering the main peak region. In determining the weights the constraint $\Sigma w_i = 0$ was applied, which results in sets of weights which subtract the baseline event by event. This method is effective in removing low frequency noise (i.e. noise at frequencies much lower than the sampling frequency).

The noise performance was measured by running the amplitude reconstruction on randomly triggered events, which measure the ADC pedestals. For the sum of nine crystals the rms noise is 129 MeV and for the sum of 25 crystals it is 224 MeV (Fig. 8). This indicates that the rms noise per channel is about 44 MeV, with little channel-to-channel correlated noise. In addition, the noise peaks of Fig. 8 are centred close to 0 MeV, showing that the pedestals and any baseline shifts have been properly subtracted.

The data with the new VFE electronics were taken using low flux tertiary electron beams of momenta 25, 50, 70 and 100 GeV/c. A $20{\times}20\,\mathrm{mm}^2$ trigger counter, roughly matching the transverse beam size, was used for all electron runs. Events were then selected where the incoming electron was incident on a $4{\times}4\,\mathrm{mm}^2$ area centred on the point at the front of the struck crystal where the response is maximum. (The point of maximum response, or maxi-
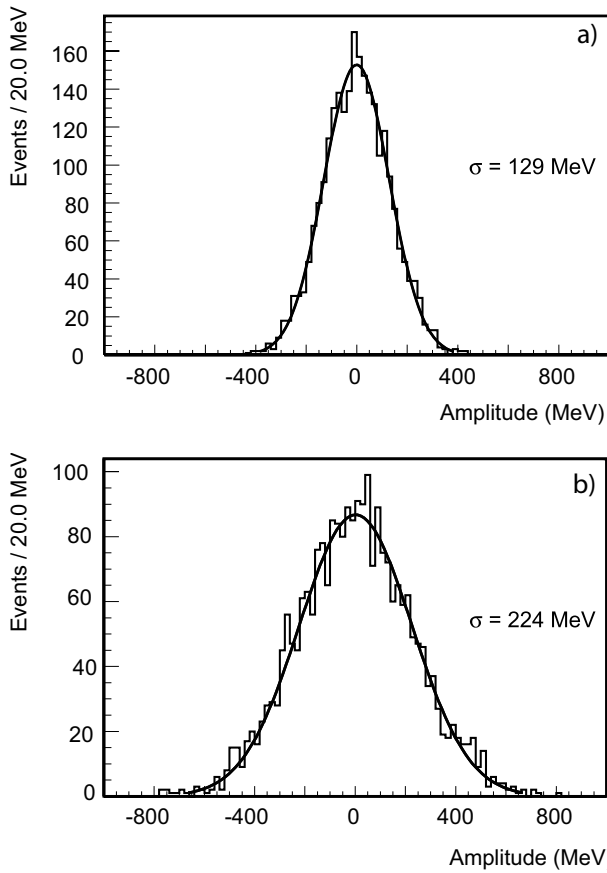
Fig. 8. The signal measured in **a** a sum of nine crystals and **b** a sum of 25 crystals, when the amplitude reconstruction is applied to events taken with a random trigger and having no signal

mum shower containment, is not the centre of the front face because the crystals point 3° away from the beam axis in both transverse directions.) This restriction on the incident coordinate was to minimise the effects of inter-calibration errors and sensitivity of the shower containment to the point of impact, since the goal was to examine the performance of the electronics. The shower energy was reconstructed by summing the energy measured in a cluster of 3×3 crystals centred on the struck crystal. The channels were inter-calibrated as described in the next section, using constants derived from the same data taking period. However, it was not possible to take inter-calibration data for all channels, and so the constants for these channels were taken to be 1. The energy resolution was measured from the reconstructed energy distribution using a Gaussian fit in an interval of $\pm 2\sigma$ around the mean. Figure 9a shows the distribution of the reconstructed energy at 100 GeV for a 3×3 crystal matrix. The non-Gaussian tail to the left of the peak is thought to be caused by energy loss in the beam line, although this could not be verified. The beam momentum spread, $\sigma(P)/P$, ranging from 0.12% at 25 GeV/c to 0.21% at 100 GeV/c, was quadratically subtracted from the fitted Gaussian width to obtain the ECAL resolution.

In Fig. 9b the resolution with the beam spread subtracted is shown as a function of energy, for 3×3 crys-
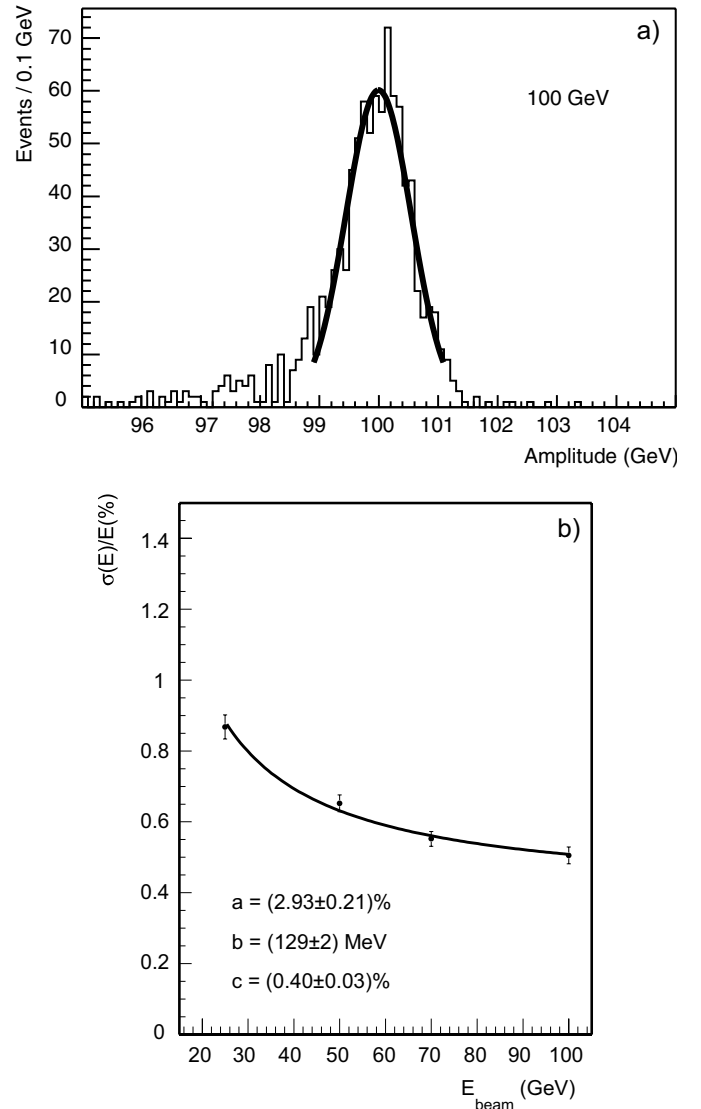

Fig. 9. a Distribution of the reconstructed energy at 100 GeV for a 3×3 crystal matrix. **b** The energy resolution as a function of energy with the beam momentum spread subtracted. The line is the result of a fit by the standard parametrisation $\sigma(E)/E = a/\sqrt{E(\mathrm{GeV})} \oplus b/E \oplus c$

tal matrices. The energy resolution as a function of energy has been fitted by the standard parameterisation, $\sigma(E)/E = a/\sqrt{E(\mathrm{GeV})} \oplus b/E \oplus c$, with the noise term b/E fixed at the value measured in the pedestal runs. The parameters of the fit meet the target specifications. Preliminary analysis of data taken in 2004 shows that this performance can be maintained for electrons incident randomly over the supermodule.

8 Inter-calibration and comparison to crystal light yield measurements

The fraction of the shower energy contained within a crystal depends on the position of incidence of an electron, which was determined in the test beam by a set of hodoscopes.
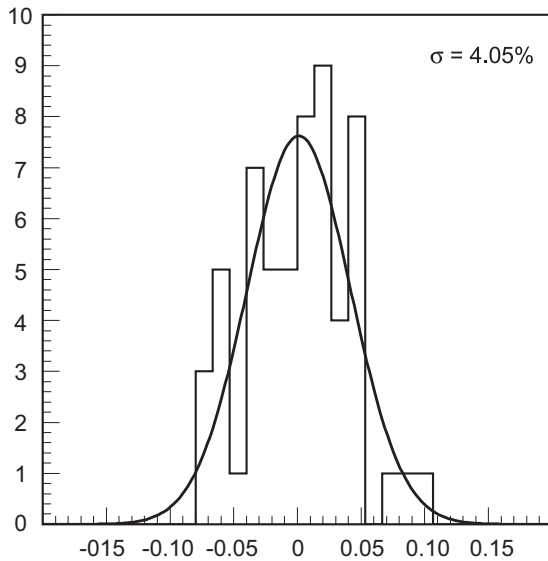
Fig. 10. Distribution of $(C_{i(\mathrm{lab})} - C_i)/C_{i(\mathrm{lab})}$ for crystals measured in 2003

Thus, to inter-calibrate the response of the crystals, a correction to the data was applied according to the incident position. The measured single crystal response as a function of the transverse incident position was fitted by a fourth order polynomial, separately in the two transverse coordinates. These two functions were then used to correct the signals of each electron according to its incident position. The resulting energy distribution, corresponding to that for electrons at the position of maximum response, was then fitted by a Gaussian whose mean value determined the calibration constant, C_i, of that crystal. The distribution of these calibration constants has a standard deviation of about 8%.

The spread in C_i is mainly due to the variation of the crystal light yield. The light yields are measured in the laboratory using a ^{60}Co source and optical transmission measurements [13] during the crystal qualification process. The reproducibility of these laboratory measurements has been determined to be about 2.5%. The results can be used to determine preliminary inter-calibration constants, $C_{i(\mathrm{lab})}$. Figure 10 shows a comparison of these constants with those determined from the relative responses measured in the test beam. The distribution of $(C_{i(\mathrm{lab})} - C_i)/C_{i(\mathrm{lab})}$ for crystals measured in 2003 has an rms of 4%. This result suggests that at the start of CMS running at the LHC, the light yields measured during the crystal qualification process can be used as a useful initial inter-calibration.

9 Conclusions

Tests of modules and supermodules of the CMS electromagnetic calorimeter with final versions of the cooling system and the high and low voltage regulation have demonstrated a performance consistent with the design goals for thermal and high voltage stability. The monitoring system has been shown to track changes in crystal transparency due to radiation damage and recovery, with an acceptably small channel-to-channel variation in the relation between response to the laser light and to electrons. Prototypes of the final design of the Very Front End electronics have demonstrated satisfactory noise levels, and results from tests in high energy electron beams have shown that the expected energy resolution can be achieved. These results are an important step in demonstrating that the CMS ECAL will fulfil its challenging physics programme at the LHC.

References

1. CMS Collaboration, The Compact Muon Solenoid Technical Proposal, CERN/LHCC 94-38 (1994)
2. CMS Collaboration, The Electromagnetic Calorimeter Technical Design Report CERN/LHCC 97-33 (1977)
3. A.A. Annenkov, P. Lecoq and M.V. Korzhik, Nucl. Instrum. Methods A **490**, 30 (2002)
4. E. Auffray et al., Nucl. Instrum. Methods A **412**, 223 (1998); G. Alexeev et al., Nucl. Instrum. Methods A **385**, 425 (1997); J.P. Peigneux et al., Nucl. Instrum. Methods A **378**, 410 (1996)
5. Z. Antunovic et al., Nucl. Instrum. Methods A **537**, 379 (2005), and references therein
6. J.P. Walder et al., IEEE Trans. Nucl. Sci., **48**(6) (2001)
7. I. Baillon et al., Design and Performance of the Cooling System for the Electromagnetic Calorimeter of CMS, to be published in: the Proceedings of 2004 IEEE Instrumentation and Measurement Technology Conference, Como, Italy, May 18–20, 2004, CMS CR-2004/030
8. A. Bartoloni, The Power Supply System for the CMS-ECAL APDs, in: Proceedings of the 7$^{\mathrm{th}}$ Workshop on Electronics for LHC Experiments LEB 2001, Stockholm, Sweden, 10–14 Sept. 2001, CERN-2001-005, 358 (2001)
9. E. Auffray et al., Nucl. Instrum. Methods A **402**, 75 (1998), and references therein
10. R.Y. Zhu, Nucl. Instrum. Methods A **537**, 344 (2005)
11. P. Bonamy et al., The ECAL Calibration: Use of the Light Monitoring System, CMS Note 1998/013
12. P. Paganini et al., Pulse Amplitude Reconstruction in the CMS ECAL Using the Weights Method, CMS Note 2004/025
13. F. Cavallari et al., A Proposal for Intercalibration of ECAL Crystals Using Laboratory Measurements, CMS Note in preparation

ELSEVIER

Simulation of a vacuum phototriode with SIMION 3D

Peter R. Hobson*, Ignacio Yaselli

School of Engineering and Design, Brunel University, Uxbridge UB8 3PH, UK

Available online 12 June 2006

Abstract

An electron-optic model of a 26 mm diameter vacuum phototriode (VPT) photodetector was developed using SIMION 3D software extended by additional code to simulate secondary emission at the dynode. The predictions of the variation of gain with magnetic field for mesh anodes with 100, 40 and 7 lines per mm and fields from 0 and 4 T are presented. The predicted time development of the signal at 0 T is presented and compared with experimental data obtained by illuminating a production VPT for the electromagnetic endcap calorimeter of CMS with 60 ps laser pulses at a wavelength of 435 nm.
© 2006 Elsevier B.V. All rights reserved.

PACS: 24.90.Mc; 41.20.−q; 85.60.Ha

Keywords: Photodetector; Photomultiplier; LHC; Simulation; Electron-optics

1. Introduction

The vacuum phototriode (VPT) is a single gain stage photomultiplier, which is very insensitive to high magnetic fields compared to a multi-stage device. It has been chosen as the photodetector for the homogeneous lead tungstate endcap electromagnetic calorimeter of the Compact Muon Solenoid (CMS) experiment [1] which is currently under construction at CERN, Geneva, Switzerland. In the endcap region the VPT is located in the full 4 T magnetic field of the CMS solenoid. Other VPT have been used in a previous generation of particle detectors, for example the endcap calorimeter of OPAL [2] and the STIC of DELPHI [3]. A VPT for CMS is shown schematically in Fig. 1.

Photoelectrons from the cathode are accelerated towards the anode by the high electric field. The anode is a partially transmitting metal mesh and the primary electrons that are not directly captured are slightly decelerated before hitting a solid dynode with a high secondary emission coefficient. The secondary electrons produced at the dynode are accelerated back towards the anode where a fraction is collected; these produce the bulk of the signal flowing in the external circuit. Those transmitted are decelerated in

the anode–cathode gap, return to the anode, where a further fraction are collected, and then back to the dynode where a further generation of secondary electrons can occur.

The simple planar geometry, coupled with small inter-electrode gaps, suggests that such a VPT structure should be fast and have good timing resolution. In this preliminary study we discuss a simulation of a model of a CMS production VPT [4] using an extended version of the SIMION 3D electron optic simulation software and present our predictions for gain at fields from 0 to 4 T. We have also made an initial measurement of the relative time delay as a function of operating potential of a VPT illuminated by 60 ps laser pulses at a wavelength of 435 nm.

2. Simulation of gain and time response

To simulate the VPT we used version 7.0 of the commercial ion/electron optic simulation program SI-MION 3D™ [5]. This enables the tracking of electrons or ions through static electric and magnetic fields defined by a three-dimensional geometric electrode model. SIMION tracks the path and calculates the time-of-flight of each particle, but once a particle hits an electrode the data relating to the particle is stored and the particle is lost. In order to simulate the secondary emission from a VPT
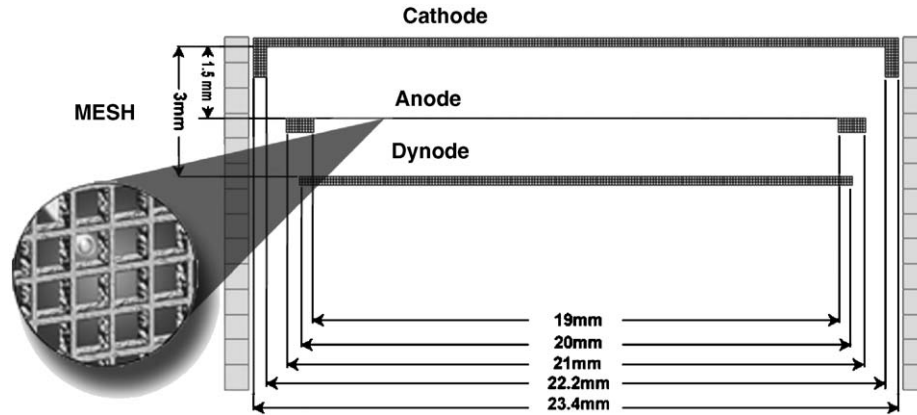

Fig. 1. Schematic of a CMS production VPT. The outside diameter of the tube is 26 mm. Only the parts modelled in the SIMION 3D simulation are illustrated. The anode is made up of a metal ring supporting a thin mesh with a transparency of approximately 50% over a diameter of 19 mm.

dynode we have integrated SIMION with our own code, which uses the hit position of the primary electrons on the dynode as the source of secondary electrons whose time origin is now equal to the flight time of the primary. This process is repeated until the incident energy of an electron hitting the dynode has fallen below a user-defined threshold.

The detailed simulation of the mesh anode is a critical element in our studies. SIMION allows for an "ideal mesh" which is fully transparent and exists just to define a surface at a constant potential through which ions or electrons can pass unhindered. In our VPT we have two different length scales at which we must simulate a potential array and track electrons. The basic size of the VPT, and its inter-electrode gaps, is on the scale of millimetres; however, the anode mesh in production tubes has 100 lines per millimetre in two orthogonal directions. In order to avoid splitting the macroscopic dimensions of the VPT into millions of fundamental cubes whose side ("grid-unit", gu) would be of order 5 μm, we used the concept of multiple instances. The large-scale structures are simulated at a resolution of 0.083 mm per gu with an ideal (100% transmission) anode mesh in order to generate the correct electrostatic potentials. Superposed on top of the ideal mesh is a very thin cylindrical volume in which a real (i.e. capable of absorbing particles) mesh is simulated at a spatial resolution appropriate to the mesh being modelled. We simulated three different meshes each with 50% optical transmission. One mesh had 7 lines per mm (0.032 mm per-gu), one had 40 per mm (0.006 mm per gu) and a third with 100 lines per mm (0.005 mm per gu). The 100 lines per mm mesh simulates the anode mesh fitted to production VPT.

The modelling of the dynode secondary emission is currently very simple. This is deliberate as we wish to understand exactly what contributes to different experimentally observed aspects of VPT performance, and with a simple model one level of complexity is removed. We used a multiplicative factor, which only depends on the incident energy of the primary electron incident on the dynode. At any given energy a constant number of secondary electrons

are produced, each with an initial energy of 5 eV. The emitted angle is randomly varied by up to 5° from the surface normal.

2.1. Gain at 0T

The gain of the VPT depends on the secondary emission of the dynode and the transparency of the mesh. A simple model [6] predicts that a transparency of around 50% is optimum. The planar geometry with small inter-electrode gaps should also result in a very fast pulse with short transit time. Although it is already known from beam tests that the speed of response of the VPT for CMS is fast (<10 ns) it has not yet been directly measured.

The predicted and measured gain, as a function of dynode voltage, at 0T field for a production VPT with a 100 lp m mesh are shown in Fig. 2. In order to obtain reasonable agreement for absolute maximum gain the secondary emission gain G was modelled as

$$G(V_{K-D}) = \frac{V_{K-D}}{40},$$

where V_{K-D} is the potential difference between the cathode and the dynode and the units are Volts.

The simulated arrival times of electrons on the anode is shown in Fig. 3. There is an increasing transit time with increasing dynode potential as the accelerating potential between the anode and dynode decreases and thus the average velocity of the secondary electrons decreases too. A preliminary measurement of relative delay has been made and is described in the next section.

2.2. Response to fast laser pulsed illumination at 0T

A preliminary experimental verification of the predicted variation of the time delay of the anode signal with dynode potential when illuminated by a fast light pulse has been made. The centre of the photocathode of a production VPT, at 0T, was illuminated by fast pulses (60 ps FWHM at 435 nm) from a PicoQuant SEPIA 808 diode laser. The
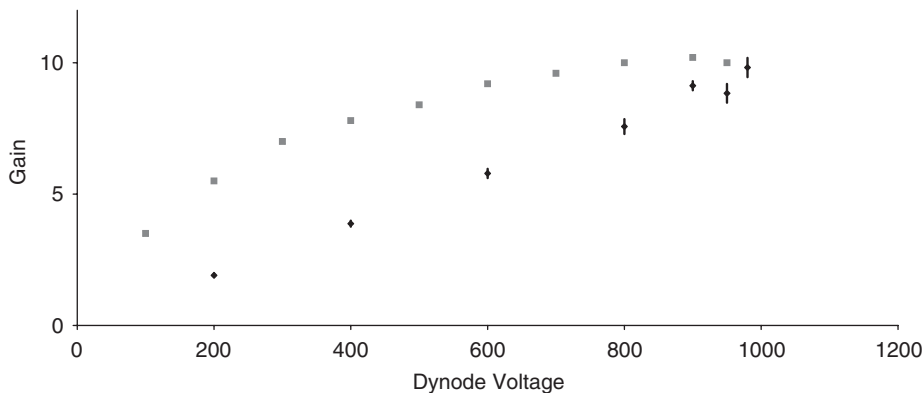
Fig. 2. The absolute gain of a real VPT (upper data points) and a simulated VPT (lower data points with standard error on the mean) as a function of V_{Dynode} for an anode potential of $+1000\,\text{V}$ and grounded photocathode.
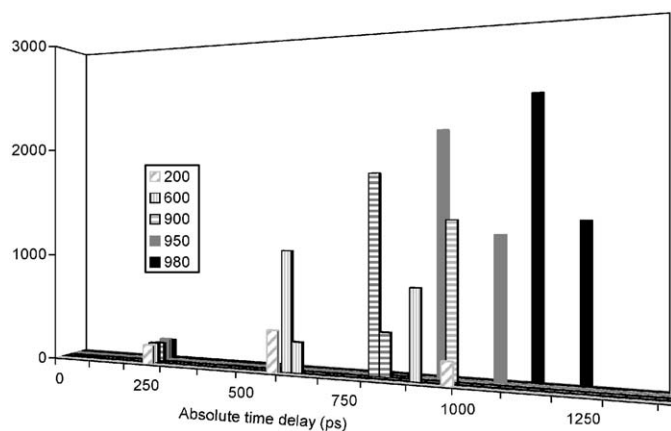

Fig. 3. The simulated arrival times of electrons at the anode for different dynode voltages. The anode potential is fixed at $+1000\,\text{V}$. The small peak at 250 ps are photoelectrons directly collected by the anode. The vertical scale is proportional to the gain of the device.
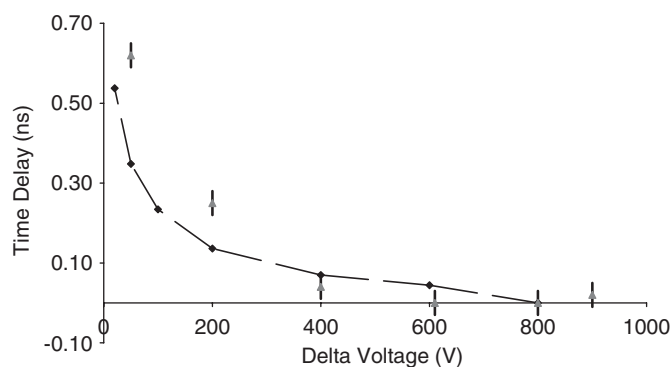

Fig. 4. The delay from laser trigger to the peak of the anode signal as a function of the anode to dynode potential difference. Experimental data from a production VPT is shown as data points with estimated systematic error shown. The points with curve to guide the eye are the time delay (mean collection time) from a SIMION simulation of a VPT with 100 lpm mesh. The time difference is defined to be zero at a voltage difference of 800 V for both the experimental and simulated data.

cathode of the VPT was held at $-1000\,\text{V}$, the dynode at variable negative potential, and the anode DC coupled to the $50\,\Omega$ input of a digital oscilloscope (LeCroy WavePro 950, 1 GHz analogue bandwidth, 16 giga-samples per second). The rise-time of the leading edge (10–90%) was around 600 ps, although this was in part limited by the oscilloscope bandwidth of 1 GHz.

The data in Fig. 4 show the expected trend of decreasing delay with increasing potential. Since the potential differences are much higher than the typical initial energy of a secondary electron one would expect that the time delay should decrease as $1/\sqrt{V_{A-D}}$. Both the experimental and simulated data are well described by such a relationship (R^2 of >0.97).

2.3. Gain at fields up to 4T

The response of the VPT to magnetic fields is of paramount importance for its application in CMS. Tubes will be located in the full 4T field. The axis of rotational symmetry of the VPT will lie at angles from $8°$ to $26°$ to the magnetic field dependent on their location in the endcap.

Our QA procedures for the production VPT evaluate their angular response to a field of 1.8T and batch sample their relative gain at a fixed angle of $15°$ to a 4T field. One aim of this programme of simulation is to check that nothing unusual is predicted to happen at other angles at the full field. To demonstrate the effect of the mesh pitch on the relative gain as a function of field, we simulated a production VPT with three different mesh pitches. Fig. 5 shows the simulated variation of gain as a function of magnetic field. In each case only the central 6 mm diameter of the photocathode is a source of photoelectrons.

3. Conclusions

We have demonstrated that a SIMION simulation of a production vacuum phototriode reproduces the major features (0T gain and relative time shift) of a real device. However, the simple dynode model does not reproduce the gain saturation effect seen in real devices. The effect of changing from fine meshes to a coarse mesh (7 lpm) illustrates a dramatic fall in gain as a function of magnetic field compared to the fine mesh used in production tubes.
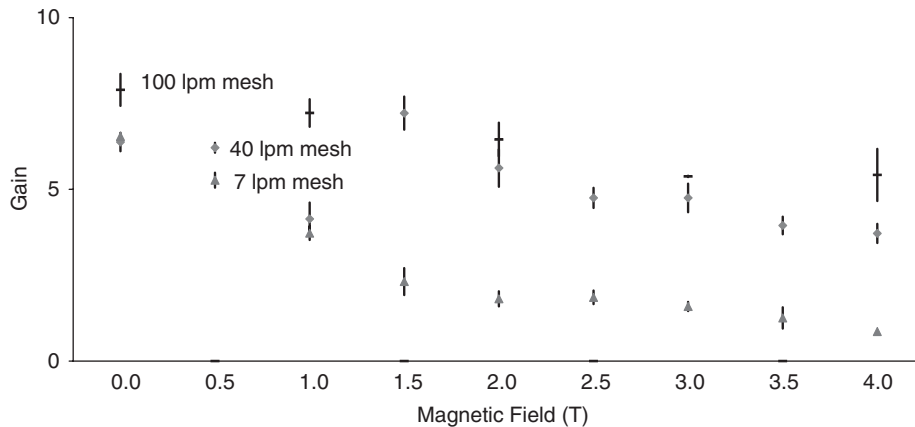
Fig. 5. The simulated variation of gain with field for a VPT at an angle of 15° to the field for three different mesh sizes (each with 50% transparency). The anode and dynode voltages were 1000 and 800 V, respectively. The standard errors on the mean are shown. The response of the 100 lpm mesh was only simulated at integer values of the magnetic field, and the error bar at 3T is comparable to the size of the symbol.

We plan to improve the dynode secondary emission model, to include saturation, statistical fluctuations of the gain and a more realistic model of the energy spectrum of the secondary electrons. We will also make further measurements of the time response and investigate the effect of manufacturing tolerances, such as gap variation or angular misalignment of the dynode, on the performance of the VPT in high magnetic fields.

References

[1] CMS: The Electromagnetic Calorimeter Project TDR", CERN/LHCC 97-3 (CMS TDR 4) 15 December 1997.
[2] R.M. Brown, et al., IEEE Trans. Nucl. Sci. NS-32 (1985) 736.
[3] P. Abreu, et al., The DELPHI collaboration, Nucl. Instr. and Meth. Phys. Res. A 378 (1996) 57.
[4] K.W. Bell, et al., IEEE Trans. Nucl. Sci. NS-51 (2004) 2284.
[5] SIMION 3D V7.0, available from Scientific Instrument Services, Inc., 1027 Old York Rd, Ringoes, NJ 08551, USA
[6] K.W. Bell, et al., Nucl. Instr. Meth. Phys. Res. A 469 (2002) 29.

TIMING PERFORMANCE OF A VACUUM PHOTOTRIODE

DAWN E. LESLIE, IGNACIO YASELLI AND PETER R. HOBSON[*]
School of Engineering and Design, Brunel University, Uxbridge UB8 3PH, UK

The timing performance of a vacuum phototriode (VPT) has recently been simulated using SIMION 3D software [1] to develop an electron-optic model [2]. In this work, more precise treatment of the approximation is detailed and comparison is made with corresponding experimental data. The origin of the signals features is investigated and interpreted, affording a deeper understanding into the operation and timing potential of these devices.

1. Introduction

The electromagnetic calorimeter of the Compact Muon Solenoid detector (CMS) [3] at the Large Hadron Collider, CERN, uses large monocrystals of the scintillator lead tungstate coupled to sensitive photodetectors, which in the endcap are vacuum phototriodes (VPT) [4] manufactured in Russia by Research Institute Electron (RIE) [5].
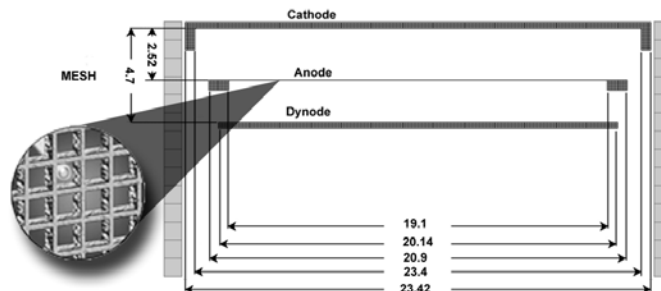

Figure 1. Illustration of VPT components (after Hobson and Yaselli [2]). The mesh anode has 50% transparency and a pitch of 10 micrometres.

The VPT characterised in this work (see Figure 1) was supplied by RIE and is a single gain-stage photomultiplier with a diameter of 26mm. In our experimental arrangement, the centre of the photocathode is illuminated by a 60ps pulse from a PicoQuant SEPIA 800 diode laser (λ = 435 nm). The

relatively simple planar geometry and small inter-electrode spacing suggests that the VPT should be very fast, with good timing resolution.

2. Initial Computer Simulation: *SIMION 3D*

The amplitude of the induced current in the anode load resistor is proportional to the intensity of the light and the gain of the VPT, controlled by the bias of the terminals: the photocathode, anode and dynode. SIMION 3D [1] has been used in conjunction with a second program written by us to simulate the behaviour of the incident photoelectrons and the resulting secondary particles in the following manner: photoelectrons from the cathode are accelerated towards the anode mesh (50% transmission) by a high electric field. Those primary electrons which are transmitted are decelerated before being incident on the solid dynode. The dynode is manufactured from a material with a high secondary electron emission coefficient. We model the secondary electron emission from this electrode with a Poisson distribution having a mean value of 20 for an incident electron energy of 1keV. These secondary electrons are accelerated back towards the anode, where a fraction (75%) is collected. The remainder travel back to the dynode and are absorbed upon impact. In the event that these electrons have enough energy to produce tertiary electrons, the simulation is continued.

Using the SIMION 3D simulation, Hobson and Yaselli [2] demonstrated the reproducibility of some of the major features of the VPT response, namely the absolute gain in zero magnetic field and relative time shift. By applying Ramo's Theorem [6] the measured signal may be approximated by calculating the current, I, induced due to an electron moving to an electrode, i.e.:

$$I = q\mathbf{v} \cdot \mathbf{F_k} \,, \tag{1}$$

where $\mathbf{v}$ is the instantaneous velocity of the charge, q, and $\mathbf{F_k}$ is the field that would exist due to q at a distance, d from the induced electrode. The solid curve in Figure 2 shows an example of the output of this model i.e. the induced current on the anode, for an anode potential (V_A) of 1000V, the cathode potential (V_K) at ground and the dynode (V_D) at 800V, whilst the dashed line gives the signal following compensation for attenuation and multiplication factors which arise due to various components of the VPT. It may be seen that the zero-crossing time of the first bi-polar signal is in good agreement with the previously simulated arrival times of electrons at the anode (250ps) [2]. At later times, the signal generated by the secondary electrons emitted from the dynode due to: their direct absorption by the anode; their traversing the anode before being returned by the cathode; and their traversing the anode, returning through the mesh before being detected at the dynode. In order to best simulate the behaviour of the VPT in the experiment, the number of primary electrons has

been calculated to be 2.6×10^6. The resulting signal exhibits a similar shape, although of an increased magnitude.
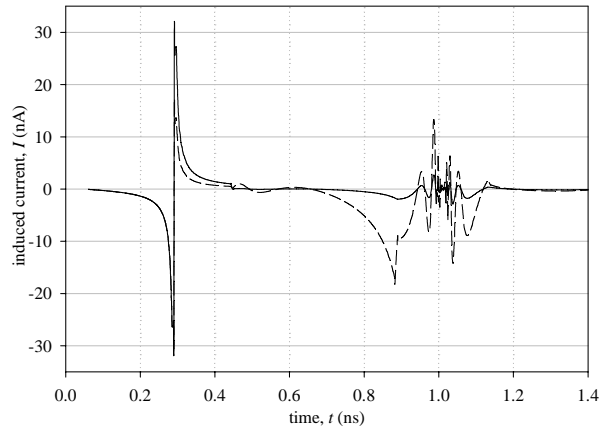

Figure 2: Simulation of current induced at anode by a single incident photoelectron: $V_K = 0V$, $V_A = 1000V$, $V_D = 800V$.

3. Experimental Data

Due to experimental constraints, which require the anode of the VPT to be DC coupled to the 50Ω input of the digital oscilloscope (LeCroy WaveMaster 8300A, 3GHz, 10 Gsamples/second), the potentials used in the above simulation equate to experimental values of V_{KX}=-1000V, V_{AX}=0V and V_{DX}=-200V.
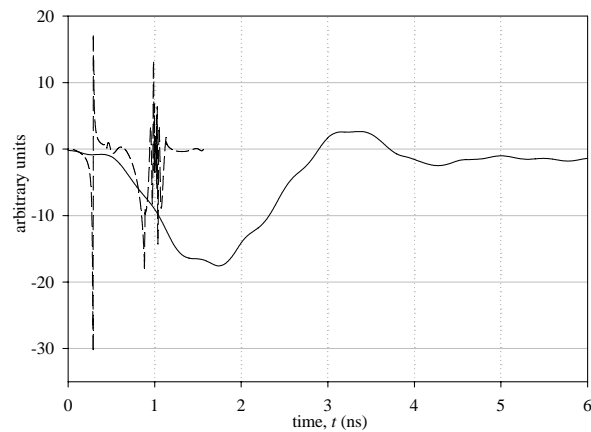

Figure 3. Comparison of simulation (---) and experimental data (— (average of 2000 sequential traces)): the time scale of the experimental data has been shifted by 2.84ns and the magnitude of the first negative peak, scaled to that seen in the simulation.

By shifting the time-zero of the experimental data by 2.84ns, and scaling the magnitude of the negative peak, these data may be compared with the initial simulation on the same axes (see Figure 3).

The results indicate that the initial signal, seen from the SIMION simulation, is reproduced, albeit with an apparent integration due to the finite bandwidth of the experimental setup, which is dominated by the effects of the stray impedances of the VPT. In order to approximate the behaviour of the experimental apparatus upon the signal, the SIMION output has been further processed using SPICE, as discussed below.

4. Further Simulation: *SPICE*

Our simulated current data, shown in Figure 3, has been used as input to SPICE (LTSpice v.2.21) [7], such that the affect of the experimental apparatus upon the signal may be determined. A piece-wise linear approximation was made to the induced current simulated by SIMION, which was then applied to the circuit shown in Figure 4 (inset) to reflect the experimental set-up.
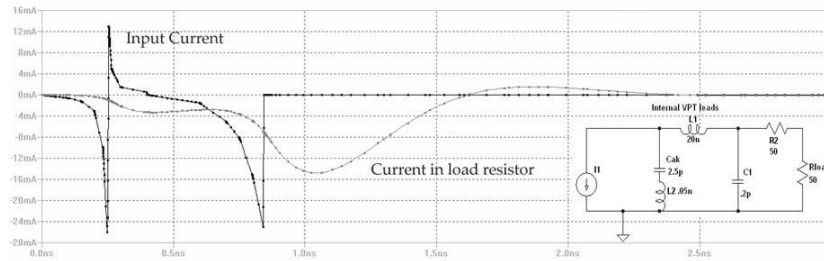

Figure 4. Comparison of input and output current in the 50Ω load resistor current from LT-Spice. The time origin of the load resistor current has been shifted to remove the effect of the delay line. Dots on the curves show the data points. Inset illustrates the circuit employed: The load resistor represents the connection to the digital oscilloscope; *Cak* represents the anode-cathode capacitance, and the value of *L1* is estimated from geometry of the internal connecting leads of the VPT; *C1* represents the stray capacitance between the VPT anode socket and ground.

The resulting signal is shown in Figure 4, from which it can be seen that a plateau appears in the signal at around 0.4ns after time-zero. This feature is also seen to appear between ~0.1–0.5ns in the experimental data (Figure 3).

Experiments have also been conducted to investigate the effect of variable V_A and V_D on the gain of the VPT. Maintaining constant potentials of V_K=0V and V_A=1000V whilst varying the V_D incrementally from 0 to 800V shows that the gain of the VPT increases to a maximum at V_D=600V, beyond which the

gain decreases, thereby confirming that the voltage gain is dependent on both the number of electrons and their velocity. By keeping the potential difference between the anode and dynode constant at 200V, it is evident that the voltage gain increases with increasing V_A. These general trends have also been confirmed from further computer simulation results.

5. Conclusions and Future Work

This paper has reported advances in the simulation process of the VPT using SIMION 3D. An experimental setup has been implemented in order to compare the simulated VPT with a production CMS VPT. Figure 4 demonstrated that the relationship between the simulated and the experimental data is that of integration due to the bandwidth limitation of the physical VPT. In order to show that the experimental timing performance of this device can match the simulated prediction, an impedance matched stripline to the anode should be built into the vacuum tube itself. With these simulation tools we are in a position to further optimise the geometric structure of vacuum photodetectors to provide very fast timing pulses for other applications.

Acknowledgments

References

[1] SIMION 3D v7.0 *Scientific Instrument Services Inc.* 1027 Old York Road, Ringoes, NJ 08551, USA
[2] Hobson, P R and Yaselli, I; *Nuclear Instruments and Methods in Physics Research A* **567** (2006) p226-229
[3] The Compact Muon Solenoid Technical Proposal, CERN/LHCC 94-38 (1994)
[4] Bell, K W et al; *Nuclear Instruments and Methods in Physics Research A* **469** (2001) p29-46
[5] National Research Institute Electron, Morisa Toreza Ave., 68, 194223 St. Petersburg, Russia
[6] Ramo, S; *Proceedings of the IRE* **27** (1939) p584-5
[7] LTSPICE, *Linear Technology*, 1630 McCarthy Blvd., Milpitas, CA 95035-7417, USA [Available: http://www.linear.com/designtools/software/]

The End